MULTI-OBJECTIVE PROCESS PLANNING METHOD FOR MASK PROJECTION STEREOLITHOGRAPHY

A Dissertation
Presented to
The Academic Faculty

by

Ameya Shankar Limaye

In Partial Fulfillment
of the requirements for the Degree of
Doctor of Philosophy in Mechanical Engineering

Georgia Institute of Technology
December 2007

MULTI-OBJECTIVE PROCESS PLANNING METHOD FOR MASK PROJECTION STEREOLITHOGRAPHY

Approved by

Dr. David W. Rosen, Chair
Professor, Mechanical Engineering
Georgia Institute of Technology

Dr. Jye-Chyi Lu
Professor, Industrial and Systems Engineering
Georgia Institute of Technology

Dr. Ali Adibi
Associate Professor, Electrical and Computer Engineering
Georgia Institute of Technology

Dr. Shreyes N. Melkote
Professor, Mechanical Engineering
Georgia Institute of Technology

Dr. Clifford L. Henderson
Associate Professor, Chemical and Biomolecular Engineering
Georgia Institute of Technology

Dr. Christiaan Paredis
Assistant Professor, Mechanical Engineering
Georgia Institute of Technology

Date approved October 1 2007

To my parents
To whom I owe an enormous debt of gratitude

ACKNOWELDGEMENTS

Today, as I enjoy a sense of achievement upon completing my PhD dissertation, I look back at my last five years as a graduate student. This PhD dissertation is a product of sincere and dedicated efforts towards research and technology development over the last five years. While I feel proud to present my dissertation, I also acknowledge that many people have contributed substantially to make this work possible.

Firstly, I would thank my MS and PhD advisor Dr. David W. Rosen for giving me such a coveted project to work on, and for guiding me through it. His insights on Additive Manufacturing technologies guided me to a level of understanding far higher than what I thought was possible. Dr. Rosen's encouragement and confidence in my abilities were a constant source of inspiration for me during my graduate studies.

My committee members: Dr. Cliff Henderson, Dr. Chris Paredis, Dr. Ali Adibi, Dr. J.C. Lu and Dr. Shreyes Melkote provided me with insightful comments during my PhD proposal and Green Light presentations. Their constant feedback was instrumental in keeping this work on schedule.

I thank Dr. Donald O'Shea of the Physics department at Georgia Tech. for strengthening my understanding of Optics.

I thank the members of the Rapid Prototyping and Manufacturing Institute for their help. Amanda O'Rourke was my under graduate research assistant who ran some of the validation experiments for me. I thank Ramesh Singh and John Morehouse for their help with the optical microscope. Andrew Layton also deserves an acknowledgement for proving me with a steady supply of Stereolithography resin for my experiments.

I thank all the members of the Systems Realization Laboratory for their camaraderie. I especially cherish the friendship of Chris, Jamal, Vincent, Benay, Lauren, Ted, Greg, Sanjay, Fei, Jeff and Yong.

Finally, I would like to thank my parents for their unconditional love and support. In my parents, I have wise friends who have guided me throughout my life. Without my parents' faith in my abilities, I would not have been where I am today.

TABLE OF CONTENTS

DEDICATION III

ACKNOWELDGEMENTS IV

LIST OF TABLES XI

LIST OF FIGURES XII

SUMMARY XIX

CHAPTER 1 INTRODUCTION AND MOTIVATION 1

1.1 Micro Stereolithography 3

1.1.1 Stereolithography 4

1.1.2 Three approaches to Micro-Stereolithography 6

1.1.3 Advantages of Mask Projection approach over Scanning approach 10

1.2 Literature review 11

1.2.1 Status of research in MPSLA 11

1.2.2 Process planning in other additive manufacturing technologies 14

1.2.3 Identifying areas where research is needed 17

1.3 Research Objective 19

1.4 Organization of this dissertation 21

CHAPTER 2 FOUNDATIONS FOR FORMLULATING PROCESS PLANNING METHOD FOR MASK PROJECTION STEREOLITHOGRAPHY 24

2.1 Fundamentals of image formation 24

2.1.1 Diffraction (Physical optics) analysis 24

2.1.2 Image modeling by Geometric Optics 32

2.1.3 Selection of modeling strategy 44

2.2 Fundamentals of resin curing 47

2.2.1 Curing mechanism of commercial Stereolithography resins 47

2.2.2 Beer Lambert's law of light absorption 49

CHAPTER 3 DESIGN OF THE MASK PROJECTION STEREOLITHOGRAPHY SYSTEM 52

3.1 Requirements list 52

3.2 Design of the MPSLA system 52

3.2.1 Collimating system 53

3.2.2 Imaging system 55

3.2.3 Build System 60

CHAPTER 4 FORMULATION OF RESEARCH QUESTIONS AND HYPOTHESES 62

4.1 Exposure modeling 62

4.1.1 Selection of optical modeling method 62

4.1.2 Reducing the computational expense of ray-tracing approach 64

4.2 Curing dimensionally accurate parts 67

4.2.1 Failed attempt at modeling print through 69

4.2.2 Modeling layer curing as a transient process 74

4.2.3 Quantifying effect of diffusion underneath cured layer 77

4.2.4 Modeling print through and implementing Compensation zone approach 79

4.3 Smoothing down facing surfaces 80

4.4 Process planning for MPSLA 81

CHAPTER 5 IRRADIANCE MODEL **85**

5.1 Geometric Optics to model image formation **85**

5.1.1 Quantifying the OPD 85

5.1.2 Irradiance model 88

5.1.3 Validating Irradiance model 98

5.2 Multi scale Irradiance model **102**

5.3 Bitmap Generation method **105**

CHAPTER 6 BUILDING ACCURATE THREE DIMENSIONAL PARTS **111**

6.1 Transient layer cure model **112**

6.2 Effect of diffusion of radicals and oxygen **118**

6.3 Modeling print through **124**

6.4 Simulating down facing profile of a test part **128**

6.5 Compensation zone approach: Inverse print-through model **138**

6.5.1 Formulation of compensation zone approach 139

6.5.2 Demonstration of compensation zone approach 140

CHAPTER 7 SURFACE FINISH OF MASK PROJECTION STEREOLITHOGRAPHY BUILDS **151**

7.1 Surface finish of down facing surfaces **152**

7.1.1 Adaptive exposure method 152

7.1.2 Implementing the adaptive exposure method 154

7.2 Surface finish of up facing surfaces **162**

7.2.1 Formulating a multi-objective optimization 162

7.2.2 Solution to the cDSP (Rosen's gradient projection method) 171

7.2.3 Adaptive slicing algorithm 175

7.2.4 Applying adaptive slicing algorithm to a test problem 176

CHAPTER 8 CASE STUDY: BUILDING A PART WITH A QUADRATIC VERTICAL PROFILE 183

8.1 Slicing the part to be built 185

8.2 Generating bitmaps to be imaged 189

8.3 Applying compensation zone approach 190

8.4 Building the test part 198

CHAPTER 9 CLOSURE AND CONTRIBUTIONS 202

9.1 Summary of the dissertation 202

9.1.1 MPSLA system designed and built 203

9.1.2 Modeling image formation 203

9.1.3 Cure modeling 205

9.1.4 Improving surface finish of MPSLA builds 206

9.2 Revisiting the research questions 207

9.3 Contributions 212

9.3.1 Contribution to fundamental knowledge 212

9.3.2 Developmental contributions 214

9.4 Future work 214

APPENDIX A. VALIDATION OF IRRADIANCE MODEL 217

APPENDIX B. MATLAB CODE FOR IMPLEMENTING MULTI-SCALE IRRADIANCE MODEL 226

APPENDIX C. MATLAB CODE TO IMPLEMENT INVERSE IRRADIANCE MODEL 235

APPENDIX D. VALIDATION OF TRANSIENT LAYER CURE MODEL 236

APPENDIX E. QUANTIFYING EFFECT OF RADICAL DIFFUSION 259

APPENDIX F. MATLAB CODE TO GENERATE DOWNFACING PROFILE OF A MULTI-LAYERED PART 274

APPENDIX G. MATLAB CODE USED TO IMPLEMENT COMPENSATION ZONE APPROACH 281

APPENDIX H. MATLAB CODE TO SIMULATE THE DOWN FACING SURFACE PROFILE OF A PART WITH THE OVERHANGING PORTION DISCRETIZED INTO TWO REGIONS 289

APPENDIX I. MATLAB CODE TO IMPLEMENT ROSEN'S GRADIENT PROJECTION ALGORITHM TO OPTIMIZE THE DEVIATION FUNCTION OF THE SLICING COMPROMISE DSP 297

REFERENCES 300

LIST OF TABLES

Table 1.1 Performance and specifications of the MPSLA systems realized by various research groups 12

Table 3.1 Requirements list for the Mask Projection Stereolithography System 52

Table 3.2 Specifications of the components used in the MPSLA system 61

Table 5.1Comparison of experimental observed and analytically computed dimensions of the test layers 101

Table 6.1 Thicknesses of experimentally cured lines against the time of exposure 115

Table 6.2 Analytically computed and experimentally measured values of layer thicknesses 117

Table 6.3 Thicknesses of lines cured with two discrete exposure doses 122

Table 6.4 Effect of waiting time on the diffusion factor 123

Table 6.5 Times of exposure of the layers to implement compensation zone approach 148

Table 7. 1 Times of exposure of the layers to implement the adaptive exposure method 157

Table 7. 2 Optimum slicing schemes for various priority schemes 180

Table 8.1 Optimum slicing schemes for various priorities to objectives 188

Table 8.2 Times of exposure for every layer 197

LIST OF FIGURES

Figure 1.1 Schematic of a Mask Projection Micro Stereolithography system, from Bertsch et al., (2001) 2

Figure 1.2 Schematic of a Stereolithography machine from Jacobs (1992) 4

Figure 1.3 Scheme of the photo-polymerization process (Jacobs, 1992) 6

Figure 1.4 Principle of Scanning Micro-Stereolithography from Beluze et al., (1999) 7

Figure 1.5 Photo chemical reaction for two-photon micro-fabrication. From (Maruo et al., 1997) 8

Figure 1.6 Optical setup for two-photon micro fabrication. From Maruo et al., (1997) 9

Figure 1.7 Principle of Mask Projection Micro-Stereolithography 10

Figure 1.8 Complex 3D microstructures fabricated by Mask Projection Stereolithography. (a) microcup made up of 80 layers of 5 μm thicknesses; (b) microturbine made of 110 layers of 4.5 μm thickness; (c) microcar made of 673 layers of 5 μm thicnkess; (d) microspring 12

Figure 1.9 Structure of Layer cure model, from Limaye and Rosen (2004) 13

Figure 1.10 Region based adaptive slicing and traditional adaptive slicing (Mani et al., 1999) 15

Figure 1.11 Nomenclature used by Reeves and Cobb (1997) 16

Figure 1.12 Surface smoothing caused by print through. From Reeves and Cobb, (1997) 17

Figure 1.13 Micro nozzle 20

Figure 1.14 Organization of this dissertation 23

Figure 2.1 Practical realization of the Fraunhofer diffraction pattern from Hecht (1987) 26

Figure 2.2 Fraunhofer diffraction from an arbitrary aperture where *r* and *R* and very large compared to the size of the hole, from Hecht (1987) 27

Figure 2.3 The light diffracted by a transparency (or object) at front focal point of a lens converges to form a far-field diffraction pattern at the back (or image) focal point of the lens 30

Figure 2.4 Transformation of plane waves into spherical waves by a converging lens 31

Figure 2.5 Spherical aberration from Smith, (1990) 34

Figure 2.6 Coma from Smith, (1990) 35

Figure 2.7 The coma patch. The image of a point source is spread out into a comet-shaped flare from Smith, (1990) 35

Figure 2.8 Astigmatism from Smith, (1990) 36

Figure 2.9 a) Pincushion or positive distortion b) Barrel or negative distortion from (Smith, 1990) 37

Figure 2.10 Optical path difference as the distance between ideal and distorted wave fronts, from Smith, (1990) 39

Figure 2.11 Symbol used in Transfer and Refraction equations. a) The physical meanings of the spatial coordinates (x,y,z) of the ray intersection with the surface and of the ray direction cosines, X, Y, and Z. b) Illustrating the system of sub-script notation from Smith,(1990) 42

Figure 2.12 Scheme of the photo-polymerization process (Jacobs, 1992) 48

Figure 2.13 Theoretical Working curve of a Stereolithography resin 51

Figure 3.1 Optical Structure to embody 53

Figure 3.2 Relative Spectral Distribution of Cure Spot 50 54

Figure 3.3 Collimating system 55

Figure 3.4 Imaging lens without a stop 56

Figure 3.5 Stop placed at the focal point of the lens (Telecentric of the object side) 56

Figure 3.6 Imaging system telecentric on both sides 57

Figure 3.7 Imaging system 58

Figure 3.8 Digital micromirror device from Nayar et al., (2004) 60

Figure 3.9 Optical schematic of the MPSLA system realized as a part of this research 60

Figure 4.1 Multi scale approach to model exposure 66

Figure 4.2 Print-through error 69

Figure 4.3 Modeling print through 70

Figure 4.4 Validating the print through model 71

Figure 4.5 Profiles of down facing surfaces (a) simulated; (b) experimentally observed 72

Figure 4.6 Different rates of radiation attenuation with respect to depth at different instances of time during exposure 75

Figure 4.7 Effect of diffusion of reactive species underneath a cured layers 78

Figure 4.8 Curing smoother down facing surfaces through "adaptive exposure" 80

Figure 4.9 Multi objective process planning method 83

Figure 5.1 Imaging system modeled in OSLO 86

Figure 5.2 OPD calculated by OSLO 88

Figure 5.3 3D transformation of the DMD to reflect the light beam downwards 90

Figure 5.4 Projected image of an 'ON' micromirror to mesh with points 92

Figure 5.5 Ray tracing to model irradiance 95

Figure 5.6 Dimensions of the test bitmap imaged onto the resin surface 98

Figure 5.7 Irradiance profile on returned by the ray tracing code 99

Figure 5.8 Layer cured by imaging the bitmap in Figure 5.6 onto the resin surface 100

Figure 5.9 Dimensions compared in Table 5.1 101

Figure 5.10 Multi scale modeling of irradiance 103

Figure 5.11 Rectangular layer to be cured 106

Figure 5.12 Bitmap generated by applying Layer cure model 106

Figure 5.13 Bitmap generated by the pixel mapping database manually smoothened 107

Figure 5.14 Rectangular layers cured by imaging bitmap in Figure 5.13 onto the resin surface 108

Figure 6.1 Modeling layer curing as a transient phenomenon 114

Figure 6.2 Characterizing the photopolymer 115

Figure 6.3 Thickness of layer cured plotted cured against exposure 117

Figure 6.4 Plot of cure depth versus time of exposure under the assumption of additive nature of exposure 119

Figure 6.5 Effect of two discrete exposures on the thickness of a layer cured 121

Figure 6.6 Effect of diffusion of radicals underneath a cured layer on the layer thickness 121

Figure 6.7 Experimentally determining the value of t' for various waiting times 123

Figure 6.8 Plot of the radical diffusion factor against the waiting time 124

Figure 6.9 Modeling the print through occurring in a "n" layered part 125

Figure 6.10 Test part to simulate the down facing profile of a MPSLA build 129

Figure 6.11 (a) Bitmap to be displayed to cure the required layer; (b) Irradiance distribution on resin surface upon imaging the bitmap 130

Figure 6.12 Simulating profile of the down facing surface for every layer exposed for 80s 131

Figure 6.13 Profile of experimentally cured part with every layer exposed for 80s 132

Figure 6.14 Part cured in order to compare cured profile with simulated profile of down facing surface 133

Figure 6.15 Comparison of the profiles of cured and simulated down facing surfaces 134

Figure 6.16 Plot of error in lateral direction of cured parts plotted against the vertical dimension of the part 136

Figure 6.17 Problem formulation for the compensation zone approach 139

Figure 6.18 Times of exposure of the (a) first; (b) second; (c) third; and (d) fourth layer 141

Figure 6.19 Simulated profile of the down facing surface for the times of exposure as given in Figure 6.18 144

Figure 6.20 Time of exposure discretized into a step function 145

Figure 6.21 Times of exposure for the (a) first; (b) second; (c) third; and (d) fourth layer approximated by a step function 146

Figure 6.22 Simulated profile of the down facing surface cured by implementing the Compensation zone approach 148

Figure 6.23 Part built on MPSLA system by applying compensation zone approach 149

Figure 7.1 Time of exposure discretized into a step function 154

Figure 7.2 Times of exposure for the (a) first; (b) second; (c) third; and (d) fourth layer approximated by a step function 155

Figure 7.3 Simulated profile of the down facing surface after discretizing the overhanging portion of every layer into two parts and applying compensation zone approach at every part 158

Figure 7.4 Part built on MPSLA system by applying compensation zone approach by discretizing the bitmap into three regions 158

Figure 7.5 Cured profile of part built without using adaptive exposure method superimposed on the ideal, i.e. required profile 159

Figure 7.6 Error in the lateral direction of the part built without using adaptive exposure 160

Figure 7.7 Cured profile of part built using adaptive exposure method superimposed on the ideal, i.e. required profile 161

Figure 7.8 Error in the lateral direction of the part built using adaptive exposure 161

Figure 7.9 Nomenclature for the derivation of cusp height as a function of orientation and layer thickness 164

Figure 7.10 Multi objective slicing problem 168

Figure 7.11 Compromise Decision Support Problem: Word formulation 169

Figure 7.12 Adaptive slicing problem modeled as a compromise DSP 170

Figure 7.13 Rosen's gradient projection method 172

Figure 7.14 Rosen's gradient projection method as a black box 175

Figure 7.15 Adaptive slicing algorithm 176

Figure 7.16 Part to be adaptively sliced 177

Figure 8.1 Process planning method for Mask Projection Stereolithography 184

Figure 8.2 Test part to demonstrate process planning method 185

Figure 8.3 Modeling the slicing problem as a compromise DSP 187

Figure 8.4 Sliced part to be built 189

Figure 8.5 Bitmap generated by bitmap generation model to cure the required layer 190

Figure 8.6 Irradiance distribution along the Y dimension of the layer to be cured 191

Figure 8.7 Times of exposure for curing the (a) first; (b) second; (c) third; and (d) fourth layer 192

Figure 8.8 Simulated profile of the down facing surface for the times of exposure as given in Figure 8.7 194

Figure 8.9 Times of exposure for the (a) first; (b) second; (c) third; and (d) fourth layer approximated by step functions 195

Figure 8.10 Simulated and ideal profiles of the down facing surface of the test part for the times of exposure as shown in Figure 8.9 198

Figure 8.11 Curing every layer by imaging two bitmaps onto the resin surface in succession 199

Figure 8.12 MPSLA part built by using the process plan developed in this chapter 200

SUMMARY

Mask Projection Stereolithography (MPSLA) is a high resolution manufacturing process that builds parts layer by layer in a photopolymer. In this research, a process planning method to fabricate MPSLA parts with constraints on dimensions, surface finish and build time is formulated.

As a part of this dissertation, a MPSLA system is designed and assembled. The irradiance incident on the resin surface when a given bitmap is imaged onto it is modeled as the "Irradiance model". This model is used to formulate the "Bitmap generation method" which generates the bitmap to be imaged onto the resin in order to cure the required layer.

Print-through errors occur in multi-layered builds because of radiation penetrating beyond the intended thickness of a layer, causing unwanted curing. In this research, the print through errors are modeled in terms of the process parameters used to build a multi layered part. To this effect, the "Transient layer cure model" is formulated, that models the curing of a layer as a transient phenomenon, in which, the rate of radiation attenuation changes continuously during exposure. In addition, the effect of diffusion of radicals and oxygen on the cure depth when discrete exposure doses, as opposed to a single continuous exposure dose, are used to cure layers is quantified. The print through model is used to formulate a process planning method to cure multi-layered parts with accurate vertical dimensions. This method is demonstrated by building a test part on the MPSLA system realized as a part of this research.

A method to improve the surface finish of down facing surfaces by modulating the exposure supplied at the edges of layers cured is formulated and demonstrated on a test part.

The models formulated and validated in this dissertation are used to formulate a process planning method to build MPSLA parts with constraints on dimensions, surface finish and build time. The process planning method is demonstrated by means of a case study.

CHAPTER 1 INTRODUCTION AND MOTIVATION

Micro-Stereolithography, with its ability to fabricate high resolution 3D parts in a free form fashion, is emerging as a promising candidate to address the needs of all those industries that need high resolution polymer parts. The potential applications of micro Stereolithography have been mentioned in packaging of MEMS devices, (Ikuta et al., 1999), fabrication of scaffolds for tissue growth (Laoui et al., 2005), fabrication of fluidic channels for BioMEMS (Ikuta et al., 1999), etc.

Micro Stereolithography is a term used to denote the adaptation of the Stereolithography process to micro applications (Gardner et al., 2001). The Stereolithography process builds parts in a layer-by-layer fashion, curing every layer by scanning the surface of a photo polymerizing resin by using a laser. There are several adaptations of this process for micro fabrication.

- Integrated hardening: where the laser spot is focused to a 5μm diameter and the resin vat is scanned underneath it to cure a layer (Ikuta et al., 1998; Ikuta et al., 1999)
- Mask Projection Micro Stereolithography: where a bitmap corresponding to the layer to be cured is displayed on a dynamic mask and is imaged onto the resin surface to cure the desired layer (Bertsch et al., 1997)
- Two photon polymerization: where an infrared femto second pulsed laser is focused in the interiors of the resin to initiate polymerization by two photon absorption (Maruo et al., 1997)

All these technologies are fairly new, only about a decade old and none of them has been applied commercially. The author's research is focused on Mask Projection Stereolithography (MPSLA).

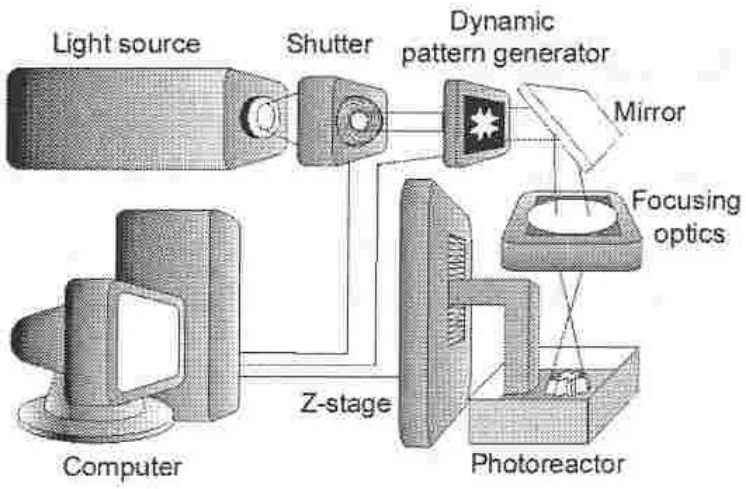

Figure 1.1 Schematic of a Mask Projection Micro Stereolithography system, from Bertsch et al., (2001)

The schematic of the MPSLA system is shown in Figure 1.1. MPSLA process starts with the CAD model of the object to be built. The object is sliced at various heights and the cross-sections of the slices are stored as bitmaps. These bitmaps are displayed on a dynamic pattern generator and are imaged onto the resin surface in order to cure a layer. The layer is built on a platform which is lowered into a vat of resin to coat the cured layer with a fresh layer of resin and the next layer, corresponding to the next cross section is cured on top on it. Likewise, by curing layers one over the other, the entire micro part is built.

Since this technology is inchoate, most work on it has been experimental in nature and very little work on process planning has been done. The process capabilities have

been demonstrated by building very high resolution 3D parts. However, analytical modeling of this process has not been done. In order to mature this technology into a high resolution manufacturing process, it needs to be studied in more detail. The author's research is focused on analyzing the MPSLA process and formulating a process planning method, which will enable the selection of the values of the process parameters to build the part of interest.

The need for a greater understanding of Mask Projection Stereolithography has been accentuated by its adoption by the additive manufacturing companies. Desktop 3D printers by 3D Systems™ , Desktop Factory™ and Envision Tec™ are expected to flood the low cost prototyping market in the near future. These printers are based on the MPSLA technology.

In Section 1.1, an introduction to Micro-Stereolithography has been provided. In Section 1.2, the status of research in MPSLA and in process planning for additive manufacturing technologies has been reviewed and the areas where research is needed are identified. In Section 1.3, the research objective for this PhD is scoped out. In Section 1.4, the organization of this dissertation is presented.

1.1 Micro Stereolithography

The Stereolithography process is explained in Section 1.1.1. The adaptations of this process for micro fabrication have been presented in Section 1.1.2. In Section 1.1.3, the advantages the Mask Projection approach over the other adaptations is presented.

1.1.1 Stereolithography

The Stereolithography process begins with the definition of a CAD model of the desired object, followed by slicing of the three dimensional (3-D) model into a series of very closely spaced horizontal planes that represent the X-Y cross sections of the 3-D object, each with a slightly different Z-coordinate value. All the cross-sections are then translated into a numerical control code and merged together into a build file. This build file is used to control the ultraviolet (UV) light scanner and Z-axis translator. The desired polymer object is then "written" into the UV-curable resist, layer by layer, until the entire structure has been defined.

The schematic of the Stereolithography process is shown in Figure 1.2

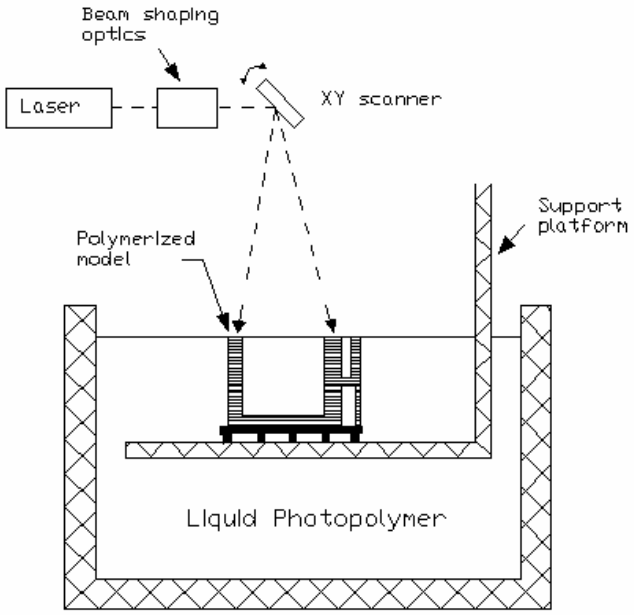

Figure 1.2 Schematic of a Stereolithography machine from Jacobs (1992)

The basic elements of a Stereolithography system are as follows:

- Laser Optics System,
- Scanning System,

- Elevator and Recoater, and
- Computer Control and Software

The laser optics system consists of the laser used to cure the resin and the beam shaping optics. The beam shaping optics is responsible for conditioning the laser beam and focusing it on the resin surface with the desired spot size.

The scanning system consists of a set of galvanometric mirrors, which direct the laser beam so that the required cross-section is scanned.

The elevator lowers the cured layer by a distance of one layer thickness. The recoater coats a fresh layer of resin on the cured layer. This layer is then scanned by the laser.

Computer and the controlling software are used to control the galvanometric mirrors. The computer also synchronizes the motion of laser, elevator and recoater.

When light is incident on a Stereolithography resin, it polymerizes. Polymerization is the process of linking small molecules (monomers) into larger molecules (polymers) comprised of many monomer units. Most Stereolithography resins contain the vinyl monomers and acrylate monomers. Vinyl monomers are broadly defined as monomers containing a carbon-carbon double bond. Acrylate monomers are a subset of the vinyl family with the carboxylic acid group (-COOH) attached to the carbon-carbon double bond. For an acrylate resin system, the usual catalyst is a free radical. In Stereolithography, the radical is generated photo chemically. The source of the photo chemically generated radical is a photo initiator, which reacts with an actinic photon as shown in the photo-polymerization scheme presented in Figure 1.3. This produces radicals (indicated by a large dot) that catalyze the polymerization process.

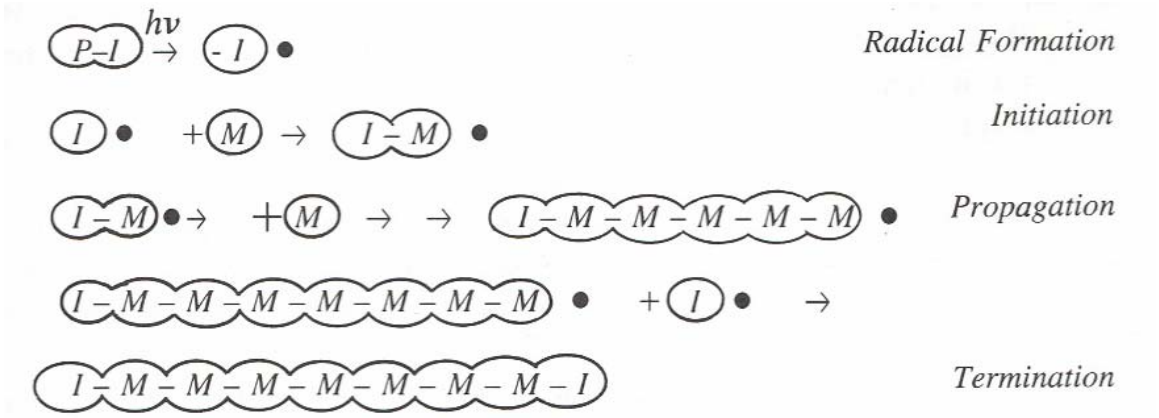

Figure 1.3 Scheme of the photo-polymerization process (Jacobs, 1992)

1.1.2 Three approaches to Micro-Stereolithography

When Stereolithography is used to fabricate micro-parts, it is called Micro Stereolithography. The principle of Micro Stereolithography is the same as Stereolithography, i.e. "Writing a cross section on a photopolymer surface by means of UV light". However, the resolution required of a Micro-Stereolithography process is much finer.

Micro-Stereolithography technologies developed so far can be divided into three categories:

- Scanning Micro-Stereolithography
- Two photon polymerization, and
- Mask Projection Micro-Stereolithography, or Integral Micro-Stereolithography

1.1.2.1 Scanning Micro-Stereolithography Systems

The scanning optical system of the conventional Stereolithography machine introduces errors in the build. Also, the spot size doesn't remain constant throughout the layer cross-section. As a result, the resolution and accuracy are low. In scanning Micro-

Stereolithography, this drawback is eliminated by keeping the light beam focused onto a stationary tight spot and scanning the layer by moving the work piece under the spot.

The principle of Scanning Micro-Stereolithography is shown in Figure 1.4.

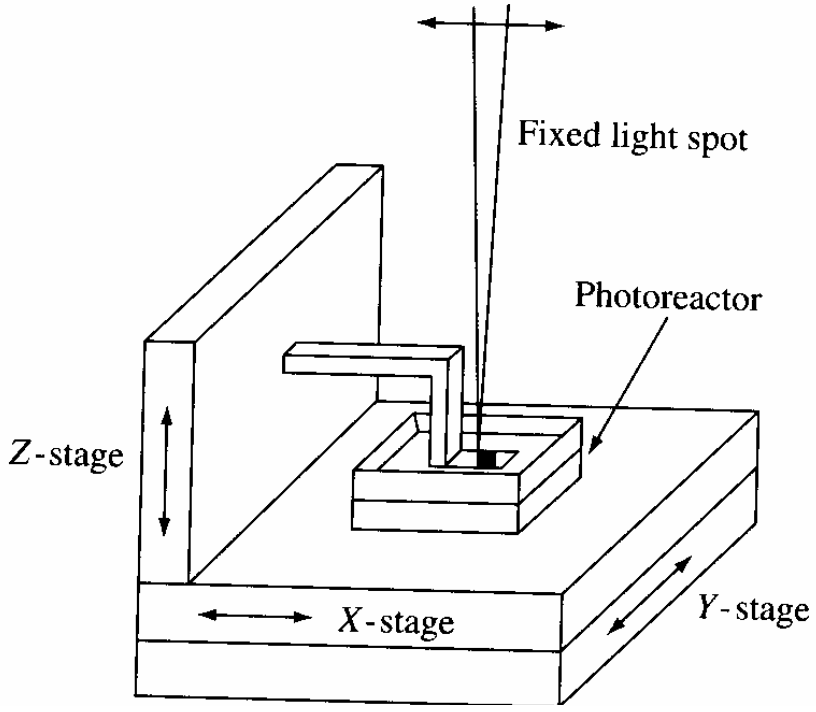

Figure 1.4 Principle of Scanning Micro-Stereolithography from Beluze et al., (1999)

Scanning Micro-Stereolithography systems have been presented in literature in (Nakamoto et al., 1996; Maruo and Kawata, 1998). The following specifications of a typical scanning Micro-Stereolithography process have been presented in (Gardner, Varadan, Awadelkarim, 2001)

- 5 μm spot size of the UV beam
- Positional accuracy is 0.25 μm (in the X-Y directions) and 1.0 μm in the Z-direction.
- Minimum size of the unit of harden polymer is 5 μm x 5 μm x 3 μm (in X, Y, Z).

- Maximum size of fabrication structure is 10mm x 10mm x 10mm.

1.1.2.2 Two photon polymerization

When near IR light, with a high peak power is focused inside a resin, the spatial density of photons becomes high at the focal point. Each initiator in the two photon absorbing (TPA) resin absorbs two near IR photons at the same time and becomes a radical. Resultant radicals break double bonds of carbon in acrylyl group in the monomers and oligomers and successively create new radicals at the ends of these monomers and oligomers. Radicals combine with another monomer. This chain reaction continues till chained radical meets another chained radical. The polymerization mechanism is shown in Figure 1.5.

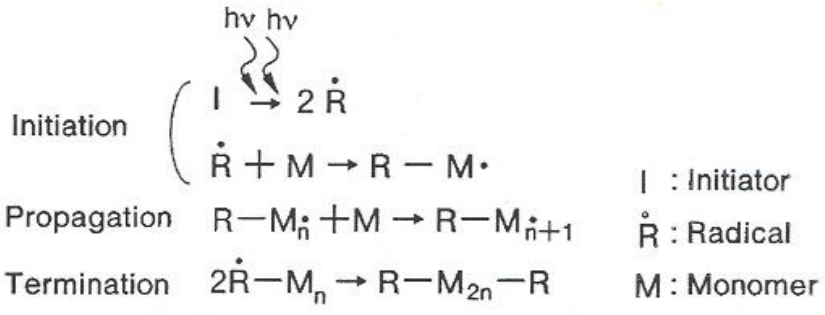

Figure 1.5 Photo chemical reaction for two-photon micro-fabrication. From (Maruo et al., 1997)

Two-photon polymerization (TPP) has been successfully used to fabricate parts with lateral resolution as small as 200nm (Stute et al., 2003).

The schematic of the TPP system realized by Maruo et al., (1997) is shown in Figure 1.6. They used a Ti Sapphire laser, with wavelength 790nm, pulse-width 200fs, and peak power 50kW. The objective lens had an NA = 0.85. The micro part was scanned bottom up.

There are two advantages of the TPP process. First, it is a high resolution process, with a resolution almost 10 times better than other Micro-SLA technologies. Secondly, it is not a layer based technology. This eliminates the errors and delays associated with recoating of resin on layers.

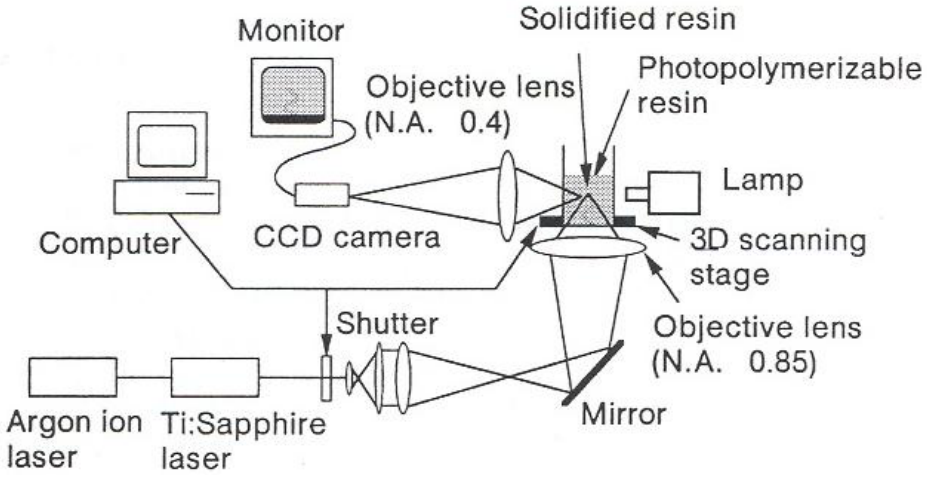

Figure 1.6 Optical setup for two-photon micro fabrication. From Maruo et al., (1997)

1.1.2.3 Mask Projection Micro-Stereolithography

In Mask Projection Micro-Stereolithography, also called Integral Micro Stereolithography, a complete layer is polymerized in one radiation only. The principle of Mask Projection Micro-Stereolithography is shown in Figure 1.7.

In this process, a pattern generator generates the shape of the layer to be cured. This shape patterns a beam of light. The beam is projected onto the resin surface to cure a pattern-shaped layer. This way, layers are built one over the other to build the entire part. Mask Projection Micro Stereolithography Systems have been presented in literature. (Bertsch et al., 1997; Chatwin, 1998; Farsari et al., 1999; Chatwin et al., 1999; Monneret et al., 1999; Bertsch et al., 2000; Farsari et al., 2000; Monneret et al., 2001; Hadipoespito et al., 2003).

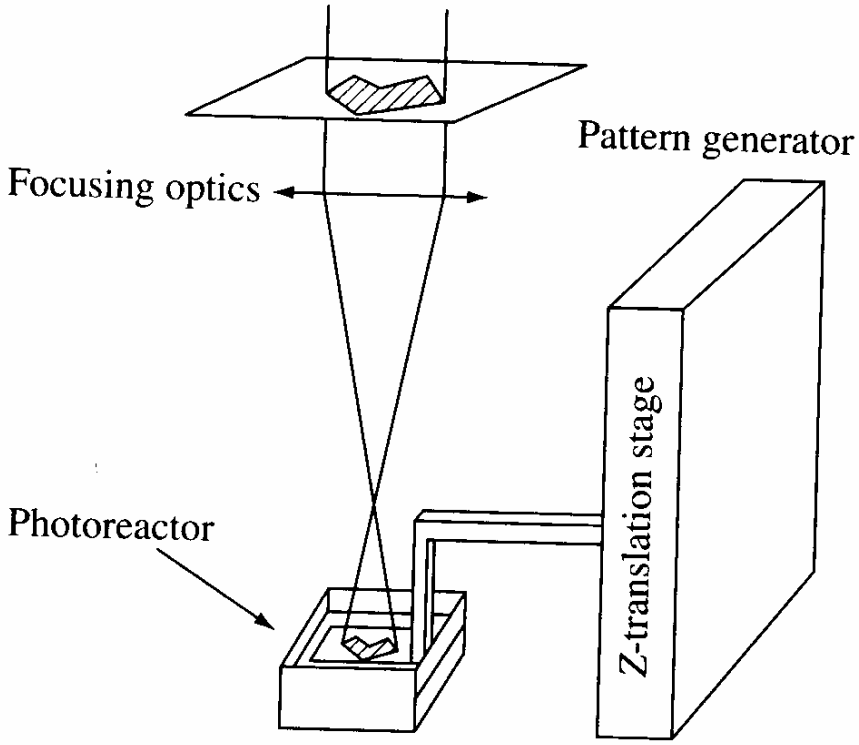

Figure 1.7 Principle of Mask Projection Micro-Stereolithography

1.1.3 Advantages of Mask Projection approach over Scanning approach

The Mask Projection Micro-Stereolithography process has the following advantages over Scanning Micro-Stereolithography.

- The light flux density arriving on the surface of the photopolymerizable resin when projecting the image of a complete layer is low compared to the one of a light beam accurately focused in one point. As a result there are no problems of unwanted polymerizations due to thermal effect.
- Mask Projection Micro-Stereolithography processes are faster than the scanning processes because vector-by-vector scanning is a slower process. The TPP

process is very slow because the spot size of the laser used is very small (~200-400nm).

- The accuracy of integral process is also better because the errors introduced by the X-Y translation stages are avoided. The only mobile element in these systems is the Z-Stage.

Due to these advantages, the author's research is focused on Mask Projection Stereolithography.

1.2 Literature review

The status of research in the field of MPSLA is presented in Section 1.2.1. A review of the research done in process planning for other Rapid Prototyping technologies is presented in Section 1.2.2. Areas which need to be researched are identified in Section 1.2.3.

1.2.1 Status of research in MPSLA

Complex 3D parts cured by MPSLA have been presented in literature by various research groups (Figure 1.8). The specifications of their systems are presented in Table 1.1.

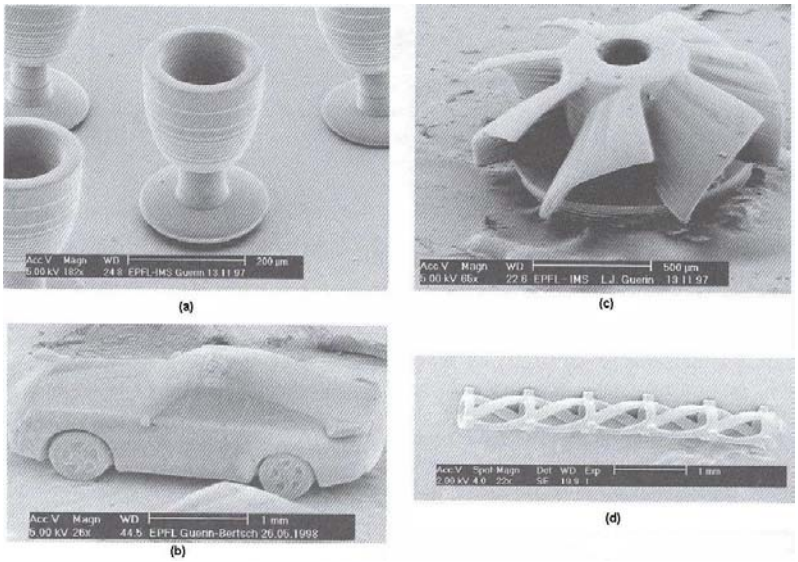

Figure 1.8 Complex 3D microstructures fabricated by Mask Projection Stereolithography. (a) microcup made up of 80 layers of 5 µm thicknesses; (b) microturbine made of 110 layers of 4.5 µm thickness; (c) microcar made of 673 layers of 5 µm thicnkess; (d) microspring

Table 1.1 Performance and specifications of the MPSLA systems realized by various research groups

Research group	Papers published	Light source	Mask	Resolution	Component size	Speed
Bertsch	(Bertsch et al., 1997)	Laser: 515 nm	LCD	5 x 5 x 5 µm	1.3 x 1.3 x 10mm^3	Not reported
Chatwin	(Chatwin et al., 1998); (Farsari et al., 1999); (Chatwin et al., 1999); (Farsari et al., 2000)	Laser: 351.1 nm	SLM	5 µm lateral resolution	Not reported	60s exposure time per layer 50µm thick
Monneret	(Monneret at al., 1999); (Monneret et al., 2001)	Broadband Visible light	LCD	2 µm lateral resolution	Not reported	10µm layers at 1 layer / minute
Bertsch	(Bertsch et al, 1999); (Beluze et al., 1999)	Lamp (Visible)	DMD	5 x 5 x 5 µm	6 x 8 x 15 mm^3	Components fabricated at the rate of 1mm/hour
Bertsch	(Bertsch et al., 2000)	Lamp (UV)	DMD	10 x 10 x 10 µm	10.24 x 7.68 x 20 mm^3	673 layer micro-car model with each layer 5µm thick in 3 hours.
Hadipoespito	(Hadipoespito et al., 2003)	Lamp (UV)	DMD	20µm lateral resolution	Not reported	Not reported
Limaye and Rosen	(Limaye and Rosen, 2004, 2005)	Lamp (UV)	DMD	6 µm lateral resolution	2 x 2 x 1 mm	90s per layer
Zhang	(Sun et al., 2005)	Lamp (UV)	DMD	0.6µm lateral resolution	Not reported	Not reported

Research in MPSLA has been largely experimental in nature. Analytical modeling has been presented only in Limaye and Rosen, (2004). In this paper, we have formulated the "Layer cure model" which models the dimensions of a single layer cured using our system in terms of the process parameters used to cure it. The structure of the Layer cure model is presented in Figure 1.9.

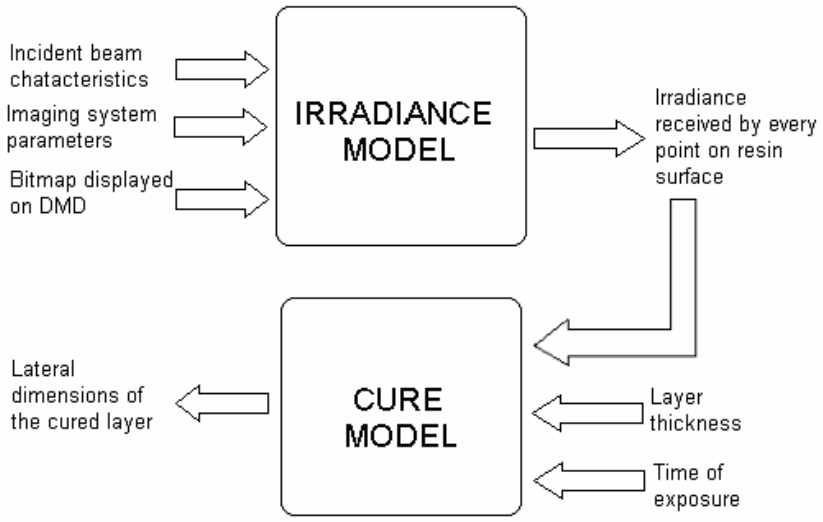

Figure 1.9 Structure of Layer cure model, from Limaye and Rosen (2004)

The Layer cure model consists of two models: the Irradiance model and the Cure model. The Irradiance model computes the irradiance received at every point on the resin surface by adopting the ray tracing procedure. Cure model computes the cure profile of a layer in terms of the irradiance incident on the resin surface and the resin properties. The Irradiance model and the Cure model can be used in conjunction to model the dimensions of the layer cured.

1.2.2 Process planning in other additive manufacturing technologies

Process planning has been done for various RP processes with different objectives, like reducing dimensional errors, improving surface finish and reducing build time. In this section, this literature has been reviewed.

Dimensional accuracy

The most common source of errors in the vertical dimensions of Stereolithography builds is print through. Print through is caused by the addition of residual energies from separate laser scans exceeding the photo polymerization threshold of the resin. This problem has been addressed in commercial Stereolithography machines by adopting the "Layer compensation" approach. Here, the lowest layer of a part being built is skipped in order to compensate for the increase in dimension that would occur due to print through (AccuMax^{TM} Toolkit User Guide, 1996).

Lynn-Charney and Rosen (2000) empirically modeled geometric tolerances of Stereolithography builds in terms of process parameters. They considered six types of geometric tolerances: positional, flatness, parallelism, perpendicularity, concentricity and circularity. Response surfaces (Myers and Montgomery, 1995) were constructed to relate these tolerances with various process parameters.

Surface finish

Surface finish is rougher along the *z*-axis of RP parts than parallel to the *xy*-plane because of the "stair stepping" effect (Paul and Voorakarnam, 2001). It is most prominent when the surface orientation is not orthogonal to the slice's vertical profile. The cusp height is considered as a measure of the surface finish of a RP prototype in the vertical direction. Cusp height is the maximum surface deviation due to stair stepping effect and

is directly dependent on the layer thickness and orientation angle. Suh and Wozny, (1994) formulated an analytical relation between the cusp height and the layer thickness to determine the maximum allowable layer thickness that would satisfy the constraint on cusp height.

Reduction in layer thicknesses leads to an increase in build time. Sabourin et al., (1996) addressed this problem by stepwise uniform refinement. They proposed using thinner slices only where the vertical profile is highly curved, while using thicker slices everywhere else, thereby reducing the build time. Mani et al., (1999) proposed region based adaptive slicing, where only the portion of layers adjacent to the edge of the part are sliced with smaller layer thicknesses while the interiors are composed of thicker layers. (Figure 1.10)

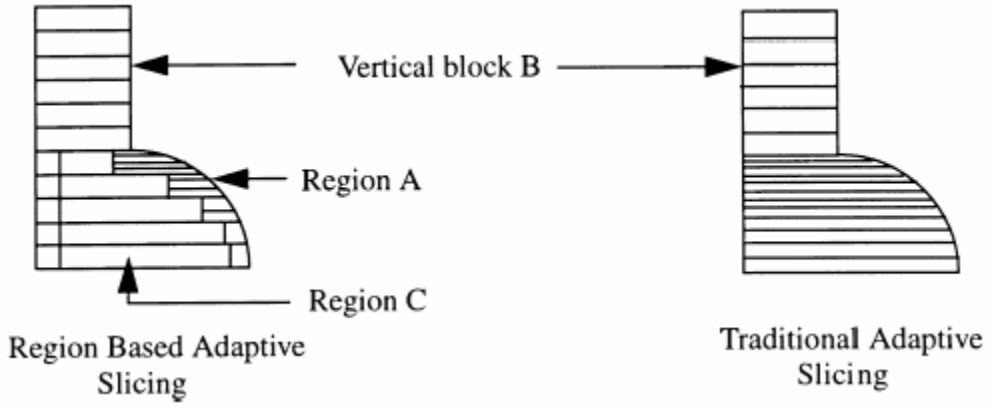

Figure 1.10 Region based adaptive slicing and traditional adaptive slicing (Mani et al., 1999)

Reeves and Cobb, (1997) expressed surface roughness of RP parts as a function of surface angle (θ), layer thickness (α) and layer profile (ϕ), as shown in Figure 1.11, to obtain the following expression for surface roughness of up- and down-facing surfaces.

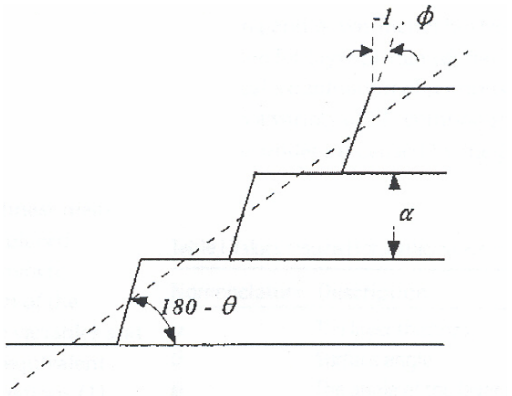

Figure 1.11 Nomenclature used by Reeves and Cobb (1997)

$$Ra_{up} = \frac{\alpha(\tan\phi\sin\theta + \cos\theta)}{4} + K$$
$$Ra_{down} = \frac{\alpha(\tan(-\phi)\sin(180-\theta) + \cos(180-\theta)}{4} + K_1 \quad (1.1)$$

where K and K_1 are factors determined experimentally.

Reeves and Cobb, (1997) observed that the surface finish of the down facing surfaces was much better than that predicted by their analytical model. They attribute this effect to 'print through'. As shown in Figure 1.12, print through causes a partial "fillet" between two layers causing a modification to the layer profile and hence, reducing the surface deviation.

Sager and Rosen (2005) formulated a process planning method to cure smooth down facing SLA surfaces by controlling the scan parameters (laser velocity and pitch of scan). They discretized the down facing surface into an array of points and chose process parameters in such a way that the sum of squares of the deviations of the exposures received by these points from the threshold exposure was minimized.

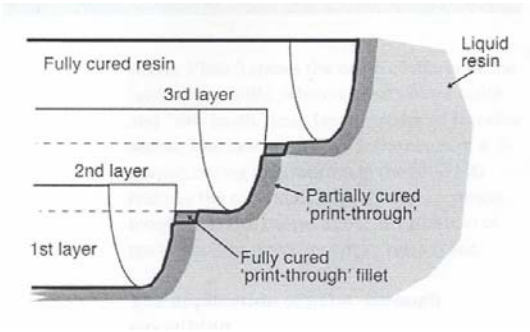

Figure 1.12 Surface smoothing caused by print through. From Reeves and Cobb, (1997)

Build time

Chen and Sullivan, (1996) formulated an algorithm to predict build time of Stereolithography parts by using detailed scan and recoat information from the build files. Other researchers have also quantified build time. All of them have broken down the part building process into its constituent steps and modeled the time required to complete each of these steps.

1.2.3 Identifying areas where research is needed

In this subsection, the areas in which research needs to be done in order to mature the MPSLA technology into a MEMS packaging technology are identified.

Dimensional accuracy of the 3D MPSLA part

In Limaye and Rosen, (2004), the dimensional accuracy of a single layer cured using MPSLA has been quantified. However, the accuracy in all the three dimensions of a MPSLA part has not been studied. While tolerances can be empirically expressed in terms of process parameters by conducting numerous experiments as done by Lynn-Charney and Rosen, (2000) this would require numerous experiments to have enough

confidence in the response surfaces. **Analytically relating the errors in dimensions to the process parameter values would aid process planning to a large extent.**

The Layer compensation approach in commercial SLA systems to compensate for errors in vertical dimensions is an ad-hoc approach that would work only if the down facing surface is horizontal and the print through is exactly equal to the thickness of the lowermost (skipped) layer. **A more rigorous approach to avoid print through errors, applicable to parts of any geometry is needed.**

Surface finish of MPSLA builds

Extensive research has been done on improving the surface finish of laser-scanning Stereolithography. The relation between layer thicknesses and surface finish has already been formulated by numerous researchers. This can be adapted to MPSLA. Though print through smoothing phenomenon has been observed in Stereolithography by Reeves and Cobb (1997), it has not been successfully employed to obtain smoother down facing surfaces due to lack of control offered by SLA machines. *"The size of the print through fillet is related to the laser energy initiating photo polymerization, which is, in turn affected by both laser power and scan speed. If either or both of these process attributes could be varied, then the size of the fillet could be modified and matched to surface angle, hence producing smoother down facing surfaces. In reality, both scan speed and laser power are complex attributes of the SLA process and out of control of the SL user"* (Reeves and Cobb, 1997). MPSLA process can achieve the gray scaling of the irradiance pattern required for print through smoothing. **Analytical model relating the gray scaling of irradiance pattern projected onto the resin surface with the surface finish is needed.**

Process planning

Process planning under multiple conflicting objectives has been done by Lynn-Charney and Rosen (2000) and West et al. (2001), for commercial Stereolithography process. A similar process planning method needs to be formulated for MPSLA.

1.3 Research Objective

In this research, the author seeks to address the research areas identified in Section 1.2.3. In this section, a motivating problem is provided that integrates all the research areas mentioned above.

Micro nozzles have numerous applications. Apart from their current use in printer heads, their usage is envisaged as propelling devices for micro/nano satellites, as micro fuel injectors and for numerous other micro fluidic applications. Micro nozzles are currently fabricated by bulk etching techniques by etching a trench of the shape of the nozzle in the plane of a wafer and anodically bonding glass on both sides (Bayt and Breuer, 2000) or by etching a 'via' in silicon using anisotropic etch (Meacham et al., 2004). However, these fabrication techniques cannot fabricate micro nozzles with any geometry in any orientation. Mask Projection Stereolithography can be used for this purpose.

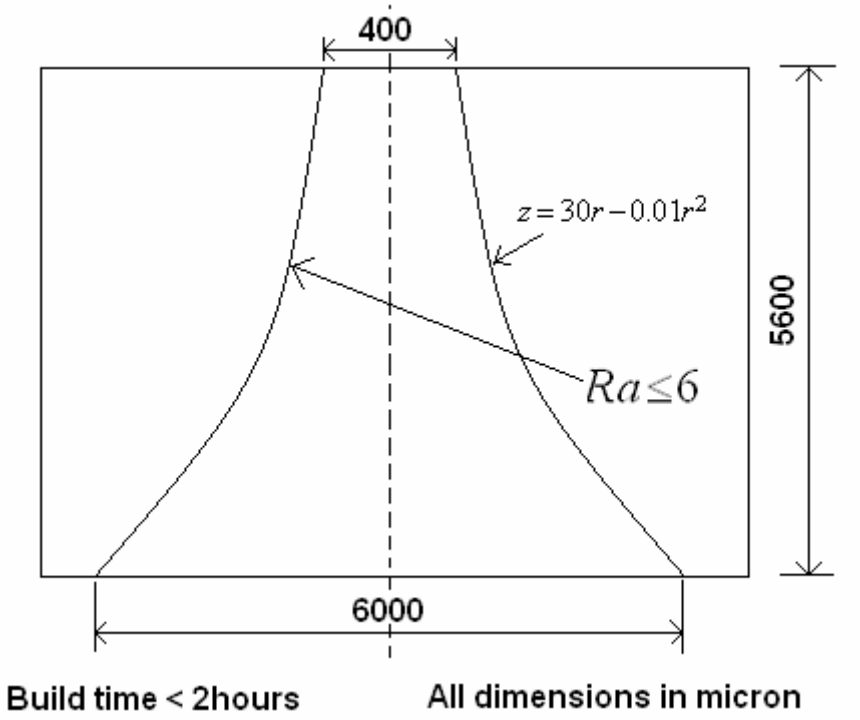

Figure 1.13 Micro nozzle

Example problem

The micro nozzle shown in Figure 1.13 is to be built in the vertical orientation. Hypothetical constraints on the dimensions of the nozzle and on its surface roughness are shown in the figure. The nozzle is to be fabricated using the MPSLA process in less than 10 minutes.

The micro nozzle example presented here is representative of the class of parts whose fabrication would be enabled by this research. From the example problem, the following research objective has been abstracted.

To formulate a process planning method to build MPSLA parts with constraints on dimensions, surface finish and build time

1.4 Organization of this dissertation

The research objective scoped out in Section 1.3 is realized in this dissertation by completing the tasks as expressed in Figure 1.14. A MPSLA system is realized as a part of this research. The part building process is modeled by adopting a multi-scale modeling strategy. This model is used to do process planning to achieve objectives of dimensional accuracy, build time and surface finish. The work done in achieving these three objectives in integrated to formulate a multi-objective process planning method that would allow a user to obtain trade-offs between these objectives. As shown in Figure 1.14, there are three research questions that would have to be addressed in order to complete these tasks. Hypotheses are formulated and tested for each of these research questions.

In Chapter 2, the foundational knowledge and theory necessary to achieve the research objective is presented.

In Chapter 3, the design of the MPSLA system realized as a part of this research is presented.

In Chapter 4, the research objective is broken down into research questions and hypotheses are formulated for these research questions. Strategies to test these hypotheses are formulated in this chapter.

In Chapter 5, the "Irradiance model" is formulated. This model computes the irradiance received by the resin surface when a given bitmap is imaged onto it for a given time. The Irradiance model is validated by building test layers on the MPSLA system.

In Chapter 6, the Print through model is formulated, which computes the print through that would occur underneath a multi- layered part. The Print through model is

used to formulate the Compensation zone approach is introduced to avoid print through errors introduced when layers are cured over each other. The Compensation zone approach is demonstrated by building test parts.

In Chapter 7, the Adaptive exposure method is formulated which can be used to cure downward facing surfaces accurately and with a good surface finish. A slicing algorithm is presented to enable a process planner slice a 3D CAD file in order to achieve the required tradeoffs between objectives of build time and surface finish of up facing surfaces is formulated

In Chapter 8, the work presented in Chapters 5, 6 and 7 is integrated to formulate a process planning method to build MPSLA parts with constraints on dimensions, surface finish and build time is formulated. This process planning method is demonstrated on a test part with quadratic up facing and down facing surfaces.

In Chapter 9, the research questions are re-visited and the contributions of this work are summarized. The limitations of the work and directions for future work are also discussed.

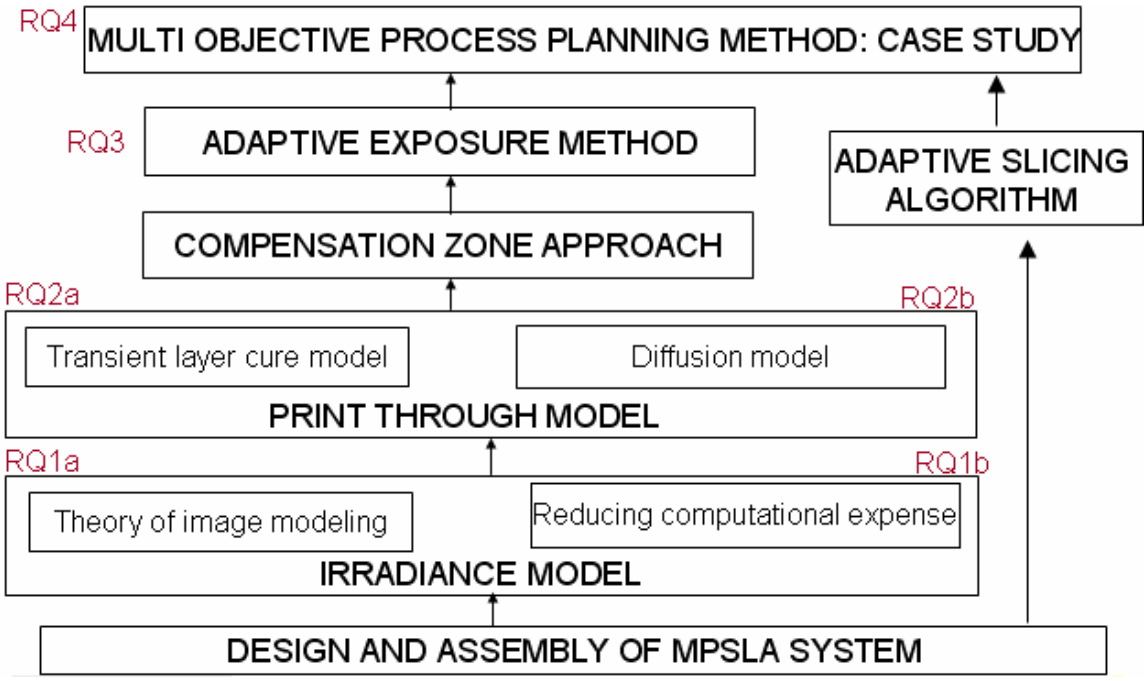

Figure 1.14 Organization of this dissertation

Summary

In this chapter, the motivation to analytically model the Mask Projection Stereolithography process and formulate a process planning method for the same is presented. Literature review has been presented on Mask Projection Stereolithography and on process planning for other additive manufacturing processes. The organization of chapters in this dissertation has been presented.

CHAPTER 2 FOUNDATIONS FOR FORMLULATING PROCESS PLANNING METHOD FOR MASK PROJECTION STEREOLITHOGRAPHY

In this chapter, the foundational knowledge required to analytically model the MPSLA process is presented. The fundamentals of image formation are discussed in Section 2.1. The fundamentals of resin curing are presented in Section 2.2.

2.1 Fundamentals of image formation

During the irradiation step, a bitmap displayed on the DMD is imaged onto the resin surface. Modeling the irradiance on the resin surface is, essentially, modeling the process of image formation by the imaging lens. There are two possible ways of modeling the process of image formation: by assuming wave nature of light; and by assuming ray nature of light. In the first case, diffraction analysis is used, while, if the second assumption is considered valid, then geometric optical analysis is used to model the image formed. In this section, both the methods of analysis are presented.

If the imaging system is 'perfect', i.e. free of aberrations, then diffraction analysis should be used. If the imaging system is imperfect, i.e. has significant aberrations, then, geometric optical analysis is to be used. This section also presents the conditions that have to be satisfied in order for either of these analyses to be used.

2.1.1 Diffraction (Physical optics) analysis

In diffraction analysis, light is considered to be propagating as waves. When light passes through an aperture in an opaque screen, it gets diffracted. If the diffracted pattern is observed far away from the screen, then, the Fraunhofer diffraction pattern is observed. The distance between the aperture and the image plane, for observing Fraunhofer

diffraction is very large. A practical method of realizing this diffraction pattern is to use a convex lens to focus the diffraction pattern onto the screen. Fraunhofer diffraction pattern is generated by the lens. The Fraunhofer diffraction pattern can be shown to be the Fourier transform of the aperture function. Thus, the lens is considered as a Fourier transformer.

In this section, apart from presenting formulae, the derivations explaining the role of a lens as a Fourier transformer are also presented in order to highlight the assumptions that are made in these derivations. It is important to be aware of these assumptions while evaluating the validity of using diffraction analysis to model image formation in practical situations. In Section 2.1.1.1, the Fraunhofer diffraction pattern for light passing through an aperture is derived. In Section 2.1.1.2, the Fraunhofer diffraction pattern is shown to be the Fourier transform of the aperture function. In Section 2.1.1.3, the role of a converging lens as a Fourier transformer is presented.

2.1.1.1 Fraunhofer diffraction

Physical optics assumes that light propagates in the form of wavefronts. Huygen-Fresnel principle states that: "*Every unobstructed point of a wavefront at a given instant in time, serves as a source of spherical secondary wavelets (with the same frequency as that of the primary wave). The amplitude of the optical field at any point beyond is the superposition of all these wavelets (considering their amplitudes and relative phases)".*

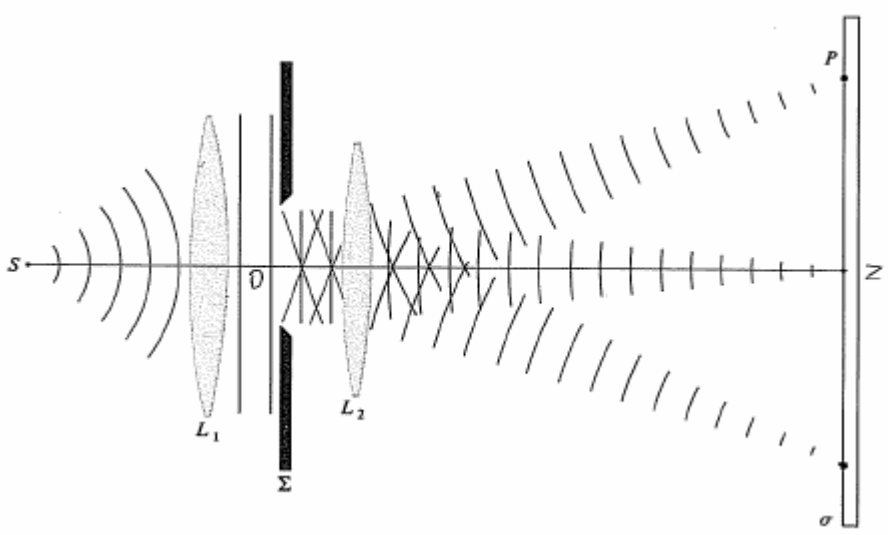

Figure 2. 1 Practical realization of the Fraunhofer diffraction pattern from Hecht (1987)

Imagine an opaque shield, Σ, containing a single small aperture illuminated by plane waves from a distant point source. Suppose the plane of observation σ is parallel to the shield and far away from Σ as shown in Figure 2.1. The waves emanating from the aperture interfere (either constructively or destructively) on σ and a diffraction pattern is formed. If the distance between the two screens is sufficiently large (or if a perfect lens is used to focus the light), Fraunhofer, or far-field diffraction pattern, can be observed on the screen σ.

Derivation of Fraunhofer diffraction from an aperture

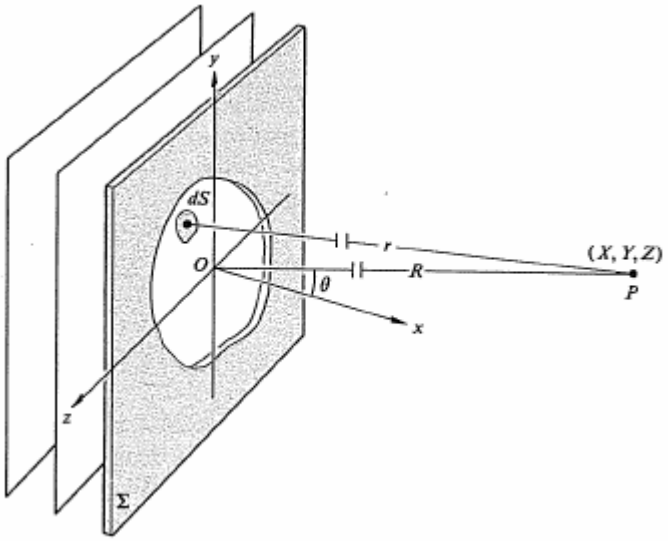

Figure 2.2 Fraunhofer diffraction from an arbitrary aperture where *r* and *R* and very large compared to the size of the hole, from Hecht (1987)

Consider the configuration depicted in Figure 2.2. A monochromatic plane wave propagating in the x-direction is incident on the opaque diffracting screen Σ. We wish to find the consequent (far-field) flux-density distribution in space, or equivalently at some arbitrary point *P*. According to the Huygens-Fresnel principle, a differential area *dS*, within the aperture may be envisioned as being covered with coherent secondary point sources. But *dS* is much smaller in extent than λ so that contributions at *P* from *dS* remain in phase and interfere constructively. If $\mathcal{E}_A$ is the source strength per unit area, assumed to be constant over the entire aperture, then the optical disturbance at *P* due to *dS* is the real part of

$$dE = \frac{\mathcal{E}_A}{r} e^{i(\omega t - kr)} dS \tag{2.1}$$

where $k = 2\pi / \lambda$

The source strength is divided by *r*, the distance of the area *dS* from point P, to account for the attenuation in strength that would occur due to distance. The distance *r* can be expressed in terms of the co-ordinates of point P and those of area *dS* as

$$r = [X^2 + (Y - y)^2 + (Z - z)^2]^{1/2} \tag{2.2}$$

Fraunhofer condition occurs when this distance approaches infinity. For such large distances, we can replace *r* by the distance $\overline{OP}$, i.e. *R*, in the amplitude term, as long as the aperture is relatively small. But the approximation of *r* in phase needs to be treated more carefully because $k = 2\pi / \lambda$ is a large number.

$$R = [X^2 + Y^2 + Z^2]^{1/2} \tag{2.3}$$

Hence,

$$r = R[1 + (y^2 + z^2) / R^2 - 2(Yy + Zz) / R^2]^{1/2} \tag{2.4}$$

In the far field case, R is very large in comparison with aperture dimensions and the term $(y^2 + z^2) / R^2$ can be neglected to obtain equation (2.5).

$$r = R[1 - 2(Yy + Zz) / R^2]^{1/2} \tag{2.5}$$

The total disturbance arriving at point *P* is

$$E = \frac{\mathcal{E}_A e^{i(\omega.t - kR)}}{R} \int_{Aperture} \int e^{ik(Yy + Zz)/R} dS \tag{2.6}$$

2.1.1.2 Fraunhofer diffraction as a Fourier transform

Equation (2.6) can be re-written by replacing the differential area term *dS* with *dydz* to get equation (2.7).

$$E(Y,Z) = \frac{\mathcal{E}_A e^{i(\omega t - kR)}}{R} \int_{Aperture} \int e^{ik(Yy + Zz)/R} dydz \tag{2.7}$$

If we limit ourselves to a small region in space over which R is essentially constant, everything in front of the integral, with the exception of $\mathcal{E}_A$, can be lumped together. $\mathcal{E}_A$ could vary within the aperture and can be expressed by the complex quantity

$$A(y,z) = A_0(y,z)e^{i\phi(y,z)} \tag{2.8}$$

which is called as the aperture function. The amplitude of the field over the aperture is described by $A_0(y,z)$ while the point to point phase variation is represented by $e^{i\phi(y,z)}$. Accordingly, $A(y,z)dydz$ is proportional to the diffracted field emanating from the differential source element $dydz$. Consolidating this much, we can reformulate equation (2.8) more generally as

$$E(Y,Z) = \int_{-\infty}^{+\infty}\int_{-\infty}^{+\infty} A(y,z)e^{ik(Yy+Zz)/R}dydz \tag{2.9}$$

The limits on the integral can be extended to $\pm\infty$ because the aperture function is nonzero only over the region of the aperture.

Let us define spatial frequencies k_Y and k_Z as

$$k_Y = kY / R \tag{2.10}$$

and

$$k_Z = kZ / R \tag{2.11}$$

The diffracted field (equation 2.9) can now be written as

$$E(k_Y,k_Z) = \int_{-\infty}^{+\infty}\int_{-\infty}^{+\infty} A(y,z)e^{i(k_Y y+k_Z z)}dydz \tag{2.12}$$

Equation 2.12 can be immediately recognized to be the Fourier transform of $A(y,z)$. Thus, the derivation proves that: *the field distribution in the Fraunhofer diffraction pattern is the Fourier transform of the field distribution across the aperture (i.e. the aperture function).* Symbolically, this is written as

$$E(k_Y, k_Z) = F\{A(y,z)\} \tag{2.13}$$

2.1.1.3 Lens as a Fourier transformer

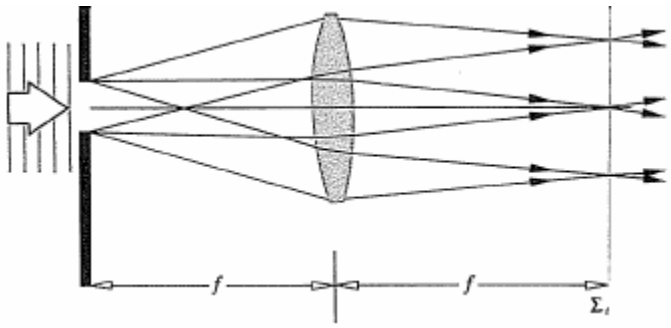

Figure 2.3 The light diffracted by a transparency (or object) at front focal point of a lens converges to form a far-field diffraction pattern at the back (or image) focal point of the lens

Figure 2.3 shows a transparency, located in the front focal plane of a converging lens, being illuminated by parallel light. The object, in turn scatters plane waves, which are collected by the lens, and parallel bundles of rays are brought to convergence at its back focal plane. If a screen was placed there, at Σ_f, the so-called transform plane, we would see the far-field diffraction pattern of the object spread across it. In other words, the electric field distribution across the object mask, i.e. the aperture function, is transformed by the lens into the far-field diffraction pattern. This diffracted field is the Fourier transform of the aperture function, as has been derived in equation 2.12. Thus, the image formed by a lens is simply the Fourier transform of the aperture function, or, the object.

The role of the lens in forming a Fraunhofer diffraction pattern on its back focal plane is described here. In Figure 2.4, when plane waves from the aperture are incident

on a convex lens, the lens transforms the plane waves into spherical waves, converging at the various points on the screen.

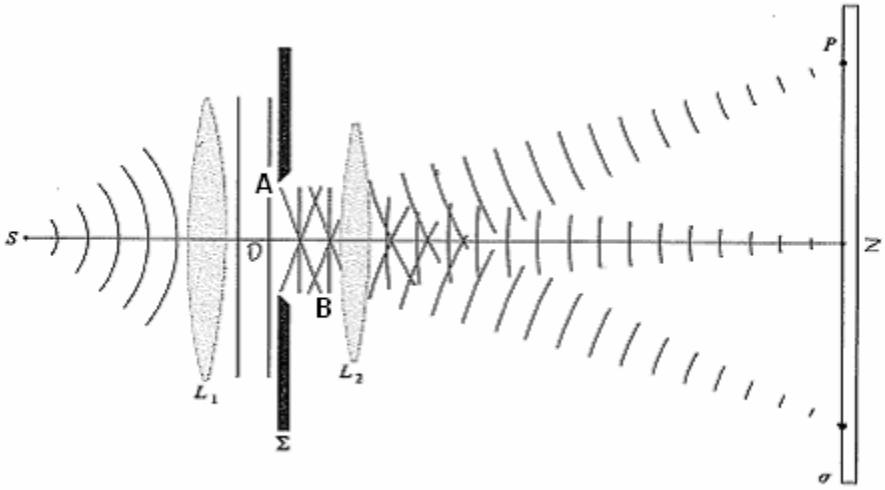

Figure 2. 4 Transformation of plane waves into spherical waves by a converging lens

Consider an off axis point P. The plane wave AB gets converted to a spherical wave, which converges at P. Since the wave converging at point P is spherical, it is equivalent to saying that the point P is **equidistant** from every point on the plane wave AB. In other words, it is equivalent to saying that, in the absence of lens, point P is located at an infinite distance from the diffracting aperture. Hence, the conditions of far field diffraction pattern are satisfied and a Fraunhofer diffraction pattern is obtained on the screen. It should thus be noted that the **lens has to transform plane waves incident on it into spherical waves to simulate a Fraunhofer diffraction pattern.** In case of real lenses with spherical surfaces, the optical aberrations distort the wavefront emanating from the lens, thereby making the wavefront non-spherical. For such a situation, the image will not be the Fourier transform of the aperture function.

Another important consideration is related to the waves that are incident on the lens from the aperture. If they are not plane waves then again, there is an error introduced in the wavefront emanating beyond the lens. Further, the light from the aperture has to be monochromatic and coherent in order to obtain Fraunhofer diffraction pattern.

2.1.2 Image modeling by Geometric Optics

In this section, an alternative approach to modeling the image formation by an imaging system is presented. This approach assumes that light travels in the form of rays, as opposed to waves. This theory is valid in case of aberration limited optical systems. In Section 2.1.2.1, an introduction to optical aberrations is provided. In Section 2.1.2.2, the concept of Optical Path Difference (OPD) is introduced as the parameter which is used to quantify the extents of optical aberrations present in an optical system. In Section 2.1.2.3, the exact ray tracing procedure, used to model imaging in an aberration limited optical system is presented.

2.1.2.1 Introduction to optical aberrations

When a perfect lens focuses any object onto an image plane, all rays emanating from any one point on the object meet at one and the same point on the image. Under this condition, the image formed is termed as the perfect image. For a thin lens, this condition occurs when the image distance (i) and the object distance (o) are related to the focal length (f) of the lens by the thin lens equation:

$$1/i - 1/o = 1/f \tag{2.14}$$

The magnification of the image is given by $M = -(i/o)$.

For a spherical lens with a finite thickness, even if the image and object distances are set as calculated using the thin-lens equation, all rays from any one point on the object do not converge to the same point on the image. Also, the focal length of a spherical lens is not the same for all object points. This results in optical aberrations. Optical aberrations can be thought of as imperfections caused in an image. They lead to the formation of a distorted image, with lower contrast. Aberrations are classified as follows:

- Spherical aberration
- Astigmatism
- Coma
- Distortion
- Chromatic aberration

Spherical aberration

Spherical aberration can be defined as variation of focus with aperture. Figure 2.5 is an exaggerated sketch of a spherical lens forming an image of an axial object point situated a great distance away. It can be seen that the rays away from the optical axis come to focus (intersect the axis) earlier than the rays closer to it. In Figure 2.5, point A is the paraxial focus. The distance from the paraxial focus to the axial intersection of the marginal rays (i.e. rays from the edges of the lens) is called longitudinal spherical aberration. LA_R is the longitudinal spherical aberration. Transverse or lateral spherical aberration is the name give to the aberration when it is measured in a direction perpendicular to the optical axis. TA_R is the transverse spherical aberration.

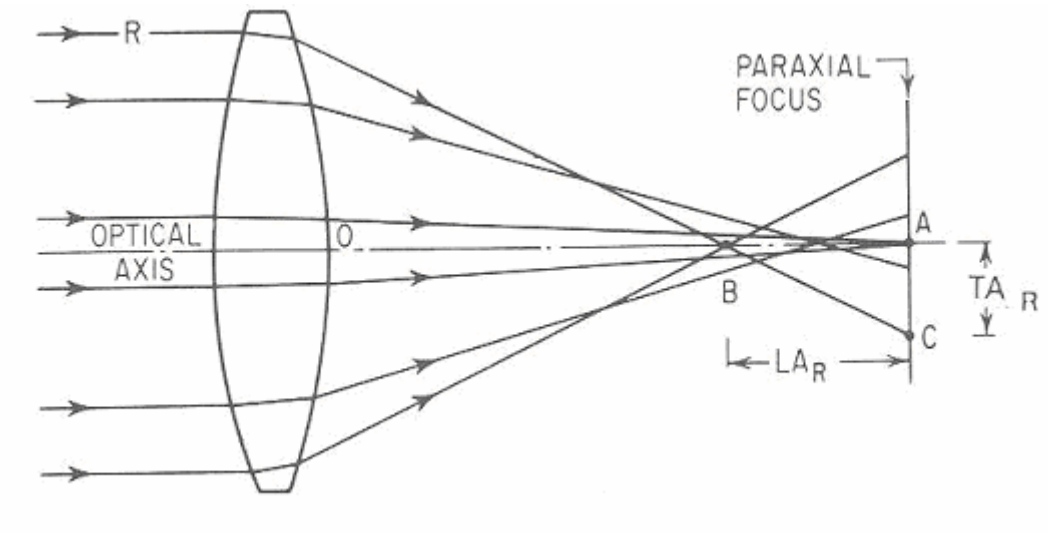

Figure 2.5 Spherical aberration from Smith, (1990)

Coma

Coma can be defined as variation in magnification with aperture. When a bundle of oblique rays is incident on a lens with coma, the rays passing through the edge portions of the lens are imaged at a different height than those passing through the center portion. In Figure 2.6, the upper and lower rim rays A and B intersect the image plane above the ray P which passes through the center of the lens. The distance from P to the intersection of A and B is called tangential coma of the lens.

$Coma_T = H_{AB} - H_p$

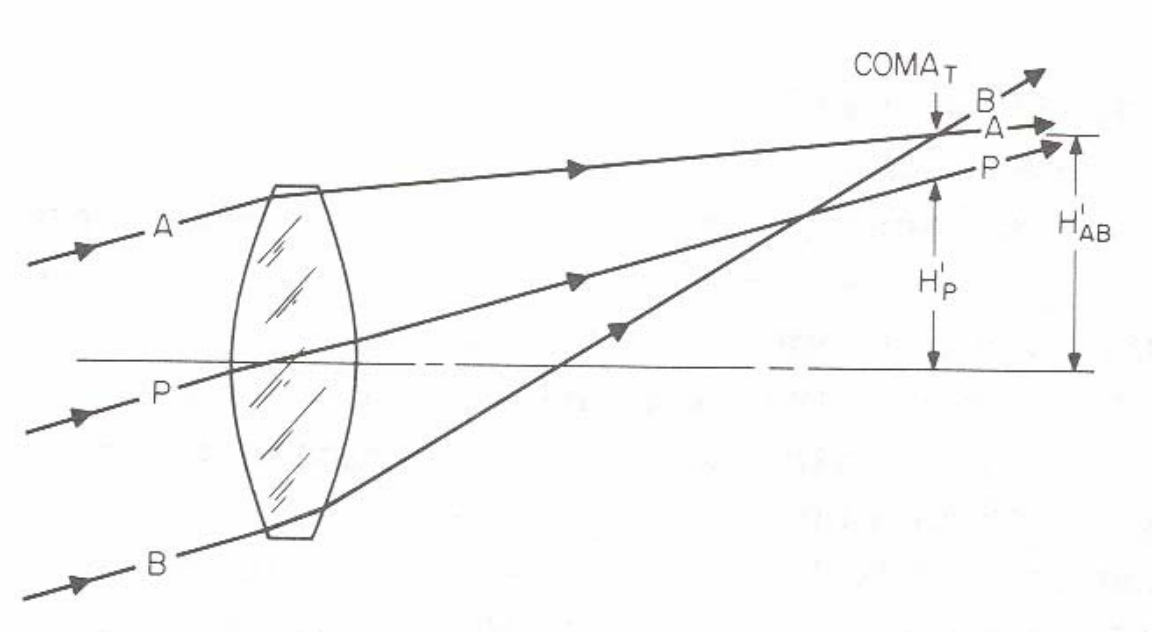

Figure 2.6 Coma from Smith, (1990)

The appearance of a point image formed by a comatic lens is indicated in Figure 2.7.

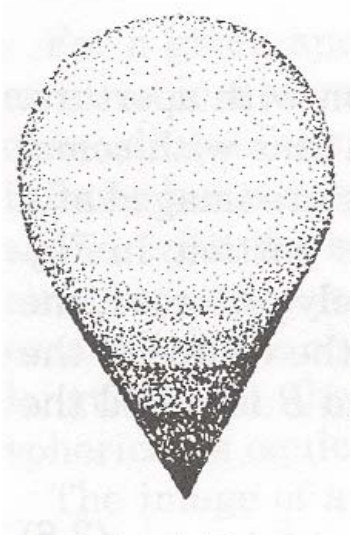

Figure 2.7 The coma patch. The image of a point source is spread out into a comet-shaped flare from Smith, (1990)

Astigmatism

Any plane through the optical axis is called as the meridional, or the tangential plane. The imaginary plane passing through the chief ray (an oblique ray passing through a point on the object and the center of the lens) and perpendicular to the meridional plane is called the sagittal plane. All the rays from the object, which lie in this plane, are called sagittal rays. See Figure 2.8.

Astigmatism occurs when the tangential and the sagittal images don't coincide. In the presence of astigmatism, the image of a point source is not a point, but takes the form of two separate lines as shown in Figure 2.8.

Unless there is some manufacturing defect in a lens, there is no astigmatism when an axial point is imaged. However, as the imaged point moves farther from the axis, the amount of astigmatism gradually increases.

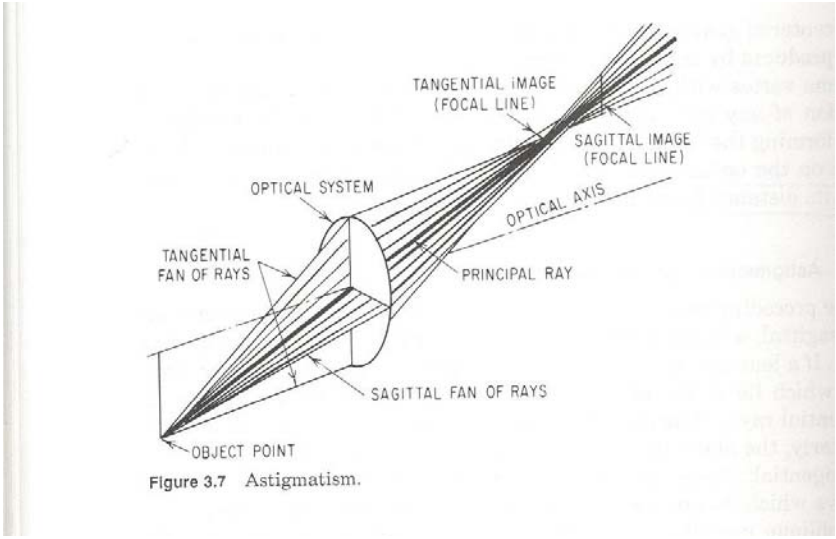

Figure 2.8 Astigmatism from Smith, (1990)

Distortion

When the image of an off axis point is formed farther from the axis or closer to the axis than the image height given by the paraxial expressions (i.e. expressions derived by assuming that rays pass through an infinitesimal threadlike region on the lens around the optical axis), the image of the extended object is said to be distorted. The amount of distortion increases as the cube of the image height. Thus, if a centered rectilinear object is imaged by a system afflicted with distortion, it can be seen that the images of corners will be displaced more than the images of the points making up the sides. In Figure 2.9, the appearance of a square figure imaged by a lens system with distortion is shown. In Figure 2.9a, the distortion is such that the images are displaced outwards from the correct position. This is called positive or pincushion distortion. In Figure 2.9b, the distortion is of opposite type and the corners of the square are pulled inward more than the sides. This is called the negative of the barrel distortion.

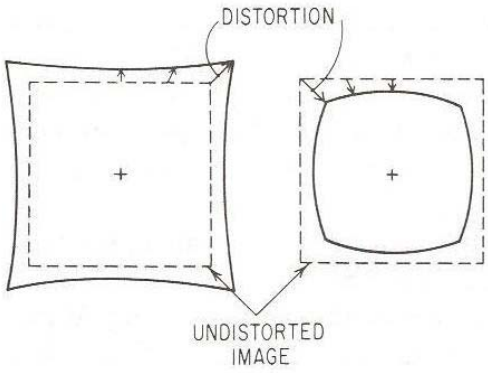

The sides of the image are curved because the amount of distortion varies as the cube of the distance from the axis. Thus, in the case of a square, the corners are distorted $2\sqrt{2}$ as much as the center of the sides.

a **b**

Figure 2.9 a) Pincushion or positive distortion b) Barrel or negative distortion from (Smith, 1990)

Chromatic Aberration

These aberrations can be understood intuitively. Chromatic aberrations are caused because the refractive index of any material is different for different wavelengths of lights.

The above section described the aberrations in terms of the inability of a lens to focus down all rays at the ideal image points. When we consider light as waves propagating along these rays, their relative phases are not the same as would be expected in case of a far field diffraction pattern. It is interesting to note the effects of aberrations on the relative phase differences in the various waves arriving at a point, from the point of view of questioning the validity of the optical analysis method. The aberrations are described in terms of the distortions produced in a wavefront in the next section.

2.1.2.2 Wavefront aberrations

The optical aberrations cause deformations in the wavefront. The extent of these deformations can be used as a quantitative measure for deciding which modeling strategy to use. If these deformations are minor, then aberrations analysis can be used to augment the diffraction analysis presented earlier. If the deformations in wavefronts however are very large, then, geometric optics should be used.

The extent of the variation of the deformed wavefront from its actual shape is denoted by measuring the “Optical Path Difference”, or OPD. In this section, the OPD introduced by a system having spherical aberrations is derived to explain the meaning of OPD.

OPD introduced by spherical aberration

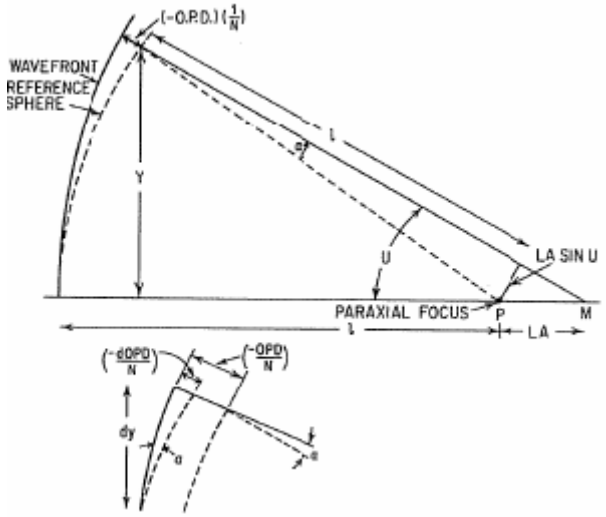

Figure 2.10 Optical path difference as the distance between ideal and distorted wave fronts, from Smith, (1990)

A wavefront converging to form a point image at the paraxial focus of a lens, P is shown in Figure 2.10. The ideal wavefront is represented by the dotted curve, while, the wavefront distorted by spherical aberration is shown by the solid line. The OPD for a given zone, i.e. radial distance from the optical axis, is given by the distance from the ideal wavefront to the distorted wavefront along the radius of the ideal wavefront. In Figure 2.10, the normal to the distorted wavefront intersects the axis at point P. The ideal wavefront, or the reference sphere, is centered at P. The angle between the normals to the two wavefronts is also equal to the angle between the two wavefronts, as indicated in the lower sketch. This angle is given by the relation

$$\alpha = \frac{-dOPD}{NdY} \tag{2.15}$$

But angular aberration is also related to the spherical aberrations, in Smith, (1990) as

$$\alpha = \frac{(LA)\sin U}{l}$$

$$= \frac{(LA)Y}{l^2} \tag{2.16}$$

By combining and solving for *dOPD*, we get

$$dOPD = \frac{-YN(LA)dY}{l^2} \tag{2.17}$$

Longitudinal spherical aberrations can be represented by the series

$$LA = aY^2 + bY^4 + cY^6 + \ldots.$$

For most optical systems, the spherical aberration is almost entirely of the third order and can be expressed as

$$LA = aY^2$$

Making this substitution and integrating throughout the zone of radius Y, we get

$$OPD = -\int_0^Y \frac{NY}{l^2}(aY^2)dY$$

$$= \frac{-NY^2}{2l^2} \cdot \frac{aY^2}{2} \tag{2.18}$$

$$= \frac{-1}{2} N \sin^2 U(\frac{aY^2}{2})$$

At the edge of the aperture, $Y=Y_m$ and $LA=LA_m$, (the subscript denoting marginal ray and marginal longitudinal spherical aberration). Substitute the value of a as:

$$a = \frac{LA_m}{Y_m^{\,2}} \tag{2.19}$$

Thus,

$$OPD = \frac{-1}{4} N \sin^2 U\left[LA_m(\frac{Y}{Y_m})^2\right] \tag{2.20}$$

Equation (2.20) gives the OPD caused only because of spherical aberrations. Real optical systems have numerous lenses and stops in series and introduce numerous kinds

of aberrations apart from spherical. Analytical computation of the OPD in the distorted wavefront that would occur due to the combined presence of all these aberrations is a non-trivial task and can be performed by means of some optical analysis software.

It is clear from the preceding discussion that the size and shape of an image formed by a lens is not intuitive. Due to optical aberrations, the thin lens equation will calculate erroneous dimensions of the aerial image formed on the resin surface. The exact image size can be calculated by adopting the procedure of tracing rays through a lens as explained in the next sub-section.

2.1.2.3 Exact ray tracing

From Section 2.1.2.1, it is clear that the size of the expected image cannot be determined from the simple lens equation. The exact size of the image can be obtained through "exact ray tracing procedures." In an exact ray trace, the object is considered as a collection of point sources. Rays in all possible directions are traced from each of these point sources. The rays undergo refraction at every surface separating two media. The refraction is governed by Snell's law:

$$\sin i / n_1 = \sin i' / n_2, \tag{2.21}$$

where i and i' are the angles of incidence and refraction, and n_1 and n_2 are the refractive indices of the media on either side of the surface on which the rays are incident. By tracing rays, their points of intersection with the image plane are calculated. The farthest points of intersections give the size and shape of the image.

Exact ray tracing is an involved procedure, especially because the angle of incidence (i) for every ray is in a different plane. In this section, the ray tracing procedure

presented in (Smith, 1990) is described. This ray tracing procedure was first published by D. Feder in the Journal of the Optical Society of America vol. 41, pp. 630-636, 1951.

Exact Ray Tracing Procedure for spherical surfaces

A skew ray is a perfectly general ray. The ray is defined by the coordinates x, y and z of its intersection with a surface and by its direction cosines X, Y and Z. The origin of the coordinate system is at the vertex of each surface. Figure 2.11 shows the meanings of these terms.

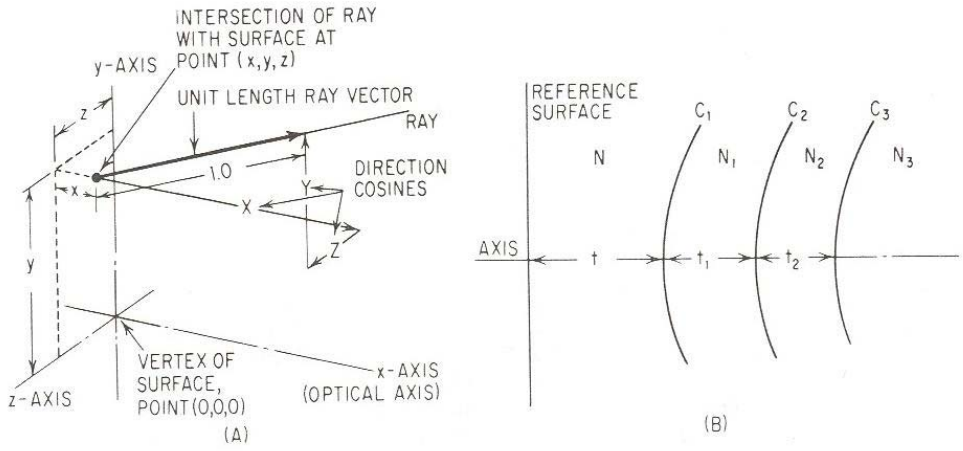

Figure 2.11 Symbol used in Transfer and Refraction equations. a) The physical meanings of the spatial coordinates (x,y,z) of the ray intersection with the surface and of the ray direction cosines, X, Y, and Z. b) Illustrating the system of sub-script notation from Smith,(1990)

The computation is opened by determining the values for x, y, z, X, Y and Z with respect to an arbitrarily chosen reference surface which is usually chosen to be the object plane. Then, the following "Transfer equations" give the coordinates (x_1, y_1, z_1) of the point of intersection of the ray with the next surface:

$$e = tX\ (xX + yY + zZ)$$

$$M_{1x} = x + ex - t$$

$$M_1^2 = x^2 + y^2 + z^2 - e^2 + t^2 - 2tx$$

$$E_1 = \sqrt{X^2 - c_1(c_1 M_1^2 - 2M_{1x})}$$

$$L = e + (c_1 M_1^2 - 2M_{1x}) / (X + E_1)$$

$$x_1 = x + LX - t$$

$$y_1 = y + LY$$

$$z_1 = z + LZ$$

The direction cosines of a ray after it undergoes refraction at a surface are given by the following "Refraction equations":

$$E_1' = \sqrt{1 - (N_1 / N_2)^2 (1 - E_1^2)}$$

$$g_1 = E_1' - (N / N_1) E_1$$

$$X_1 = (N / N_1) X - g_1 c_1 x_1 + g_1$$

$$Y_1 = (N / N_1) Y - g_1 c_1 y_1$$

$$Z_1 = (N / N_1) Z - g_1 c_1 z_1$$

In the above Transfer and Refraction equations, the symbols have the following meanings:

t	Distance between two surfaces
x, y, z	The spatial coordinates of the ray intersection with the reference surface

x_1, y_1, z_1	The spatial coordinates of the ray intersection with surface #1
M_1	The distance (vector) from the vertex of surface # 1 to the ray, perpendicular to the ray
M_{1x}	The x component of M_1
E_1	The cosine of the angle of incidence at surface #1
L	The distance along the ray from the reference surface (x, y, z) to surface #1 (x_1, y_1, z_1)
E_1'	The cosine of the angle of refraction (I') at surface #1
X, Y, Z	The direction cosines of the ray in space between the reference surface and surface #1 (before refraction)
X_1, Y_1, Z_1	The direction cosines after refraction by surface #1
c	The curvature (reciprocal radius = 1/R) of the reference surface
c_1	The curvature of surface #1
N	The refractive index between the reference surface and surface #1
N'	The refractive index following surface #1
T	The axial spacing between the reference surface and surface #1

2.1.3 Selection of modeling strategy

In Sections 2.1.1 and 2.1.2, two strategies of modeling the image formation process have been presented: Physical Optics, which assumes the wave nature of light,

and Geometric Optics, which assumes the ray nature of light. The selection of the Optical modeling strategy would depend upon the kind of optical system that is being used.

2.1.3.1 When to use Physical Optics?

Physical Optics can be used to model image formation is the system is "diffraction limited". Goodman (1968) says that "*an imaging system is said to be diffraction limited if a diverging spherical wave, emanating from a point-source object, is converted by the system into a new wave, again perfectly spherical, that converges towards an ideal point in the image plane. Thus, the terminal property of a diffraction limited lens system is that a diverging spherical wave is mapped into a converging spherical wave at the exit pupil. For any real imaging system, this property will, at best be satisfied over only a finite region of the object plane. If the object is confined to that region, the system may be regarded as diffraction limited*".

Rayleigh Quarter-wave limit

The effect of optical aberrations is to distort the wave emerging from an optical system from its ideal spherical shape. The Rayleigh quarter wave limit is used as a measure of the amount of distortion that can be tolerated, for diffraction analysis to be used. According to Rayleigh, there is no appreciable deterioration of image if the phase differences introduced do not exceed $\pi/2$. In other words, the image quality is not seriously impaired if the wavefront aberration does not exceed $\lambda/4$. If the wavefront aberrations are within the Rayleigh quarter wave limit, then diffraction analysis is used. In order to secure this high degree of correction, it is usually necessary to employ a complicated and expensive optical system.

2.1.3.2 When to use Geometric Optics?

Geometric optics is used for modeling image formation if the aberrations introduced by the imaging system are significant. When the thin lens and the paraxial approximations are not valid, the aberrations become significant. In such cases, diffraction theory cannot be used. Goodman (1968) states: "*The conclusion that a lens composed of spherical surfaces maps an incident plane wave into a spherical wave is dependent on the paraxial approximation. Under nonparaxial conditions the emerging wavefront will exhibit departures from perfect sphericity (called aberrations) even if the surfaces of the lens are perfectly spherical."*

The optical aberrations cause deformations in the wavefront which are not accounted for in Physical optics. The extent of these deformations can be used as a quantitative measure for deciding which modeling strategy to use. If these deformations are minor, then aberrations analysis can be used to augment the diffraction analysis presented earlier. If the deformations in wavefronts however are very large, then, Geometric optics should be used. The choice of modeling strategy is summarized well in Smith, (1990) as: "*for small departures from perfection (i.e. aberrations which cause a deformation of wavefront amounting to less than one or two wavelengths), it is appropriate to consider the manner in which an aberration affects the distribution of energy in the diffraction pattern. For larger amounts of aberration, however, the illumination distribution, as described by raytracing can yield a quite adequate representation of the performance of the [optical] system. Thus, it is convenient to divide the considerations into (1) the effects of small amounts of aberration, which we treat in terms of the wave nature of light, and (2) the effects of large amounts of aberration, which may be treated geometrically."*

2.2 Fundamentals of resin curing

In this section, the chemistry behind the photo polymerization reactions that occur when a Stereolithography resin cures is presented. Most commercial Stereolithography resins are a mixture of acrylic monomers and epoxy resins. The acrylic monomers are polymerized using a process called "Free Radical Photopolymerization", while the epoxy resins are cured using a process called "Cationic Photopolymerization". The curing mechanism of a commercial Stereolithography resin (SL 7510) is proposed in Rosen, (2002). In this section, the curing mechanism of a commercial resin containing a mixture of acrylates and epoxies is explained in Section 2.2.1. The Beer Lambert's law of radiation attenuation and the threshold model of resin cure is presented in Section 2.2.2.

2.2.1 Curing mechanism of commercial Stereolithography resins

Commercial SLA resins are a mixture of acrylates, epoxies, radical photo initiators and cationic photoinitiators. When radiant energy is incident upon the resin, the photoinitiators initiate polymerization reactions. In addition to these constituents, the resins also contain photosensitizers, which increase the UV absorbance and increase the initiation efficiency. The mechanisms of polymerization for acrylate and epoxy resins are different. The "Free Radical Photopolymerization" mechanism of curing of acrylate resins is described in Section 2.2.1.1. The "Cationic Photopolymerization" mechanism of curing of epoxy resins is presented in Section 2.2.1.2. The polymer network formation is discussed in Section 2.2.1.3.

2.2.1.1 Free Radical Photopolymerization

Polymerization is the process of linking small molecules (monomers) into larger molecules (polymers) comprised of many monomer units. Most Stereolithography resins

contain the vinyl monomers and acrylate monomers. Vinyl monomers are broadly defined as monomers containing a carbon-carbon double bond. Acrylate monomers are a subset of the vinyl family with the carboxylic acid group (-COOH) attached to the carbon-carbon double bond. For an acrylate resin system, the usual catalyst is a free radical. In Stereolithography, the radical is generated photo chemically. The source of the photo chemically generated radical is a photo initiator, which reacts with an actinic photon as shown in the photo-polymerization scheme presented in Figure 2.12. This produces radicals (indicated by a large dot) that catalyze the polymerization process.

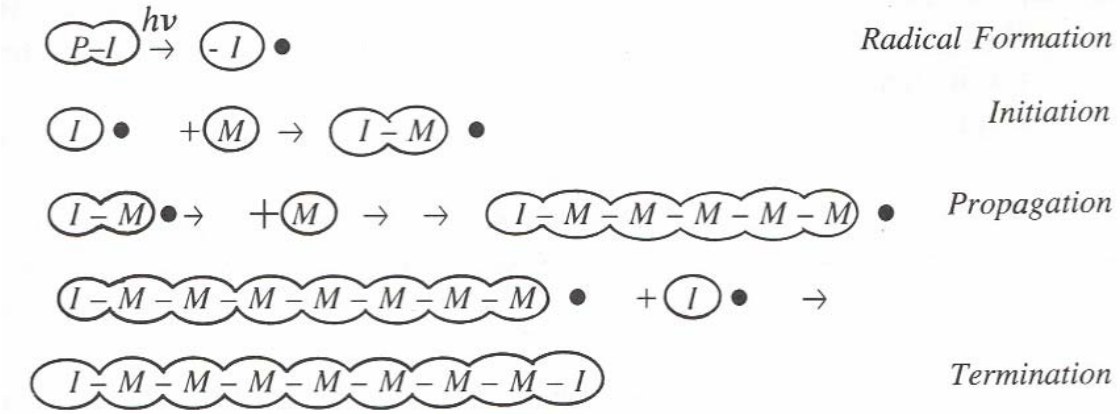

Figure 2.12 Scheme of the photo-polymerization process (Jacobs, 1992)

The free radical photopolymerization of acrylate systems is very fast, but of lower density. This process is exothermic which is beneficial for activating the heat activated cationic photoinitiators.

2.2.1.2 Cationic Photopolymerization

The most important cationic photoinitiators are the onium salts, particularly the triarylsulphonium and diaryliodonium salts. The photodecomposition mechanism of triarylsulphonium is described in Rosen, (2002). When light is incident on the cationic

photointiator, a Bronted acid (H^+X^-) is generated by photolysis. The Bronsted acid acts as a catalyst for the polymerization of the epoxide groups. The polymerization occurs by a chain reaction, initiated by a protonated epoxide group. The termination of the chain reaction is not immediate. The cationic polymerization once initiated continues over a period of few hours to even a few days. It is speculated in Rosen, (2002) that hydroxyl compounds are added to the mixture to terminate the chain reaction.

2.2.1.3 Interpenetrating polymer network formation

When the acrylate and epoxy groups polymerize, they form their respective networks. In the presence of each other, an interpenetrating network gets formed. An interpenetrating network is defined as a combination of two polymers in network form, at least one of which is synthesized and/or cross linked in the immediate presence of the other. Thus, the polymers are formed in network form, and are not just mechanically mixed. The formations of the acrylate and epoxy networks influence each other's formation. The reaction of acrylates increases the photospeed, reduces the energy requirements of the epoxy reaction and also reduces the inhibitory effects of humidity on the epoxy polymerization. The epoxy monomers also favor the acrylate photopolymerization reaction. The epoxy monomer acts as a plasticizer, which increases the molecular mobility, which favors the acrylate chain reaction. Further, the acrylate is less sensitive to oxygen in a hybrid acrylate-epoxy system.

2.2.2 Beer Lambert's law of light absorption

As the photons penetrate the resin, they are progressively absorbed by initiators. According to Beer Lambert's law of absorption, the exposure (mJ/cm^2) decreases exponentially with depth.

$$E(z) = E_{max}\, exp(-z/D_p) \quad (2.22)$$

where D_p is the resin "penetration depth" (a resin parameter) at the given wavelength and E_{max} is the exposure at the surface of the resin ($z = 0$).

In practice, polymerization doesn't proceed beyond a limited depth where the exposure falls below a threshold value. This is primarily due to oxygen inhibition (Drobny 2002), which imposes a minimal threshold to start polymerization. The exposure level where the gel point is reached is still higher. The exposure threshold for the formation of gel is known as the "Critical Exposure" (E_c).

Suppose that a point on the resin surface receives an exposure E_{max}. If the point gets cured to a depth C_d then the exposure received at the depth C_d will be equal to E_c.

Putting $z = C_d$ and $E(z) = E_c$ in Beer Lambert's law:

$E_c = E_{max}\, exp\ (-C_d/D_p)$

Rearranging the terms,

$$C_d = D_p\, ln(E_{max}/E_c) \quad (2.23)$$

Thus, the plot of C_d versus $ln(E_{max})$ is straight line with slope equal to D_p and the X intercept = $ln\ (E_c)$ (Jacobs, 1992).This plot is called as the Working curve of the Stereolithography resin. See Figure 2.12.

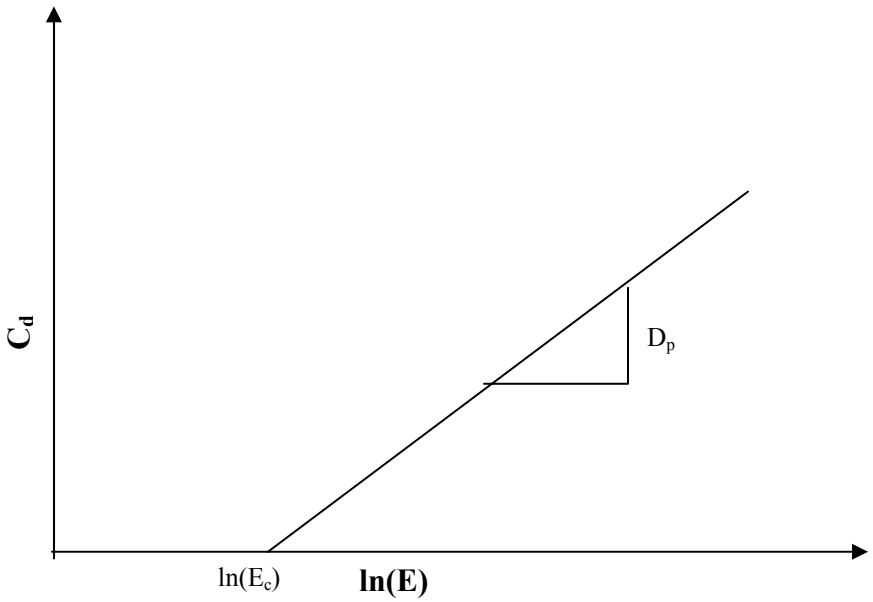

Figure 2.13 Theoretical Working curve of a Stereolithography resin

The values of E_c and D_p are fixed for any resin and so, the working curve of any resin is, theoretically, invariant.

Summary

Analytically modeling the Mask Projection Stereolithography process entails modeling the optical process of imaging a bitmap onto the resin surface and modeling the curing process that occurs after the bitmap is imaged. The fundamental knowledge related to optical imaging is presented in Section 2.1. Geometric optics and Physical optics are the two theories that can be used for modeling image formation. The assumptions made in these theories are presented and the method of image modeling using both these methods is presented. In Section 2.2, the fundamentals of resin curing has been presented. The polymerization mechanism of acrylate and epoxy based resins is presented. The relation between the cure depth of a layer and the exposure supplied to it is presented.

CHAPTER 3 DESIGN OF THE MASK PROJECTION STEREOLITHOGRAPHY SYSTEM

In this chapter, the design of the Mask Projection Stereolithography System realized as a part of this research is presented. The primary modules of a MPSLA system are identified in Limaye, (2004) as Collimation system; Imaging system; and Build system. In this chapter, the design of all these systems is presented. In Section 3.1, the requirements from the system to be designed are presented. In Section 3.2, the design of every module is presented.

3.1 Requirements list

Prior to designing any system/machine, the performance requirements from that system should be explicit identified. The requirements from the MPSLA system are presented in Table 3.1. They are classified as "Demands", which *have* to be fulfilled and "Wishes", whose fulfillment is *preferred*.

Table 3.1 Requirements list for the Mask Projection Stereolithography System

REQUIREMENTS LIST FOR THE MASK PROJECTON STEREOLITHOGRAPHY SYSTEM *Formulated by Ameya Limaye*	
Demand/Wish	**Requirement**
Demand	The largest cured layer dimension in one exposure should be greater than 10mm x 5 mm
Demand	The largest vertical dimension of a cured part should be greater than 5mm
Wish	The distortions due to optical aberrations should be as less as possible
Wish	The lateral resolution should be better than 20μm
Wish	The vertical resolution of the system should be better than 100μm
Wish	The system should have as much depth of focus as possible
Demand	The total cost of realizing the system should be less than $16000

3.2 Design of the MPSLA system

The optical schematic of a M PSLA system has been presented in Limaye, (2004), as shown in Figure 3.1.

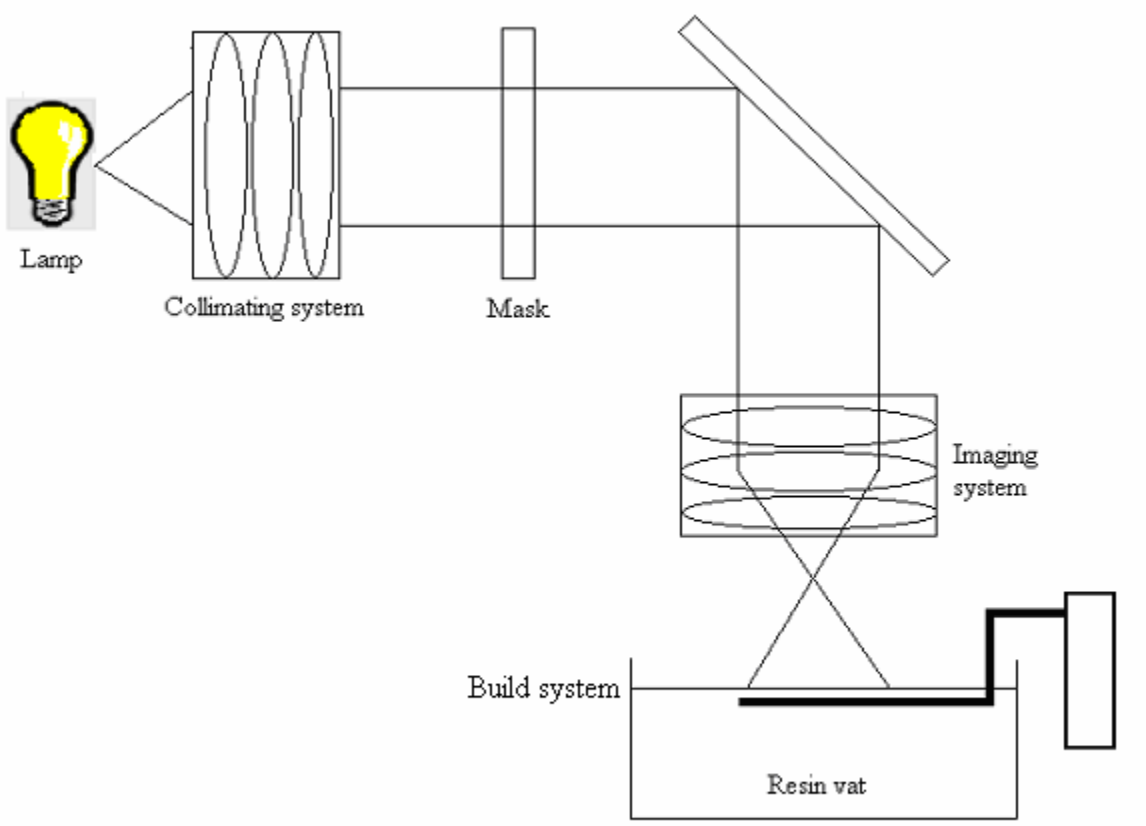

Figure 3.1 Optical Structure to embody

3.2.1 Collimating system

The function of the collimating system is to collect the diverging rays emerging from the lamp and send out parallel or almost parallel rays. Rays parallel to the optical axis reduce the Coma that would be introduced by the imaging system subsequently.

The light source should emit radiation in the UV range, mostly at around 365nm. The light source selected is ADAC^{TM} System's Cure Spot ^{TM} 50. This lamp emits 3000 + mW/cm^2 at 365 nm. The Spectral distribution of the lamp is as shown in Figure 3.2. The typical half cone divergence angle of the light emitted from the light guide is given to be

30^{o}. This lamp is selected because it is the most inexpensive lamp available, which emits in the required spectrum.

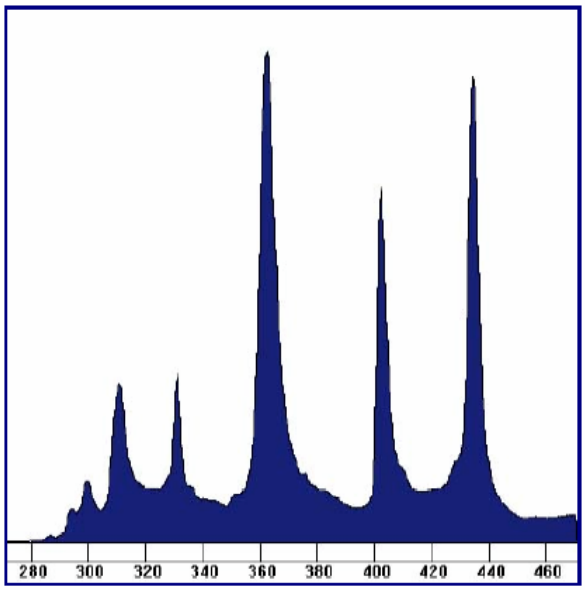

Figure 3.2 Relative Spectral Distribution of Cure Spot 50

A pinhole is placed immediately after the light guide of the lamp, to simulate a point source of light. A plano convex lens is placed one focal length away from the pinhole, to collect the rays from the point source and form its image at infinity (send out parallel rays). Definitely, all the rays are not parallel due to spherical aberration. Greater the focal number of the lens, greater is the angle of the cone subtended by the lens at the point source and hence, greater is the amount of light collected. So, a fast lens is to be used. A plano convex lens with effective focal length 40mm is used. A plano convex lens is chosen with its convex side facing the aperture because this lens is known to introduce less spherical aberrations than a bi-convex lens.

A filter, allowing only 365nm wavelength to pass through, was placed after the collimating lens. However, it was found that the light intensity coming out of the filter was unacceptably low. So, the filter was removed from the system.

The final collimating system is shown in Figure 3.3

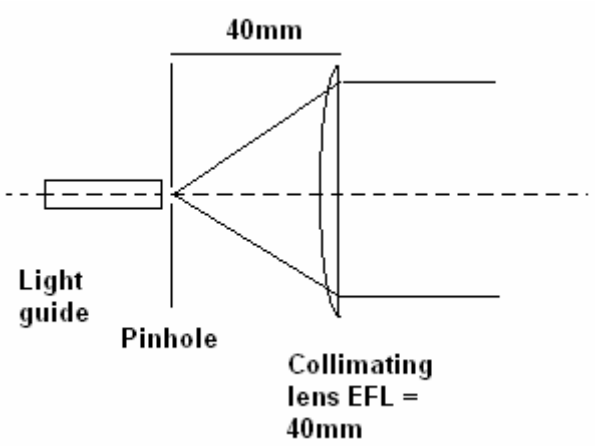

Figure 3.3 Collimating system

3.2.2 Imaging system

The function of the imaging system is to image the pattern displayed on the DMD onto the photopolymer resin. The requirements for this system are that it should introduce minimum optical aberrations; and it should give the best possible depth of focus and lateral resolution. To minimize the optical aberrations and to increase the depth of focus, a telecentric optic system is used.

Telecentric system

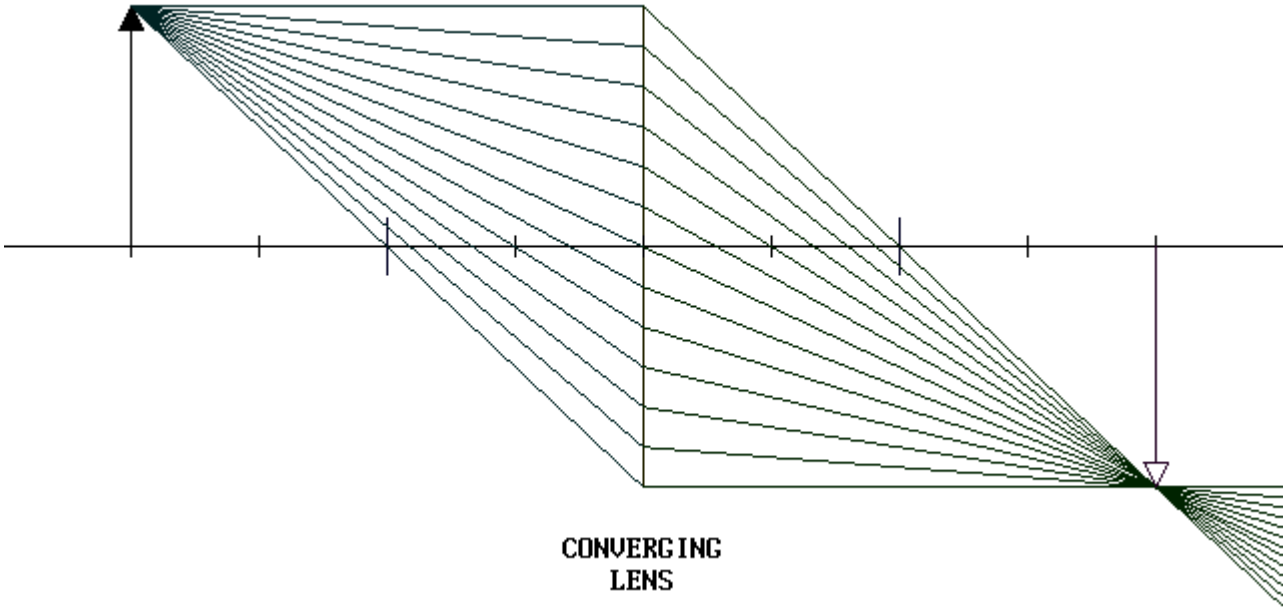

Figure 3.4 Imaging lens without a stop

Consider the lens shown in Figure 3.4. The lens itself acts as an aperture stop and all the rays emanating from every object point, which are collected by the lens are focused by the lens onto the image.

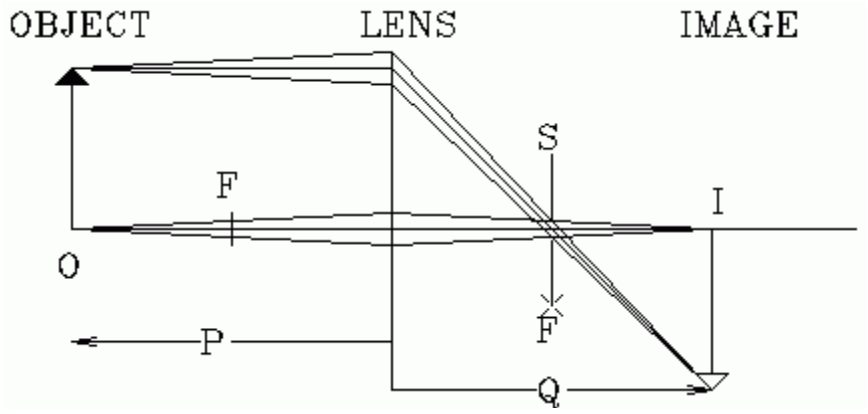

Figure 3.5 Stop placed at the focal point of the lens (Telecentric of the object side)

In Figure 3.5, a small stop ‘S’ is placed at the focal point of the lens. This stop allows only a narrow bundle of rays emanating from every object point to pass through it. Since the stop is located at the focal point of the lens, only a small cone of rays emanating from every object point, parallel to the optical axis can pass through the aperture. In such a situation, since the image is formed mostly by rays parallel to the optical axis, if the object is moved nearer or farther from the lens, every ray reaches the object plane at the same point. Thus, the magnification of the image is constant with respect to the object position. Such an imaging system is called “telecentric on the object side”.

Due to finite size of the stop, rays not exactly parallel to the optical axis also reach the image plane, which produce what is called as a “circle of confusion”. The smaller the size of the stop, the smaller is the circle of confusion.

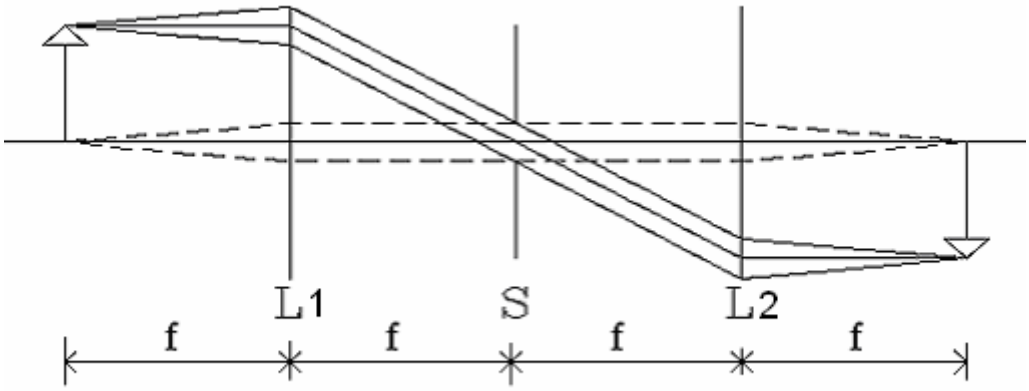

Figure 3.6 Imaging system telecentric on both sides

In Figure 3.6, lens 1, stop and lens 2 are each spaced once focal length apart from each other. The rays pass through the stop in parallel bundles. This system is telecentric on both, the object as well as the image side. Such a system has less coma and astigmatism in the image. It shows less effect of field curvature in the image and other

geometric distortions. In fact, coma and astigmatism would theoretically approach zero as the aperture stop diameter approaches zero.

A telecentric imaging system as shown in Figure 3.7 is realized for the MPSLA system. The imaging system utilizes two bi convex lenses with effective focal lengths of 40mm. An aperture stop of diameter 1.5mm is placed between the two lenses. The distances from the DMD to lens 1, from lens 1 to aperture stop, from aperture stop to lens 2 and from lens 2 to the resin surface are, each, 40mm.

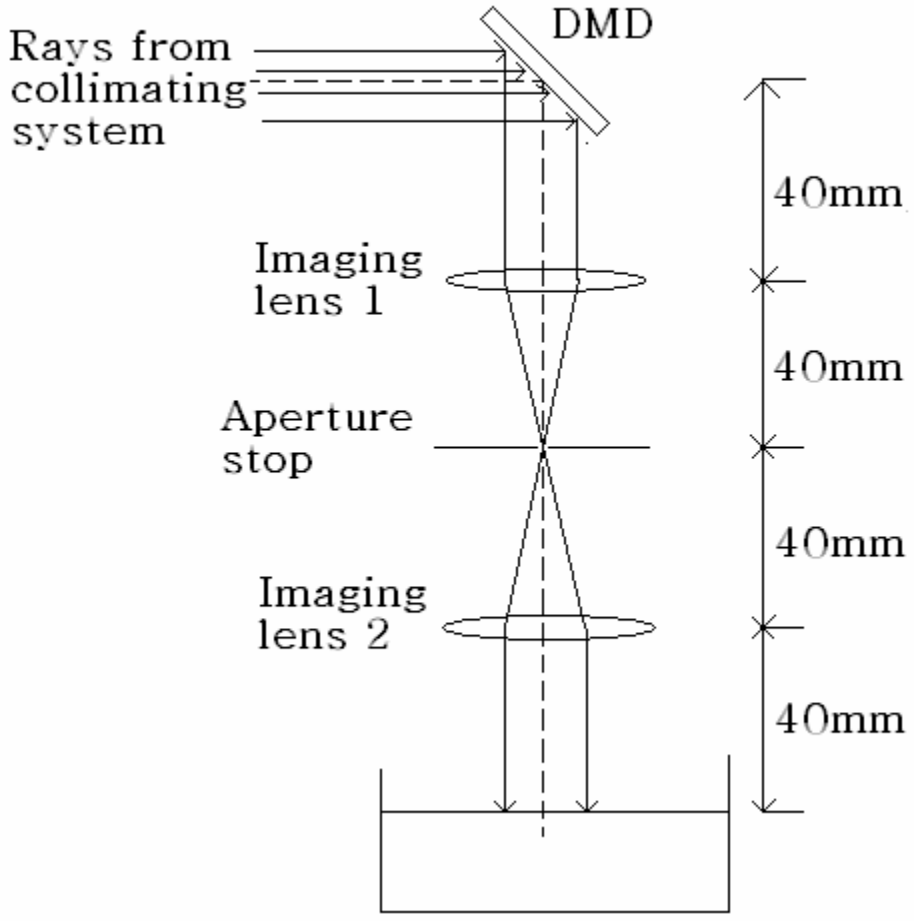

Figure 3.7 Imaging system

A system telecentric on both the sides has the following advantages for the MPSLA system.

- The optical aberrations (coma, astigmatism, distortions) are minimized and hence the layers are cured with fewer distortions.
- The system is more robust to variations in the resin level.
- The system is robust to the angular mounting of the DMD.

Mask

The Digital Micromirror Device (DMD^{TM}) is an array of individually addressable, bi-stable micro-mirrors (Dudley et al., 2003). A bitmap can be displayed on the DMD by selectively orienting its mirrors in one direction. As opposed to the Liquid Crystal Display (LCD) and Spatial Light Modulator (SLM), the DMD is a reflective mask. As a mask, the DMD has advantages over LCD and SLM. The pixel density of the DMD is higher because the mirrors are smaller in size than the LCD and SLM pixels (12.7μm square as opposed to 24μm square in LCD and SLM) and also because the spacing between mirrors is much less than that between the LCD and SLM pixels.

The DMD is mounted so as to direct the beam of light incident on it is reflected downwards.

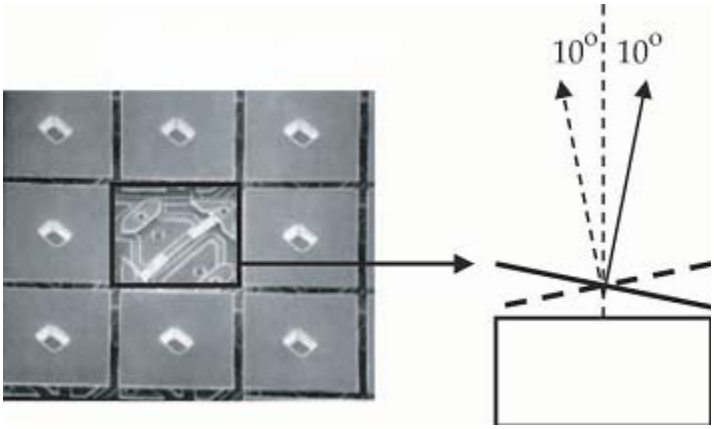

Figure 3.8 Digital micromirror device from Nayar et al., (2004)

3.2.3 Build System

The Build system consists of a vat and a platform mounted on a XYZ translation stage. The platform can be translated vertically into the resin vat under computer control. In addition, the platform can also be translated in the lateral direction. The translation stage has a resolution of 100nm.

DSM SOMOS 10120 resin is used with this setup. This resin was used because it was the lowest viscosity commercial Stereolithography resin that was readily available in the laboratory.

The final system is as shown in Figure 3.9. The description of every component is presented in Table 3.2.

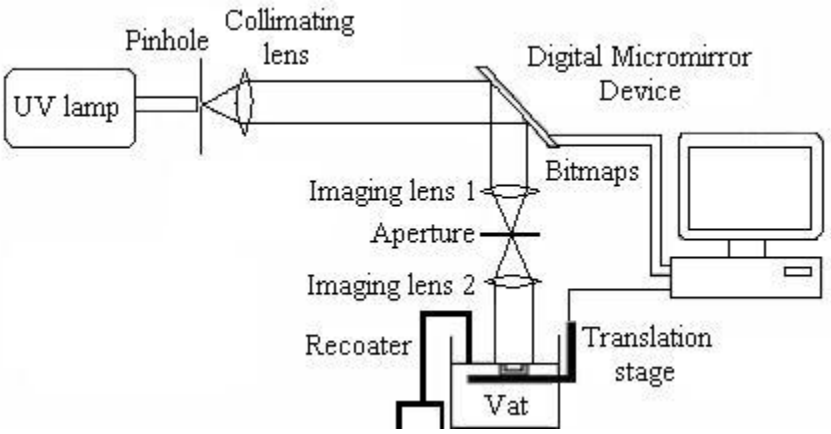

Figure 3.9 Optical schematic of the MPSLA system realized as a part of this research

Table 3.2 Specifications of the components used in the MPSLA system

Component	Description	Model/Manufacturer
Broadband UV lamp	Broadband Mercury vapor lamp. Peak at 365nm. 3000mW at 365nm.	ADAC System Cure Spot 50/ Dymax Corporation
Aperture 1	Adjusted to 4mm diameter	Thorlabs Catalog # SMO5D5
Collimating lens	Fused silica Plano convex lens Effective focal length = 40mm Diameter = 25.4mm Radius of surface 1 = 18.4mm Radius of surface 2 = infinity (plane) Lens thickness = 7.1mm Material refractive index = 1.460	Thorlabs Catalog # LA4306-UV
DMD	1024 X 768 array of micromirrors Dimension of micromirror = 12.65µm square. Spacing between mirrors = 1µm	Texas Instruments. Distributed by Prodsys Inc.
Imaging Lens 1 and Imaging Lens 2	Fused silica Plano convex lens Effective focal length = 40mm Diameter = 25.4mm Radius of surface 1 = 35.7mm Radius of surface 2 = 35.7mm Lens thickness = 6.7mm Material refractive index = 1.460	Thorlabs Catalog # LB4030
Aperture 2	Adjusted to 1.5mm diameter	Thorlabs Catalog # SM05D5
Translation stage	XYZ translation stage; 100nm resolution	Applied Scientific Instruments Model # MS2000
Photopolymer resin	Ec, Dp to be found experimentally	DSM SOMOS 10120

Summary

In this chapter, the design of the Mask Projection Stereolithography system realized as a part of this research has been explained in detail. Using the optical schematic presented in Figure 3.9 and the specifications of components, presented in Table 3.2, it will be possible for a reader to assemble a similar MPSLA system. The analytical models that shall be formulated later in this dissertation shall be validated by building parts on this system.

CHAPTER 4 FORMULATION OF RESEARCH QUESTIONS AND HYPOTHESES

The research objective presented in Section 1.3 can be achieved by completing the tasks proposed in Figure 1.14. The proposed research effort is explained in detail in Sections 4.1 to 4.4. In Section 4.1, a multi scale modeling strategy for modeling the exposure on the resin surface in terms of process parameters is proposed (Exposure model). In Section 4.2, the compensation zone approach is proposed to cure dimensionally accurate parts. In Section 4.3, an adaptation of the Compensation zone approach to improve the surface finish of downward facing parts is proposed. In Section 4.4, the structure of a multi objective process planning method, which would enable the building of MPSLA parts with requirements on dimensions, surface finish and build time, is proposed.

In this chapter, research questions that need to be tackled in order to formulate a process planning method for MPSLA are identified. Hypotheses to these research questions are presented and tasks that will be undertaken to test these hypotheses are enunciated.

4.1 Exposure modeling

4.1.1 Selection of optical modeling method

Image formation can be modeled in two ways. One is by assuming the wave nature of light, and the principles of physical optics. The second is by assuming ray nature of light and using the fundamentals of geometric optics. This leads us to the first research question.

Research Question 1a *Should the image formation process in the MPSLA system under consideration by modeled using physical optics or using geometric optics?*

Hypothesis *The theory of geometric optics is more suitable than that of physical optics to model the image formation by the MPSLA system under consideration.*

Explanation

At a first glance, it seems that geometric optics should be used as opposed to physical optics, because of the following reasons.

1. The light used in the setup is incoherent. A diffraction pattern is not obtained with incoherent light.

2. The imaging system is expected to be aberration limited.

Tasks

As explained in Chapter 2, Section 2.1.3, physical optics theory should be used to model image formation by a diffraction limited system, while the theory of geometric optics should be used to model image formation by an aberration limited system. If the Optical Path Difference (OPD), as explained in Section 2.1.2.2 is comparable with the Rayleigh limit ($\lambda/4$), the system is diffraction limited and physical optics should be used to model image formation. In case the OPD is several times the Rayleigh limit, the imaging system is aberration limited. In order to test the hypothesis to Research Question 1a, the following tasks shall be performed

Task 1 Quantify the Optical Path Difference

The OPD introduced by the aberrations in the imaging system shall be quantified to see if it exceeds the Rayleigh quarter wave limit by several times.

Task 2 Cure test layers

A ray tracing algorithm shall be formulated to obtain the exposure on the resin surface given the bitmap to be imaged. A test bitmap shall be fed to this algorithm and the lateral extents of the exposed region shall be measured. This bitmap shall be imaged onto the resin surface for a long time and a layer will be cured. The lateral extents of the exposed regions, returned by the algorithm, shall be compared with the lateral extents of the cured layer. The extent agreement of the two results could shed some light on the validity of using the geometric optics approach to image modeling.

4.1.2 Reducing the computational expense of ray-tracing approach

Ray tracing approach is a high fidelity approach which takes into account the optical aberrations introduced by the imaging system and thereby accounts for the distortions in the image and variation in irradiance across it that occurs due to aberrations. The downside of the ray-tracing approach is that a large number of rays need to be traced through the imaging system in order to converge to the irradiance profile on the resin surface. If the model is to be implemented at a higher resolution, an even larger number of rays would have to be traced. This leads us to our next research question.

Research Question 1b: *How to model the exposure profile on the resin surface with the fidelity of the ray tracing approach, in a computationally inexpensive way?*

Hypothesis: *A multi scale modeling approach can be adopted. The irradiance profile can be thought of as a collection of pixels overlapping each other. Modeling should be done at two levels:*

1. Curing of individual pixels (computationally expensive part)

2. Overlapping of pixels to give the exposure profile on the resin surface (computationally inexpensive part)

Explanation

Whenever any bitmap displayed on the DMD is imaged onto the resin surface, every micro mirror in the "ON" state is imaged as a pixel on the resin surface. Depending upon the time that a micro mirror is imaged, every pixel will get some exposure dose. Thus, every micro mirror results in the exposure of a single pixel. Within a single layer, adjacent pixels overlap each other laterally. The shape and dimensions of a pixel as well as the exposure distribution across it will depend upon the location of the micromirror exposing it, on the DMD.

It is proposed to model the exposure profile on the resin surface in two steps. First, a 'Pixel Image database' shall be populated which would record the irradiance at every pixel in terms of the optical parameters of the MPSLA system. Then, the Pixel overlap model will be formulated that would compute the exposure profile on the resin surface. The imaging of pixels, which is a computationally intensive process, will be computed only once and a database recording the location and dimensions of every pixel, including the irradiance distribution across it, shall be created. The proposed multi scale strategy for modeling irradiance is shown in Figure 4.1.

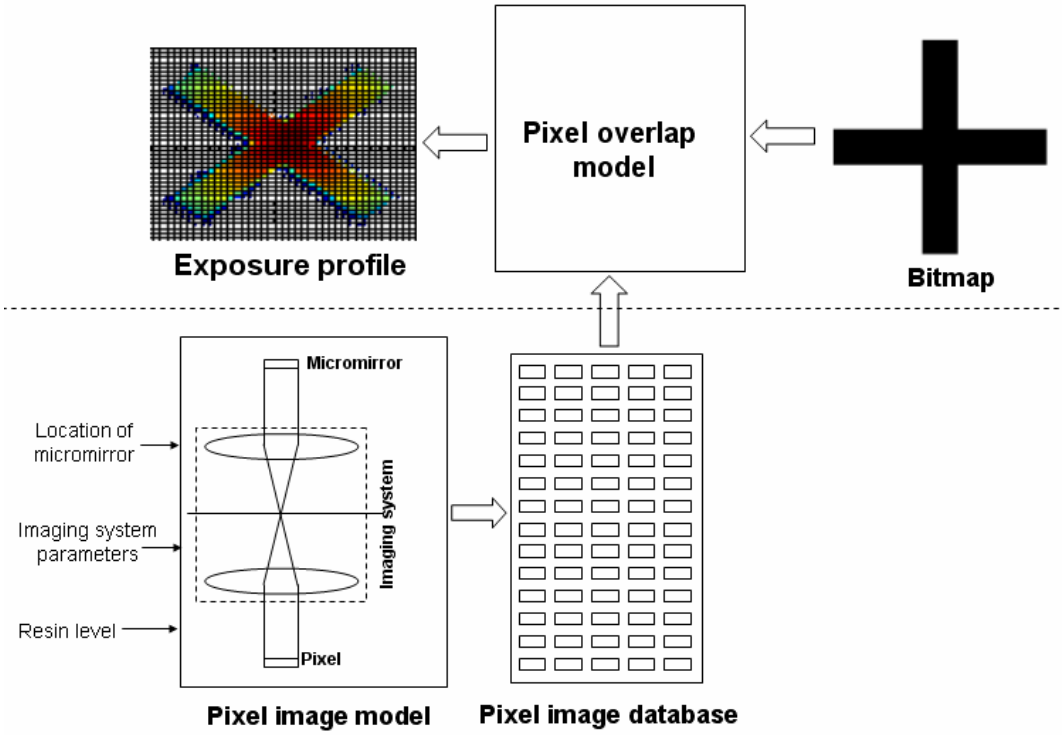

Figure 4.1 Multi scale approach to model exposure

Tasks

In order to test this hypothesis, the following tasks shall be undertaken.

Task 1 Formulate the Pixel image model

First the resin surface shall be discretized into elements 10μm square each. In the Pixel image model, rays will be traced from every micromirror on the DMD in all directions. The lateral extents of the irradiated area (pixel) would encompass numerous elements. The radiation (in mW/cm^2) at these elements shall be stored in the pixel image database. Let us denote the radiation received by the element (p,q) on the resin surface due to rays emanating from the micromirror given by coordinates (a,b) as $H_{pq,ab}$. Suppose the micromirror (a,b) is imaged for time T_{ab}. Due to the radiation received solely from the micromirror (a,b) for time T_{ab}, the element (p,q) will receive an exposure dosage of $E_{pq,ab}$

$$E_{pq,ab} = H_{pq,ab} \times T_{pq,ab} \tag{4.1}$$

Task 2 Formulate the Pixel summation model

When pixels overlap laterally, they would share some element(s). At a shared element, the total exposure would simply be the algebraic sum of the exposure it receives from all the micromirrors that end up irradiating it. Suppose the element *(p,q)* is shared between various pixels. Then, the irradiance at the element (*p,q*) due to the overlap is given by equation 4.2.

$$E_{pq} = \sum E_{pq,ab} \text{ with } a,b \text{ across all the pixels which overlap at } (p,q) \tag{4.2}$$

Task 3 Test the model

The exposure profile obtained by imaging a test bitmap on the resin surface shall be computed by using the multi-scale approach proposed above and the computational time shall be quantified.

4.2 Curing dimensionally accurate parts

The first step towards curing a dimensionally accurate MPSLA part is to cure dimensionally accurate layers. The lateral extents of every layer can be meshed with pixels from the Pixel image database (Section 4.1.2) and then, the pixels can be mapped onto the micromirrors on the DMD to generate the bitmap to be displayed on the DMD. The next step is to determine the vertical dimension of the voxels that would be cured at these pixels. The vertical dimensions of any Stereolithography part are prone to errors because of print through errors.

When a layer is cured, radiation penetrates beyond its intended thickness. While penetration of radiation beyond the layer is desirable in order to bind it to the layer

underneath it, the radiation also penetrates to the bottom surface of the part being built, causing print-through errors. As the radiation propagates through the resin, it gets attenuated according to the Beer Lambert's law of absorption. The exposure received by the resin at a depth z from the surface is given by

$$E(z) = E_0 e^{-z/D_p} \tag{4.3}$$

where $E(z)$ is the exposure at the depth z in resin,

E_0 is the exposure at the resin surface,

D_p is the depth of penetration, which is a resin constant.

The resin beneath a MPSLA build gets exposed due to radiation penetrating to it from all the layers cured above it. Exposure being additive, a point is reached when the exposure received by the resin underneath the MPSLA part equals its threshold exposure for polymerization (E_c). This unwanted curing causes an increase in the vertical dimension of the part. This error is called as the print-through error. The source of print-through error is depicted pictorially in Figure 4.2. The author aims to minimize the print through errors through efficient process planning.

Research Question 2: *How to reduce print through errors in MPSLA builds?*

Hypothesis: *Print through errors can be reduced by subtracting a tailored volume (compensation zone) from underneath the CAD model which is used to build the part, in such a way that the exposure received by the down facing surface of the part is exactly equal to the threshold exposure of polymerization (E_c).*

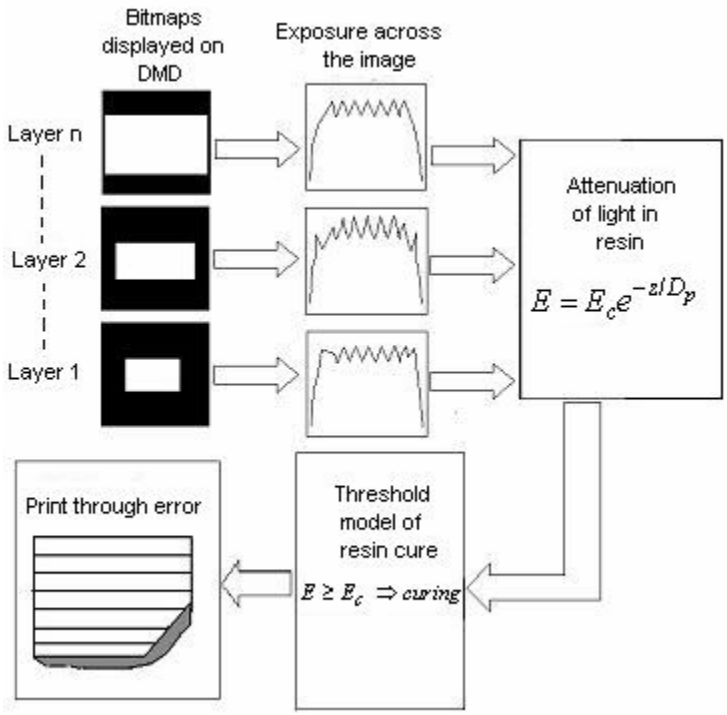

Figure 4.2 Print-through error

Explanation

The idea behind compensation zone approach is to subtract that volume which would exactly compensate for increase in vertical dimension that would occur due to print through. Radiation penetrating from all layers results in print through. Thus, given a slicing scheme, the exposure supplied to the various layers should be controlled in such a way that the exposure reaching the bottom surface of the part being cured is exactly equal to E_c.

4.2.1 Failed attempt at modeling print through

In order to implement the Compensation zone approach, the author modeled print through using Beer Lambert's law of resin attenuation and the threshold model of resin cure (both explained in Section 2.2). This attempt failed because of some assumptions

made in the cure modeling in Jacobs, (1992). In this sub-Section, the author's failed attempt at modeling and validating print-through is presented.

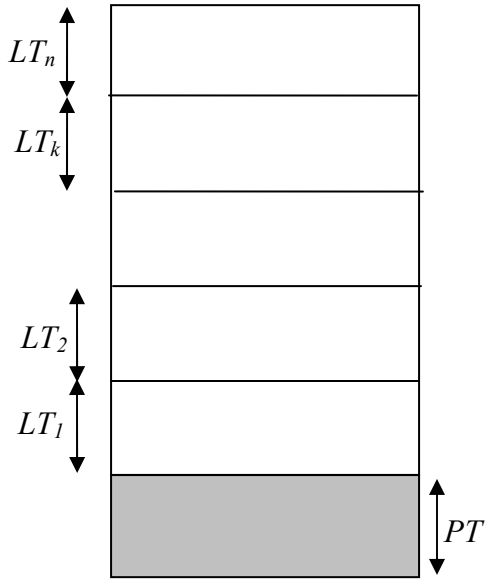

Figure 4.3 Modeling print through

Suppose an n layered part is built as shown in Figure 4.3. The total print through will be caused by the energies penetrating to the bottom surface from all the layers cured above it. If exposure E_k is provided to cure the k^{th} layer, the energy *penetrating* to the bottom surface from the k^{th} layer can be computed using Beer Lambert's law, as given by equation 4.4

$$E_{bk} = E_k \exp(-\sum_{m=1}^{m=k} LT_m / D_p) \tag{4.4}$$

The total exposure that will cause print through will be given by the summation of the exposures penetrating from all the layers.

$$E_b = \sum_{k=1}^{n} E_{bk} \tag{4.5}$$

This exposure would cause print through as given by equation (4.6)

$$PT = D_p \ln \frac{E_b}{E_c} \tag{4.6}$$

The total height of the part thus cured will be given by the summation of the layer thicknesses and the print through as given in equation 4.7.

$$h = \sum_{k=1}^{n} LT_k + PT \tag{4.7}$$

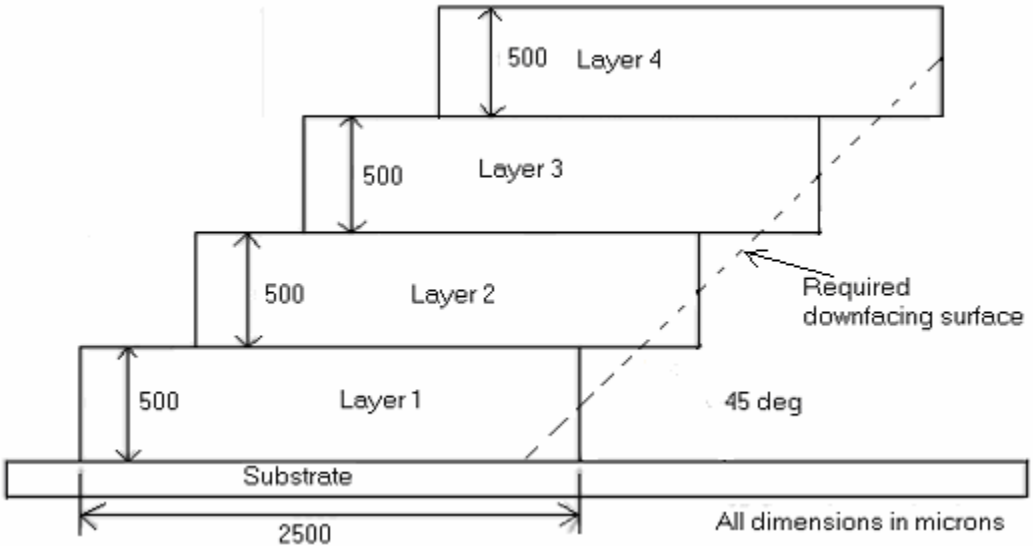

Figure 4.4 Validating the print through model

The author tested this model by building the four layer test part as shown in Figure 4.4. The part consists of four identical layers of lateral dimensions 2500µmX600µm and 500µm thick. These layers were offset over each other by 500µm by translating the part being built beneath the imaging system. The irradiance profile across the layer was modeled using the "Irradiance model" as formulated in Limaye and Rosen, (2007) (explained in this dissertation in Section 5.1) to obtain the value of irradiance (H) received at every pixel. The layers were exposed for 80s. The print through was calculated at every lateral location on the extents of the part using equation 4.5 and

the profile of the down facing surface was simulated. The test part was built and its profile was compared with the down facing surface profile of the part. The profiles did not agree even qualitatively. See Figure 4.5. This disagreement was observed for various combinations of the times of exposures for the layers.

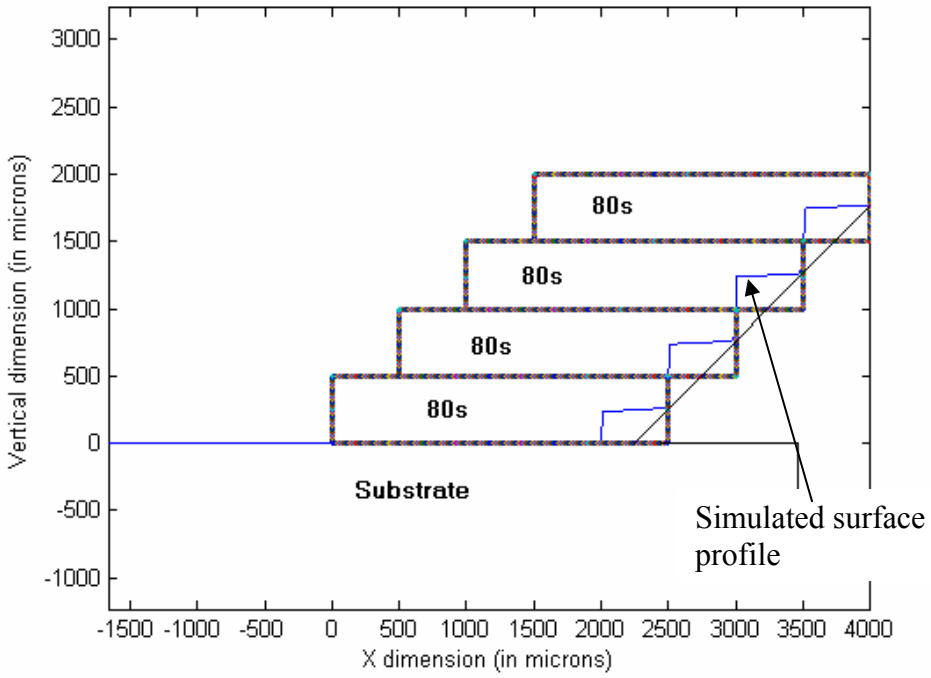

(a)

Figure 4.5 Profiles of down facing surfaces (a) simulated; (b) experimentally observed

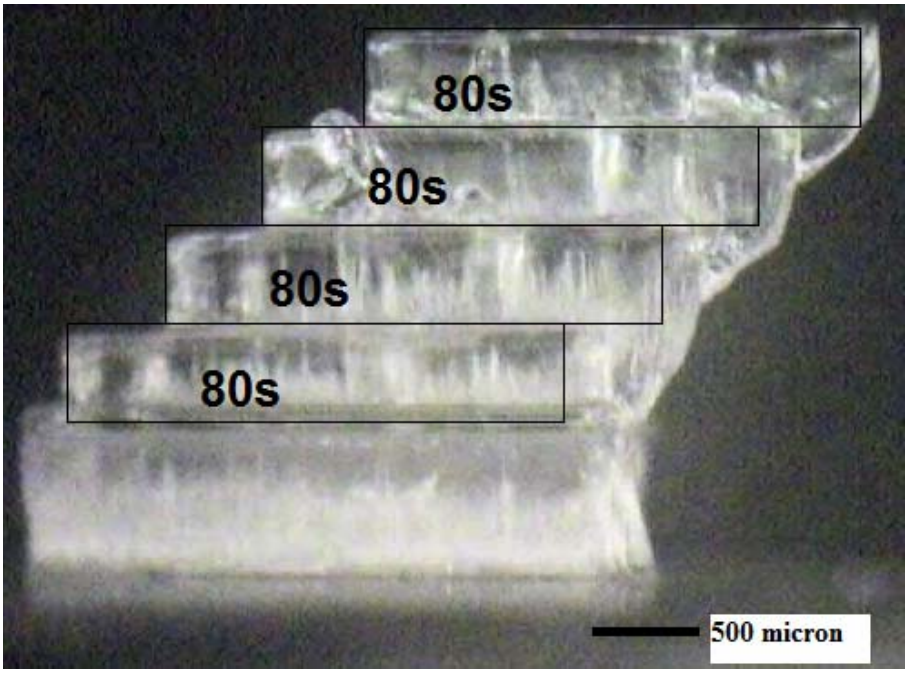

(b)

Figure 4.5 (continued)

In both the figures, rectangles are shown corresponding to the layers that would have been cured had there been no print through and no irradiance variation across a cured layer. It can be seen from the simulation results in Figure 4.5 (a) that the cure depth is smaller than the layer thickness. This is because the irradiance falls sharply at the edges, where the exposure received is not enough to cure resin up to the layer thickness. Also, it can be seen that the simulation predicts almost same profiles for the overhanging portions under each of the four layers. This is also expected since we are using very thick layers. The radiation attenuation, being exponentially decreasing is less than 1% beyond a depth for 1000μm.

It can be seen from the experimentally cured profile that there is a significant amount of print through actually happening. The simulation results based upon the calculation of print through using equation 4.6 do not account for this excessive observed

print through. This made the author questions some of the fundamental assumptions made in the formulation of equation on 4.6. Two assumptions were identified as explained in Section 4.2.2 and Section 4.2.3.

4.2.2 Modeling layer curing as a transient process

The print through model presented in equation 4.6 assumes that when any layer is cured, all the energy supplied to cure the layer is supplied in an instant and the depth of cure is proportional to the logarithm of exposure. Suppose that irradiance H is incident on the resin surface for a duration t. It would supply an exposure $E = H \cdot t$. This energy would get attenuated as it enters the resin, according to the Beer Lambert's law. The exposure at a depth z is given by $E_z = E \exp(-z / D_p)$. Curing occurs at all points where exposure is greater than or equal to E_c. The thickness of the layer cured will thus be given by equation (4.8).

$$C_d = D_p \ln(H \cdot t / E_c) \tag{4.8}$$

where D_p is the depth of penetration of the resin (a measure of attenuation of radiation), and

E_c is the threshold exposure for polymerization.

This model assumes that the attenuation of radiation through a cured layer is the same as that through uncured resin, given by the parameter D_p. This assumption is highly suspicious, because most of the photo-initiator is consumed in cured resin. The chemical composition of cured resin is significantly different from that of uncured resin, which will definitely alter its rate of absorption of light. In other words, the depth of penetration for a cured layer D_{pS} is expected to be different from that of liquid resin D_{pL}.

Suppose that the thickness of the layer that is cured after a time t_1 during exposure is equal to C_{d1}, and the thickness cured after time t_2 is equal to C_{d2}, as shown in Figure 4.6. Suppose that an infinitesimal amount of energy δE is incident on the top surface of the layer being cured. This energy will get attenuated as it passes through the cured layer and then through the uncured resin. The plot of energy versus depth into the resin vat is shown in Figure 4.6. Consider the fraction of the incident energy δE that would reach an arbitrary depth z from the top surface of the layer. In the first case, an energy equal to $\delta E.\exp(-C_{d1}/D_{pS})\exp(-[z-C_{d1}]/D_{pL})$ will reach the depth z. In the second case where the thickness of the layer already cured is equal to C_{d2}, the energy reaching the depth z will be equal to $\delta E.\exp(-C_{d2}/D_{pS})\exp(-[z-C_{d2}]/D_{pL})$.

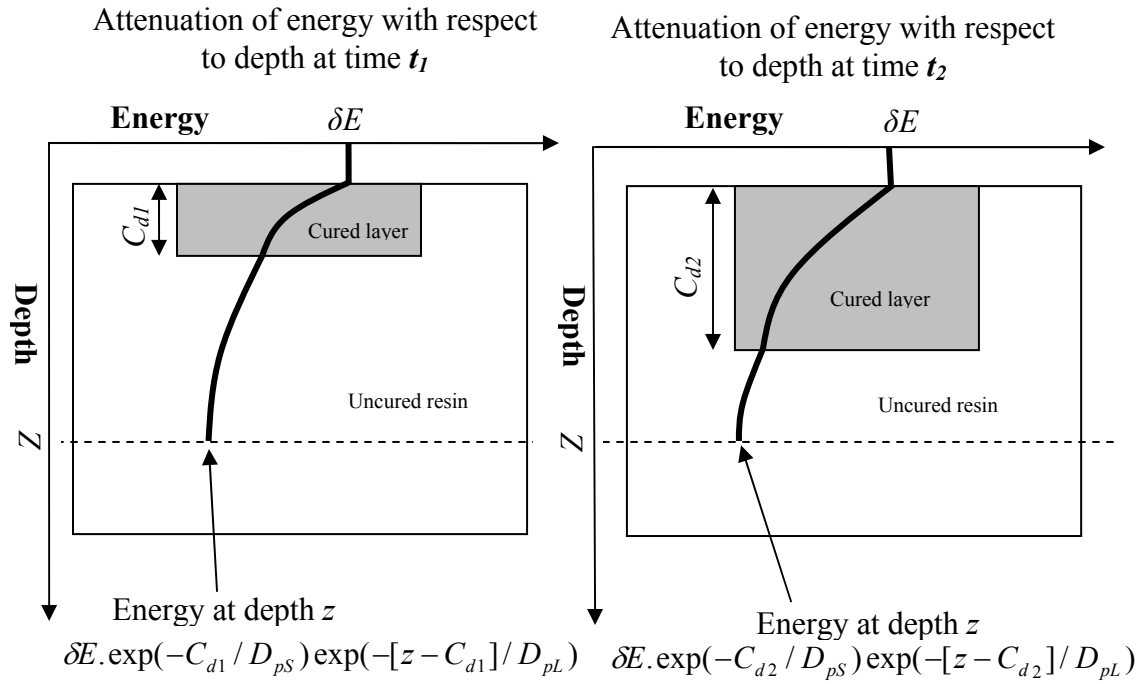

Figure 4.6 Different rates of radiation attenuation with respect to depth at different instances of time during exposure

Thus, the average attenuation of radiation per unit depth will vary with respect to time. In other words, the rate of radiation attenuation with respect to depth, will vary with respect to time. It is necessary to capture this effect of varying rate of attenuation on the depth of cure. This leads us to Research Question 2a.

Research Question 2a: *How to capture the effect of the varying rate of radiation attenuation throughout the duration of exposure, as a layer gets cured?*

Hypothesis: *The effect of varying rate of attenuation as a layer gets cured can be captured by modeling layer curing as a transient phenomenon, by discretizing the time domain.*

Explanation

Suppose the depth of penetration for a cured layer is D_{pS} and that for the liquid resin is D_{pL}. By discretizing the time domain into infinitesimal time intervals (dt), we can formulate a differential equation relating the incremental curing (dz) that would occur during the time interval dt. By solving this differential equation, we can obtain a relationship between the depth of cure and time of exposure.

By conducting experiments on our MPSLA system, we can see if we get the same relationship between cure depth and exposure as that predicted by solving the differential equation. This would validate our theory of the transient layer curing.

Task 1: Formulate the transient layer cure model

A differential equation relating the incremental curing dz and the infinitesimal time interval dt shall be formulated and solved

Task 2: Validate the transient layer cure model

Layers shall be cured for various times of exposures and plotted against the exposure supplied to cure them to validate the transient layer cure model

4.2.3 Quantifying effect of diffusion underneath cured layer

The print through model makes another assumption. It assumes that exposure is additive (equation 4.5). In other words, it assumes that the total energy that would cause print through is simply the algebraic summation of the energies that reach the bottom surface from all the layers cured above it. The author finds this assumption highly invalid for the MPSLA process. In case of the MPSLA process used by the author, a time interval of up to one minute is allowed for the resin surface to level itself before any layer is cured. The author expects that during this duration, reactive species underneath the partially cured part would diffuse out into the vat and would carry energy away with them. In addition, oxygen from the surrounding resin would diffuse towards the solid-liquid interface and quench the excited species, thereby further reducing the amount of energy carried by excited species at the bottom surface. These two diffusion phenomena are expected to cause a fall in the net energy available at the bottom surface. The author intended to pose his suspicion as Research Question 2b.

Research Question 2b: *Is exposure at the bottom surface of a cured layer additive or does it get significantly affected by diffusion of radicals and oxygen into the resin vat?*

Hypothesis: *The exposure is not additive because there is a significant diffusion of radicals and oxygen in the resin vat.*

Explanation

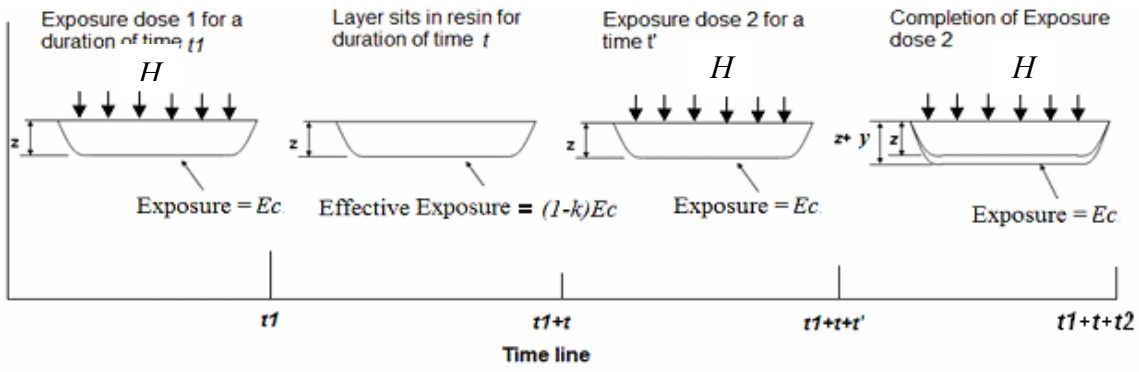

Figure 4.7 Effect of diffusion of reactive species underneath a cured layers

Figure 4.7 shows a time line from the time that the radiance was first incident on the resin surface to the time t_1+t+t_2. Suppose that radiance H is incident on the resin surface for a time duration t_1 and causes curing up to a depth z. Reactive species in their excited state are present at the solid-liquid interface of this cured layer and the effective exposure at this interface is equal to the threshold exposure of polymerization (E_c). This cured layer is allowed to remain in the resin vat for a time t. During this time, the cure depth remains unchanged. During the time t though, reactive species would diffuse out from the bottom surface of the layer, while oxygen from the surrounding resin would diffuse towards the layer and quench the reactive species. As a result of this diffusion, the effective exposure at the bottom surface would drop to $(1-k)E_c$. This is shown in Figure 4.7 at the time t_1+t. Now, the top surface of the cured layer is exposed to the same radiance H for a second time interval of duration t_2. This second dose of energy will pass through the transparent layer and will add up with the exposure at the bottom surface.

Further incremental curing will start only after the energy lost due to diffusion of radicals and oxygen is replenished by the incoming radiation. After a time t' into the

second exposure dose, the lost energy will be replenished and the effective exposure at the bottom surface will once again be equal to E_c. This is shown on the time line in Figure 4.6 at the time t_1+t+t'.

At the end of the second exposure dose of duration t_2, the effective exposure at the bottom surface will be as given in equation 4.9.

$$E_b = (1-k)E_c + (H \cdot t_2)\exp(-z / D_{pS}) \tag{4.9}$$

This exposure is what will cause incremental curing upto a depth y as shown in Figure 4.7. The value of 'k' (let us call it as "Radical diffusion factor") in equation (4.9) is expected to be a strong function of time. We shall compute this factor experimentally.

Task 1: Validate the theory of diffusion of radicals

Single layered parts, as shown in Figure 4.7 shall be cured by supplying two discrete exposure doses and by allowing different durations in between the two exposures to allow time for the radicals and oxygen to diffuse. By measuring the thickness of the layers cured, the value of the radical diffusion coefficient k shall be plotted and it shall be seen if it is a logarithmic function of the time allowed for diffusion t (typical for diffusion-based phenomena). If it is, then we can take a leap of faith to conclude that radical diffusion occurs underneath a cured part.

4.2.4 Modeling print through and implementing Compensation zone approach

After having done the preceding work, the author again intends to pursue modeling print through and hopes to get much better agreement between experimental and analytical results. Using this model, it would be possible to simulate a down facing surface and then, solve the print through equation to obtain the reduction in layer

thicknesses that would compensate for print through. Thus, the compensation zone approach shall get implemented.

4.3 Smoothing down facing surfaces

Research Question 3: *How to implement the print through smoothing approach to obtain smoother down facing surfaces in MPSLA builds?*

Hypothesis: *Print through smoothing can be achieved by gray scaling the pixels near the edges of a layer to cure voxels of different heights that conform to the part's vertical profile. This method shall be called as "adaptive exposure" since it involves adapting the exposure to suit the part's vertical profile.*

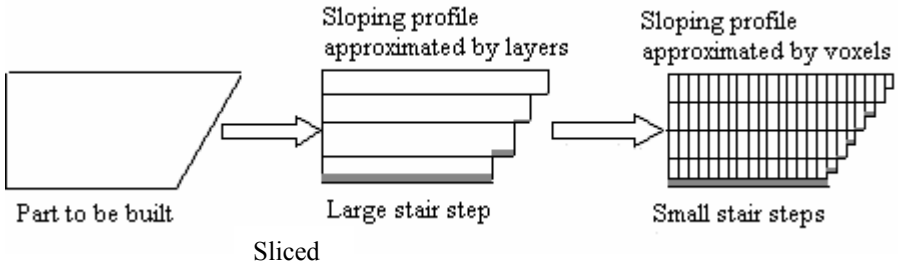

Figure 4.8 Curing smoother down facing surfaces through "adaptive exposure"

Explanation

The idea in adaptive exposure is to mesh every layer with voxels with vertical dimensions better approximating the part's vertical profile. With this method, the down facing surface's approximation will be limited by the voxel dimensions and not by the layer thicknesses (Figure 4.8).

Task: Demonstrate Adaptive exposure method

Improvement in surface finish due to adaptive exposure shall be demonstrated on a test part.

4.4 Process planning for MPSLA

Suppose the part with quadratic up and down facing surfaces as shown in Figure 4.8 is to be built. There are requirements on the part's lateral dimensions, vertical dimensions, surface finish as well as build time. The curing of dimensionally accurate parts has been addressed in Research Questions 2. Improvements to surface finish through intelligent process planning have been addressed in Research Question 3. The build time of an MPSLA part can be easily modeled by breaking down the part building process into its constituent steps and summing the time required to complete each of those steps.

Research Question 4: *How to build a MPSLA part with multiple objectives of dimensional accuracy, surface finish and build time?*

Hypothesis: *Process planning can be done in two steps. First, a multi-objective optimization method, like the compromise DSP (Mistree et al., 1994) should be formulated and solved to select the slicing scheme, i.e. layer thicknesses that would obtain a tradeoff between the objectives of surface finish and build time. For this slicing scheme, the compensation zone approach should be adopted to obtain part with accurate vertical dimensions*

Explanation

The layer thicknesses have the largest effect on two of our process objectives: surface finish and build time. It can be intuitively seen that larger the number of layers, greater would be the build time. Also, larger the number of layers to build a given a part, smaller will be the layer thicknesses and thus, smoother would be the up facing surface. Thus, a compromise DSP can be formulated and solved to generate slicing schemes that

would achieve tradeoffs between the goals of surface finish and build time. A set of slicing schemes that are acceptable would be selected. The Compensation zone approach shall be applied on each of these slicing schemes to reduce the print through errors.

Task: Formulate and test the multi objective process planning method

The following are the proposed steps of the process planning method.

1. Slice the CAD model and populate the slices with elements so that the surface finish and build time requirements are satisfied as well as the lateral dimensional requirements are satisfied.
2. Choose a couple of "likely to succeed" slicing schemes that would satisfy the build time and surface finish requirements and pass them on to the second c-DSP.
3. Now, choose the combination of compensation zone thickness, and cure depths that will give the required vertical dimension, i.e. satisfy equations 4.3, 4.4 and 4.5. The structure of the proposed process planning method is shown in Figure 4.8.

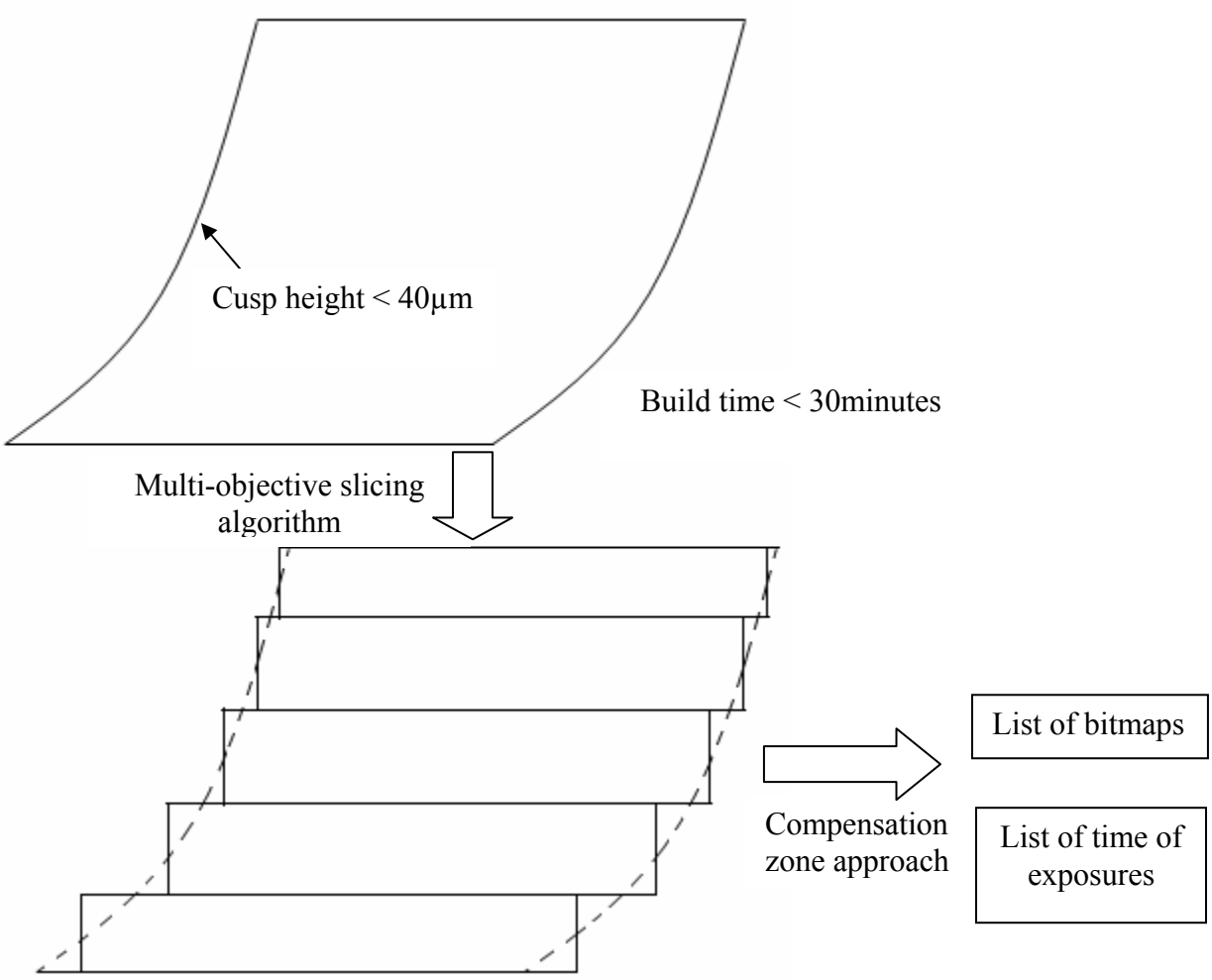

Figure 4.9 Multi objective process planning method

Summary

This chapter identifies the research questions that need to be addressed in order to meet the research objective of formulating a process planning method for Mask Projection Stereolithography. Research Question 1 deals with the modeling of image formation in a computationally inexpensive manner. Research Question 2 deals with the rigorous modeling and validation of the print through that occurs when multi-layered parts are built. Research Question 3 deals with achieving print-through smoothing for down facing surfaces, a phenomenon observed in laser scanning Stereolithography systems, but never demonstrated in Mask Projection Stereolithography. Research

Question 4 deals with the formulation of a process planning method that will utilize all the research done in answering research questions 1 to 3, in order to formulate a multi-objective process planning method for Mask Projection Stereolithography.

CHAPTER 5 IRRADIANCE MODEL

In this chapter, Research Questions 1a and 1b, as presented in Chapter 4, are tackled. In Section 5.1, the validity of the geometric optics approach to model the image formation process for the MPSLA system is verified. In Section 5.2, the multi scale modeling approach to model the irradiance distribution, is implemented and tested.

5.1 Geometric Optics to model image formation

Research Question 1 dealt with the approach to be used to model the image formation process. The hypothesis was that geometric optics is a better approach than physical optics to model the image formation process. This hypothesis is validated in this section. In Section 5.1.1, the imaging system is modeled using the optical design software OSLO^{TM} to quantify the optical path difference (OPD) introduced due to aberrations. This OPD is compared with the Rayleigh quarter wavelength criterion to show that the system is 'aberration limited', as opposed to 'diffraction limited'. In Section 5.1.2, the ray tracing algorithm is used to model the dimensions of an image formed on the resin. These dimensions are compared by curing a layer in the resin. This is used to quantify the accuracy of the geometric optics approach for modeling image formation.

5.1.1 Quantifying the OPD

It has been observed that the imaging system of the realized MPSLA machine can image an area comprising of 300x300 micromirrors or smaller with acceptable amounts of distortions. Thus, the active area of the mask is only 300x300 pixels. The pitch of the micro-mirrors (pixels) on the mask is 13.65μm. The maximum distance of any point on a pattern displayed on the mask, from the optical axis, is 150 x 13.65 = 2047μm, i.e. 2.047

mm. We wish to determine the optical path difference introduced due to distortion of the wavefront by aberrations introduced by the imaging system when an object as large as 2.047mm is imaged. In Section 2.1.2.2, the OPD introduced by an imaging system having spherical aberrations is derived. In reality, an imaging system has numerous types of aberrations (defocus, spherical, astigmatism, coma, distortion). Computing the OPD introduced by all these aberrations acting simultaneously is not possible analytically. Hence, the author has used optical design software OSLO^{TM}.

The imaging system data is input to OSLO as shown in Figure 5.1. The radii of all surfaces, the clear apertures of these surfaces, the distances between the surfaces, the height of the object being imaged and the refractive indices of spaces are fed to the software. It can be seen that the height of the image is calculated by OSLO as 2.098370mm.

The imaging system thus modeled is depicted in OSLO as shown in Figure 5.1.

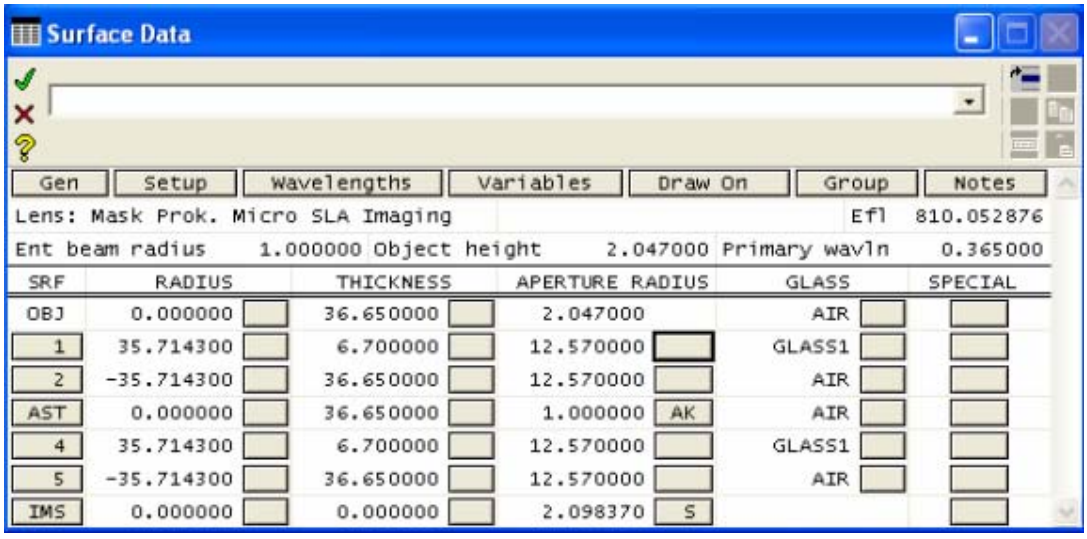

Figure 5.1 Imaging system modeled in OSLO

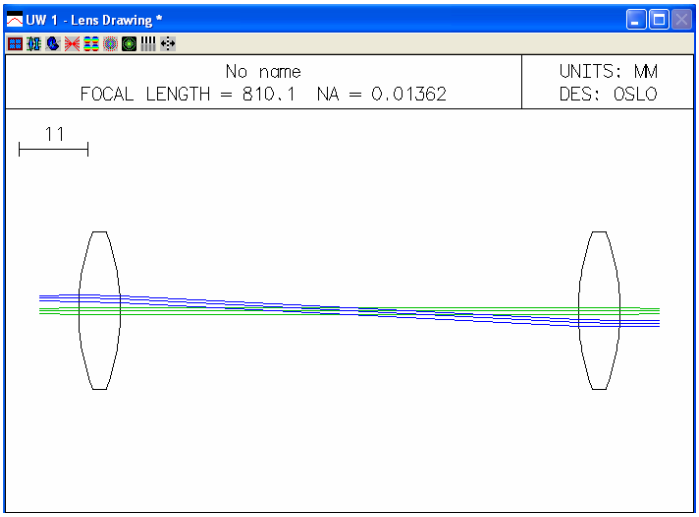

Figure 5.1 (continued)

Across the entire field of radius 2.047mm, the peak to valley OPD is calculated as 0.49637mm. See Figure 5.2. Since most of the light is in the i-line spectrum, the wavelength is assumed to be 365nm. The Rayleigh quarter wave criterion is λ/4, i.e. 91.25nm. Thus, the peak to valley OPD is more than 5400 times the Rayleigh quarter wave criterion. This shows that the imaging system is severely aberration limited and hence, geometric analysis should be used to model the image formation process (Smith, 1990).

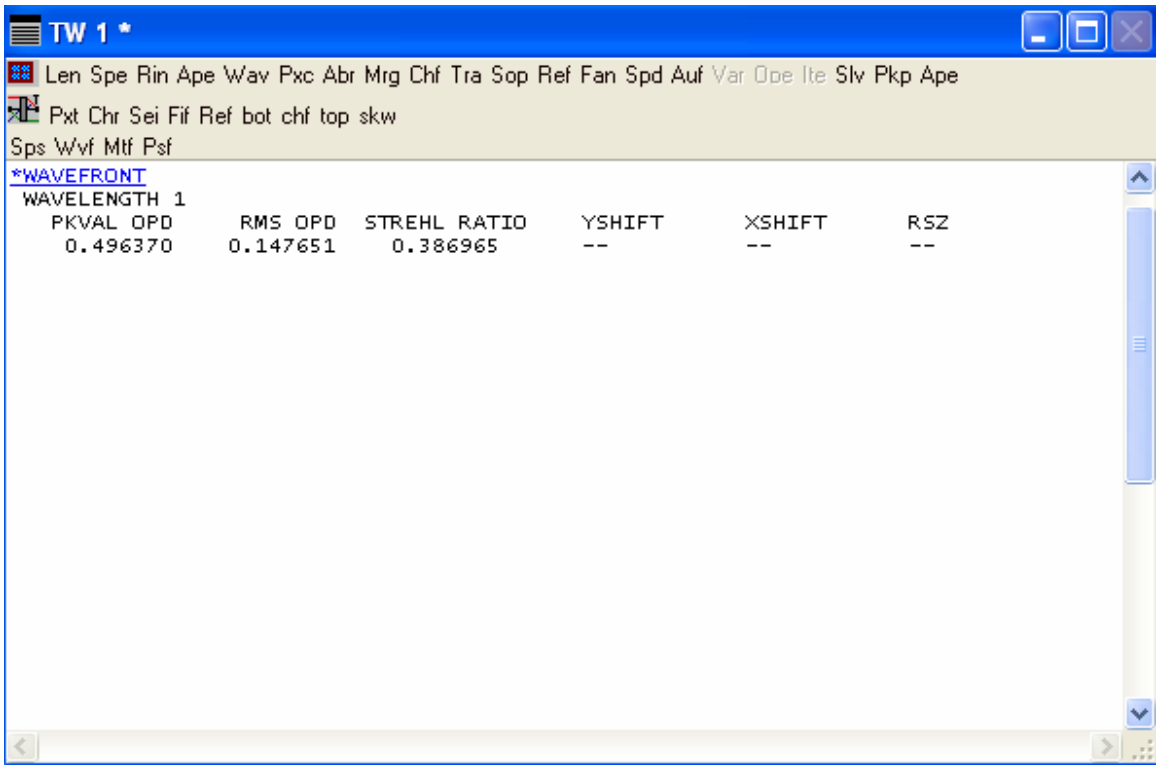

Figure 5.2 OPD calculated by OSLO

5.1.2 Irradiance model

Ray tracing is the method to model the irradiance across an image formed by an aberration limited optical system. An exact ray tracing algorithm is formulated to trace rays through the imaging system of the MPSLA system. The ray tracing equations presented in Section 2.1.2.3, as presented in Smith, (1990), are used to formulate the ray tracing algorithm.

The DMD is arranged so as to reflect a horizontal beam of light coming from the collimating system downwards towards the imaging system. The orientation of a displayed bitmap pattern in the three dimensional space and hence the co-ordinates of the points from which rays shall be traced are computed before starting the ray tracing.

In the Figure 5.3(a), the starting orientation of the DMD chip is shown with its plane perpendicular to the beam coming from the collimating system The global co-

ordinate system [XYZ] is defined as shown in the figure. X axis is the axis along the beam coming from the collimating system, Z axis is vertically downwards and the Y axis is perpendicular to the X and Z axes, along the plane of the DMD chip. The micromirrors, in their neutral state, are parallel to the DMD chip as shown in Figure 5.3 (a). The co-ordinate system [$X_m Y_m Z_m$] of one of the micromirrors on the DMD chip is exactly aligned with the global co-ordinate system in the beginning as shown in Figure 5.3(a). The global co-ordinate system is centered at the midpoint of the chip. The local co-ordinate system of every micro-mirror is centered at its midpoint. In the figure, the origins of the global co-ordinate system and that of the micro-mirror being considered are shown to be co-incident, but this is not necessary. In its 'ON' state, a mirror is tilted about its diagonal by 10^0. The DMD needs to be oriented in such a sense, so that a micro-mirror in its 'ON' state would reflect the horizontal beam coming from the collimating system vertically downwards. Since the beam is coming along the global X axis, an 'ON' micro-mirror needs to be tilted at an angle 45^0 about the global Y axis. Since the micro-mirror tilts about its diagonal, the diagonal needs to be aligned parallel to the global Y axis. We align the DMD in such a way that this is achieved. The DMD chip is rotated about the X axis by 45^0 to make the diagonal along which the micromirror would tilt, parallel to the global Y axis. This is shown in Figure 5.3(b). Now, the DMD chip is rotated by 55^0 about the global Y axis, so that when the micro-mirror tilts by 10^0 in its 'ON' state, it will be effectively tilted at 45^0 along the global Y axis and would thus direct the beam vertically downwards

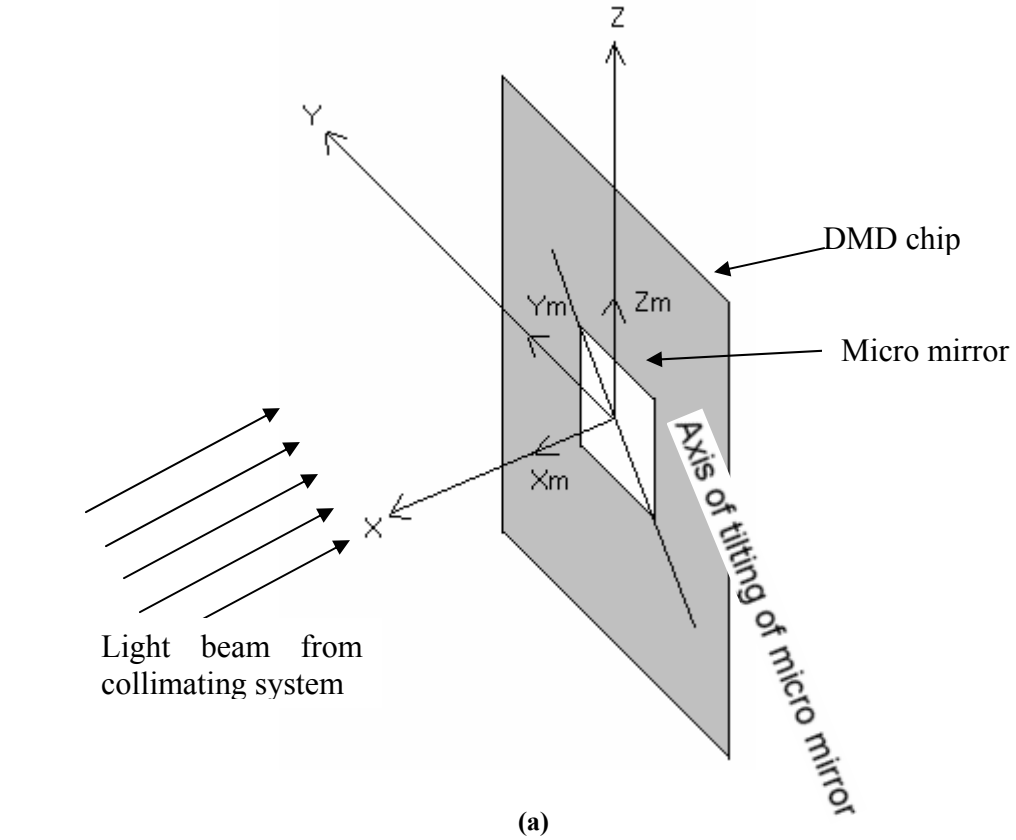

(a)

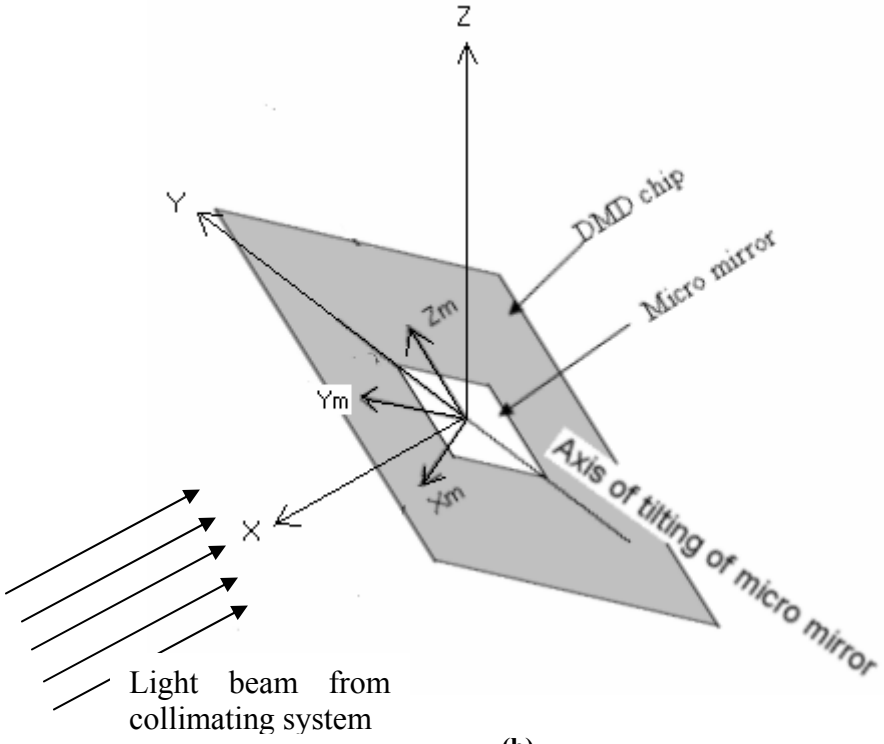

(b)

Figure 5.3 3D transformation of the DMD to reflect the light beam downwards

.

When any bitmap is input to the Irradiance model, geometric transformations are applied to the bitmap to account for the above mentioned alignment procedure. Then, every 'ON' micro-mirror on the DMD is meshed with points and rays are traced from each of these points to compute the irradiance distribution on the resin surface. This procedure is explained in detail in Sections 5.1.2.1 to 5.1.2.3.

5.1.2.1 Geometric transformations to determine center of every 'ON' micromirror

Given a bitmap, the 'ON' micro-mirrors on the DMD are identified. The co-ordinates of the center of each micro-mirror is passed through the 3D transformations that occur due to the alignment of the DMD as explained above. Suppose the global co-ordinates of the center of a micro-mirror are given by (x_1, y_1, z_1). It is passed through the following transformations:

- Rotation about the X axis would change the co-ordinates to (x_2, y_2, z_2)

$$\begin{aligned} z_2 &= z_1 \cos(45) - y_1 \sin(45) \\ y_2 &= z_1 \sin(45) + y_1 \cos(45) \\ x_2 &= x_1 \end{aligned} \tag{5.1}$$

- Rotation about Y axis would change the co-ordinates to (x_3, y_3, z_3)

$$\begin{aligned} z_3 &= z_2 \cos(55) + x_2 \sin(55) \\ x_3 &= -z_2 \sin(55) + x_2 \cos(55) \\ y_3 &= y_2 \end{aligned} \tag{5.2}$$

Since $z_2 = 0$, equation (5.2) gets simplified as:

$$\begin{aligned} z_3 &= x_2 \sin(55) \\ x_3 &= x_2 \cos(55) \\ y_3 &= y_2 \end{aligned} \tag{5.3}$$

In Appendix B, the co-ordinates of the midpoint of every 'ON' micro mirror are computed using the Matlab code "bitmap_read.m".

5.1.2.2 Meshing every 'ON' micro mirror with points

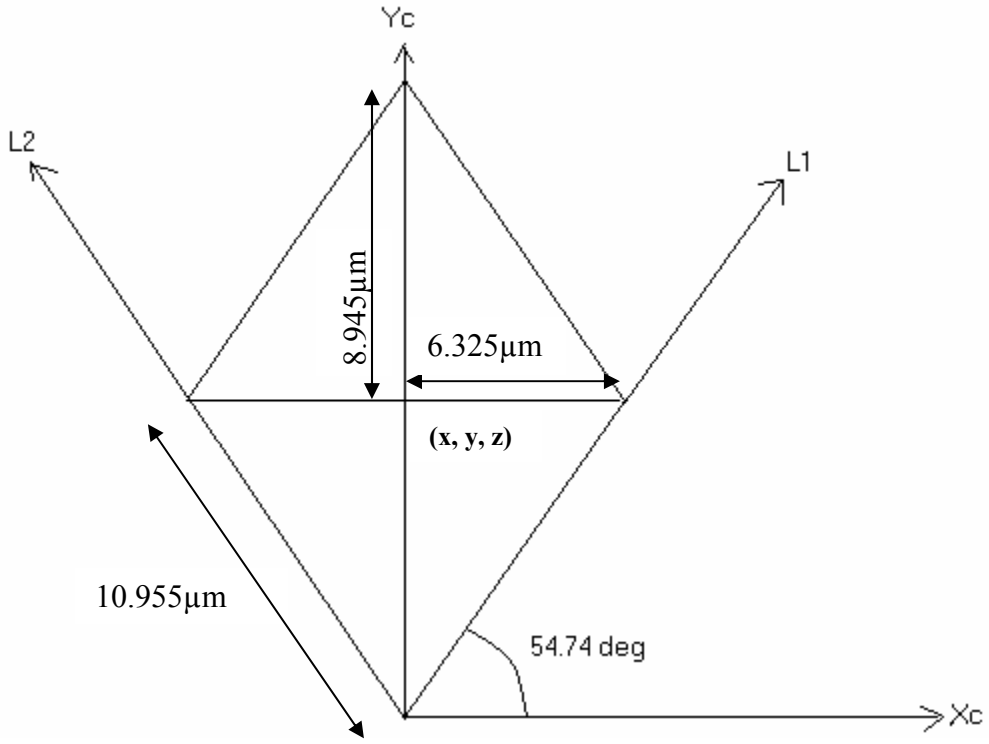

Figure 5.4 Projected image of an 'ON' micromirror to mesh with points

Using equation 7.1 and 7.2, the center of every 'ON' micromirror is computed as (**x, y, z**). The 'ON' micro-mirrors are all tilted at an angle about the global Y axis by 45^0. We mesh the projection of these micromirrors on the horizontal plane with equally spaced points from which to trace rays. The projected image of a micro mirror is meshed and not its true extents, in accordance to the laws of radiometry (O'Shea, 1985).

Figure 5.4 shows the projection of a micromirror tilted at 45^0 to the horizontal. The true dimensions of the micro-mirror are 12.65µm square. Using the Pythagoras theorem, the length of its diagonal can be computed to be 17.89µm. In Figure 5.4, this is

the dimension of the diagonal along the global Y axis. Due to the tilting by 45^0, the shorter diagonal will be of length $17.89\cos(45^0) = 12.65\mu m$. From the dimensions of the diagonals, it is possible to compute the side of the projected parallelogram in Figure 5.4, using Pythagoras theorem, to be 10.955µm.

Consider a two dimensional co-ordinate system [XcYc] centered at the corner of the projected micro mirror as shown in Figure 5.4. Consider another two dimensional co-ordinate system [L1L2] centered at the same corner, with axes along the sides of the projected image of the micro-mirror. The angle between the axes Xc and L1 is 54.74^0, as can be found out using trigonometry.

The projected image of the micro-mirror is meshed by 121 points, by dividing every side into 11 points. Given the location of a point in the [L1L2] co-ordinate system as (*a,b*), we need to determine the co-ordinates of that point in [XcYc] co-ordinate system and then, in global [X,Y] coordinate system. The transformations of the co-ordinates of a point from the [L1L2] co-ordinate system to the global [XY] co-ordinate system is achieved as follows.

Let l_1 and l_2 be unit vectors along the axes L1 and L2 respectively and x_c *and* y_c be unit vectors along the Xc and Yc axes respectively. The relationship between these unit vectors from different co-ordinate system can be obtained by projecting l_1 and l_2 on Xc and Yc, as given in equation 5.4.

$$\begin{aligned} l_1 &= \cos(54.74)x_c + \sin(54.74)y_c \\ l_2 &= -\cos(54.74)x_c + \sin(54.74)y_c \end{aligned} \tag{5.4}$$

Any point with the co-ordinates (*a,b*) in the (L1,L2) co-ordinate system can be expressed by the vector

$$al_1 + bl_2 \tag{5.5}$$

Substituting from equation 5.4, the point can be represented by a vector in the (Xc,Yc) co-ordinate system as

$$a[\cos(54.74)x_c + \sin(54.74)y_c] + b[-\cos(54.74)x_c + \sin(54.74)y_c]$$

Simplifying, the point can be represented by the vector

$$[a-b]\cos(54.74)x_c + [a+b]\sin(54.74)y_c$$

Thus, the co-ordinates of the point in (Xc,Yc) co-ordinate system are

$$([a-b]\cos(54.74),[a+b]\sin(54.74))$$

In the global co-ordinate system, the (X,Y) co-ordinates would thus be

$$([a-b]\cos(54.74)+\mathbf{x},[a+b]\sin(54.74)+\mathbf{y}-8.945) \quad (5.6)$$

where (**x,y**) are the co-ordinates of the center of the micro-mirror in global co-ordinates.

The *Z* co-ordinate of the point on the micro-mirror corresponding to a point with given (X,Y) co-ordinates on the projection will simply be equal to the Z co-ordinate of the mid-point of the micro mirror plus the X co-ordinate of that point multiplied by tangent of 45^0. Thus, the Z-co-ordinate of the point (*a,b*) in (L1L2) co-ordinate system will be $[a-b]\cos(54.74)\tan(45)$.

Thus, the [XYZ] co-ordinate of a point with coordinates (*a,b*) in the [L1L2] co-ordinate system is

$$([a-b]\cos(54.74)+\mathbf{x},[a+b]\sin(54.74)+\mathbf{y}-8.945,[a-b]\cos(54.74)\tan(45)) \quad (5.7)$$

In Appendix B, a given micro-mirror is meshed with 121 points and the co-ordinates of every point are computed as explained above, in the Matlab code "pointselector.m". This code is called as a function from "bitmap_read.m".

5.1.2.3 Tracing rays from a selected point

Once the co-ordinates of every point from which rays need to be traced are determined, direction cosines of the vectors along which rays need to be traced through the imaging system are formulated. Equally spaced direction vectors are traced within a cone of half cone angle 4^0. The computation of the direction vectors along which rays need to be traced from a given point is performed in the Matlab code "psf.m" in Appendix B. The code "psf.m" is called as a function from the code "pointselector.m".

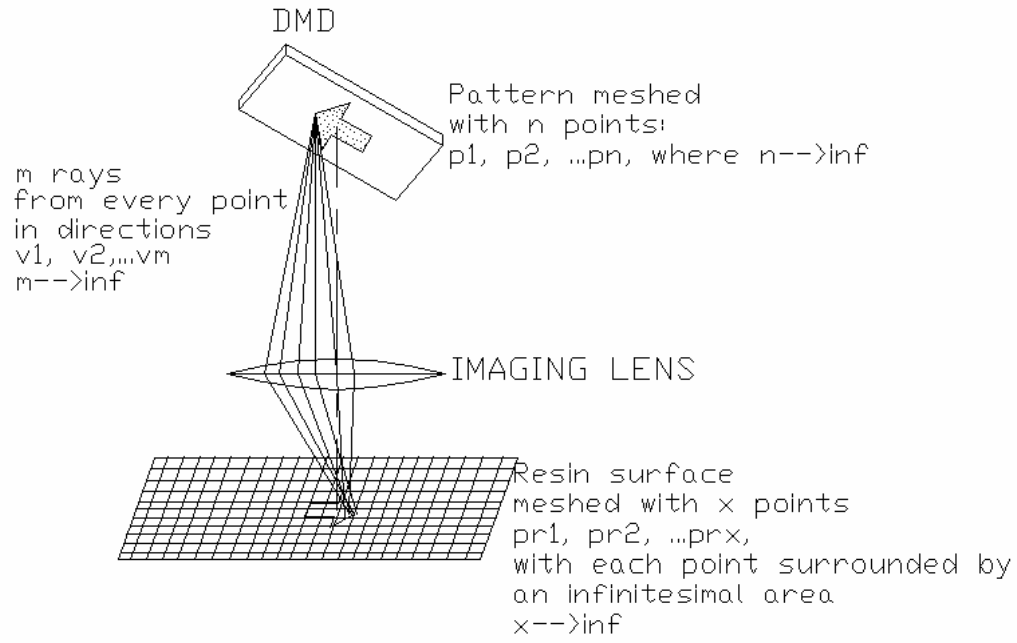

Figure 5.5 Ray tracing to model irradiance

Rays are traced through the imaging optical system following the equations of the exact ray tracing procedure, presented in Section 2.1.2.3 to compute the location of the point of intersection of every ray with the resin surface. The resin surface is meshed with 10μmX10μm squares and the number of rays incident in each of these squares is counted. We introduce a function δ which evaluates whether a particular ray will strike an

infinitesimal area centered on a given point on the resin surface or not. Suppose that in all, n points are used to mesh any bitmap displayed on the DMD and m rays are traced from each of these n points as shown in Figure 5.5.

If a ray starting from point p_j, along a direction vector v_k intersects the resin surface in one of the 10μmX10μm squares, centered on the point pr_i on the resin surface, then,

$\delta(p_j, v_k, pr_i) = 1;$

else,

$\delta(p_j, v_k, pr_i) = 0$

The function δ is evaluated by adopting the exact ray tracing procedure as explained in (Smith, 1990). In an exact ray trace the path of every ray is traced through the lens, and the coordinates of the point where it intersects the image plane are analytically computed. The imaging system parameters are used in the evaluation of the function δ. The procedure of ray tracing has been explained in Section 2.1.2.3.

The irradiance received by any point on the resin surface will be proportional to the number of rays striking an infinitesimal area centered on that point. The number of rays striking a 10μmX10μm area centered at point pr_i on the resin surface will be given by the function:

$$N(pr_i) = \sum_{j=1}^{n} \sum_{k=1}^{m} \delta(p_j, v_k, pr_i) \tag{5.8}$$

Since the irradiance at a point on the resin surface is proportional to the number of rays striking that point, the irradiance can be given by:

$$H(pr_i) = c \sum_{j=1}^{n} \sum_{k=1}^{m} \delta(p_j, v_k, pr_i) \tag{5.9}$$

where c is a constant.

The constant c is calculated as follows:

Using a radiometer, the average irradiance across an aerial image can be measured. Let the average irradiance be H_{av}. The average number of rays striking a point on the resin surface will be given by (total number of rays/total number of points on the resin surface) = nm/x. So, nm/x rays correspond to an irradiance of H_{av}. The constant c is thus determined to be $H_{av}/(nm/x)$. Substituting for c in the equation (6.3),

$$H(pr_i) = (H_{av}x / nm)\sum_{j=1}^{n}\sum_{k=1}^{m}\delta(p_j, v_k, pr_i) \qquad (5.10)$$

Equation (5.10) will give accurate results when $n \rightarrow \infty$ *and* $m \rightarrow \infty$.

In equation 5.10, all rays are assumed to carry the same amount of energy. This is because only a small portion of the center of the beam incident on the DMD is sampled by the active area of the mask (300X300 pixel area). The power in this small area can be assumed to be constant. Also, only a small portion at the center of the cone of rays emitted from every point on every micro-mirror is allowed to pass through the telecentric optic system. The power across this small cone (of less than 4^0 half cone angle), can also be safely assumed to be constant.

While conducting the ray tracing, it is checked if the ray would passed through the 2mm diameter aperture at the center of the telecentric imaging system. The tracing of a ray from a given point on a given micro-mirror in a given direction is conducted by means of the Matlab code “raytrace.m”. This code is called as a function from the Matlab code “psf.m”. The code “raytrace.m” is also presented in Appendix B.

5.1.3 Validating Irradiance model

The bitmap in Figure 5.6 was run through the Irradiance model to generate the irradiance distribution on the resin surface, the top view of which is shown in Figure 5.7. The bitmap in Figure 5.6 was imaged onto the resin surface for a long duration of time (160s) to cure single layer parts. For such a long duration of exposure, the entire irradiated area would cure and the dimensions of the cured layer would be the same as the dimensions of the irradiated area on the resin surface. One such cured layer in shown in Figure 5.8.

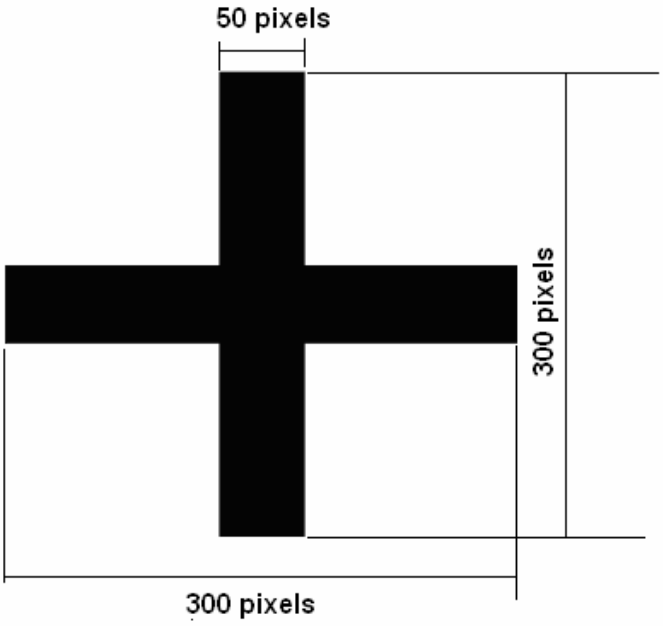

Figure 5.6 Dimensions of the test bitmap imaged onto the resin surface

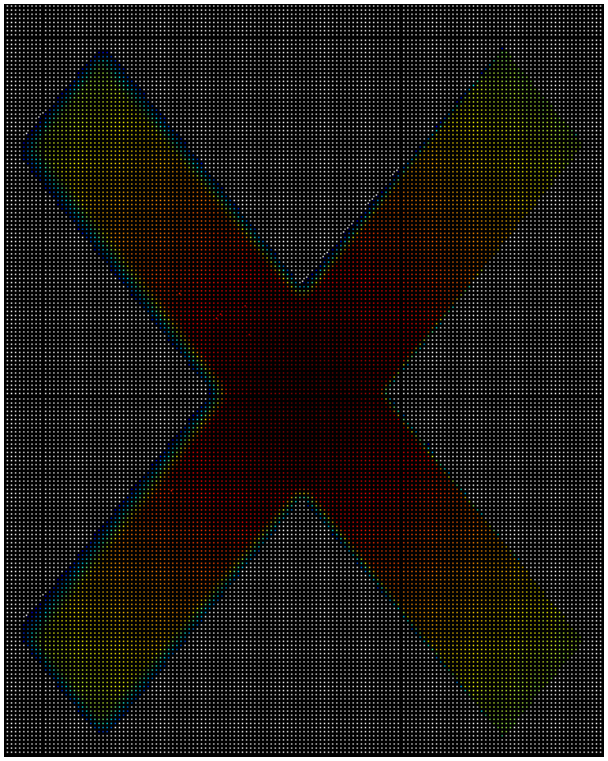

Figure 5.7 Irradiance profile on returned by the ray tracing code

Figure 5.8 Layer cured by imaging the bitmap in Figure 5.6 onto the resin surface

In all, 8 such layers were cured. The pictures of all these layers are presented in Appendix A. The dimensions of these layers were compared with those of the irradiance pattern returned by the Irradiance model. The dimensions that are measured are shown in Figure 5.9 and the dimensions are presented in Table 5.1.

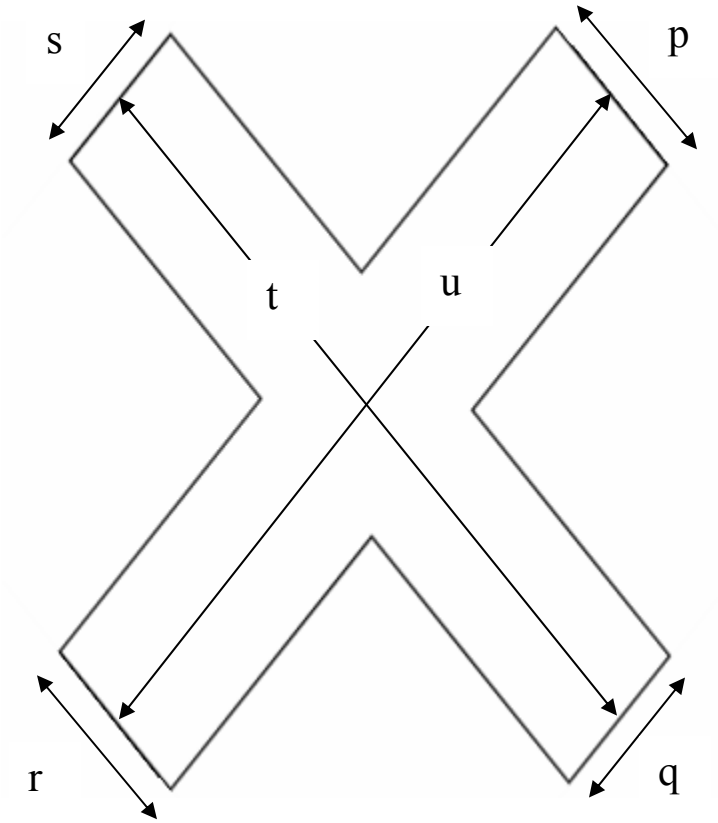

Figure 5.9 Dimensions compared in Table 5.1

Table 5.1Comparison of experimental observed and analytically computed dimensions of the test layers

Test layers	Dimension in µm					
	p	**q**	**r**	**s**	**t**	**u**
Layer #1	716.7	699.9	699.9	699.9	3899.6	3866.3
Layer #2	716.7	699.9	699.9	699.9	3899.6	3899.6
Layer #3	716.7	699.9	716.7	699.9	3899.6	3899.6
Layer #4	699.9	699.9	666.7	666.7	3866.3	3833.9
Layer #5	699.9	683.3	666.7	699.9	3866.3	3833.9
Layer #6	699.9	699.9	699.9	699.9	3866.3	3866.3
Layer #7	733.3	699.9	699.9	699.9	3899.6	3866.3
Layer #8	716.6	699.9	699.9	699.9	3866.3	3882.9
Average	**712.5**	**697.8**	**693.7**	**695.7**	**3882.9**	**3868.6**
Std. Deviation	**11.82**	**5.87**	**17.64**	**11.74**	**17.8**	**25.5**
Simulation	**718.7**	**718.7**	**640.6**	**640.6**	**3718.7**	**3718.7**
Error	**6.2**	**20.9**	**-53.1**	**-55.1**	**-164.2**	**-149.9**
% Error	**0.86**	**2.91**	**-8.29**	**-8.6**	**-4.42**	**-4.03**

It is clear from Table 5.1 that the image dimensions obtained by the ray tracing algorithm very closely match the dimensions of the layer cured. Thus, the hypothesis that geometric optics can be used to model the image formation by the MPSLA system is validated. The errors observed in the dimensions are expected to have their origins in the misalignment of the optical system and in the diffraction effects that have been ignored.

5.2 Multi scale Irradiance model

Consider the modeling the irradiance distribution obtained by running the test bitmap as shown in Figure 5.6 through the ray tracing algorithm. In order to generate the irradiance distribution, 2816 million rays were traced through the optical system. The computation time was more than 152 hours. Research Question 2 dealt with reducing the computation time of running the ray tracing approach for modeling image formation. A multi-scale modeling method is proposed in Hypothesis 2 to speed up the computation of irradiance distribution. According to this method, the irradiance is modeled at two scales: pixel scale; and bitmap scale. At the pixel scale, a high resolution database documenting the irradiance across the resin surface obtained when each micro-mirror is individually imaged onto it, is populated by ray tracing. At the bitmap scale, this database is used to compute the irradiance distribution across the resin surface when any bitmap is imaged onto it. This approach is depicted in Figure 5.10.

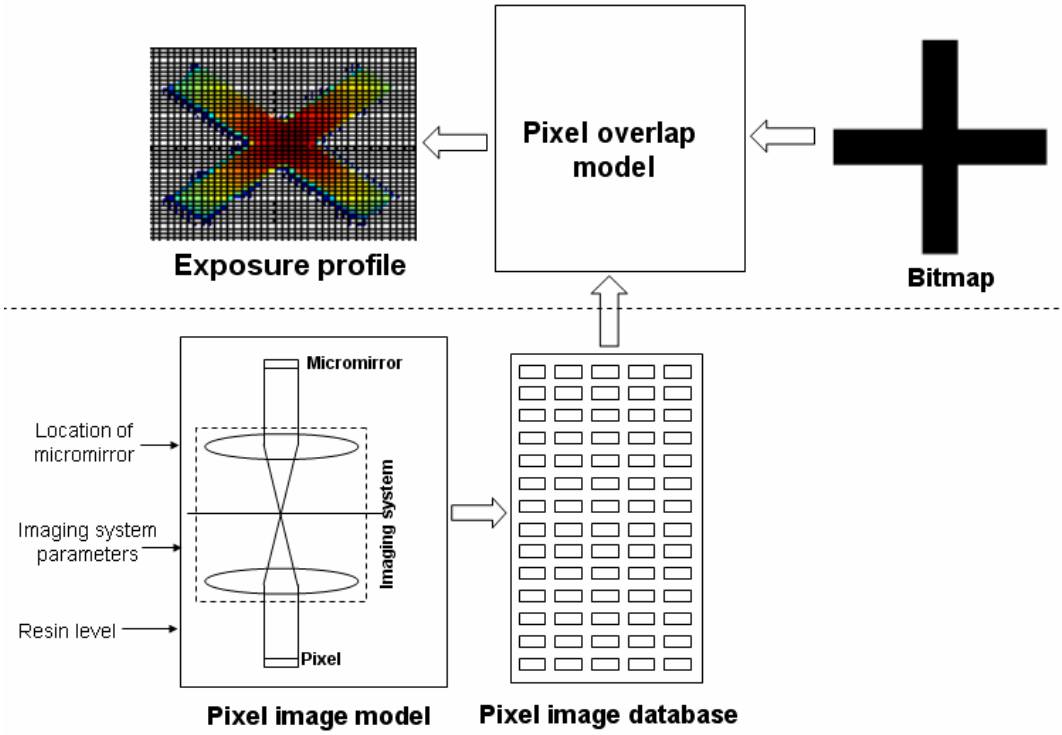

Figure 5.10 Multi scale modeling of irradiance

There are two models formulated as a part of the Multi-scale Irradiance model: Pixel Image model and Pixel Summation model.

Pixel Image model

As shown in Figure 5.10, the Pixel Image model is used to populate the "Pixel Image database". The Pixel Image model takes in the location of every micro-mirror on the DMD individually as an input. The projection of this micromirror on the horizontal plane is meshed with points and rays are traced from each of these points, following the procedure as explained in Section 5.1.2. The irradiance distribution on the resin surface obtained due to the imaging of this micro-mirror is recorded in the form of a matrix. A 6mmX6mm area on resin surface is meshed with 10µmX10µm squares. The irradiance on the resin surface is thus recorded in the form of a 601X601 matrix. Thus, in general,

the irradiance from a micro-mirror with indices (p,q) is recorded in the Pixel Image database as a 601X601 matrix H_{pq}.

In Appendix B, the Matlab code that implements the Pixel Image model to populate the Pixel Image database is presented as "massive_database.m". In order to populate the database, the functions "pointselector.m", "psf.m" and "raytrace.m", as documented in Appendix B and called by this code "massive.database.m".

The population of the Pixel Image database entailed tracing of billions of rays. The database populated is of size 7.65GBytes. It took around 500 hours to populate it.

Pixel Summation model

Given any bitmap, the co-ordinates of the 'ON' micro-mirrors on the DMD can be obtained from the black pixels on bitmap. Given a set on 'ON' micro-mirrors, their corresponding 601X601 matrices recording the irradiance on the resin surface can be mined from the Pixel Image database. These matrices then are simply added to obtain the irradiance distribution that would result when the bitmap is imaged onto the resin surface. This is given by equation 5.11.

$$H = \sum H_{pq} \tag{5.11}$$

where (p,q) are indices of all the 'ON' micro-mirrors on the DMD.

The Pixel Summation model (Equation 5.11) is implemented for the test bitmap as shown in Figure 5.6, in the Matlab code "bitmap_read_database.m", as presented in Appendix B.

The test bitmap as shown in Figure 5.6 was passed through the Pixel Summation model and the irradiance distribution across the resin surface was computed. This irradiance distribution, as expected, was found to be exactly the same as that obtained by

running the same bitmap through the Irradiance model. The time required to generate this irradiance distribution by using the Pixel Image database only 15 minutes. Thus, the computation time has been reduced from 152 hours to 15 minutes by adopting this multi scale modeling method.

5.3 Bitmap Generation method

The Multi scale Irradiance model can compute the lateral extents of the aerial image that will be formed on the resin surface when a bitmap displayed on the DMD is imaged onto it. The bitmap generation method uses the Pixel Image database to do just the opposite, i.e., generate the bitmap to be displayed on the DMD in order to irradiate a given area on the resin surface.

Using the Pixel Image database, the center of the pixel irradiated by every micro-mirror is determined. A second database relating the location of the central element irradiated by every micro-mirror on the DMD with the micro-mirror irradiating it is created. This, we call as the "Element-Micromirror Mapping" database. Given the area to be irradiated on the resin surface, it is meshed with 10μmX10μm elements, just like those used in populating the Pixel Image database. Using the "Element Micromirror Mapping database, every element composing the layer is checked to see if it is at the center of one of the pixels irradiated by one of the micro-mirrors. If it is, then that micro-mirror is deemed as 'ON'. Knowing the micro mirrors that are 'ON', it is possible to generate the bitmap with a black pixel corresponding to every 'ON' micro mirror and a white pixel corresponding to every 'OFF' micro mirror. The Inverse Irradiance model is in the form of a computer code which accomplishes the above mentioned tasks.

The Bitmap generation method is demonstrated by curing the layer as shown in Figure 5.11. The layer is in the form of a rectangle of dimensions 2500µmX600µm. It is to be cured parallel to the global X axis. This layer is meshed with pixels, which are mapped onto the micro-mirrors on the DMD, to generate the bitmap as shown in Figure 5.12. The Matlab code implementing the Layer Cure model is presented as the Matlab code "element_micromirror_mapping.m", presented in Appendix C.

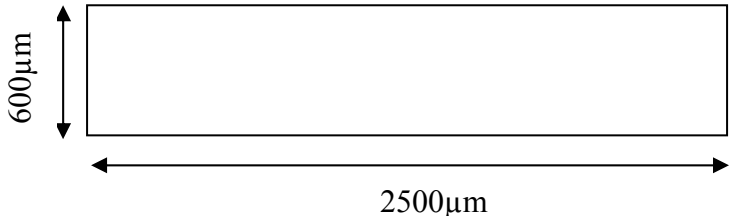

Figure 5.11 Rectangular layer to be cured

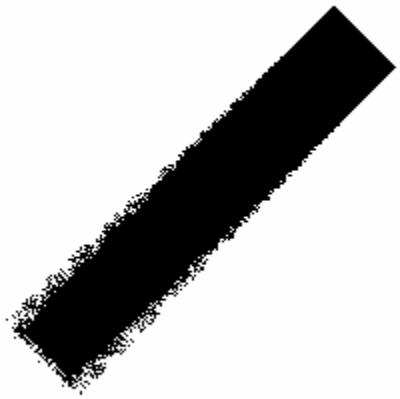

Figure 5.12 Bitmap generated by applying Layer cure model

The bitmap in Figure 5.12 can be seen to be getting blurry towards the part corresponding to the global negative Z axis. This blurriness is related to the mapping of elements on the resin surface with the micro-mirrors and also with the focusing errors. Due to the tilted mounting of the DMD, the object distances change along the Z axis. There are focusing errors towards the negative Z axis, and the shapes of the pixels irradiated by micro-mirrors in that region are irregular in shape. This causes errors and approximations in the determination of the central element irradiated by micro-mirrors that are located towards the negative Z direction. When the elements on the layer are mapped onto the micro-mirrors, some of the micro-mirrors are not identified as 'ON' because their approximated center of the irradiated pixel is not a part of the layer.

Hence, a manual step is performed, in which the 'OFF' micro-mirrors (corresponding to white pixels) dotting in between the 'ON' micro-mirrors (black pixels) are manually turned on (i.e. pixels are turned black.). This smoothing of the bitmap is performed to obtain the bitmap presented in Figure 5.13.

Figure 5.13 Bitmap generated by the pixel mapping database manually smoothened

Note that the smoothing out is done manually by the author by exercising his own judgment. A better filtering or an edge detection algorithm should be implemented in future to do the smoothing.

The smoothened bitmap was imaged onto the resin surface to cure three layers, as shown in Figure 5.13. The lengths and widths of each of these layers were measured to be 2433µm and 566.67µm respectively. This good agreement between the required and the obtained dimensions of the rectangular layer demonstrates the Inverse Irradiance model and also further bolsters the Irradiance model itself.

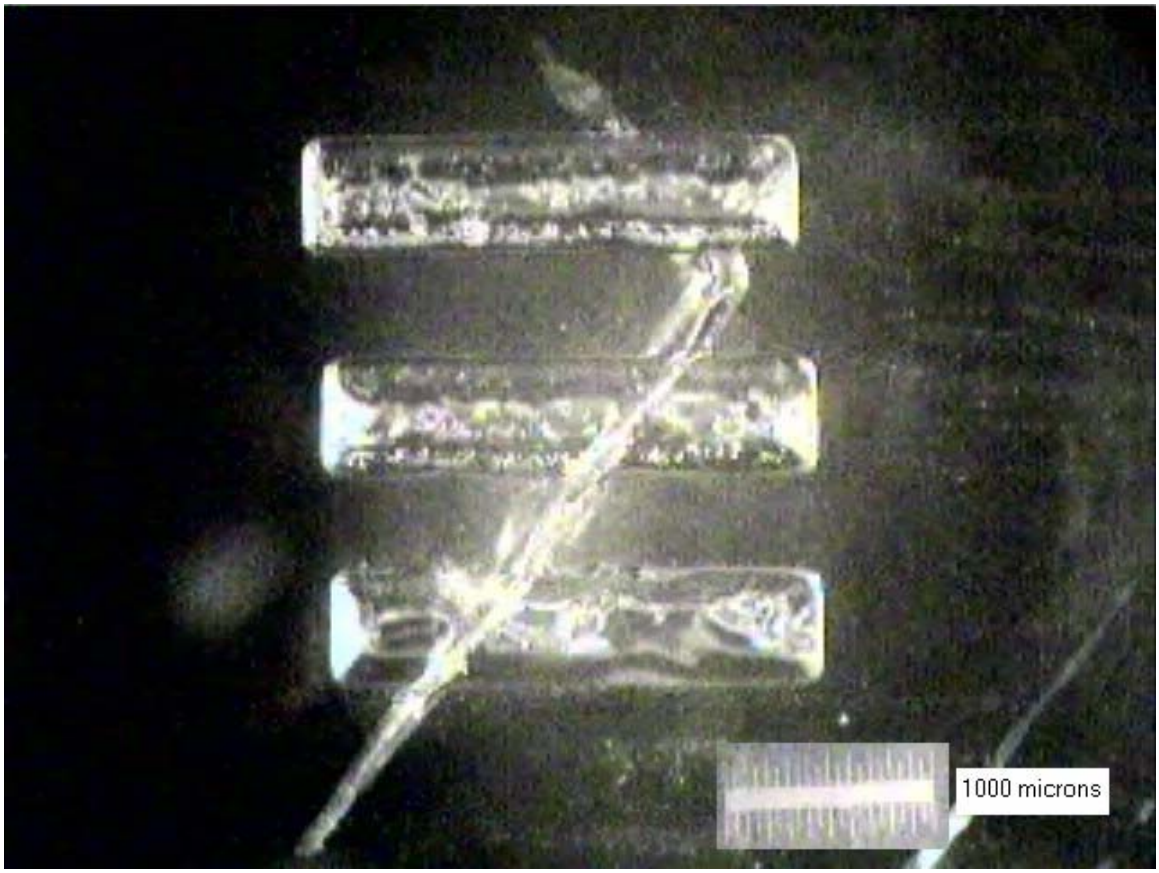

Figure 5.14 Rectangular layers cured by imaging bitmap in Figure 5.13 onto the resin surface

Summary

In this chapter, the modeling of irradiance that would be supplied to the resin surface when a given bitmap is imaged onto it is modeled. The geometric theory of optics is shown to be valid for the modeling of image formation in case of an aberration limited system such as the author's. A ray tracing algorithm is formulated to model the image formation process. Test layers have been cured on the MPSLA part and the ray tracing algorithm has been shown to be valid within 8.6% error.

A multi scale modeling approach, which allows the computationally intensive task of computing image formation through ray tracing manageable is also presented.

The chapter ends with the Bitmap Generation model, which generates the bitmap to be displayed on the DMD in order to irradiate a given area on the resin surface.

Progress made towards answering research questions

In this chapter, research questions 1(a) and 1(b) are answered. Research question 1(a) dealt with choosing the optical theory to model image formation by the MPSLA system. There are two theories for modeling image formation: geometric optics and physical optics. In this chapter, the Optical Path Difference (OPD) of the telecentric imaging system of the MPSLA system designed as a part of this research (Chapter 3) is quantified. The OPD is shown to be more than 4000 times the Rayleigh limit ($\lambda/4$), and thus the imaging system is shown to be aberration limited. The image formation for aberration limited systems is modeled using the theory of geometric optics. A ray tracing algorithm is formulated in this chapter to formulate the "Irradiance model". The Irradiance model computes the irradiance on the resin surface when a given bitmap is

imaged onto it. The model is validated by curing test layers on the MPSLA system and comparing the dimensions of these layers with those of the irradiate area computed by using the Irradiance model.

Research question 1(b) was concerning reducing the computation time involved in implementing a ray tracing algorithm, which entails tracing of billions of rays through the imaging system. A multi scale modeling strategy has been presented in this chapter to reduce the computational expense of executing Irradiance model. “Pixel image model” is formulated that traces rays from each micro mirror on the DMD individually and computes the irradiance on the resin surface when that particular micro mirror is imaged onto it. A “Pixel image database” which stores the irradiance across the pixels irradiated by all the micro-mirrors on the DMD is populated. Once this database is formulated, the image modeling can be done very rapidly. Give a bitmap to be imaged onto the resin surface, the ‘ON’ pixels of the bitmap are identified, the corresponding pixels are mined from the Pixel image database and are overlapped to obtain the irradiance on the resin surface. The improvement in computational efficiency is demonstrated in this chapter by modeling the image formation of a test bitmap without using the multi scale modeling approach and using the multi scale modeling approach. The reduction in computation time was found to be from 114 hours to 15 minutes.

CHAPTER 6 BUILDING ACCURATE THREE DIMENSIONAL PARTS

In Chapter 5, the Irradiance model was formulated which computes the irradiance received by the resin surface when a bitmap is imaged onto it. This enables curing of dimensionally accurate layers. In this chapter, the print through errors that would result when layers are cured over each other are modeled. Research Question 2 deals with avoiding the print through errors by adopting the "compensation zone" approach. Research Question 2 has been broken down into two sub research questions, questioning long held assumptions about the curing process of Stereolithography resins. The hypotheses presented for these research questions are tested in this chapter.

In Section 6.1, the transient model of layer curing is formulated and validated. This model takes into account the changing rate of attenuation of light in resin during exposure. In Section 6.2, the effect of diffusion of reactive species and oxygen molecules underneath a part being built, on the print through, is modeled and validated. In Section 6.3, the models formulated in Sections 6.1 and 6.2 are utilized to model the print through that would occur when multiple layers are built over each other. The down facing surface profile of the four-layered part presented in Figure 4.4 is simulated and validated in Section 6.4. In Section 6.5, the compensation zone approach is implemented, utilizing the derivations made in Sections 6.3 and 6.4, to compute the process parameters that would build the required test part with accurate down-facing surface.

Research Question 3 was regarding employing the compensation zone approach to smoothen the down facing surfaces of MPSLA builds. In Section 6.6, an implementation of the compensation zone approach to smoothen the down facing surfaces of MPSLA builds is demonstrated.

6.1 Transient layer cure model

The cure model presented in standard Stereolithography texts, like Jacobs (1992), is fairly simple. It assumes that the depth of cure is proportional to the logarithm of exposure and assumes the threshold model of resin cure. Suppose that irradiance H is incident on the resin surface for a duration t. It would supply an exposure $E = H \cdot t$. This energy would get attenuated as it enters the resin, according to the Beer Lambert's law. The exposure at a depth z is given by $E_z = E \exp(-z / D_p)$. Curing occurs at all points where exposure is greater than or equal to E_c. The thickness of the layer cured will thus be given by equation (6.1).

$$C_d = D_p \ln(H \cdot t / E_c) \tag{6.1}$$

where D_p is the depth of penetration of the resin (a measure of attenuation of radiation), and

E_c is the threshold exposure for polymerization.

This model assumes that the attenuation of radiation through a cured layer is the same as that through uncured resin, given by the parameter D_p. The author has observed experimentally that the rate of radiation attenuation through a cured layer is significantly less than that through liquid resin. Thus, the depth of penetration for a cured layer D_{pS} is expected to be different from that for the liquid resin D_{pL}. The effect of these different rates of attenuation on the cure depth is captured in this section by modeling layer curing as a transient phenomenon.

Suppose irradiation H is incident on the resin surface at a particular location. It will initiate curing after time t_c (let us call it as "critical time"), when the exposure received by the resin equals E_c.

$$t_c = \frac{E_c}{H} \tag{6.2}$$

A thin film of cured resin shall be formed on the surface. The energy now incident on the top surface of the cured film will have to pass through this film of cured resin and then, through the uncured resin under the film. The attenuation of radiation will now be a function of the attenuation through the cured film and that through uncured liquid resin. This effective attenuation will go on changing as the cured film gets thicker during exposure.

Suppose that, as shown in Figure 6.1, the thickness of the film cured after time t is equal to z. The exposure at the bottom surface of this film is equal to E_c. At time $t+dt$, the next dose of energy equal to $H \cdot dt$ will be incident on the top of the cured film. This energy will get attenuated following the Beer Lambert's law of attenuation as it would pass through the cured layer of thickness z and the energy reaching its bottom surface would be $H \cdot dt \exp(-z / D_{pS})$. Here, it will add up with E_c, the energy already at the bottom of the film and cause an incremental curing equal to dz. This incremental curing will be given by

$$dz = D_{pL} \ln[\frac{H \cdot dt \exp(-z / D_{pS}) + E_c}{E_c}] \tag{6.3}$$

This is a first order differential equation with the initial condition: $z = 0$ at $t = t_c$.

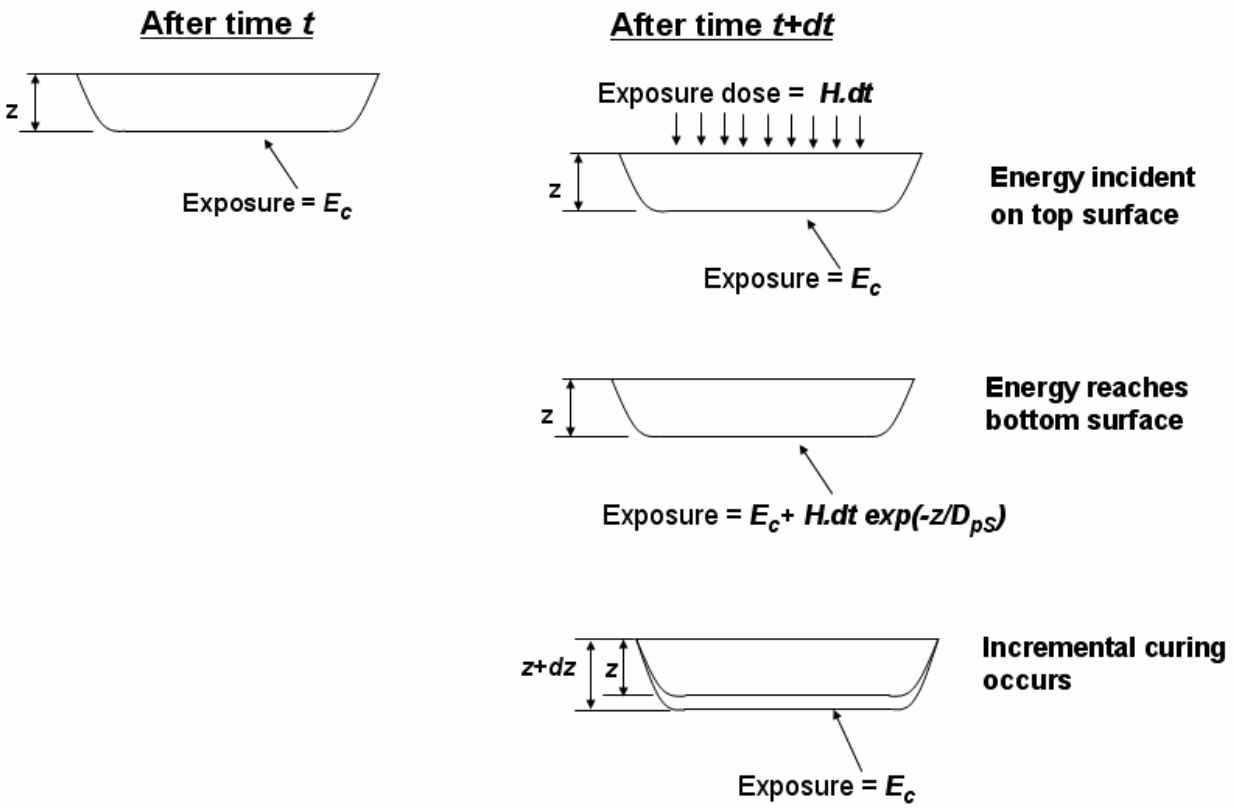

Figure 6.1 Modeling layer curing as a transient phenomenon

Equation 6.3 was solved numerically to obtain the relationship between the depth of cure (z) and the time of exposure (t). The solution to equation 6.3 converged when the time domain was discretized to dt = 0.1s. In equation 6.3, the parameters D_{pL}, D_{pS} and E_c are to be determined experimentally.

Characterizing the resin

In order to determine these parameters, the experimental procedure as shown in Figure 6.2 was adopted. An optical window was placed in contact with the free surface of resin contained in a vat and lines were imaged onto the resin surface for various time durations. Curing was first noticed at 15s. The time durations were incremented in steps of 5s, from 15s to 50s. This range of the times of exposure is fairly close to the typical times of exposure for the author's MPSLA system. Three lines were cured for each time

of exposure and the average of the cure depth of the lines cured was for each time of exposure was calculated. The micro scope images of the test layers are shown in Appendix D. The thicknesses of the three lines are documented against the time of exposure in Table 6.1.

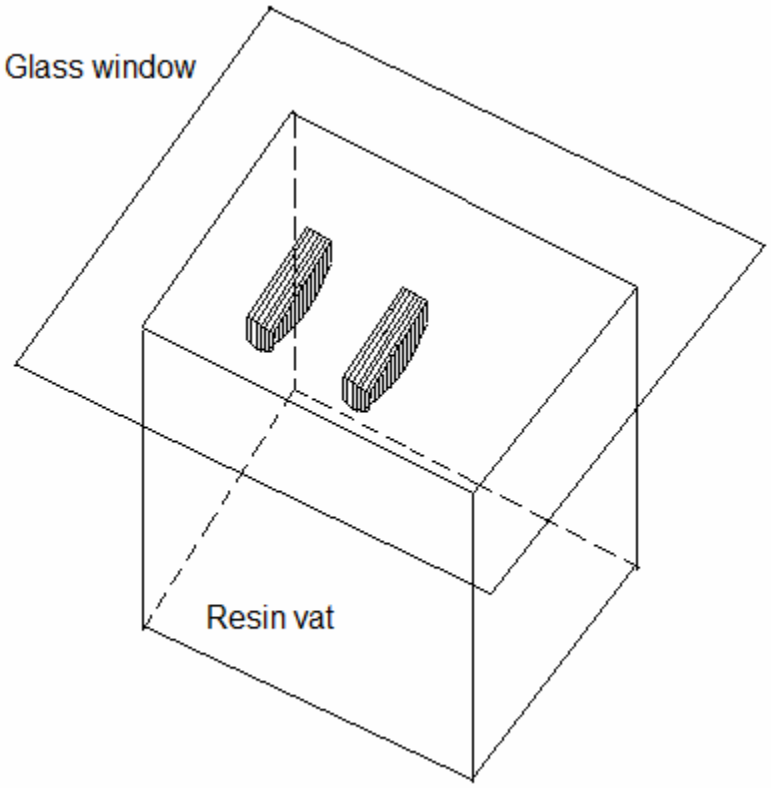

Figure 6.2 Characterizing the photopolymer

Table 6.1 Thicknesses of experimentally cured lines against the time of exposure

Time of exposure (s)	**Thickness of the cured lines (µm)**			
	Experiment 1	Experiment 2	Experiment 3	Average
15	0	0	0	0
20	48.38	56.45	56.45	53.76
25	120.96	129.03	129.03	126.34
30	201.61	201.61	193.55	198.92
35	274.19	282.26	282.26	279.57
40	354.83	362.90	346.77	354.84
45	419.35	411.28	411.29	413.97
50	483.87	467.74	467.74	473.12

The plot of the average cure depth of the line cured versus the time of exposure was found to be linear, as shown in Figure 6.3. Hadipoespito et al, (2003) have characterized the same photopolymer (DSM SOMOS 10120) using their Mask Projection Stereolithography system and have also observed a linear relationship between cure depth and time of exposure. The linear relationship between cure depth and time of exposure cannot be explained by the standard SLA theory which assumes equal rates of radiation attenuation through cured and uncured resin.

Equation 6.3 was integrated numerically, by discretizing the time domain into durations of 0.1s. The analytical and experimental results agreed the best when the values of the unknown parameters were chosen to be:

D_{pL} = 0.192mm

D_{pS} → infinity

E_c = 10.2 mJ/cm^2

From Table 6.2, it can be seen that the experimental and analytical values of cure depths agree very well. The value of the depth of penetration through liquid resin (D_p) and that of the threshold exposure of polymerization (E_c) are specified by the manufacturer to be 0.16mm and 9.81mJ/cm^2 respectively. These values agree very closely with the values that have been measured. It should be noted that the value of depth of penetration through cured resin (D_{pS}) tends to infinity, indicating that a cured layer is almost transparent to radiation.

Table 6.2 Analytically computed and experimentally measured values of layer thicknesses

Time of exposure (s)	Exposure (mW/cm^2)	Experimental value of layer thickness (μm)	Analytical value of layer thickness(μm)
15	10.5	0	0
20	14	53.76	68.26
25	17.5	126.34	136.52
30	21	198.92	204.77
35	24.5	279.57	273.03
40	28	354.84	341.29
45	31.5	413.97	409.55
50	35	473.12	477.81

The thicknesses of the lines cured on the author's system have been plotted against the times of exposure in Figure 6.3. It is seen that the plot can be best approximated by a straight line, which indicates that the relationship between the thickness of a cured layer and the time of exposure is linear. The relationship is given in equation 6.4.

$$z = 19.172.E - 195.59 \tag{6.4}$$

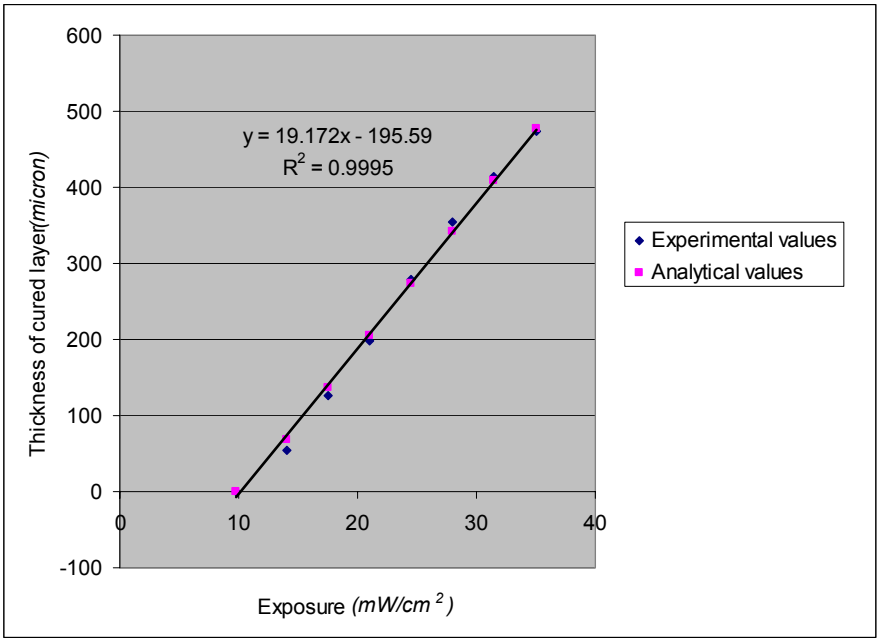

Figure 6.3 Thickness of layer cured plotted cured against exposure

In general, the author postulates that the working curve for a Stereolithography resin used with a Mask Projection Stereolithography system is linear, of the form

$$z = D_{pM} \cdot (E - E_c) \tag{6.5}$$

where D_{pM} is the effective slope of the working curve, which is the rate at which the cure-front propagates into the resin depth; and

E_c is the threshold exposure of polymerization.

For the MPSLA system under consideration,

D_{pM} = 19.172 μm/(mW/cm^2), or 1.9172mm^3/mW and

E_c = 10.2 mW/cm^2

It should be noted that linear relationship between cured depth and time of exposure will be observed only for those resins for which the rate of radiation attenuation through cured resin is negligible compared to that through uncured resin.

6.2 Effect of diffusion of radicals and oxygen

Jacobs, (1992) assumes exposure to be additive. This assumption means that if a particular location in the depth of resin receives multiple doses of exposures, their effect is the same as if the combined exposure was continuous. The author has experimentally found that the additive nature of exposure is a strong function of time.

Suppose that, irradiance H is incident on the resin surface for a time duration t_1 and causes curing up to a depth z. This is plotted in Figure 6.4. This cured layer is allowed to remain in the resin bath for a time t. Now, the top surface of the cured layer is supplied the radiance H for a second time interval of duration t_2. This second dose of energy will pass through the transparent layer and will add up with the exposure at the

bottom surface. The assumption of additive exposure says that the exposure at the bottom surface will be equal to

$$E_b = E_c + (H \cdot t_2)\exp(-z / D_{pS}) \tag{6.6}$$

Since $D_{pS} \rightarrow \infty$,

$$E_b = E_c + H \cdot t_2 \tag{6.7}$$

This exposure will cause further incremental curing underneath the already cured layer. The plot of cure depth versus time of exposure will thus be expected to be linear and continuous as shown in Figure 6.4.

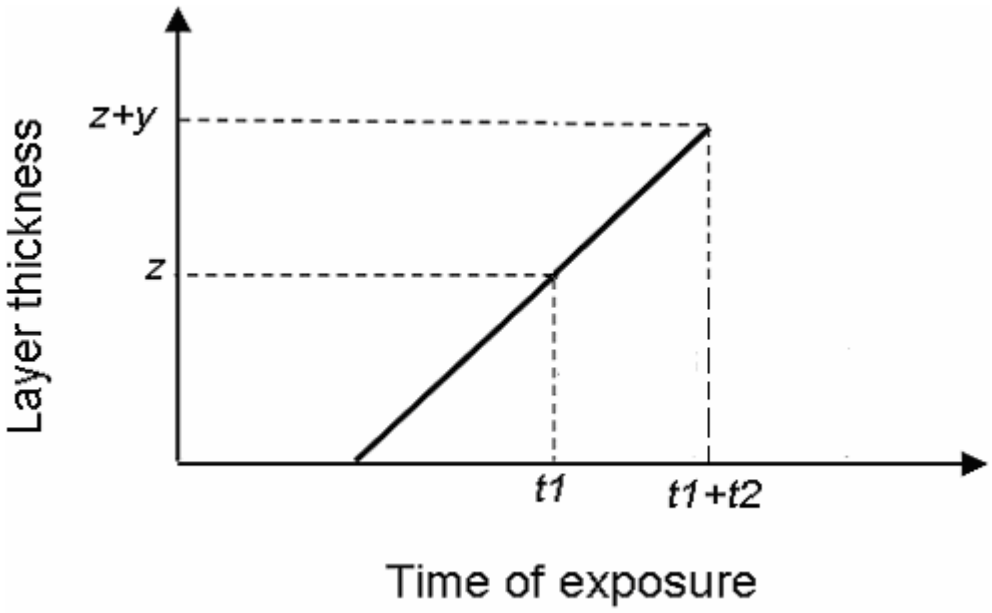

Figure 6.4 Plot of cure depth versus time of exposure under the assumption of additive nature of exposure

In reality the exposure is not additive. When the layer cured after the first exposure dose is allowed to sit in the resin vat for time *t*, there will be a diffusion of the reactive species away from, and diffusion of oxygen molecules towards, the bottom surface of the cured layer. The reactive species diffusing out will carry energy away with

them. Also, the oxygen diffusing in will combine with the reactive species underneath the layer and 'quench' them. As a result of this diffusion, an energy equal to $k \cdot E_c$ will be lost from the bottom surface of the cured layer. This will reduce the effective exposure underneath the cured layer to $(1-k)E_c$. This is shown along the time line in Figure 6.5 at the location (t_1+t). Thus, after the second exposure dose, the exposure at the bottom surface will be less than that calculated in equation (6.7), and will be equal to

$$E_b = (1-k)E_c + H \cdot t_2 \tag{6.8}$$

The value of 'k' (let us call it as "diffusion factor") in equation 6.8 is found to be a strong function of time. As a result of the diffusion of reactive species and oxygen, the incremental curing does not start the moment the second exposure reaches the bottom surface, but only after the energy carried lost due to diffusion is compensated for. Thus, curing starts only after a time t' where

$$t' = \frac{kE_c}{H} \tag{6.9}$$

This can be observed at the location (t_1+t+t') along the time line shown in Figure 6.5. The remainder of the second exposure dose, beyond time t', will cause incremental curing.

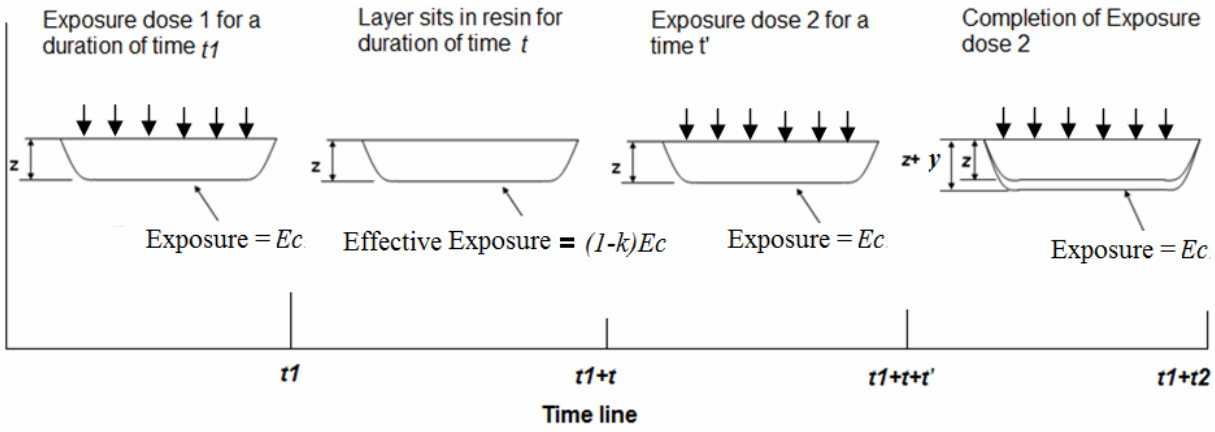

Figure 6.5 Effect of two discrete exposures on the thickness of a layer cured

Thus, the plot of cured depth against time of exposure will not be continuous linear as presented in Figure 6.4, but will have a discontinuity as shown in Figure 6.6. The portion of the plot parallel to the time axis is the time it takes for the second exposure dose to compensate for the energy lost because of diffusion.

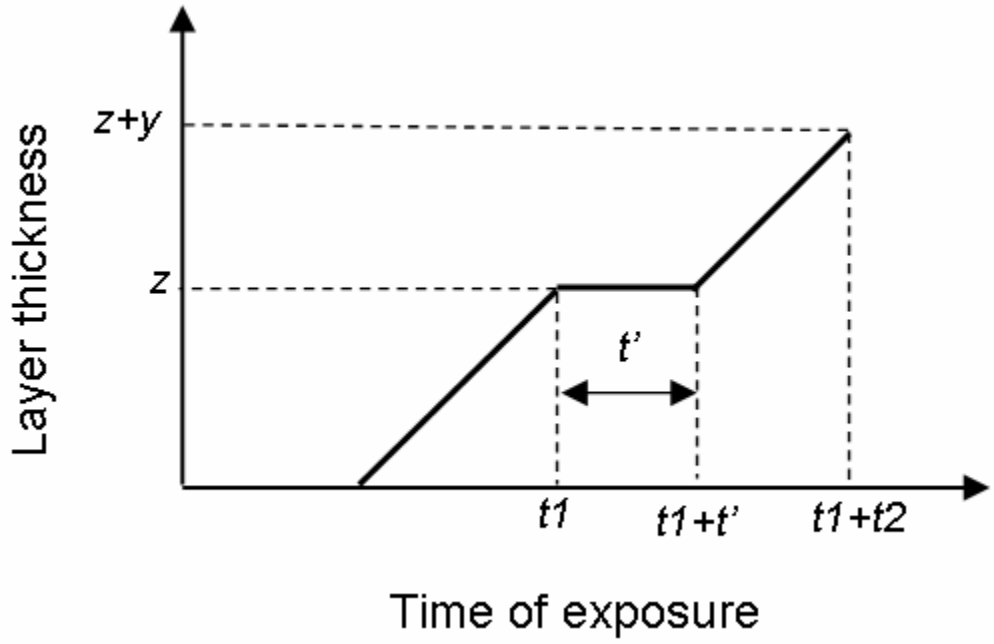

Figure 6.6 Effect of diffusion of radicals underneath a cured layer on the layer thickness

Measuring the value of *k*

The value of diffusion factor '*k'* is measured experimentally as follows. The same experimental arrangement as shown in Figure 6.2 is used, with a glass window kept flush with the free surface of resin held in a vat. A single layer is cured sticking to the glass, for by imaging a line onto the resin for 25s. This layer is allowed to remain in the vat for a variable duration of time, called 'waiting time', (*t* seconds) and then, the same line is again imaged onto the resin surface for 25s. The cure depth of the line cured after this two exposure dose was measured. The micro scope images of the test layers are presented in Appendix E. In all three replicate experiments were conducted for each duration of 'waiting time'. The final thicknesses of the lines cured after the two exposure doses are tabulated against the waiting time in Table 6.3.

Table 6.3 Thicknesses of lines cured with two discrete exposure doses

Waiting time between exposures (s)	Thickness of the line cured after two exposure doses (μm)			
	Experiment 1	Experiment 2	Experiment 3	Average
4	467.7	483.9	-	475.8
30	375	388.9	368.1	377.3
60	333.3	347.2	340.3	340.3
120	312.5	305.6	305.6	307.9
180	298.6	291.7	263.9	284.7

The value of t' which gave the best agreement with the depths of the cured line was obtained experimentally. The plots are shown in Figure 6.7.

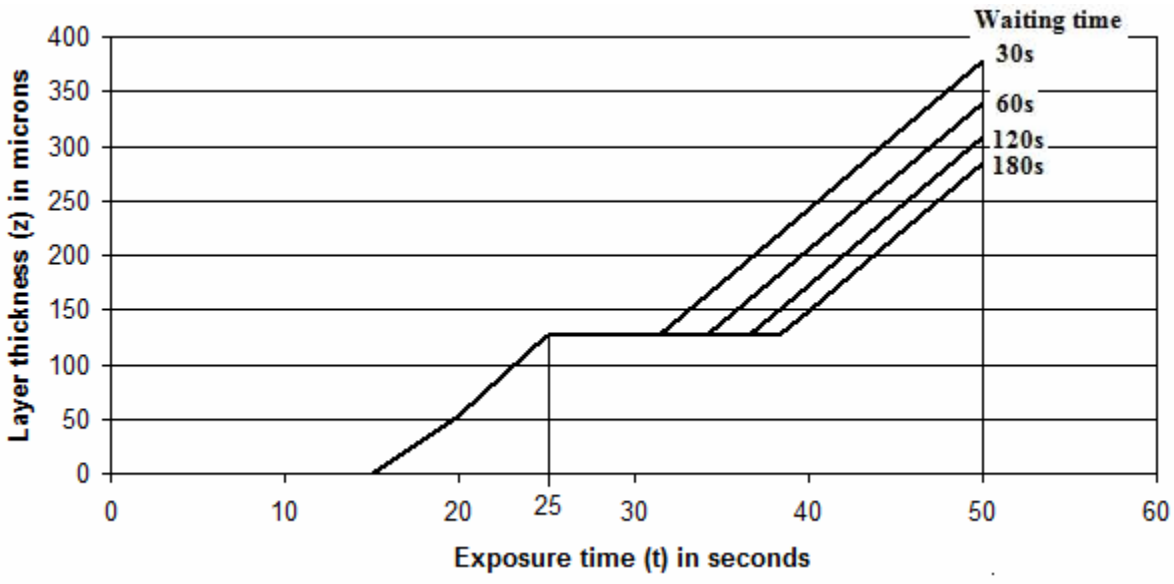

Figure 6.7 Experimentally determining the value of t' for various waiting times

It was experimentally found that the effect of diffusion of radicals and oxygen on the cure depth was negligible till the value of waiting time t was up to 4s. The waiting time was then increased in steps of half a minute till three minutes. The values of the diffusion factor 'k' were computed from the values of $t^{'}$ using equation 6.9. The values of t', and hence, those of k are tabulated against the waiting times (t), i.e. the times that the layers were allowed to sit in resin before receiving the second dose of exposure, in Table 6.4. A logarithmic curve is fitted to the data, as shown in Figure 6.8. The relationship between the diffusion factor and the waiting time is given by equation 6.10

Table 6.4 Effect of waiting time on the diffusion factor

Waiting time (t) in seconds	Time required to compensate for diffusion of reactive species (t') in seconds	Diffusion factor (k)
4	0	0
30	6.4	0.439
60	9.2	0.631
120	11.7	0.803
180	13.4	0.920

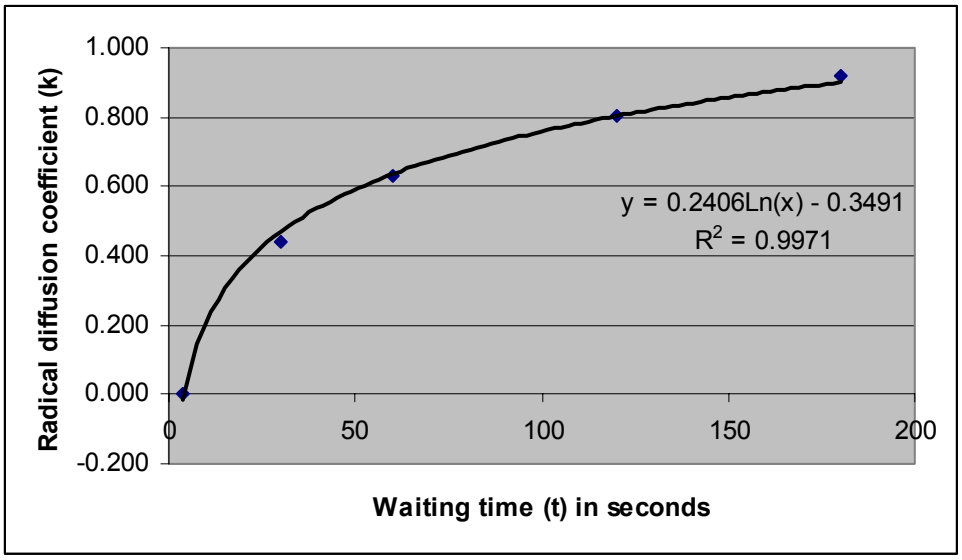

Figure 6.8 Plot of the radical diffusion factor against the waiting time

$$k = 0.2406\ln(t) - 0.3491 \tag{6.10}$$

The general form of equation relating the diffusion factor and time allowed for diffusion is

$$k = B\ln(t) - C \tag{6.11}$$

where B and C are constants that will depend upon the resin, the temperature of resin and even the size of the vat.

Thus, the energy at a cure front, i.e. at solid-liquid interface sitting in a resin vat for t seconds will be given by

$$\begin{aligned} E_t &= (1-k)E_c \\ E_t &= [1 + C - B\ln(t)] \cdot E_c \end{aligned} \tag{6.12}$$

6.3 Modeling print through

Based on the transient layer cure model and the diffusion model developed in Sections 6.1 and 6.2, it is possible to model the print-through that would occur when a

multi-layer part is cured. Suppose that an n layered part, as shown in Figure 6.9 is built. Irradiance H is incident on the layers. Let the thickness of the k^{th} layer be given by LT_k. and the exposure supplied to cure it be given by E_k. Suppose the time allowed for the resin to settle before exposing the k^{th} layer is t_k seconds.

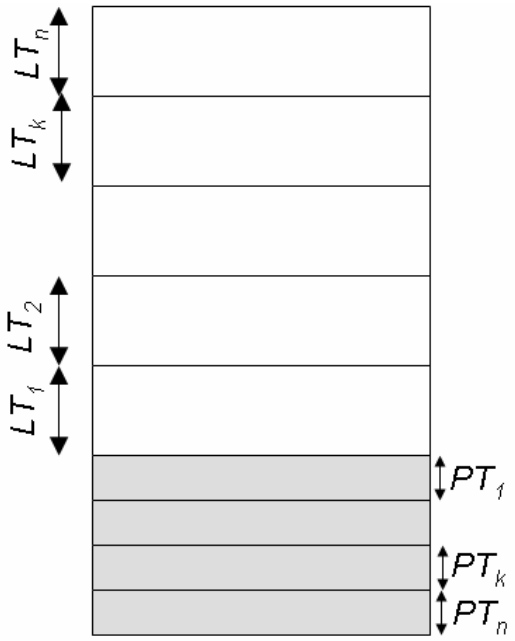

Figure 6.9 Modeling the print through occurring in a "n" layered part

We now model PT_k: the print through that would occur because of radiation penetrating from the k^{th} layer. From equation 6.5, it can be seen that an exposure equal to $(LT_k / D_{pM}) + E_c$ is sufficient to cure the layer to the cure depth LT_k. The exposure in excess of this value will penetrate down, un-attenuated, through all the cured layers underneath the k^{th} layer, and will cause print-through. Let us denote this exposure as E_{PTk}. It is given by equation 6.13.

$$E_{PTk} = E_k - (LT_k / D_{pM}) - E_c \tag{6.13}$$

This energy will add to the energy already existing at the bottom surface. The energy at the bottom surface, after the $(k\text{-}1)^{th}$ layer is cured, will be equal to the threshold

exposure of polymerization E_c. The diffusion of radicals would have occurred at the bottom surface for a time t_{dk}, given as the summation of the time that was allowed for the resin to settle before exposing the k^{th} layer, and the time that it took for the k^{th} layer to be cured.

$$t_{dk} = t_k + [(LT_k / D_{pM}) + E_c]/H \tag{6.14}$$

After the diffusion of reactive species and oxygen that would occur during the time t_{dk}, we can compute the effective exposure at the bottom surface of the part being cured by applying equation (6.12).

$$E_b = [1 + C - B\ln(t_{dk})]E_c \tag{6.15}$$

The print-through will be caused by exposure E_{bk} at the bottom surface, given as the addition of the exposures given by equations 6.13 and 6.15.

$$E_{bk} = E_k - (LT_k / D_{pM}) - E_c + [1 + C - B\ln(t_{dk})]E_c \tag{6.16}$$

Simplifying,

$$E_{bk} = E_k - (LT_k / D_{pM}) + [C - B\ln(t_{dk})]E_c \tag{6.17}$$

The print through caused by this exposure can be easily derived from equation 6.5 as

$$PT_k = D_{pM}(E_{bk} - E_c) \tag{6.18}$$

$$PT_k = D_{pM}\{E_k - (LT_k / D_{pM}) + [C - B\ln(t_{dk}) - 1]E_c\} \tag{6.19}$$

The total print through will be equal to

$$PT = \sum_{k=1}^{n} PT_k \tag{6.20}$$

The total height of the part cured will thereby be equal to

$$h = \sum_{k=1}^{n} LT_k + \sum_{k=1}^{n} PT_k \tag{6.21}$$

Simplifying equation 6.21 by plugging in the value of print through from equation 6.19, we get

$$h = \sum_{k=1}^{n} LT_k + \sum_{k=1}^{n} [D_{pM} \{E_k - (LT_k / D_{pM}) + [C - B \ln(t_{dk}) - 1] E_c\}] \tag{6.22}$$

where

$E_k = H \cdot t_k$ (t_k being the time of imaging)

$t_{dk} = t_k + [(LT_k / D_{pM}) + E_c]/H$

$D_{pM} = 1.9172 \text{mm}^3/\text{mW}$

$B = 0.2406$

$C = 0.3491$

$E_c = 10.2 \text{ mJ/cm}^2$

Effect of layer thickness on the height of the pixel column

Equation 6.22 can be further simplified as

$$h = \sum_{k=1}^{n} LT_k + \sum_{k=1}^{n} [D_{pM} \{E_k + [C - B \ln(t_{dk}) - 1] E_c\} - LT_k]$$

$$h = \sum_{k=1}^{n} LT_k + \sum_{k=1}^{n} D_{pM} \{E_k + [C - B \ln(t_{dk}) - 1] E_c\} - \sum_{l=1}^{n} LT_k$$

$$h = \sum_{k=1}^{n} D_{pM} \{E_k + [C - B \ln(t_{dk}) - 1] E_c\} \tag{6.23}$$

It would appear from equation 6.23 that there is no terms LT_k in the equation that gives the height of the pixel column and hence, might indicate that the height of a pixel column that will be cured is independent of the layer thicknesses. However, the reader must note that the variable t_{dk} in equation 6.23, which is the time allowed for diffusion of reactive species and oxygen molecules is dependent upon the layer thicknesses.

Also, the minimum limit on the exposure E_k incident on the k^{th} layer is dependent upon the thickness of the k^{th} layer, i.e. LT_k. Thus, the values of the layer thicknesses will influence equation 6.23 even though no LT_k terms appear in it. The layer thickness will decide the time allowed for diffusion (t_{dk}) before the k^{th} layer is imaged and the limit on exposure (E_k) supplied to cure the k^{th} layer.

6.4 Simulating down facing profile of a test part

In this section, the print through model developed in Section 6.3 is used to simulate a test part. This simulation is validated by building the part on the MPSLA system. The part shown in Figure 6.10 is chosen as the test part. The part consists of four layers, each 2500µmX600µm in lateral dimensions and 500µm thick. The bitmap to be displayed is generated by using the inverse layer cure model presented in Section 5.4. The irradiance distribution across the bitmap was obtained by inputting it to the irradiance model developed in Chapter 5. The bitmap and the irradiance distribution are shown in Figure 6.11.

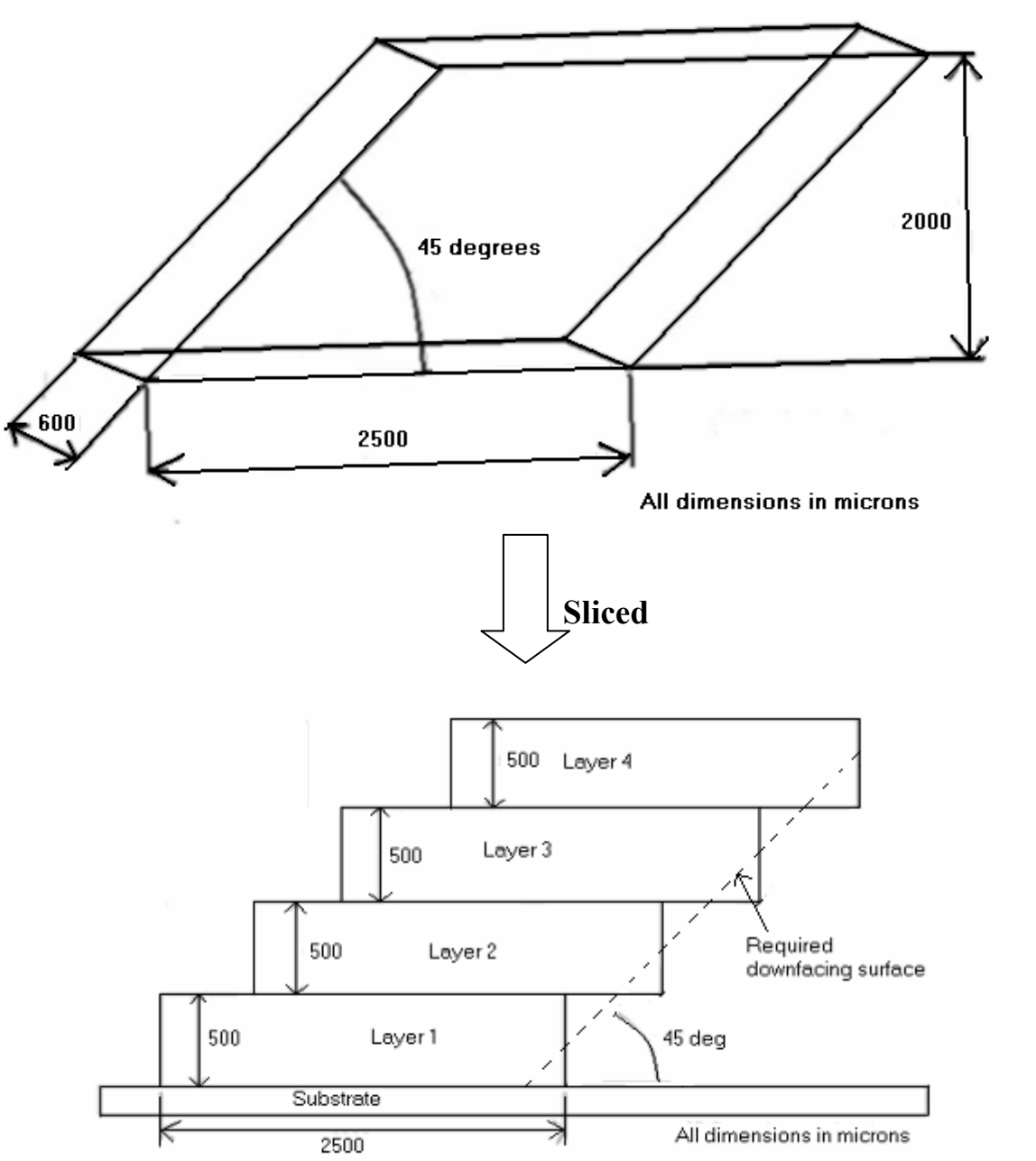

Figure 6.10 Test part to simulate the down facing profile of a MPSLA build

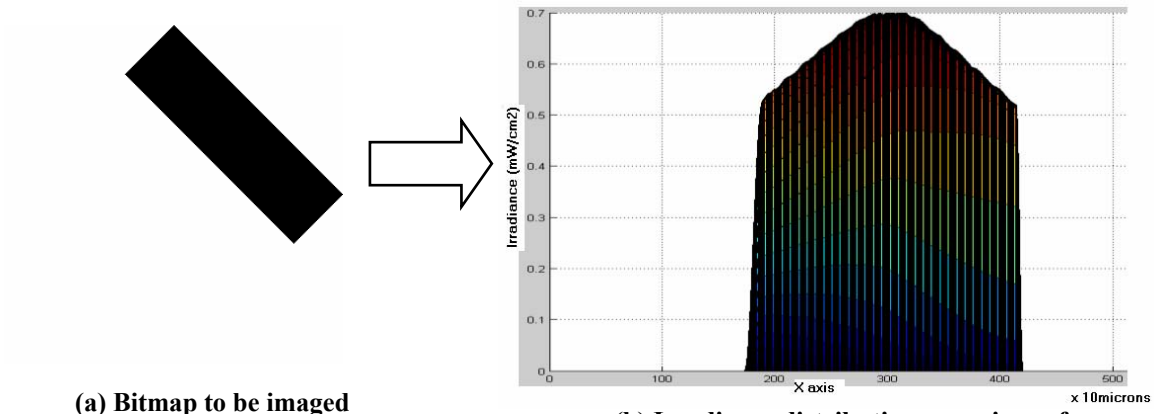

(a) Bitmap to be imaged

(b) Irradiance distribution on resin surface

Figure 6.11 (a) Bitmap to be displayed to cure the required layer; (b) Irradiance distribution on resin surface upon imaging the bitmap

The irradiance (H) at the center of every pixel on the resin surface was obtained from the irradiance distribution as shown in Figure 6.11. The minimum irradiance across the irradiance profile is at its left-most edge, equal to 0.47mW/cm^2. In order to ensure that the layer at this location cures down and binds to the layer underneath it, the time of exposure for the layers is calculated to be 80s, by using equation 6.5. Every layer is alike and was built by imaging the same bitmap on the resin surface for the same time of exposure (80s). The layers were built offset by 500µm by translating the platform laterally under the imaging system. The time allowed for the resin to settle before exposing any layer was 60s, i.e. t_k = 60s. The value of print through at every lateral location on the built part was computed using equation 6.20 and the down facing surface was simulated as shown in Figure 6.12. The Matlab code written to generate the simulated profile is documented in Appendix F.

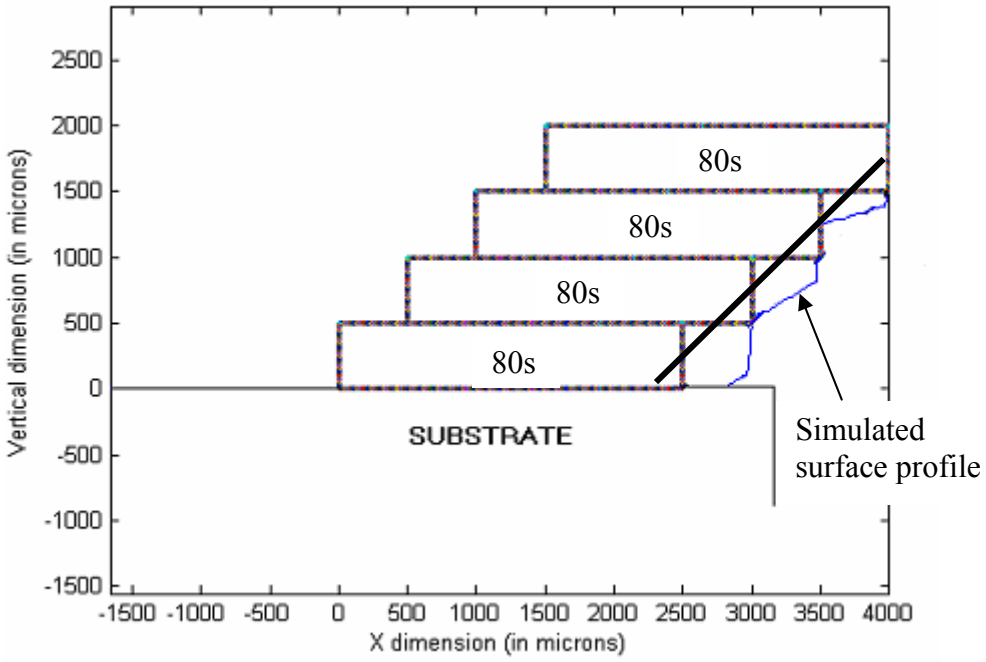

Figure 6.12 Simulating profile of the down facing surface for every layer exposed for 80s

The four layered part was built on the MPSLA system using the same parameters as those used in the simulation. The part's profile, as shown in Figure 6.13, can be seen to be qualitatively agreeing with the simulated profile. In Figures 6.12 and 6.13, rectangles are shown corresponding to the layers that would have been cured had there been no print through and no irradiance variation across a cured layer. The ideal down facing surface is shown by the line at 45^0 as shown in Figures 6.12 and 6.13. It is seen in both the figures that there is extra curing than required.

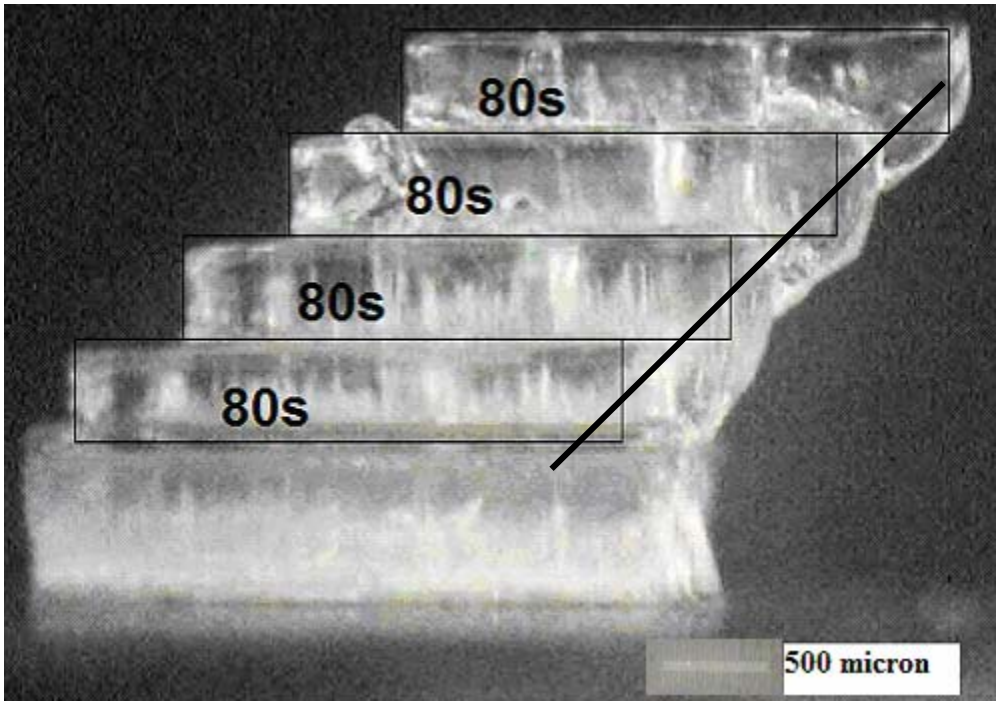

Figure 6.13 Profile of experimentally cured part with every layer exposed for 80s

Explaining the disparity between experimental and analytical results

It can be seen from Figures 6.12 to 6.13 that the cured surface is smoother than the simulated surface. The author surmises that it is because of partially cured photopolymer lodged in between the nooks of the down facing surface. The simulation is based on the threshold model of resin cure and ignores any partial curing that might occur. The threshold model makes the assumption that there is a sharp transition between liquid and solid resin at the threshold exposure of polymerization. In reality, the phase change occurs over a range of exposure centered about the threshold exposure of polymerization. As a result, exposures approaching but not yet E_c, result in the formation of viscous, partially polymerized gels. The author surmises that this gel gets lodged in between the stair-steps on the down-facing surface, as shown in the simulations and ends up creating a fillet, thereby smoothing the surface.

In order to shed some light on the causes of the disparity between simulated and experimentally cured profile, two more part profiles were cured and simulated. The simulated and cured profiles of the parts are presented along with the times of exposure of every layer in Figure 6.14. The times of exposure for the part shown in Figure 6.14(a) is exactly equal to the time of exposure supplied to cure the part shown in Figure 6.13. The times of exposures of the part shown in Figure 6.14 are also similar to the times of exposures supplied to cured part in Figure 6.13, except that the overhanging portions of the top three layers are exposed for 70s.

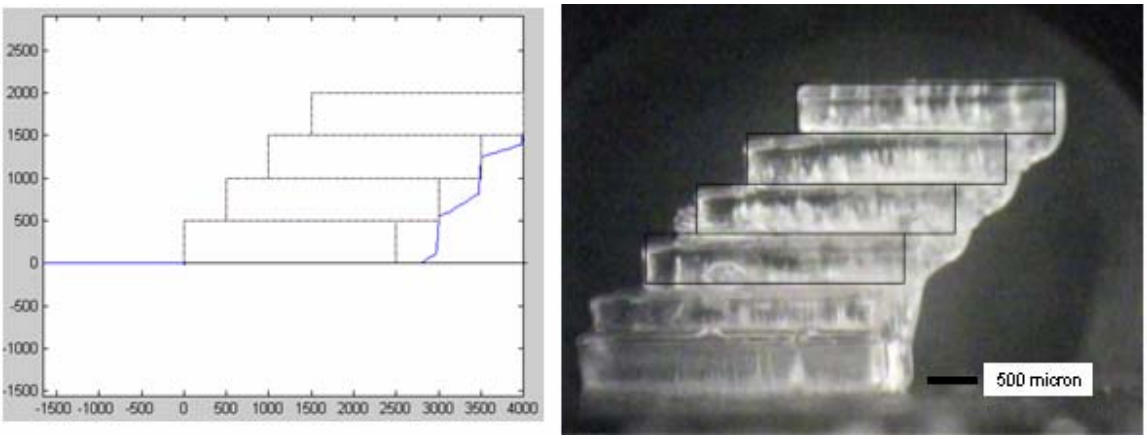

(a)

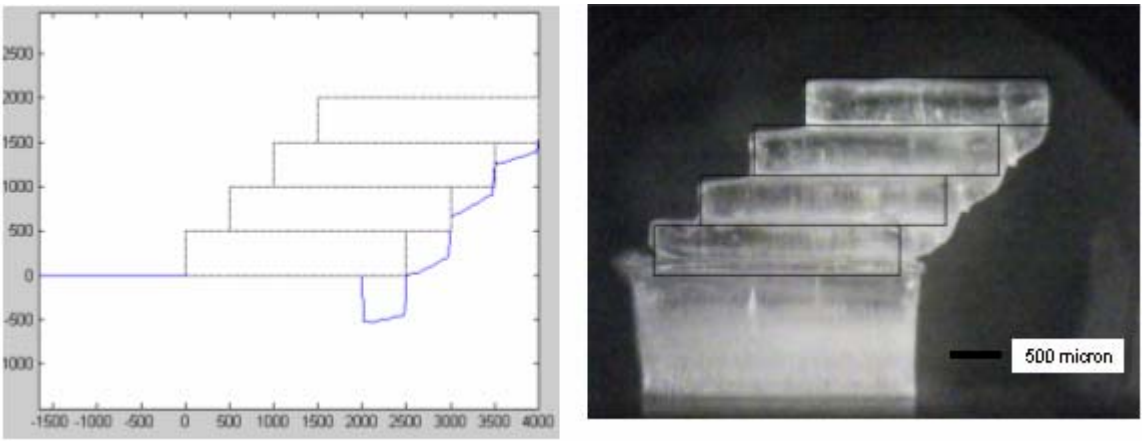

(b)

Figure 6.14 Part cured in order to compare cured profile with simulated profile of down facing surface

The profiles of the parts cured in Figures 6.13 and 6.14 are superimposed on the simulated profile for comparison. The superimposed profiles are shown in Figure 6.15.

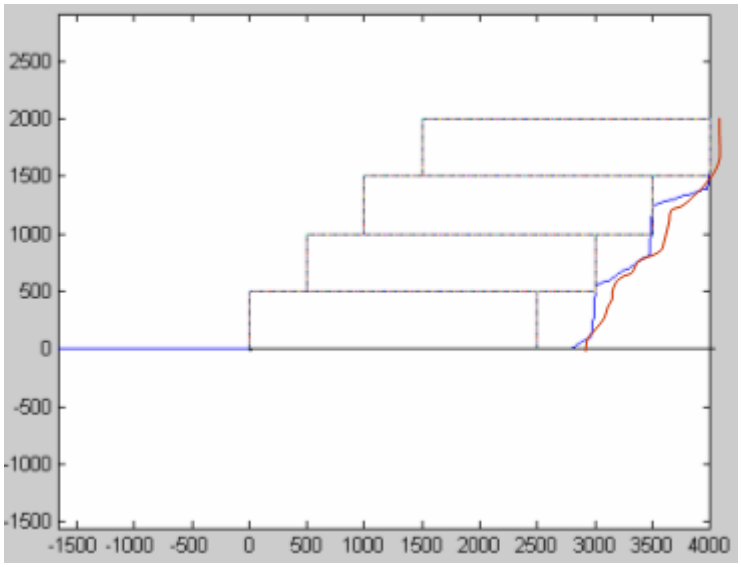

(a) Profile of part in Figure 6.13

Figure 6.15 Comparison of the profiles of cured and simulated down facing surfaces

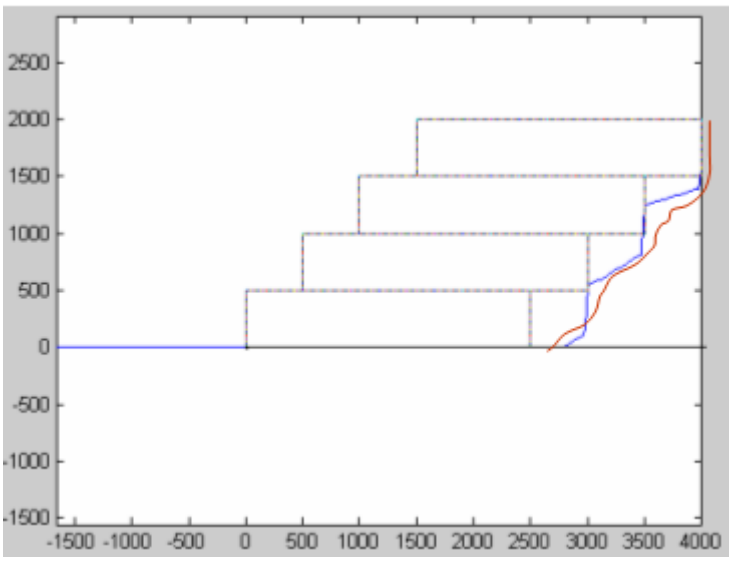

(b) Profile of part in Figure 6.14 (a)

Figure 6.15 (continued)

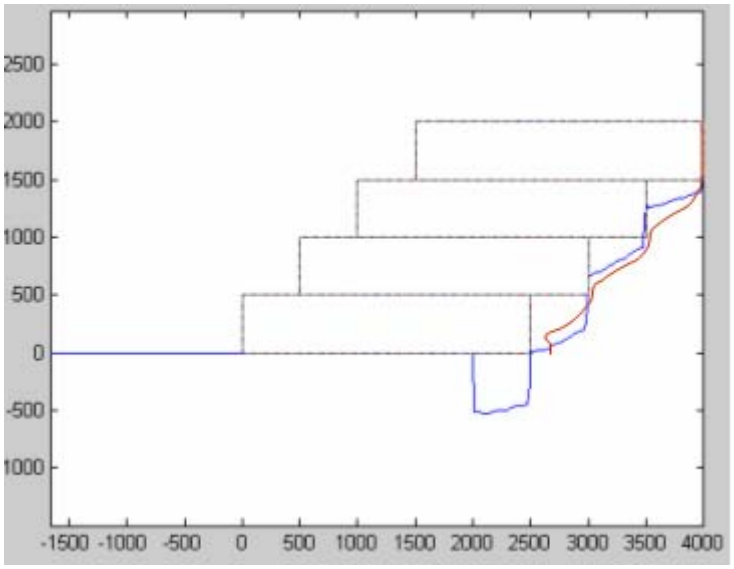

(c) Profile of part in Figure 6.14(b)
Figure 6.15 (continued)

In Figure 6.15, the cured profile is shown in red, while the simulated profile is shown in blue. It can be seen in Figure 6.15 that the red line is to the right of the blue line, indicating extra curing than expected for most part. Only at the very bottom of the part does the red line appear to the left of the blue line indicating less amount of curing. The error in the part cured is the difference between the cured and the simulated dimension. If the red line is to the right of the blue line, it means that there is a positive error. If the blue line is to the right of the red line, it would indicate a negative error. The error is plotted against the vertical dimension of the part (2000μm), measured from top to bottom, in Figure 6.16. Figure 6.16 also documents the maximum, minimum and the root mean square (RMS) value of the errors.

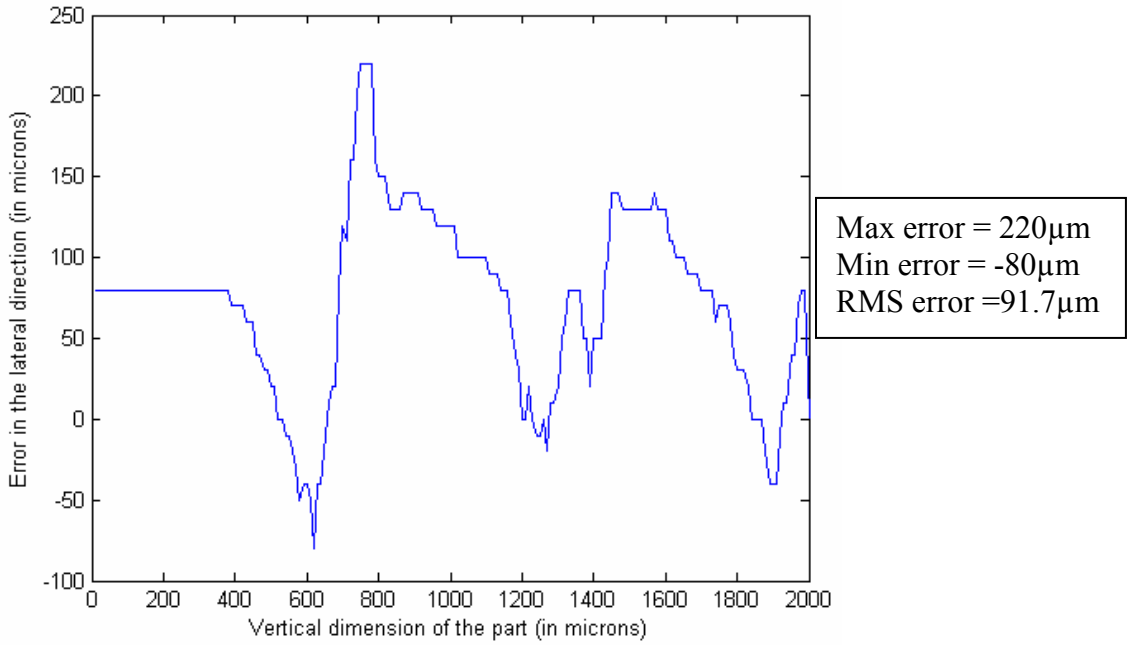

(a) Error plot for part presented in Figure 6.13

Figure 6.16 Plot of error in lateral direction of cured parts plotted against the vertical dimension of the part

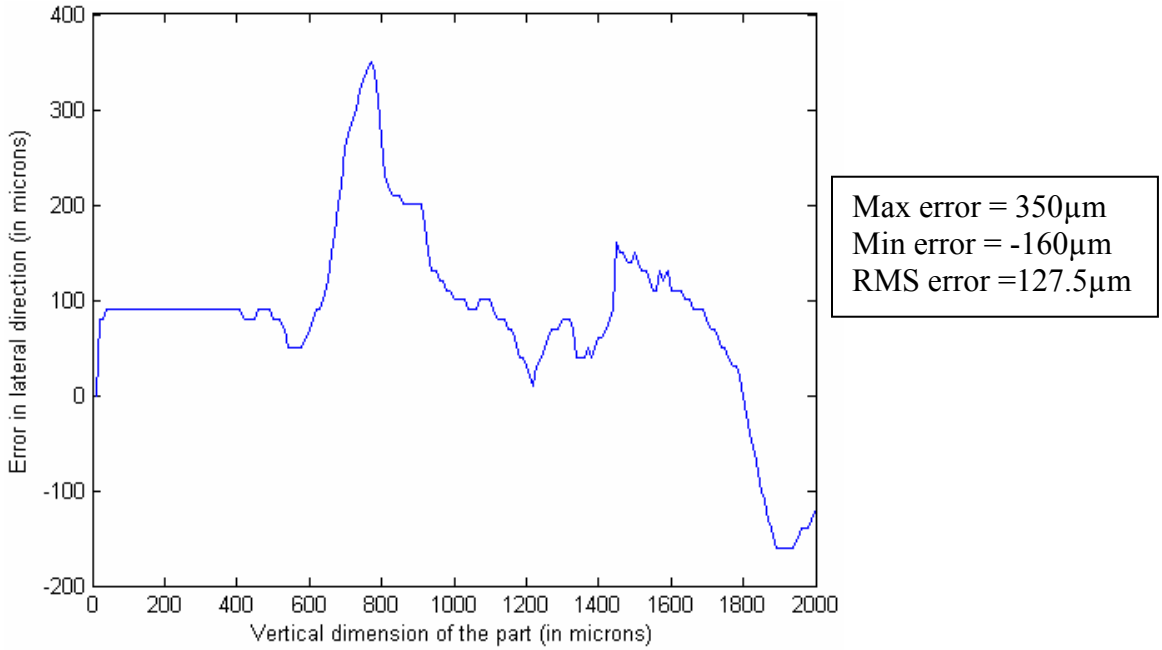

(b) Error plot for part presented in Figure 6.14(a)

Figure 6.16 (continued)

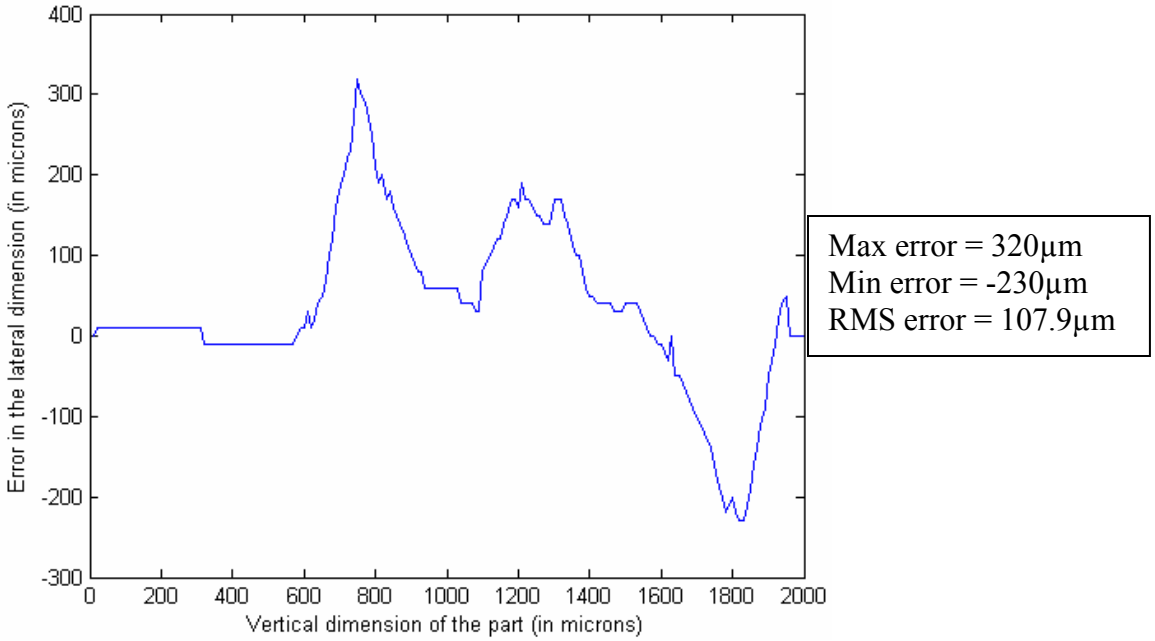

(c) Error plot for part presented in Figure 6.14(b)

Figure 6.16 (continued)

A general trend can be observed from the error plots presented in Figure 6.16. All plots have a positive peak at around 800µm from the top of the part. This corresponds to the portion where the stair step corresponding to the third and fourth layer. The second larges peak appears at around 1400µm from the top, which corresponds to the stair step formed by the second and third layer. These observations indicate that a greater amount of positive error is observed where there are nooks in the simulated profile. Perhaps it is because the partially cured resin occupies these nooks.

A valley is observed in all these profiles towards the bottom of the part, at around 1850µm from the top. The appearance of the peaks and valleys in all the error plots indicate the presence of some systematic error in the model. There are two peaks in all three error plots and the second peak is smaller than the first one. Also, there is a valley, indicating that there is less than expected curing, beyond the second peak. This indicates

that the print through model formulated in this research is consistently over-computing print through as we go towards the bottom of the part. The author speculates that this is because the rate of radiation attenuation through a cured layer is not exactly zero, as assumed in the print through model. Some amount of finite loss of energy occurs as the radiation travels through the cured layers. This error gets compounded towards the bottom regions of the part which receive radiation penetrating to it through larger cured depths.

The maximum error along the part profiles can be seen to be varying from 220µm to 350µm. The minimum error varies from -230µm to -80µm. Thus, the presence of some random errors can also be seen. From the error plots, the following conclusions can be drawn:

1. There is some extra curing expected at the location where the simulated profile predicts a nook.
2. The amount of extra curing is expected to be a couple of hundreds of µm
3. Some negative error is expected towards the bottom of the part. It is expected to be a couple of hundreds of µm too.

6.5 Compensation zone approach: Inverse print-through model

Now that the simulation of print through and hence the down-facing surface is validated, it is possible to solve equation (6.22) in order to determine the values of layer thicknesses and times of exposures to build a dimensionally accurate part. In this section the compensation zone approach is formulated and demonstrated on a test part.

6.5.1 Formulation of compensation zone approach

At every lateral location on a MPSLA part to be built, the compensation zone approach is would tailor the time of exposure at the lowermost layer in order to compensate for print through. At every pixel, equation 6.22 is solved. In addition, for all layers above the bottom-most layer, at the given pixel location, the time of exposure (t) should be such that the curing depth should be at least equal to the layer thickness plus the overcure. This condition is captured in equation 6.24.

$$t_k \geq \frac{(LT_k + OC)/D_{pM} + E_c}{H} \tag{6.24}$$

The value of constants in equation 6.22 for the MPSLA system at RPMI being:

D_{pM} = 1.9172mm^3/mW
OC = 40µm
E_c = 10.2 mJ/cm^2
The compensation zone approach can thus be expressed as shown in Figure 6.17.

At every pixel column at pixel (a,b),

Given

- Height of the column (h)
- Irradiance at the pixel (H)
- Number of layers (n)
- Thicknesses of the layers (LT_k)
- Overcure (OC)
- Time allowed for settling resin before exposure k^{th} layer (T_k)

Find

- Time of exposure of pixel at every layer (t_k)

Satisfy

- For k = 2 to n, $t_k \geq \frac{(LT_k + OC)/D_{pM} + E_c}{H}$
- $h = \sum_{k=1}^{n} LT_k + \sum_{k=1}^{n} [D_{pM}\{E_k - (LT_k / D_{pM}) + [C - B\ln(t_{dk}) - 1]E_c\}]$

Figure 6.17 Problem formulation for the compensation zone approach

6.5.2 Demonstration of compensation zone approach

Suppose we want to compute the exact profile of the part as shown in Figure 6.10. The down-facing surface is to be linear, as opposed to an approximation to linear surface. This can be achieved by applying the compensation zone approach at every pixel location of the part.

The part consists of four rectangular layers of dimensions 2500μmX600μm and 500μm thick. The same bitmap is used to cure every layer. The layers are offset from each other by 500μm along their lengths by translating the build underneath the imaging system. The bitmap to be displayed on the DMD is generated by applying the inverse irradiance model, presented in Section 5.4. The bitmap generated and the irradiance distribution on the resin surface upon imaging this bitmap onto the resin surface is shown in Figure 6.11.

Thus, all the inputs to the Compensation zone problem formulation, as presented in Figure 6.17 are available as follows:

- Height of the pixel column (h): Obtained from the geometry of the part
- Irradiance at every pixel (H) : Generated using the irradiance model
- Number of layers (n) = 4
- Thickness of every layer (LT_k) = 500μm
- Overcure (OC) = 40μm
- Settling time before imaging every layer (T_k) = 60s

The unknowns in the problem formulation are the times of imaging of every micro mirror. For simplification, the time of exposure of the "bodies" of all the layers, as shown

in Figure 6.10, i.e. the portion of every layer that binds to the layer underneath it is assumed to be 80s.

At every pixel location, with the values of t_k for all layers but the bottom most layer computed as 80s, the value of the time of exposure for the micro mirror at the bottom-most layer (t_1) at that pixel location can be determined by solving equation 6.22, re-written here.

$$h = \sum_{k=1}^{n} LT_k + \sum_{k=1}^{n} [D_{pM}\{E_k - (LT_k / D_{pM}) + [C - B\ln(t_{dk}) - 1]E_c\}] \tag{6.22}$$

The Matlab code implementing the Compensation zone approach at every micro mirror location is presented in Appendix G. The time of exposure for every layer is plotted against the X dimension of that layer as shown in Figure 6.18.

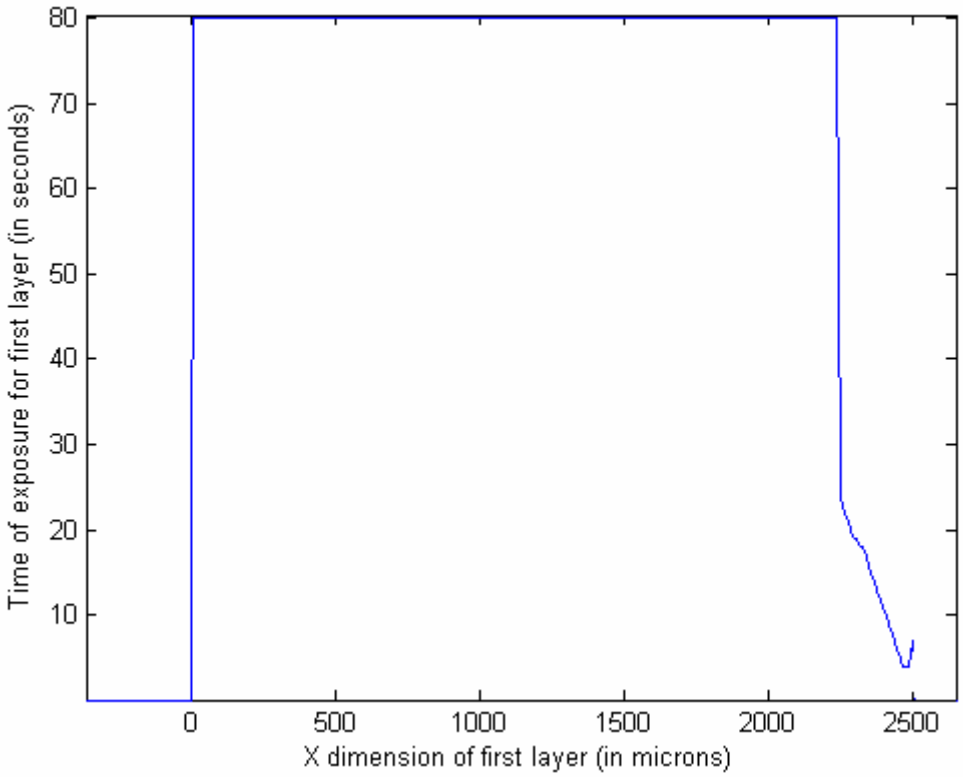

(a) Time of exposure across first layer

Figure 6.18 Times of exposure of the (a) first; (b) second; (c) third; and (d) fourth layer

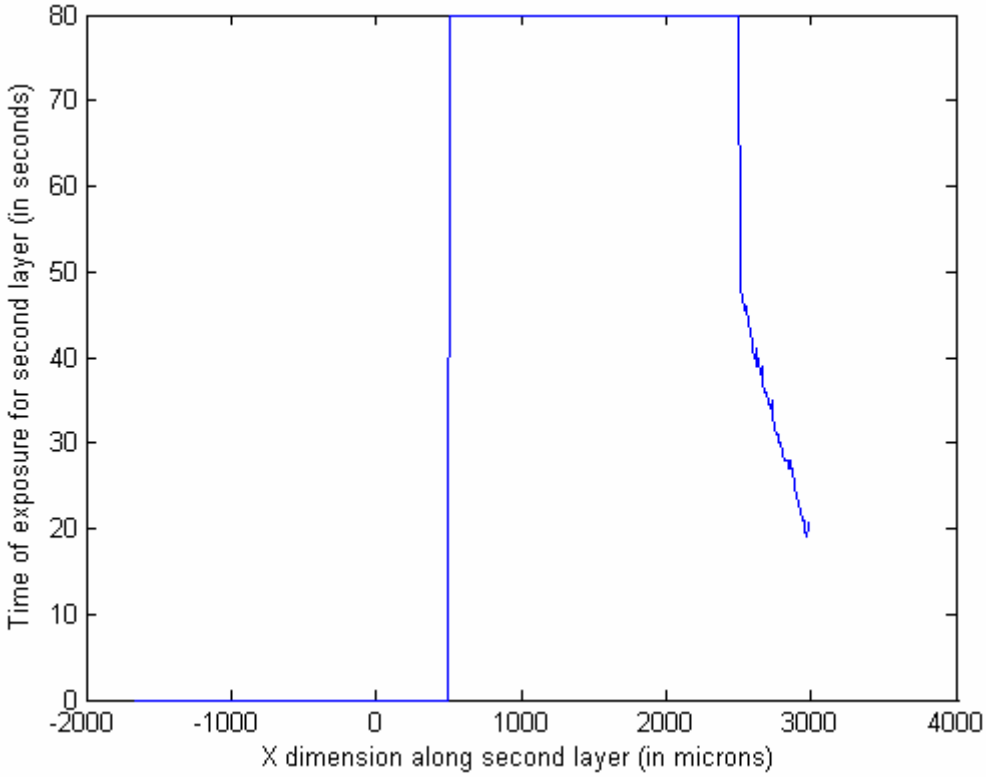

(b) Time of exposure across second layer

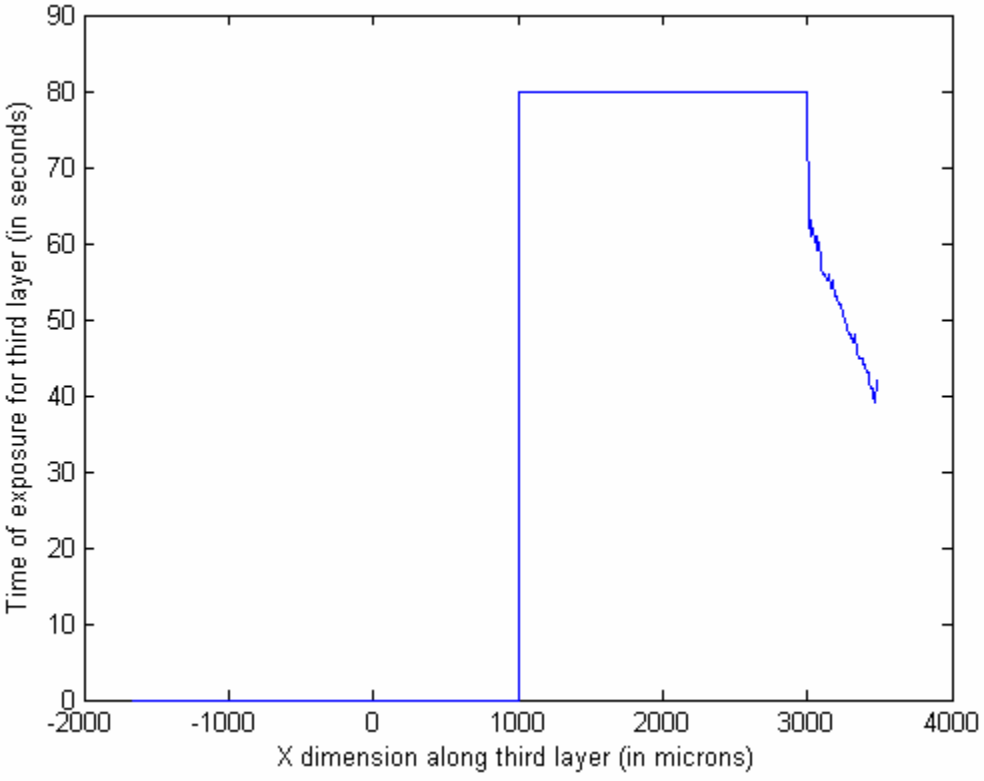

(c) Time of exposure across third layer

Figure 6.18 (continued)

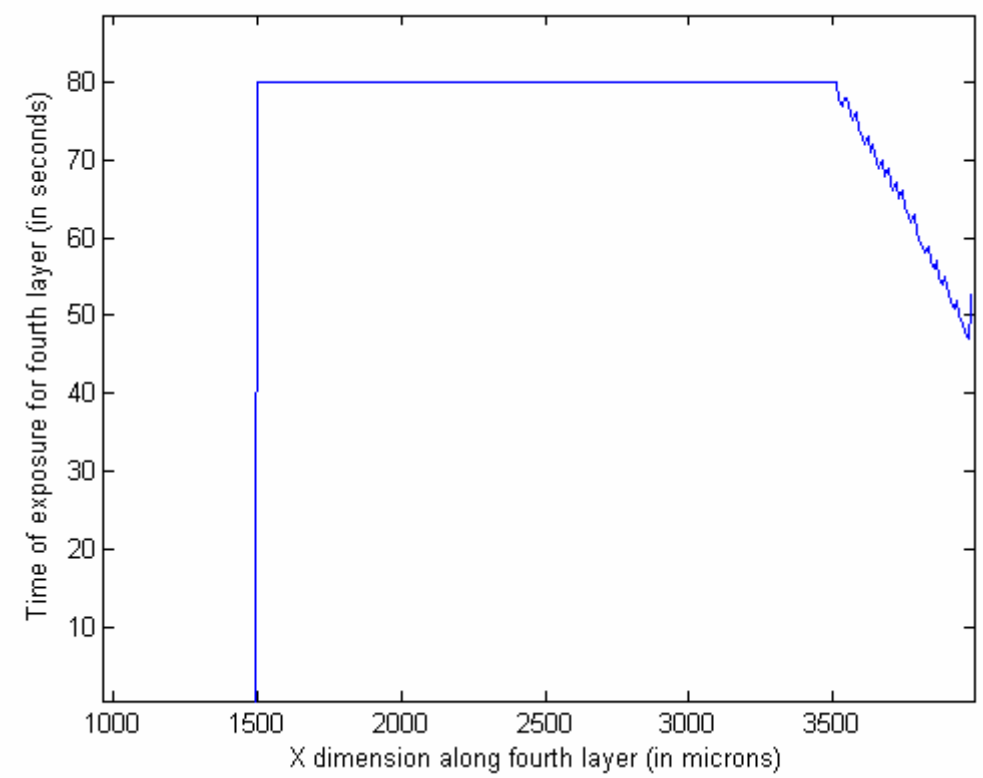

(d) Time of exposure of the fourth layer

Figure 6.18 (continued)

From Figure 6.18, we can see that the time for which the overhanging portion of every layer needs to be exposed varies along its length. The simulated profile of the down facing surface that would be cured for these values of times is shown in Figure 6.19, as exactly linear.

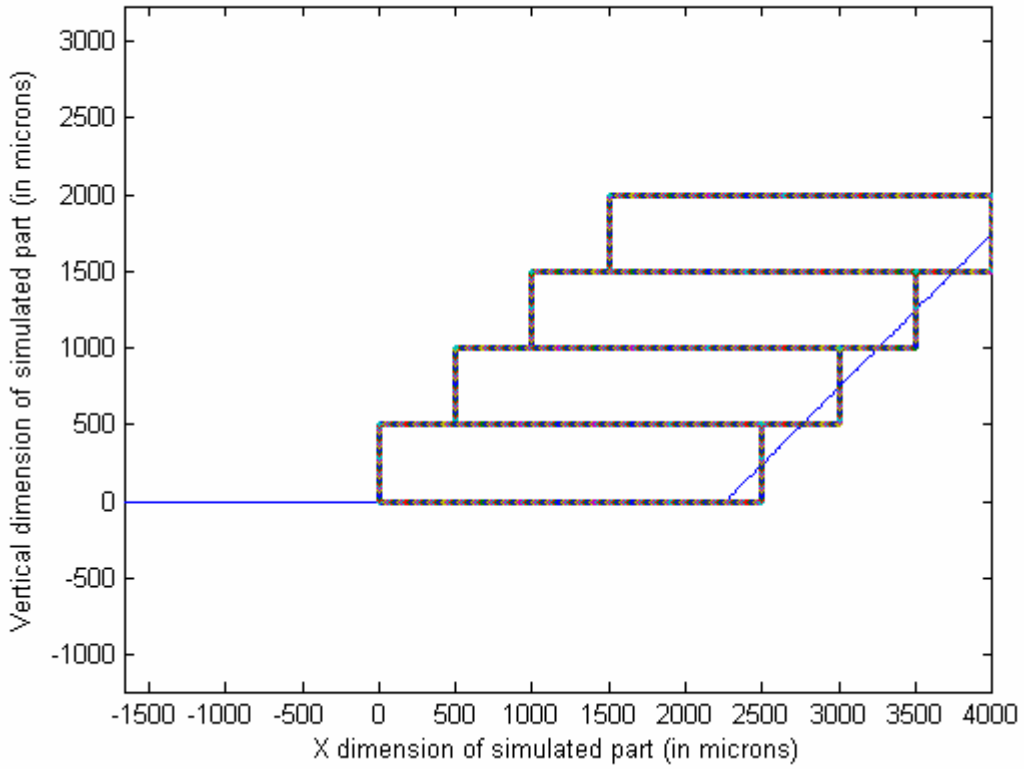

Figure 6.19 Simulated profile of the down facing surface for the times of exposure as given in Figure 6.18

In order to supply the times of exposure as given in Figure 6.18, it would be necessary to display and image every micro-mirror on the bitmap irradiating the overhanging portion of the layer separately for a given duration of time. Since this is not possible to do manually, the author computed the average time of exposure across the overhanging portion of the bitmap. This has been illustrated in Figure 6.20.

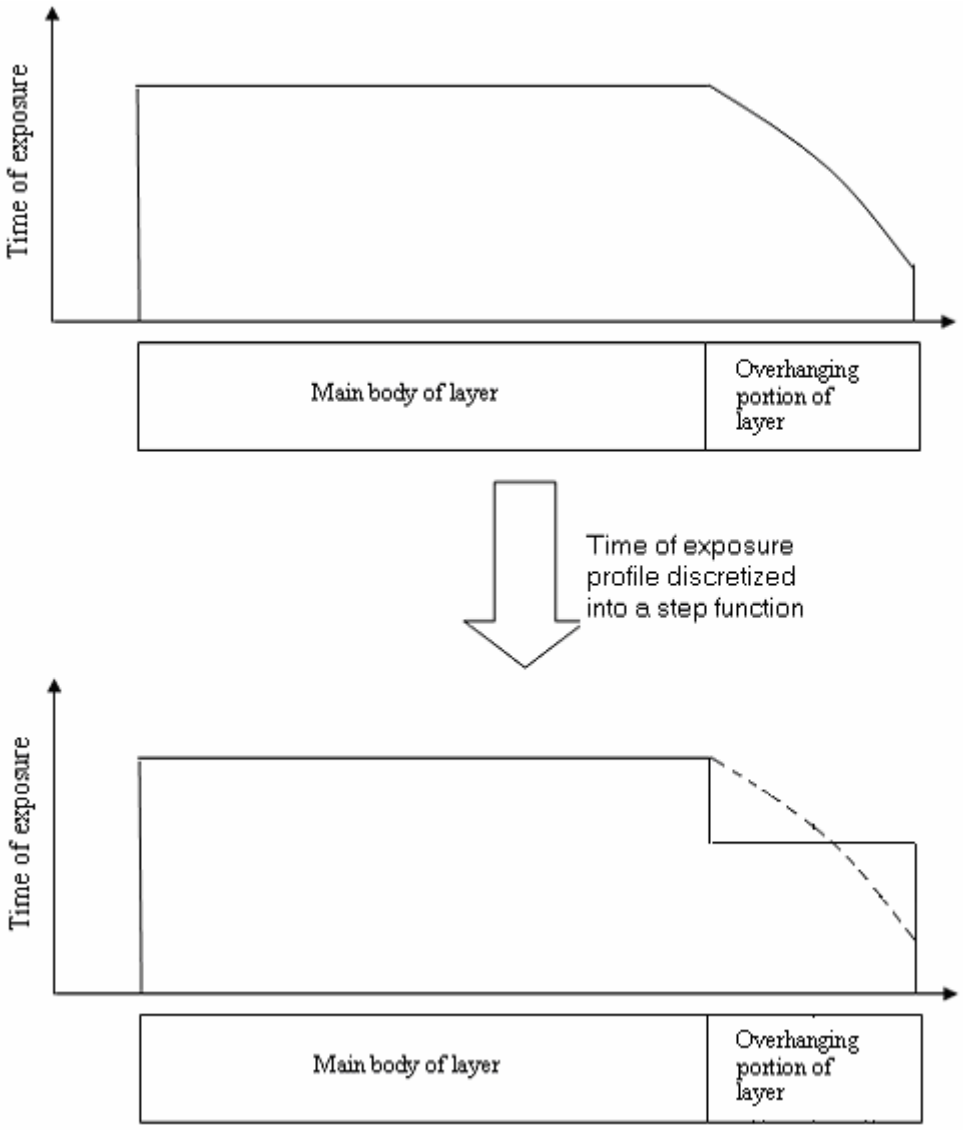

Figure 6.20 Time of exposure discretized into a step function

Likewise, the times of exposure as presented in Figure 6.18 are discretized for every layer into step functions. These step functions are presented in Figure 6.21. The times of exposure for every layer is shown in Table 6.4.

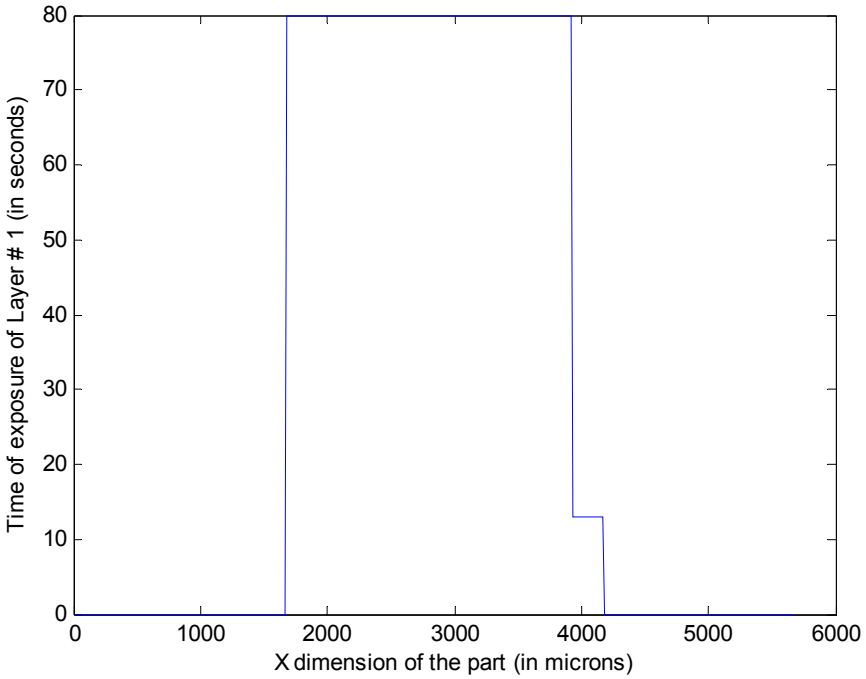

(a) Time of exposure for first layer approximated by a step function

Figure 6.21 Times of exposure for the (a) first; (b) second; (c) third; and (d) fourth layer approximated by a step function

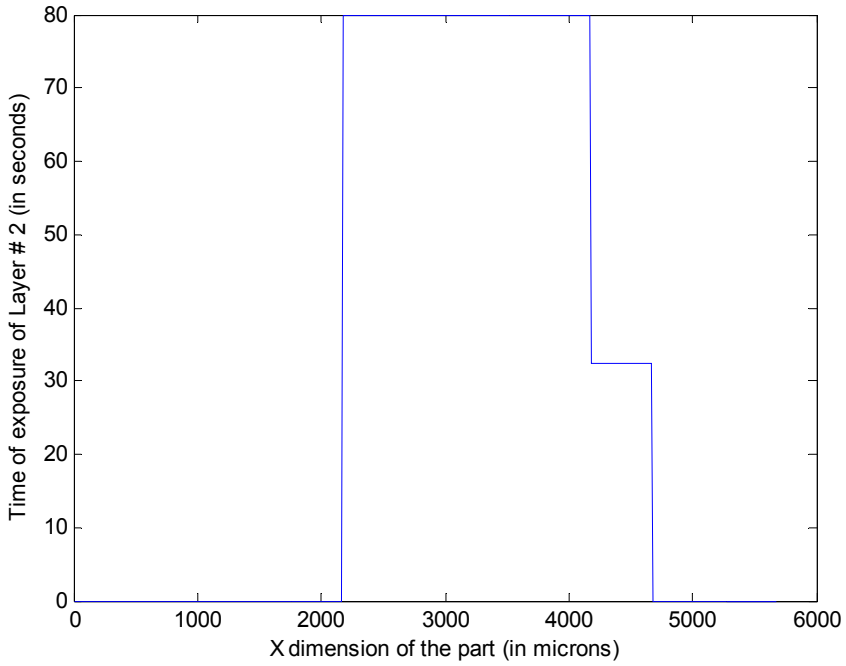

(b) Time of exposure for second layer approximated by a step function

Figure 6.21 (continued)

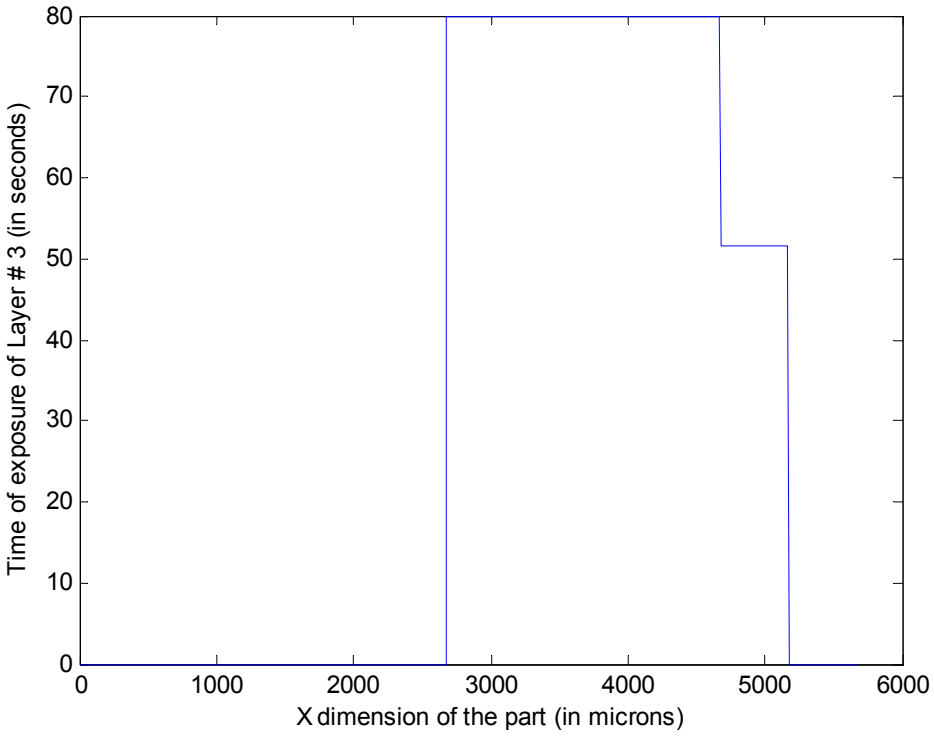

(c) Time of exposure for second layer approximated by a step function

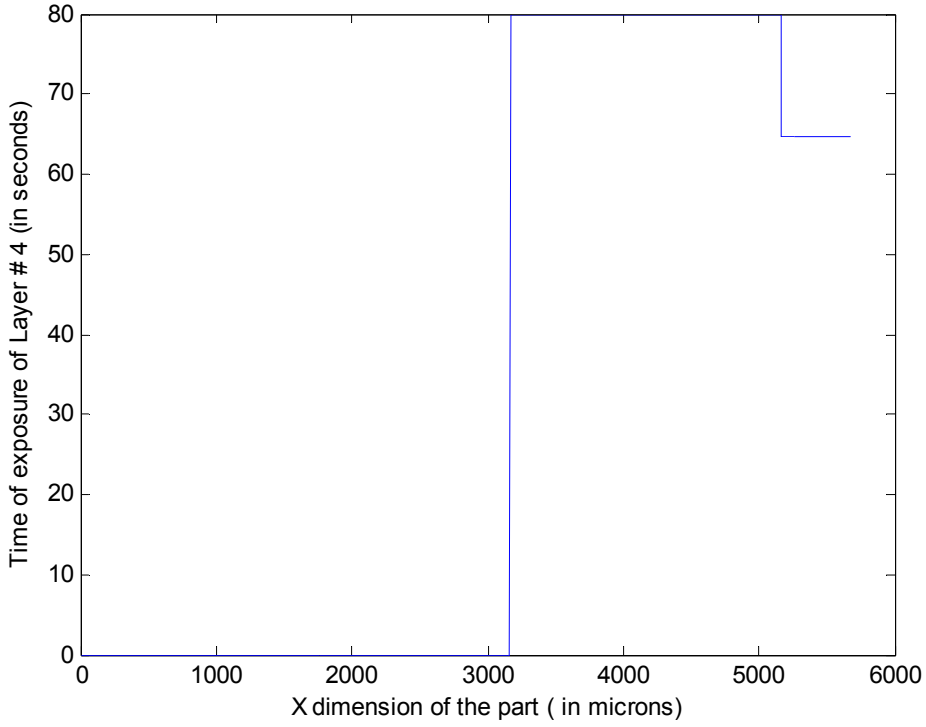

(d) Time of exposure for second layer approximated by a step function

Figure 6.21 (continued)

Table 6.5 Times of exposure of the layers to implement compensation zone approach

Layer # (Bottom most to top most)	Time of exposure (s)	
	Body of layer	Overhang of layer
Layer 1	80	12.9
Layer 2	80	32.5
Layer 3	80	51.6
Layer 4	80	64.6

It should be remembered that the body of every layer (i.e. the part that bonds to the layer underneath it), is exposed for 80s.

These times of exposures were run through the simulation code to obtain the profile as shown in Figure 6.22. The simulation code with the bitmap discretized into two portions is presented in Appendix G.

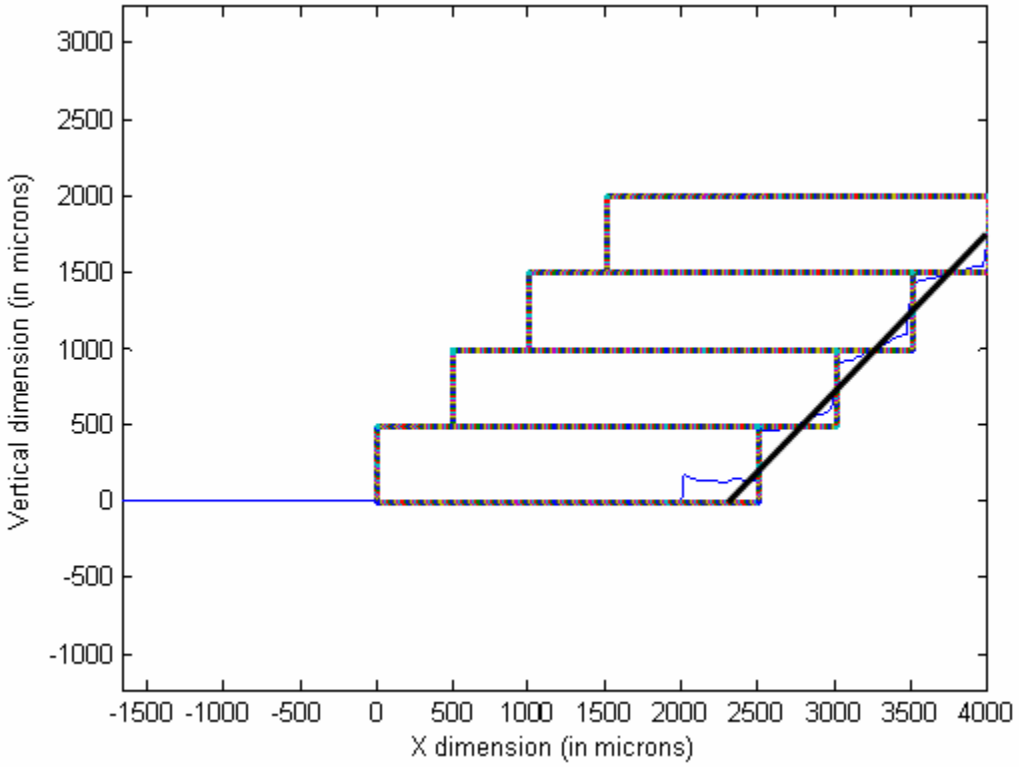

Figure 6.22 Simulated profile of the down facing surface cured by implementing the Compensation zone approach

The part was built on the MPSLA system using the times of exposure as given in Table 6.4 to build the part as shown in Figure 6.23.

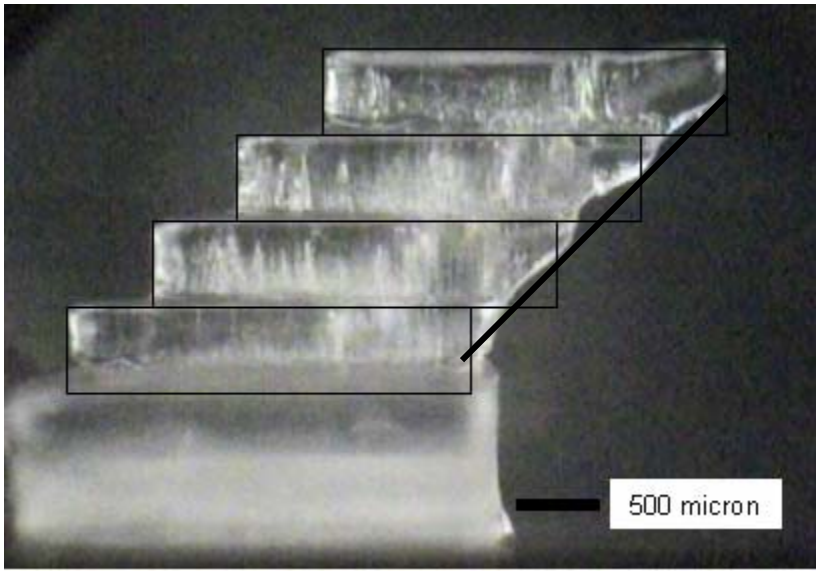

Figure 6.23 Part built on MPSLA system by applying compensation zone approach

It can be seen that the part cured in Figure 6.23 approximates the desired linear down facing surface much better. This validates and demonstrates the compensation zone approach.

Summary

In this chapter, two new theories have been presented and validated: the transient nature of curing of layer and the non-additive nature of exposure. In Section 6.1, the transient layer cure model has been formulated which models layer curing as a transient phenomenon. In Section 6.2, the loss of energy from the bottom surface of a part being built due to diffusion of reactive species and oxygen molecules is quantified. The additive nature of exposure is thereby shown to be a function of time. These theories have been used to compute the print through that occurs when a multi-layered part is cured. The

compensation zone approach is presented as a method to avoid the print though errors and build parts with accurate down-facing surfaces.

Progress made towards answering the research questions

Research question 2(a) dealt with the transient nature of layer curing. Conventional SLA theory assumes the rate of radiation attenuation with respect to distance to be constant during exposure. Layer curing is hypothesized in this chapter to be a transient curing process, in which the rate of attenuation of radiation with respect to distance, goes on varying during exposure. This hypothesis is tested by modeling the curing as a transient process, by discretizing the time domain. A differential equation relating the increment in cure depth with the increment in time is formulated and solved numerically. The resin constants are determined by curing test layers.

Research question 2(b) was concerning the additive nature of exposure. Conventional SLA theory assumes that exposure is additive, meaning that the effect of two discrete exposure doses on cure depth is the same that of a single, combined exposure dose. The author has hypothesized that the additive nature of exposure is a strong function of time. It has been shown in this chapter that when the layer remains in the resin in between the two exposures, there is a significant loss of energy from the bottom surface of the layer. This loss of energy is shown to vary as the logarithm of the time for which the layer sits in the resin. Thus, it has been shown that some diffusion based phenomenon is at work for reducing the energy available at the bottom surface of the layer. Thus, the additive nature of exposure is shown to be a function of time.

CHAPTER 7 SURFACE FINISH OF MASK PROJECTION STEREOLITHOGRAPHY BUILDS

Surface finish is rougher along the *z*-axis of RP parts than parallel to the *xy*-plane because of the "stair stepping" effect (Paul and Voorakarnam, 2001). In this chapter, methods to improving surface finish and to achieve a trade off between surface finish and build time of MPSLA builds is presented. The issues of improvement of surface finishes of up- and down facing surfaces have been handled separately in this chapter.

In case of down facing surfaces, print through results in filleting in the stair steps, thereby smoothing the down facing surface (Reeves and Cobb, 1999). This has also been observed by the author in this dissertation (Chapter 6). Research Question 3 was regarding employing print through smoothing to approximate the vertical profiles of MPSLA builds beyond the approximation possible by the stair steps created by layers, by modulating the exposure supplied at the edges of the layers. This method of modulating the exposure to better approximate down facing surface is referred to, in this dissertation, as the "adaptive exposure" method. In Section 7.1, and adaptive exposure method to improve surface finish of a down facing surface is explained in detail and is demonstrated on a test part.

The surface finish of up-facing surfaces of MPSLA parts is limited by the stair stepping phenomena. There is no print through to smoothen out the top facing surface. Meniscus smoothing, in which the resin meniscus lodged between the stair steps is cured, is proposed as a method to smoothen up facing surfaces (Cobb and Reeves, 1997), but this method is not repeatable and controllable. Thus, the only method to improve the surface finish of up facing surfaces is to use thinner layers to build the part. This

however increases the build time of the part. On the other hand, larger layer thicknesses result in shorter build times, but poorer surface finish. Adaptive slicing algorithms are in use since a long time to obtain Stereolithography builds to improve surface finish of Stereolithography parts, without a commensurate increase in build time. The algorithms have been presented in Hope et al., (1997), Tyberg and Bohn, (1998), Mani et al., (1999), Zhao and Laperriere, (2000), amongst other papers. These algorithms populate those features of a Stereolithography build, which subtend small angles with the vertical with thicker layers and the features subtending large angle with the vertical with thin layers. Alternatively, thin layers are used only where a very good approximation to the desired geometry is required. Thicker layers are used elsewhere in order to reduce the build time.

Adaptive slicing has been implemented by numerous authors using different mathematical techniques. In this dissertation, the author has used a gradient projection optimization method to implement the adaptive slicing. An adaptive slicing algorithm, employing a gradient projection method has been formulated and implemented on a test part in Section 7.2.

7.1 Surface finish of down facing surfaces

The adaptive exposure method to obtain MPSLA builds with smooth down facing surfaces is presented in this chapter. In Section 7.1.1, the concept of the adaptive exposure method is explained. In Section 7.1.2, it is demonstrated on a test part.

7.1.1 Adaptive exposure method

The surface finish of down facing surfaces can be improved by modulating the exposure at the edges of layers in such a way that the edge profiles of layers better

approximate the down facing profile of the part. To demonstrate the adaptive exposure method, we consider the same test part as used to demonstrate the compensation zone approach in Chapter 6. The reader can refer to the four layered part, with up-and down facing surfaces at 45^0 to the horizontal is shown in Figure 6.10. This part was sliced into layers 500μm thick. The time of exposure of these layers was computed using the compensation zone approach in Section 6.5.2. The times of exposure for every layer have been plotted against their X dimensions in Figure 6.18. In implementing the compensation zone approach, the author averaged the time of exposure along the overhanging portion of every layer. Thus, every layer was cured by exposing it in two steps. In the first step, the body of the layer (the part which binds to the layer underneath it) was exposed for certain duration of time so that the layers bind to each other. In the second step, the overhanging portion of the layer was exposed for a duration equal to that obtained by averaging out the time of exposure across it, presented in Figure 6.21. This method has been pictorially explained in Chapter 6, in Figure 6.20. The simulated profile of the part that will be cured by implementing the compensation zone has been presented in Figure 6.22 and the actually cured part has been presented in Figure 6.23. From both these figures, we can see than the approximation to the down facing profile is not exact. Also, the effect of stair steps is visible.

A better approximation can be obtained by modulating the exposure at the overhanging portion of every layer. This can be achieved by discretizing the overhanging portion of every layer into two regions. The time of exposure can be averaged out along these two regions separately. This is illustrated in Figure 7.1. Thus, every layer will be cured in three steps. In the first step, the body of the layer will be cured for a time

duration such that it binds to the layer underneath it. In the second step, the first discretized region will be exposed in such a way that it approximates the down facing profile of the part. In the third step, the second discretized region of the overhanging portion of layer will be imaged for a time so that it approximates the down facing profile too.

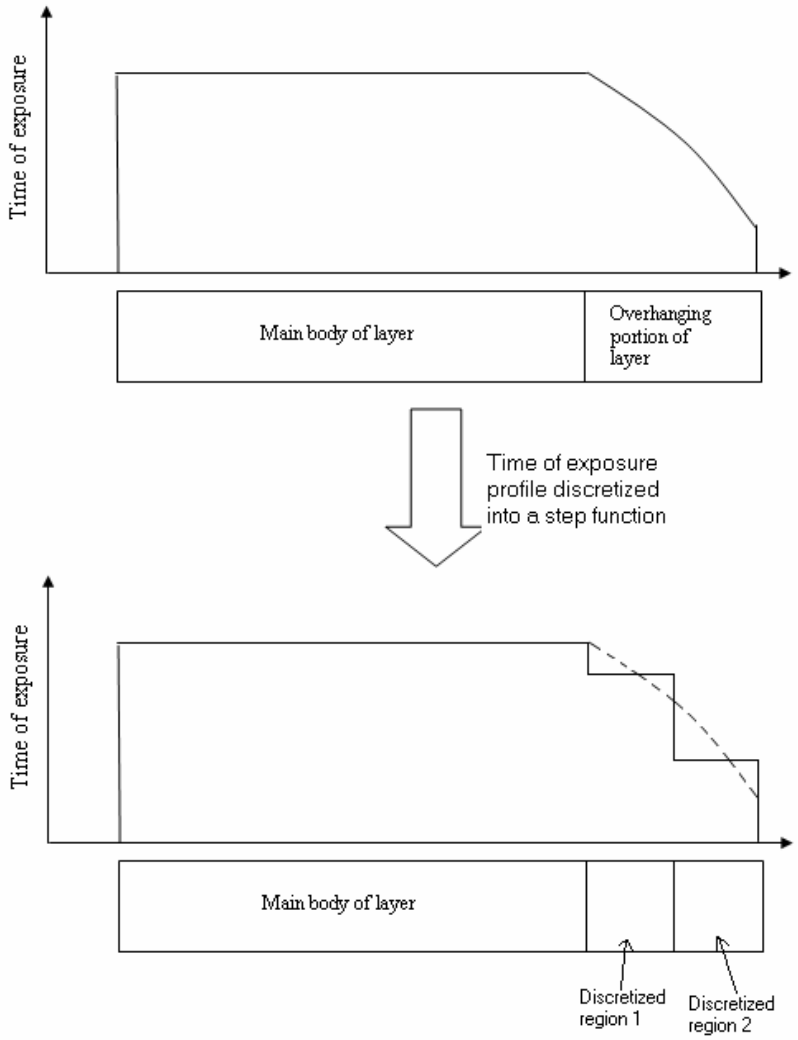

Figure 7.1 Time of exposure discretized into a step function

7.1.2 Implementing the adaptive exposure method

Consider the test part presented in Figure 6.10. It is a four layered part, each layer 500µm thick. Each layer is cured by imaging the same bitmap on the resin surface. As

explained in Section 7.1.1, we divide the overhanging portion of every layer into two regions and average out the time of exposure across each of these regions. The time of exposure to be supplied to cure every layer after averaging the time of exposure over the discretized regions is shown in Figure 7.2. The time of exposures are presented in Table 7.1.

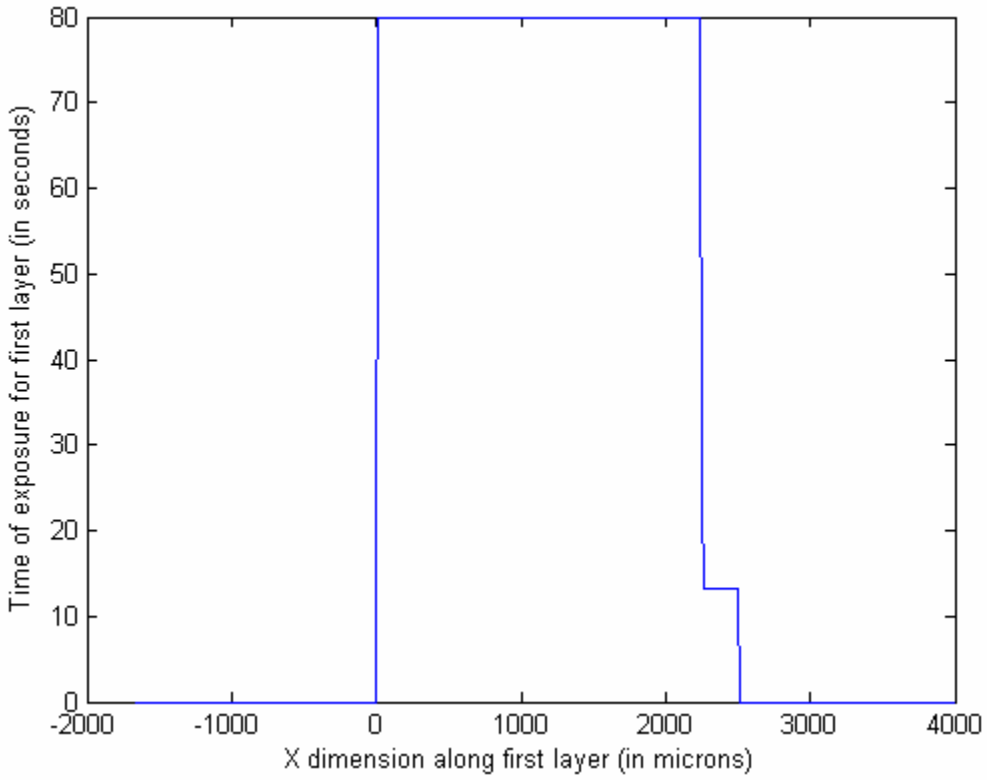

(e) Time of exposure for first layer approximated by a step function

Figure 7.2 Times of exposure for the (a) first; (b) second; (c) third; and (d) fourth layer approximated by a step function

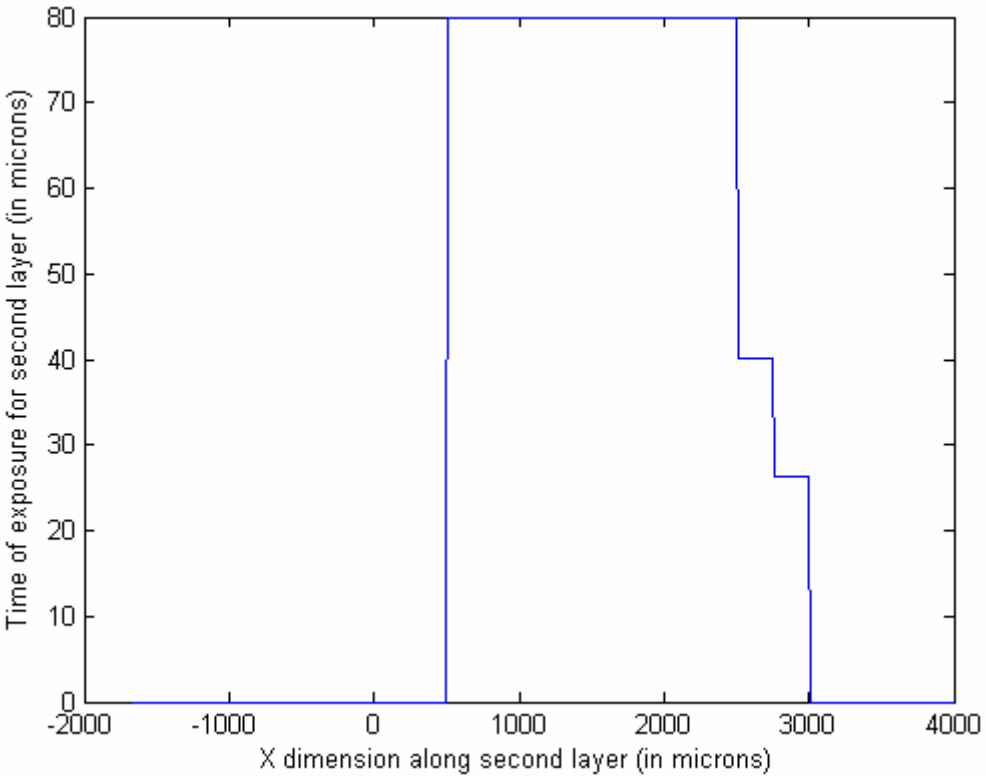

(f) Time of exposure for second layer approximated by a step function

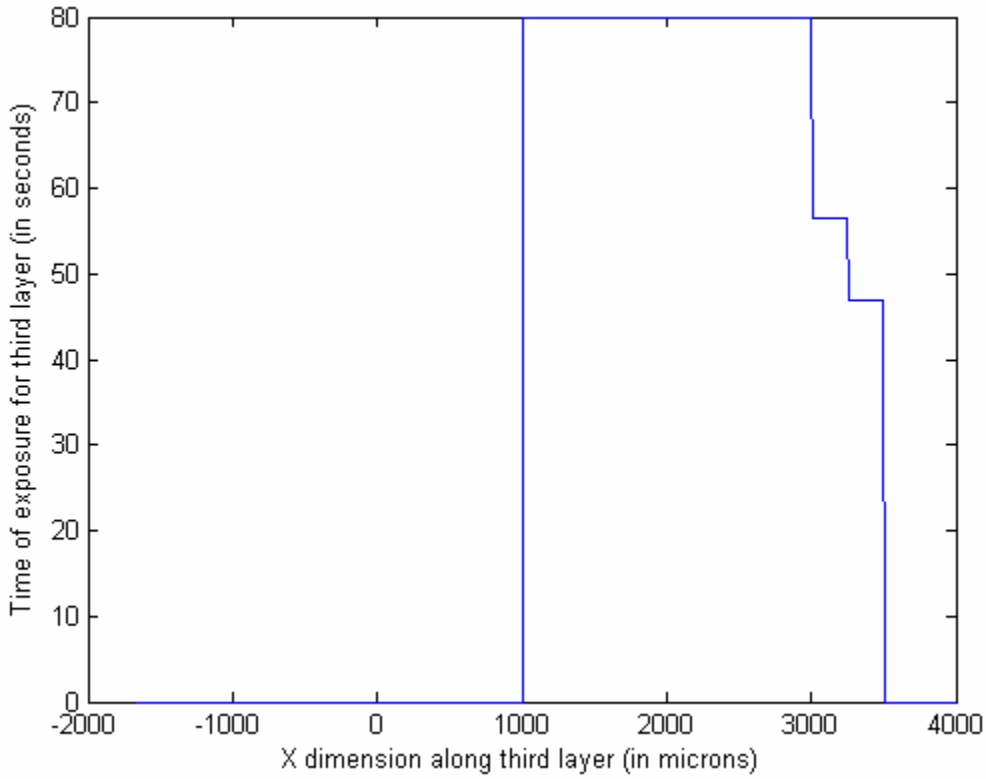

(g) Time of exposure for second layer approximated by a step function

Figure 7.2 (continued)

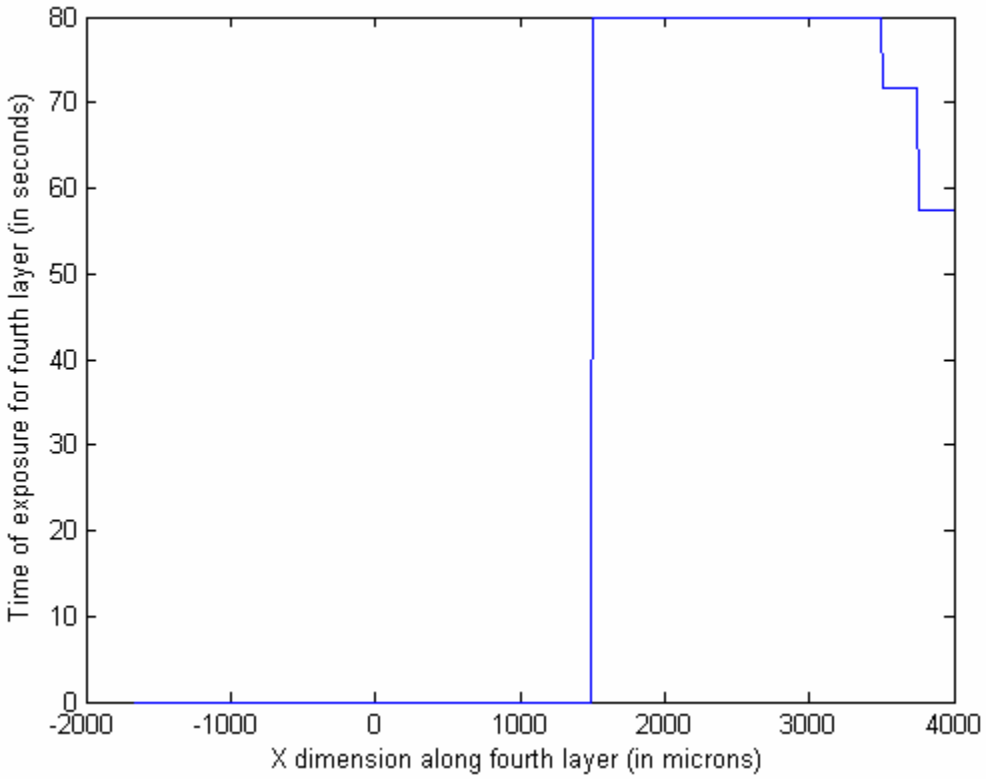

(h) Time of exposure for second layer approximated by a step function

Figure 7.2 (continued)

Table 7. 1 Times of exposure of the layers to implement the adaptive exposure method

Layer # (bottom most to top most)	**Time of exposure (s)**		
	Body of layer	Overhang (Discretized region 1)	Overhang (Discretized region 2)
Layer 1	80	12.9	--
Layer 2	80	40.1	26.3
Layer 3	80	56.4	46.8
Layer 4	80	71.8	57.4

Note that due to the nature of slicing, there is only one discretized region for the bottom most layer.

The down facing profile of the part that would be built with these times of exposure was simulated by implementing the print through model. The simulated profile is presented in Figure 7.3. The Matlab code for this simulation is documented in Appendix H.

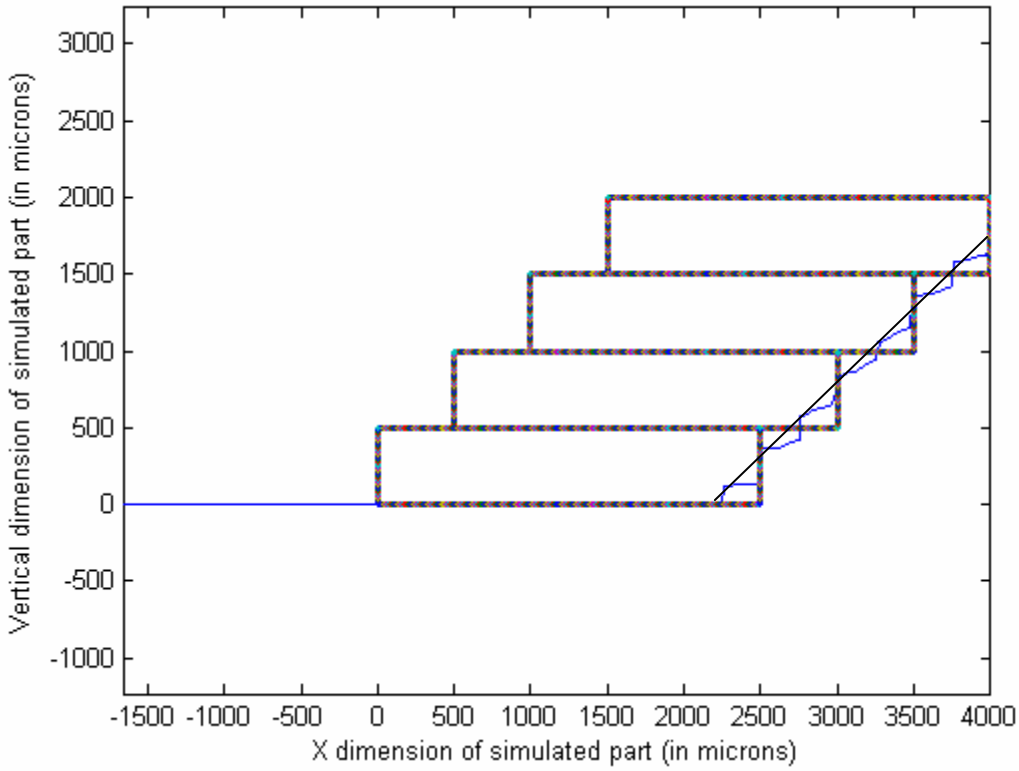

Figure 7.3 Simulated profile of the down facing surface after discretizing the overhanging portion of every layer into two parts and applying compensation zone approach at every part

The part was built on the MPSLA system using the said times of exposures to obtain the part as shown in Figure 7.4.

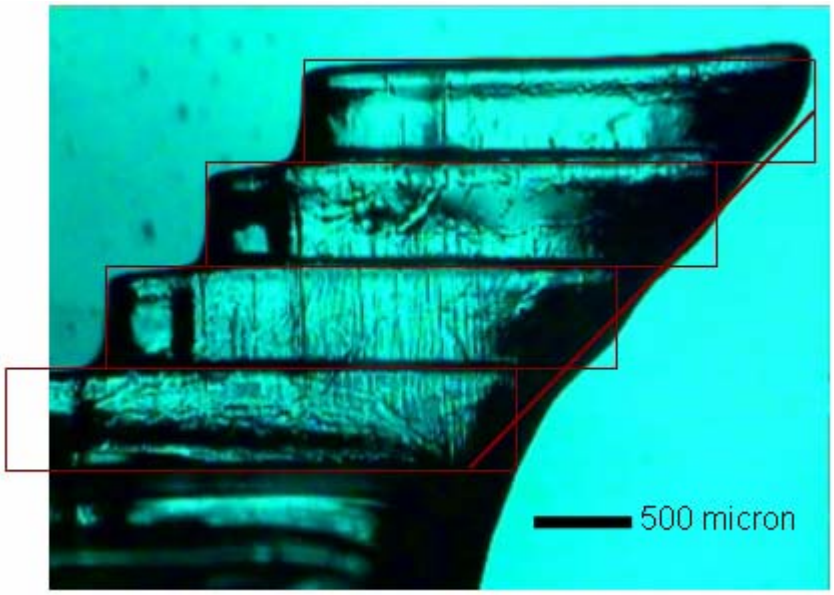

Figure 7.4 Part built on MPSLA system by applying compensation zone approach by discretizing the bitmap into three regions

By comparing the surface finish of the down facing surface of the part cured by discretizing the bitmap to be imaged into two regions (Figure 6.23) and by discretizing it into three regions (Figure 7.4), it can be seen that the surface finish can be improved by increasing the discretizations. The improvement in surface finish has been quantified by super imposing the cured profiles of the part built without using adaptive exposure and the part built using the adaptive exposure method.

The cured profile of the part built without using the adaptive exposure method is shown in Figure 6.23. In Figure 7.5, the cured profile, in red is superimposed on the ideal profile (solid black line) for that part. The distance between the cured profile and the ideal profile is the error. The error in the lateral direction is plotted along the vertical dimension of the part in Figure 7.6.

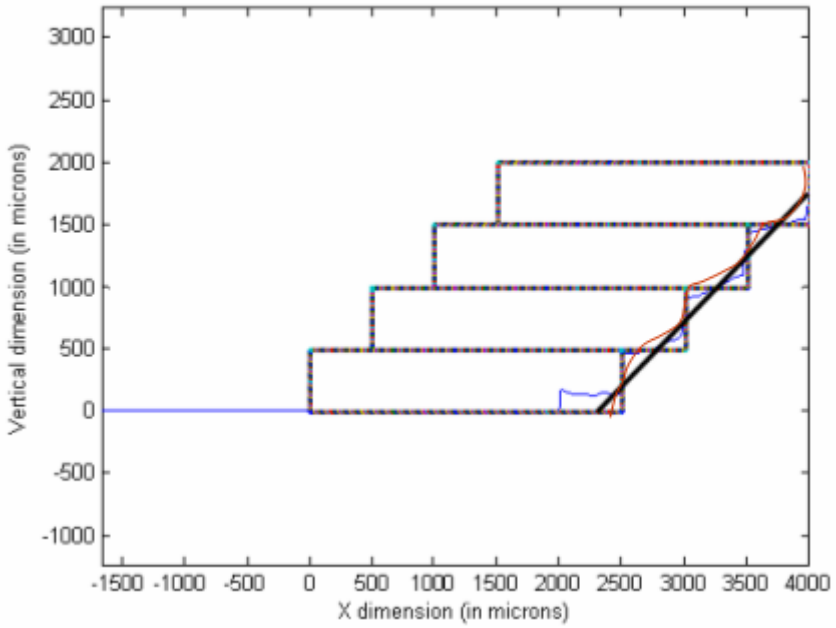

Figure 7. 5 Cured profile of part built without using adaptive exposure method superimposed on the ideal, i.e. required profile

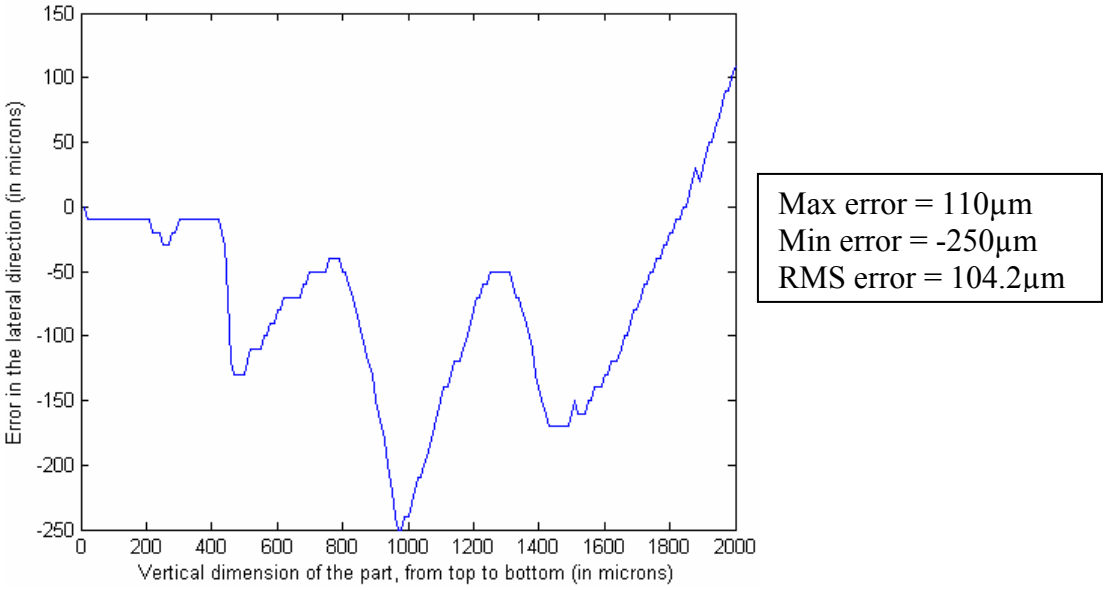

Figure 7. 6 Error in the lateral direction of the part built without using adaptive exposure

The cured profile of the part built using the adaptive exposure method is shown in Figure 7.4. In Figure 7.7, the cured profile, in red is superimposed on the ideal profile (solid black line) for that part. The distance between the cured profile and the ideal profile is the error. The error in the lateral direction is plotted along the vertical dimension of the part in Figure 7.8.

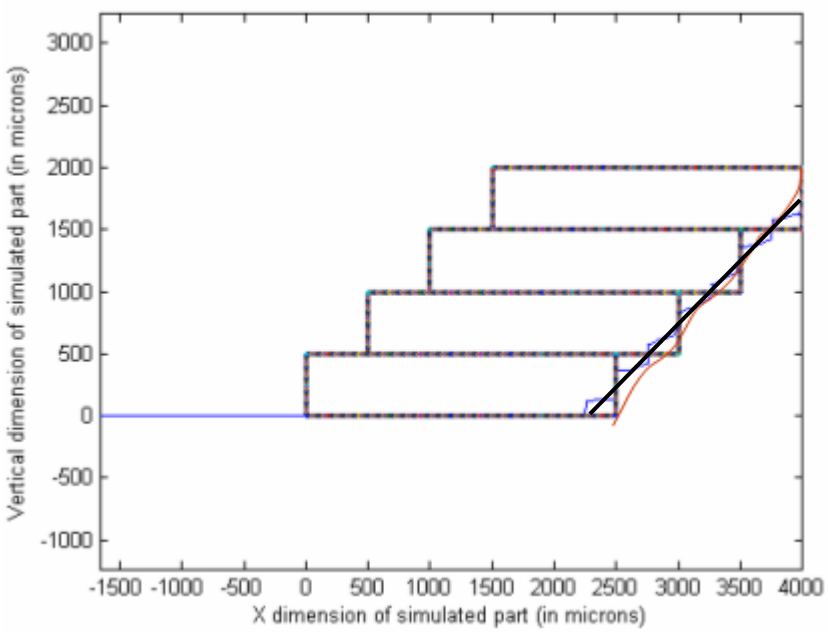

Figure 7. 7 Cured profile of part built using adaptive exposure method superimposed on the ideal, i.e. required profile

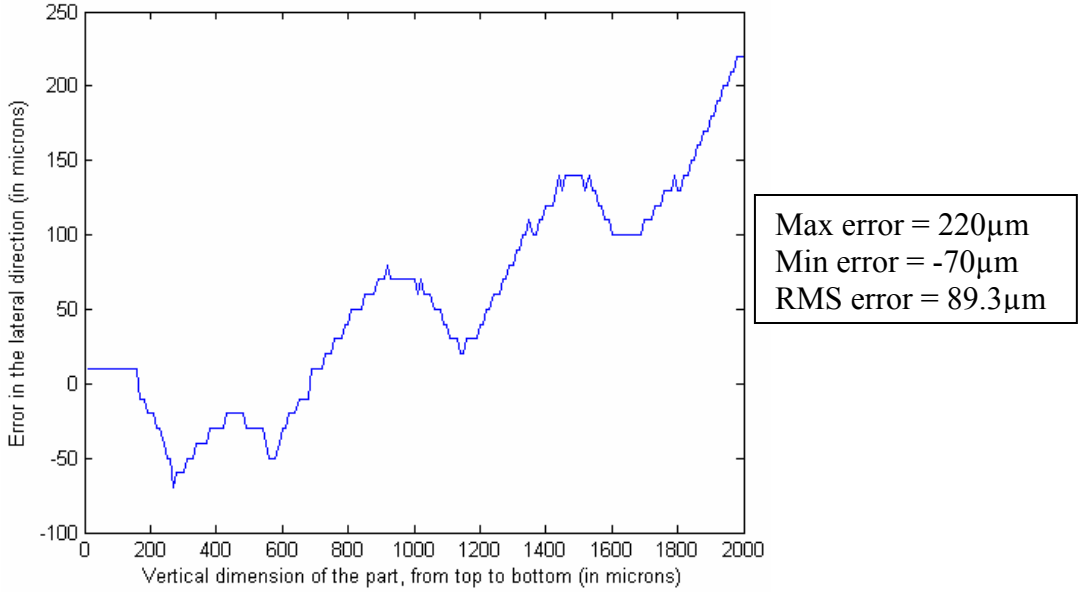

Figure 7. 8 Error in the lateral direction of the part built using adaptive exposure

From Figures 7.6 and 7.8, it can be seen that there are more fluctuations in the error profile in case of the part built without using adaptive exposure method. In case of the part built using the adaptive exposure method, the fluctuations can be seen to be less. However, a systematic error can be observed in the part built using the adaptive exposure

method. The positive error in the lateral direction can be seen to be increasing from top of the part to the bottom of the part.

Thus the adaptive exposure method has been shown to improve the surface finish of the test part. However, a systematic error in observed in the part built with adaptive exposure, in which the amount of positive deviation from the ideal profile goes on increasing from the top to bottom.

7.2 Surface finish of up facing surfaces

Surface finish of an up-facing surface and the build time of a MPSLA part are directly affected by the layer thicknesses. In choosing a slicing scheme, a process planner needs to achieve a trade-off between surface finish and build time. In this section, an adaptive slicing algorithm employing a gradient projection optimization method is formulated and implemented on a test part. In Section 7.2.1, the tradeoff between the two objectives of build time and surface finish is modeled as a compromise Decision Support Problem (cDSP), which is a multi-objective optimization problem. In Section 7.2.2, Rosen's gradient projection method (Belegundu and Chandrupatla, 1999) is explained as a method to solve the multi-objective optimization problem. In Section 7.2.3, the adaptive slicing algorithm employing the gradient projection method is presented. The slicing algorithm is implemented on a test part in Section 7.2.4.

7.2.1 Formulating a multi-objective optimization

Consider a general MPSLA system that can lay down layers as thin as LT_{min} and as thick as LT_{max}. Let the height of a MPSLA part to be built be h units. The variables for this problem are the thickness of every layer, with the bounds on the layers being LT_{min}

and LT_{max}. Another related variable is the number of layers n. The constraint on the part is an equality constraint, which states that the summation of all the layers is equal to the height of the part h. The variables and constraints are summarized as:

Variables:

$$LT \in [LT_{\min}, LT_{\max}]$$
$$n \in [\frac{h}{LT_{\max}}, \frac{h}{LT_{\min}}] \tag{7.1}$$

Constraints:

$$\sum_{k=1}^{n} LT_k = h \tag{7.2}$$

We now derive the objective functions of surface finish and build time.

7.2.1.1 Derivation of objective function for surface finish

Consider a MPSLA part sliced as shown in Figure 7.9. The thickness of every layer that this part is sliced into is given as LT_1, LT_2 ... LT_n. The lateral axis is denoted as "R" and the vertical axis is denoted as "Z". The vertical profile of the part is given by

$$z = f(r) \tag{7.3}$$

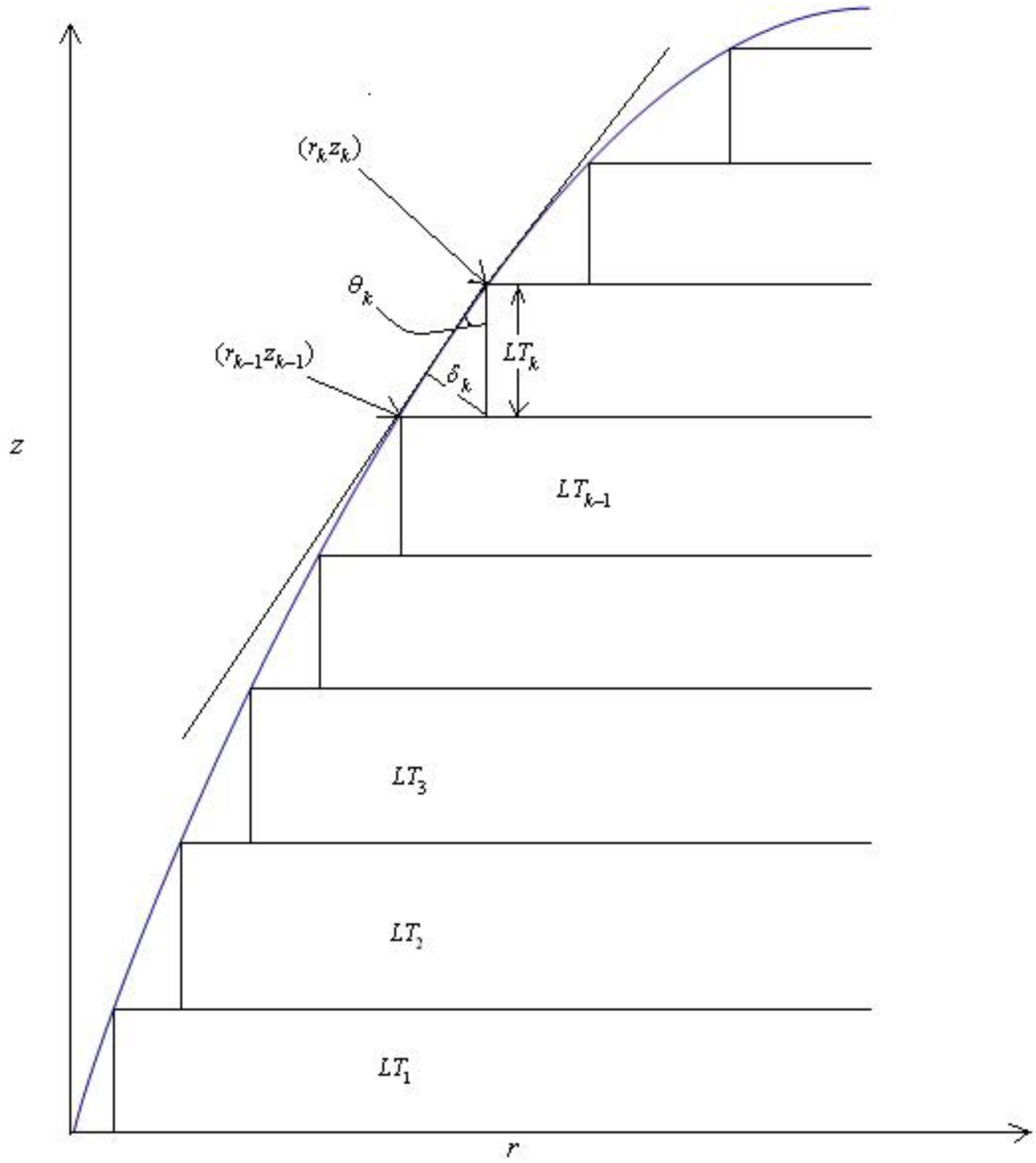

Figure 7.9 Nomenclature for the derivation of cusp height as a function of orientation and layer thickness

West et al., (2001) have associated the 'cusp' (which is a function of both the layer thickness and orientation), as a measure of the surface finish of a part. The aim of minimizing surface roughness can be treated as the goal of minimizing the cusp height. The cusp height is shown in Figure 7.9 as δ_k. The formula for cusp height is given by equation 7.4.

$$\delta_k = LT_k \sin\theta \tag{7.4}$$

In general, if the vertical profile of a part is given by the function $z = f(r)$, the Z-coordinate of the (k-1)th layer will be z_{k-1} given by equation

$$z_{k-1} = \sum_{i=1}^{k-1} LT_i \tag{7.5}$$

and that of the kth layer will be z_k given by equation

$$z_k = \sum_{i=1}^{k} LT_i \tag{7.6}$$

The r-coordinates of the points on the intersection of the $k\text{-}1^{th}$ and k^{th} layer would be given by equations

$$r_{k-1} = f^{-1}(z_{k-1})$$

$$r_k = f^{-1}(z_k) \tag{7.7}$$

The angle θ as shown in Figure 7.9 would thus be given by equation

$$\theta_k = \tan^{-1}\left(\frac{r_k - r_{k-1}}{z_k - z_{k-1}}\right)$$

$$\theta_k = \tan^{-1}\left(\frac{r_k - r_{k-1}}{LT_k}\right) \tag{7.8}$$

The cusp height at the kth layer would be given by equation

$$\delta_k = LT_k \sin(\theta_k) \tag{7.9}$$

The maximum cusp height will be given by

$$\delta_{\max} = \max[\delta_k], \text{ k}\rightarrow 1 \text{ to } n \tag{7.10}$$

Thus, the first objective: "to minimize the surface finish", is given in terms of the variables LT_k and n by making substitutions from equation 7.5 to 7.10 as:

Objective 1:

Minimize

$$\delta_{\max} = \max[LT_k \sin\{\tan^{-1}(\frac{f^{-1}(\sum_{i=1}^{k} LT_i) - f^{-1}(\sum_{i=1}^{k-1} LT_i)}{LT_k})\}] \quad (7.11)$$

7.2.1.2 Derivation of objective function for build time

Chen and Sullivan, (1996) formulated an algorithm to predict build time of Stereolithography parts by using detailed scan and recoat information from the build files. Other researchers have also quantified build time. All of them have broken down the part building process into its constituent steps and modeled the time required to complete each of these steps.

The build time of an MPSLA build can be calculated by breaking down the process of building a part into its constituent steps. A MPSLA part is built by performing the following steps for every layer cured:

1. Lower platform into resin (Deep dip). Translate the platform underneath the recoater blade, raise it to the required level and bring it back to the required position.
2. Wait for the resin film to settle to its final thickness. This is a function of the layer thickness.
3. Expose the layer for the required time. This time is a function of the layer thickness.

The first step involves the translation of the platform and will take approximately the same time, regardless of the layer thickness. Let us denote this time as T_{trans}. After the second step, there is a slight bulge on top of the part being cured (Jacobs, 1992). The

second step is to allow the resin film to settle to its final thickness, and the bulge to disappear. This duration is dependent upon the layer thickness. The smaller the thickness of the layer to be cured, the greater is the time required to allow the resin to settle. Let us denote the time as T_{settle}, given by the function $\mathbf{T_{settle}}$. The time taken for the resin film to settle before the k^{th} layer is exposed is will be given by equation 7.12.

$$T_{settleK} = \mathbf{T_{settle}}\ (LT_k) \tag{7.12}$$

The third step is to expose the layer. The time of exposure is dependent upon the layer thickness. In fact, it is a linear function of the layer thickness, as shown in Chapter 6, equation 6.5. Let us denote the time of exposure by the variable T_{exp}, given by the function $\mathbf{T_{exp}}$. The time of exposure of the k^{th} layer is will be given by equation 7.13.

$$T_{expK} = \mathbf{T_{exp}}(LT_k) \tag{7.13}$$

The total time required to build the part will be given by the summation of the time required for completing all the three steps for every layer. Thus, build time is given by equation 7.14 as

$$BT = \sum_{k=1}^{n} [T_{trans} + T_{settleK} + T_{\exp_k}] \tag{7.14}$$

The second objective: "to minimize build time" is given in terms of the free variables in equation 7.15

Objective 2:

Minimize

$$BT = \sum_{k=1}^{n} [T_{trans} + \mathbf{T}_{settle}(LT_k) + \mathbf{T}_{\exp}(LT_k)] \tag{7.15}$$

7.2.1.3 Modeling Formulating multi objective optimization problem

The multi-objective optimization problem for slicing a general MPSLA part is formulated as shown in Figure 7.10.

Given

- Part profile — $z = f(r)$
- Height of part — h
- Functions and constants related to build time — T_{trans}; $\mathbf{T}_{\mathbf{settle}}$; $\mathbf{T}_{\mathbf{exp}}$

Find

- Number of layers — n
- Layer thicknesses — LT_k

Satisfy

- Sum of layer thicknesses equals part height — $\sum_{k=1}^{n} LT_k = h$
- Bounds on layer thickness — $LT \in [LT_{\min}, LT_{\max}]$

Minimize

- Maximum cusp height

$$\delta_{\max} = \max[LT_k \sin\{\tan^{-1}(\frac{f^{-1}(\sum_{i=1}^{k} LT_i) - f^{-1}(\sum_{i=1}^{k-1} LT_i)}{LT_k})\}]$$

- Build time

$$BT = \sum_{k=1}^{n} [T_{trans} + \mathbf{T}_{settle}(LT_k) + \mathbf{T}_{\exp}(LT_k)]$$

Figure 7.10 Multi objective slicing problem

The multi-objective slicing problem can be modeled using the compromise Decision Support Problem formulation. Compromise DSP (c-DSP) is a multi objective decision model which is a hybrid formulation based on Mathematical Programming and Goal Programming. Refer to Mistree et al. (1994). In the c-DSP, each goal, A_i, has two associated deviation variables d_i^+ and d_i^- which indicate the extent of the deviation of the target (G_i). The deviation variables d_i^+ and d_i^- are always non negative, and the product

constraint: $d_i^+ \cdot d_i^- = 0$ ensures that at least one of the deviation variables for a particular goal is always zero.

Weights are assigned to different goals depending upon their relative importance. A deviation function is formulated by multiplying every deviation variable with its corresponding weight and adding up of all these weighted deviation functions. The mathematical form of the c-DSP is shown in Figure 7.11.

Given

An alternative to be improved through modification; Assumptions used to model the domain of interest.

The system parameters:

n	number of system variables	p+q	number of system constraints
p	equality constraints	q	inequality constraints
m	number of system goals	$G_i(X)$	system constraint function

$f_k(d_i)$ function of deviation variables to be minimized at priority level k for the preemptive case.

Find

Values for the system variables X_i $i = 1, \ldots, n$

Values for the deviation variables d_i^-, d_i^+ $i = 1, \ldots, m$

Satisfy

System constraints (linear, nonlinear)

$g_i(X) = 0$; $i = 1, \ldots, p$ $\quad g_i(X) \geq 0$; $i = p+1, \ldots, p+q$

System goals (linear, nonlinear)

$A_i(X) + d_i^- - d_i^+ = G_i$; $i = 1, \ldots, m$

Bounds

$X_i^{min} \leq X_i \leq X_i^{max}$; $i = 1, \ldots, n$

Deviation variables

$d_i^-, d_i^+ \geq 0$; $d_i^- \cdot d_i^+ = 0$; $i = 1, \ldots, m$

Minimize

Preemptive deviation function (lexicographic minimum)

$\mathbf{Z} = [f_1(d_i^-, d_i^+), \ldots, f_k(d_i^-, d_i^+)]$

Archimedain deviation function

$\mathbf{Z} = \sum W_i(d_i^- + d_i^+)$ where $\sum W_i = 1$, $W_i \geq 0$

Figure 7.11 Compromise Decision Support Problem: Word formulation

Suppose the targets for the surface finish and build time are given as δ_{target} and BT_{target} respectively. In case of the adaptive slicing problem, both the targets are related to minimization. Hence, the deviation variables d_1^- and d_2^- are 0. The aim is to find the values of layer thicknesses LT_k such that the deviation function formulated in the cDSP is minimized. The adaptive slicing problem modeled as a cDSP is presented in Figure 7.12.

Given

- Part profile — $z = f(r)$
- Height of part — h
- Functions and constants related to build time — T_{trans}; $\mathbf{T}_{\mathbf{settle}}$; $\mathbf{T}_{\mathbf{exp}}$
- Deviation variables — $d_1^- = 0; d_2^- = 0$

Find

- Number of layers — n
- Layer thicknesses — LT_k
- Deviation variables — d_1^+, d_2^+

Satisfy

- Sum of layer thicknesses equals part height — $\sum_{k=1}^{n} LT_k = h$
- Bounds on layer thickness — $LT \in [LT_{\min}, LT_{\max}]$

Goals

- Meet low target of surface finish

$$\max[LT_k \sin\{\tan^{-1}(\frac{f^{-1}(\sum_{i=1}^{k} LT_i) - f^{-1}(\sum_{i=1}^{k-1} LT_i)}{LT_k})\}] + d_1^- - d_1^+ = \delta_{t\,\mathrm{arg}\,et}$$

- Meet low target for build time

$$\sum_{k=1}^{n}[T_{trans} + \mathbf{T}_{settle}(LT_k) + \mathbf{T}_{\exp}(LT_k)] + d_2^- - d_2^+ = BT_{t\,\mathrm{arg}\,et}$$

Minimize

Deviation function

Example scenarios:

- Both goals rated equally: $Z = \frac{1}{2}(d_1^- + d_1^+) + \frac{1}{2}(d_2^- + d_2^+)$
- Surface finish rated more than Build time: $Z = \frac{3}{4}(d_1^- + d_1^+) + \frac{1}{4}(d_2^- + d_2^+)$
- Build time rated more than Surface finish: $Z = \frac{1}{4}(d_1^- + d_1^+) + \frac{3}{4}(d_2^- + d_2^+)$
- Surface finish not important: $Z = 0 \cdot (d_1^- + d_1^+) + 1 \cdot (d_2^- + d_2^+)$
- Build time not important: $Z = 1 \cdot (d_1^- + d_1^+) + 0 \cdot (d_2^- + d_2^+)$

Figure 7.12 Adaptive slicing problem modeled as a compromise DSP

7.2.2 Solution to the cDSP (Rosen's gradient projection method)

In this chapter, an optimization method to minimize the deviation function of the cDSP presented in Figure 7.12 is presented. Rosen's gradient projection Method (Belegundu and Chandrupatla, 1999) works the best when there is a linear equality constraint and is hence chosen as the optimization method to solve the cDSP. In Section 7.2.2.1, the theory behind Rosen's gradient projection method is explained. In Section 7.2.2.2, the method is applied to the adaptive slicing problem at hand.

7.2.2.1 Theory of Rosen's gradient projection method

Consider problems that can be expressed in the form

Minimize $f(x)$

Subject to $a_i x - b_i <= 0 \; i = 1, \ldots, m$ (7.16)

$a_i x - b_i = 0 \; i = m+1, \ldots, m+l$

Let t = number of active constraints, consisting of all the equalities and active inequalities.

Assume that x_k is the current feasible start point, as shown in Figure 7.13. x_k lies on the linear constraint in equation 7.16. The task in any optimization algorithm is to determine a direction vector **d** followed by a step length along this direction that would give us a new and better feasible point. We repeat this iterative process until we arrive at the optimum. If we are at an interior point then the steepest descent direction is the obvious choice: $-\nabla f(x_k)$. After moving along the direction of steepest descent by some step size, a projection is obtained on the multi- dimensional plane corresponding to the equality constraint.

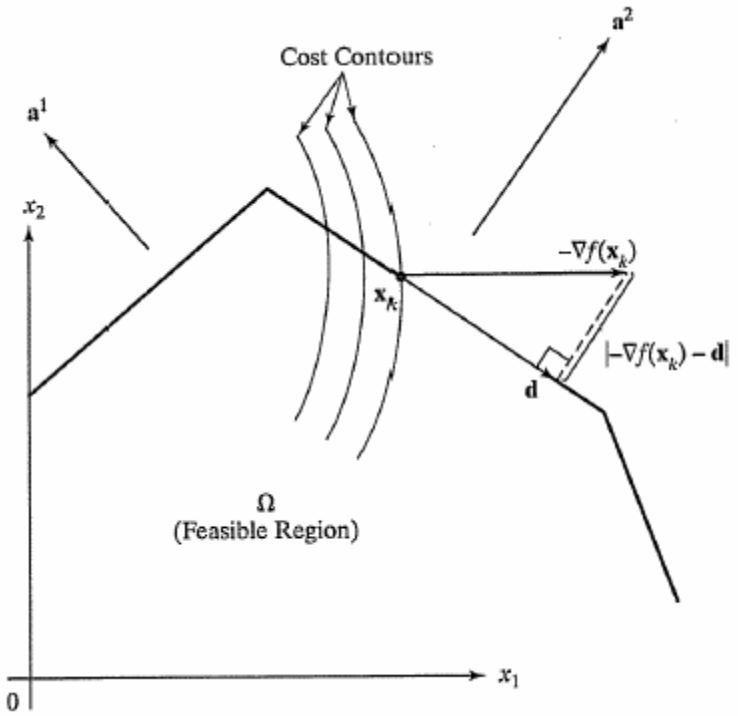

Figure 7.13 Rosen's gradient projection method

In other words, the direction **d** is found by projecting the step taken along $-\nabla f(x_k)$ in such a way that $\left|-\nabla f(x) - \mathbf{d}\right|$ is the minimum possible. Suppose we define a matrix **B** as consisting of rows of the gradient vectors of the active constraint, then we can get the relation

$$\mathbf{Bd} = \mathbf{0} \tag{7.17}$$

Thus, we need the direction **d** such that which shall be the solution of:

$$\text{Minimize } (-\nabla f(x) - \mathbf{d})^T (-\nabla f(x) - \mathbf{d}) \tag{7.18}$$

Subject to $\mathbf{Bd} = \mathbf{0}$

Defining the Lagrangian $L = (\nabla f + \mathbf{d})^T (\nabla f + \mathbf{d}) + \beta^T \mathbf{Bd}$, we have the optimality conditions:

$$\frac{\partial L^T}{\partial \mathbf{d}} = (\nabla f + \mathbf{d}) + \mathbf{B}^T \beta = 0 \tag{7.19}$$

Pre-multiplying by **B** and substituting equation 7.17, we get

$$[\mathbf{B}\mathbf{B}^T]\beta = -\mathbf{B}\nabla f \tag{7.20}$$

For a detailed explanation of Lagrangian formulations to find exact minimum, please refer to Belegundu and Chandrupatla, (1999).

From equation 7.19, we can get a relation for the direction **d** as

$$\mathbf{d} = -\nabla f - \mathbf{B}^T \beta \tag{7.21}$$

Substituting the value of β from equation 7.20 into equation 7.21, we get

$$\mathbf{d} = -\nabla f + \mathbf{B}^T [\mathbf{B}\mathbf{B}^T]^{-1} \mathbf{B}\nabla f \tag{7.22}$$

Combining the matrices multiplying $(-\nabla f)$, we can write

$$\mathbf{d} = -\mathbf{P}(-\nabla f) \tag{7.23}$$

where **P** is the "projection matrix", which is given by

$$\mathbf{P} = [\mathbf{I} - \mathbf{B}^T [\mathbf{B}\mathbf{B}^T]^{-1} \mathbf{B}] \tag{7.24}$$

The vector **d** obtained by solving equation 7.23 can be shown to be the descent direction. When the optimum (minimum) point is reached, **d** becomes equal to 0.

7.2.2.2 Applying Rosen's gradient projection method for adaptive slicing

In case of the problem at hand, the solution is supposed to lie on the equality (active) constraint $\sum_{k=1}^{n} LT_k = h$. The starting point is chosen to be any point that satisfied this constraint. For a given value of number of layers *n*, we can choose the starting feasible solution that all the layers are of the same thickness. Thus, the starting solution is given by equation 7.25.

$$LT_k = \frac{h}{n} \tag{7.25}$$

There are bounds on the layer thickness. These bounds are captured in the objective function by modifying the deviation function by adding penalty functions, as presented in equation (7.26).

Minimize

$$Z = \frac{1}{2}(d_1^- + d_1^+) + \frac{1}{2}(d_2^- + d_2^+) + Penalty$$

where $Penalty = 10^9(Penalty1 + Penalty2)$ (7.26)

where $Penalty1 = (LT_{min} - LT_k)$, if $LT_k < 50$
$= 0$, otherwise.
and
$Penalty1 = (LT_k - LT_{max})$, if $LT_k > 1000$
$= 0$, otherwise.
where $k \rightarrow 1$ to n

For a given number of layers (n), the matrix **B** is a column matrix with n elements, since there is only one active constraint to consider.

$$B = [1,1,1,....\text{n times}]^T \tag{7.27}$$

The projection matrix **P** can be obtained from equation (7.24). The gradient of the objective function at the starting point x_k can be obtained numerically. The direction **d** is obtained from equation (7.23). The step size is obtained by using a "pattern search" algorithm (Belegundu and Chandrupatla, 1999). The Matlab code to implement the gradient projection algorithm has been presented in Appendix I.

The gradient projection method can thus be represented as a black box, with inputs and outputs as shown in Figure 7.14. Inside the black box, the optimization process as explained above occurs.

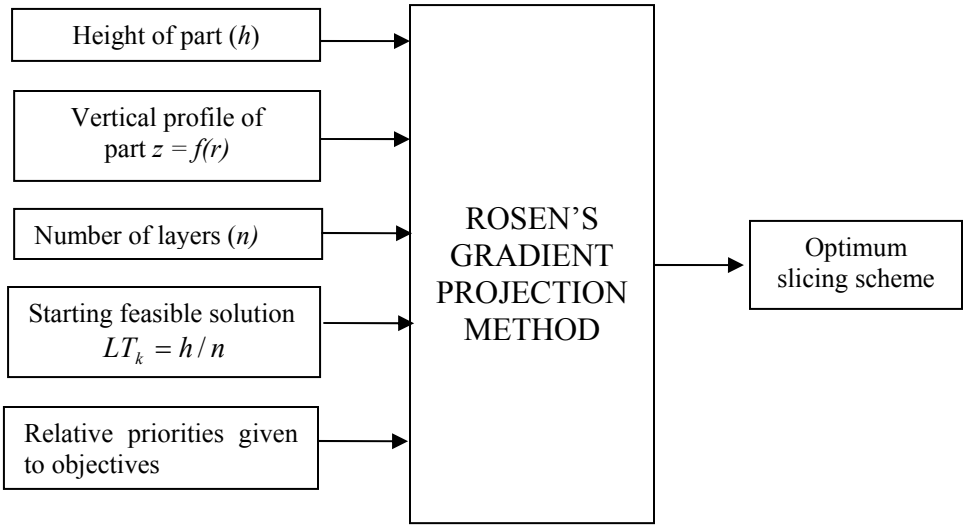

Figure 7.14 Rosen's gradient projection method as a black box

7.2.3 Adaptive slicing algorithm

In this section, we present the algorithm used to solve the cDSP presented in Figure 7.12. Using Rosen's gradient projection method as a black box, we can optimize the layer thicknesses, provided we supply to it the number of layers. Thus, the algorithm is formulated in which we conduct an exhaustive search across the number of layers that the part can be populated by (n), and find the optimum slicing scheme for every value of n. The generated optimum slicing schemes can be compared to see which scheme gives the least value of the deviation function Z in the compromise DSP.

The adaptive slicing algorithm is presented in Figure 7.15.

GIVEN: Height of part (h), Vertical profile (f), bounds on layer thickness $[LT_{min}, LT_{max}]$, priorities given to objectives,

Minimum number of layers $n_{min} = h/LT_{max}$

Maximum number of layers $n_{max} = h/LT_{min}$

(where n_{min} and n_{max} are closest feasible integers)

FOR Number of layer $n = n_{min}:1:n_{max}$

Starting feasible solution: $LT_k = h/n$

Apply Rosen's gradient projection method

Generate optimum slicing scheme for number of layers = n

Compute deviation function of the slicing scheme

END

FOR $i = n_{min}:1:n_{max}$

Compare optimum values of dev. functions obtained for all values of n

END

Figure 7.15 Adaptive slicing algorithm

7.2.4 Applying adaptive slicing algorithm to a test problem

Suppose that the bell shaped part as shown in Figure 7.16 needs to be sliced. The up facing surface of the part can be seen to be composed of two quadratic curves. The part needs to be built on the MPSLA system realized at RPMI, in such a way that the build time is less than or equal to 80 minutes and the maximum cusp height is not more than 40μm. The bounds on the layer thicknesses are assumed to be [60μm, 600μm].

The compromise DSP formulated in Figure 7.8 can be particularized to the MPSLA build at hand.

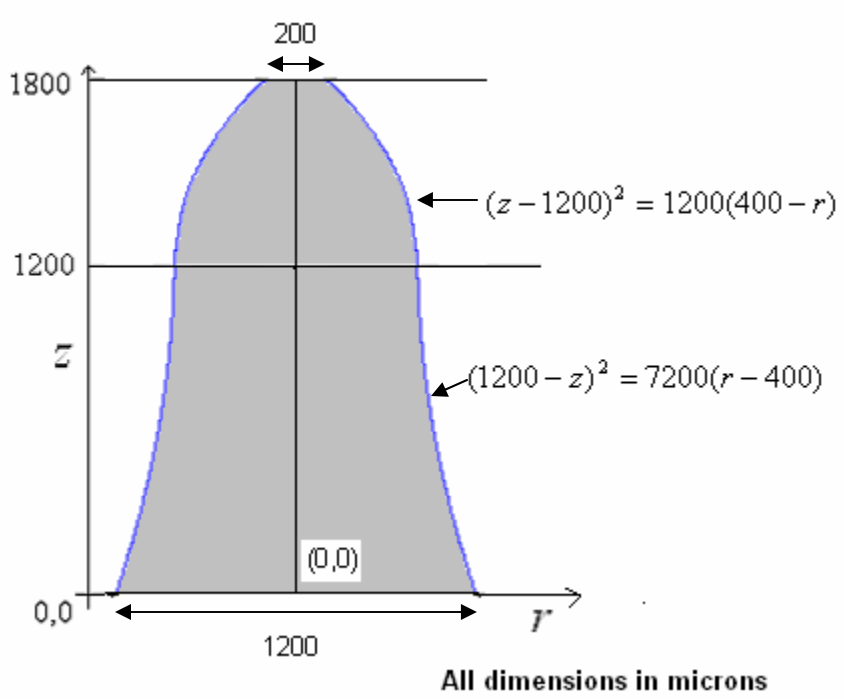

Figure 7.16 Part to be adaptively sliced

The slicing is effected by executing the algorithm presented in Figure 7.15. We first determine the values of the constants and functions related to the build time: T_{trans}; $\mathbf{T_{settle}}$; $\mathbf{T_{exp}}$. T_{trans} is the time taken by the platform to translate underneath the recoater and to bring it back to the required position. This translation time has been measured to be 10s. This time is almost constant regardless of the layer thickness. The function $\mathbf{T_{settle}}(LT_k)$ returns the time required to settle the free surface of resin, before supplying an exposure dose to cure it. The time required to settle the resin if the thickness of a layer is 500μm has been timed by the author to be 60s. The time required to settle the resin for lower layer thicknesses has not been measured and so, we do not have the function $\mathbf{T_{settle}}$. So, we simply assume the function to be inversely proportional to the layer thickness. We assume the function $\mathbf{T_{settle}}$ in equation (7.28) for our system to be to be

$$T_{settleK} = 30000/LT_k \tag{7.28}$$

where

$T_{settleK}$ is in seconds; and

LT_k is in μm

$\mathbf{T_{exp}}$ is the function which acts on the layer thickness and return the time of exposure. This function can be formulated by using the relationship between the cure depth and exposure, presented in Chapter 6, in equation 6.5.

$$z = D_{pM} \cdot (E - E_c) \tag{6.5}$$

where

where D_{pM} is the slope of the working curve, which is the rate at which the cure- front propagates into the resin depth, and

E_c is the threshold exposure of polymerization.

For our system,

D_{pM} = 19.172 μm/(mW/cm^2), or 1.9172mm^3/mW and

E_c = 10.2 mW/cm^2

For our system, we have determined that an overcure of 40μm is necessary for the layer to bind to each other. Thus, the depth of cure is LT_k+OC

Rearranging equation 6.5,

$$E = z / D_{PM} + E_c \tag{7.29}$$

Assuming the average irradiance (H) to be 0.7mW/cm^2, the function $\mathbf{T_{exp}}$ can be particularized as given in equation 7.30.

$$t_{\exp K} = [\frac{LT_k + 40}{19.172} + 10.5] / 0.7 \tag{7.30}$$

Given:

Height of part h = 1800μm

Bounds on layer thickness $LT \in [60\mu m, 600\mu m]$

Bounds on number of layers $n \in [\frac{1800}{600}, \frac{1800}{60}]$, i.e. [3,30]

Vertical profile of part: $z = 1200 - \sqrt{7200(r - 400)}$ for $z \in [0,1200]$

$$z = \sqrt{1200(400 - r)} + 1200 \text{ for } z \in [1200,1800]$$

For n = 3:1:30

Starting feasible solution: LT_k = 1800/n

Applying Rosen's gradient projection method

END

FOR i = 3:1:30

Compare optimum values of dev. functions obtained for all values of n

END

The Matlab code implementing of this algorithm is Rosen's gradient projection method for this part is presented in Appendix I.

The results of the adaptive slicing algorithm for various values of weighting factors given to the objectives of surface finish and build time are shown in Table 7.2.

Table 7. 2 Optimum slicing schemes for various priority schemes

Weights given to		Optimum no. of layers (n)	Layer thicknesses (μm)	Objective function (Z)
Surf. finish	Build time			
0.5	0.5	14	149.4;149.4;149.4;149.4;149.4;149.4; 149.4;149.4;149.4;148.4;89.2; 66.8;75.6;75.1	0.1419
0.25	0.75	14	149.4;149.4;149.4;149.4;149.4;149.4; 149.4;149.4;149.4;148.4;89.2; 66.8;75.6;75.1	0.0709
0.75	0.25	18	108;108;108;108;108;108;108;108;108;108;108;108;108;108;84.6;74.1; 65.9;62.9	0.1845
1	0	30	60;60;60;60;60;60;60;60;60;60;60;60;60;60;60;60;60;60;60;60;60;60; 60; 60;60;60;60;60;60;60;	0.0331
0	1	3	600;600;600	0

Validating the adaptive slicing algorithm

The following observations can be made from the optimum slicing schemes presented in Table 7.2.

- When weight given to build time is increased and that given to surface finish is decreased, the optimum number of layers decreases and the layer thicknesses increase. Conversely, when the weight given to surface finish is increased and that given to build time is decreased, the optimum number of layers increases and the layer thicknesses decrease.
- When weight given to the objective of build time is made 1 and that given to the objective of surface finish is made 0, the optimum slicing scheme comprises of the thickest possible layers (600μm)
- When weight given to the objective of surface finish is made 1 and that given to the objective of build time is made 0, the optimum slicing scheme comprises of the thinnest possible layers (60μm).
- For any scenario, the optimum slicing scheme consists of thicker layers at the lower portion of the part and thinner layers are the upper top portion. This is

because the bottom portion of the vertical profile subtends lesser angle with the vertical, while the upper portion of the vertical profile subtends a larger angle with the vertical. Thus, adaptive slicing has been implemented.

All the above observations make intuitive sense and hence, validate the adaptive slicing algorithm.

Summary

In this chapter, work has been presented on surface finish of MPSLA parts. Adaptive exposure method is presented as a method to improve the down facing surfaces of MPSLA builds. This method is an implementation of the Compensation zone approach, to modulate the exposure supplied to the edge of every layer so that the edge profile of the layer approximates the MPSLA part's down facing surface better. The adaptive exposure method is presented in a test part.

An adaptive slicing algorithm is formulated that slices a CAD model so as to obtain the required tradeoff between build time and surface finish of up facing surfaces of the part. This slicing algorithm models the trade off as a compromise Decision Support Problem (cDSP) and then solves the cDSP by using a gradient projection algorithm. The slicing algorithm is demonstrated in a test part.

Progress made towards validating research questions

Research question 3 was concerning implementing print through smoothing to obtain a better approximation to the down facing surface. The adaptive exposure method is formulated in this chapter to implement print through smoothing on MPSLA parts. The overhanging portion of every layer of a test part is cured by supplying two separate exposure doses. The exposure doses are carefully controlled to ensure that the cure

profile of the overhanging region of every layer approximates the part's down facing surface profile. A part with a better surface finish of the down facing surface is built by implementing the adaptive slicing algorithm. The RMS deviation from the ideal, or required surface was improved from 104.2µm to 89.3µm. The fluctuations from the ideal surface were also significantly reduced, as shown in the error profiles in Figures 7.6 and 7.8. However, a systematic error seems to have been introduced by implementing the adaptive exposure method, in that the positive error goes on increasing from the top to the bottom of the part. Thus, the demonstration of adaptive exposure lends support to the hypothesis that adaptive exposure can be used to effect print through smoothing in MPSLA builds.

CHAPTER 8 CASE STUDY: BUILDING A PART WITH A QUADRATIC VERTICAL PROFILE

Research Question 4 was regarding formulating a process planning method in order to cure a MPSLA part with constraints on dimensions, surface finish and build time. Using the models formulated and validated in Chapters 5, 6 and 7, it is now possible to present a process planning method to cure a 3D MPSLA part with multiple constraints. In this chapter, the process plan is described and its implementation to cure a test part is demonstrated.

The process planning method is as shown in Figure 8.1.

Given: CAD model, targets on surface finish and build time, relative importance of the targets.

1. Compute the vertical profile of the up-facing surface
2. Apply the "adaptive slicing algorithm" to obtain a required tradeoff between surface finish of up-facing surface and build time. Slicing scheme will be generated.
3. Generate the bitmaps to cure every layer
4. Apply the compensation zone approach to compute the time of exposure of every bitmap
5. Approximate the time of exposure across some of the bitmap pixels (if required)
6. Build part

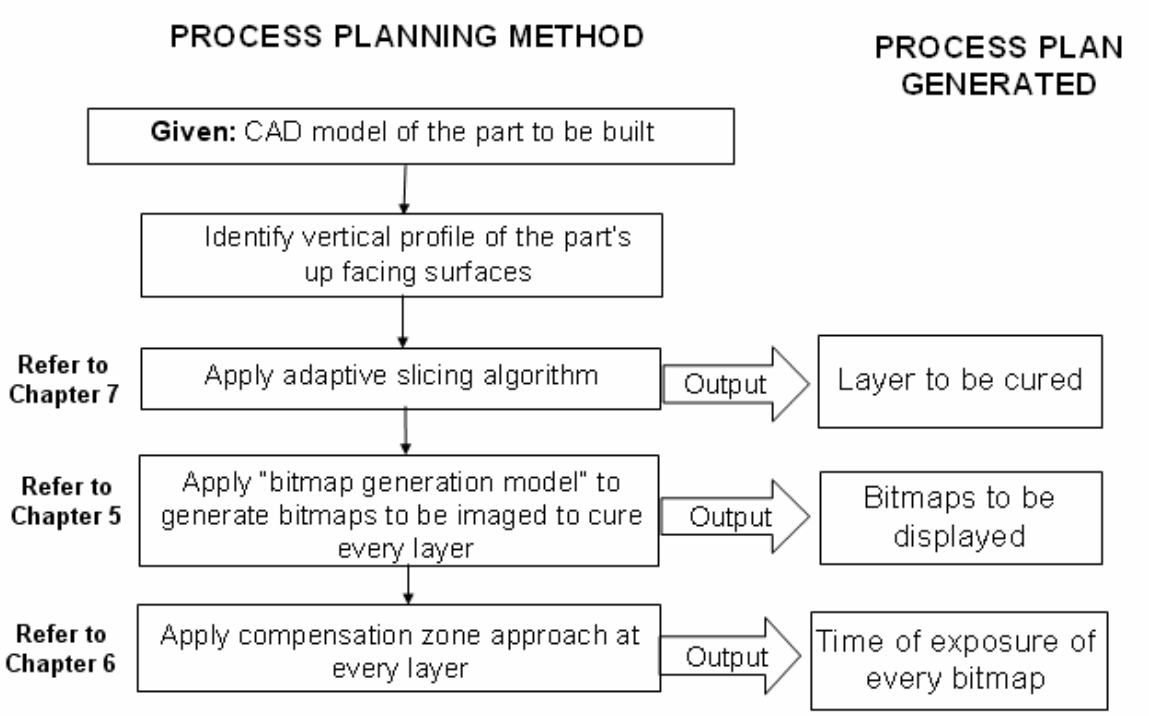

Figure 8.1 Process planning method for Mask Projection Stereolithography

In this chapter, the process planning method is Figure 8.1 is applied on a test part shown in Figure 8.2. The test part has quadratic up and down facing surfaces, the vertical profile of which is given by equation 8.1.

$$z = 0.0005y^2 + y \tag{8.1}$$

The cross-section of the part is a rectangle of dimensions 2600µmX400µm. The height of the part is 2000µm and its larger dimension is to be built parallel to the global Y axis. It should be noted that the part used to validate the compensation zone approach in Chapter 6 was built along the global X axis. The maximum allowable cusp height on the up and down facing surfaces is 40µm. The build time of the part is required to be less than 30 minutes.

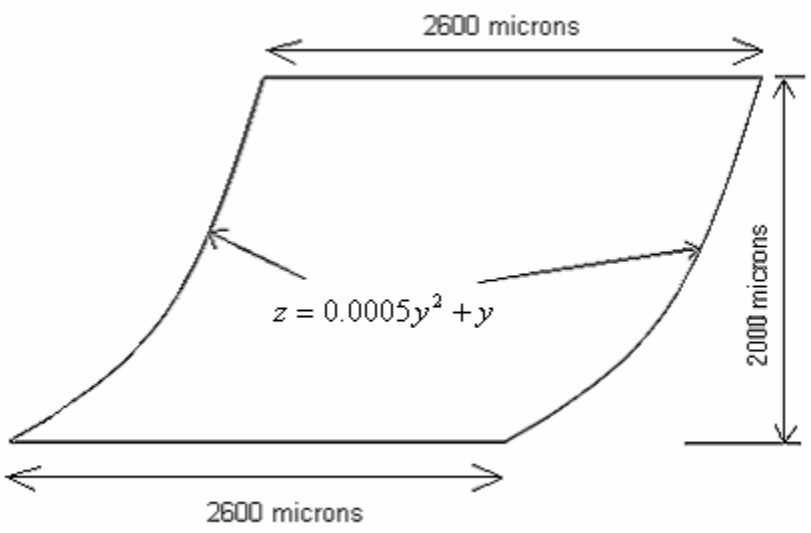

Figure 8.2 Test part to demonstrate process planning method

In Section 8.1, the test part is sliced using the adaptive slicing algorithm presented in Chapter 7, to obtain the required tradeoff between the build time and the surface finish of the up facing surface. One of the slicing schemes is selected for executing further steps of process planning. The bitmaps to be imaged onto the resin surface in order to cure the required layers are generated using the "bitmap generation model", presented in Chapter 5. In Section 8.3, the irradiance distribution incident on the resin surface when these bitmaps are imaged onto it is computed using the multi-scale irradiance model, presented in Chapter 5. Using the irradiance distributions as inputs to the compensation zone approach presented in Chapter 6, the times of exposure of these bitmaps are computed. The part is built on the MPSLA system by using the generated process plan. The built part is presented in Section 8.4 and its geometry is compared to the required geometry.

8.1 Slicing the part to be built

The vertical profile of the CAD model presented in Figure 8.2 is quadratic, given by equation 8.1. The slicing algorithm for obtaining tradeoff between build time and

surface finish is presented in Chapter 7. As explained in Chapter 7, only the top facing surface is of interest in executing the slicing algorithm for MPSLA, because the down-facing surface is significantly smoother than the top-facing surface because of print through.

The bounds on the layer thickness are taken to be 50μm to 500μm. In reality, the MPSLA system realized as a part of this research cannot build layers thinner than 400μm. However, purely to demonstrate the execution of the adaptive slicing algorithm, the author has chosen the bounds on layer thicknesses to be [50μm, 500μm]. The part with vertical dimension 2000μm can thus be meshed with a minimum of 40 layers and maximum of 4 layers. The problem is modeled as a compromise DSP as shown in Figure 8.3.

Given

- Part profile $z = f(y)$: $z = 0.0005y^2 + y$
- Height of part 2000μm
- Functions and constants related to build time
  Time taken to translate platform underneath recoated: $T_{trans} = 10\text{s}$
  Time taken for resin to settle before exposure: $T_{settleK} = 30000/LT_k$
  Time of exposure for the bitmap $t_{\exp K} = [\frac{LT_k + 40}{19.172} + 10.5]/0.7$
- Deviation variables $d_1^- = 0; d_2^- = 0$

Find

- Number of layers n
- Layer thicknesses LT_k
- Deviation variables d_1^+, d_2^+

Satisfy

- Sum of layer thicknesses equals part height $\sum_{k=1}^{n} LT_k = 2000$
- Bounds on layer thickness $LT \in [50\mu m, 500\mu m]$

Goals

- Meet low target of surface finish
$$\max[LT_k \sin\{\tan^{-1}(\frac{f^{-1}(\sum_{i=1}^{k} LT_i) - f^{-1}(\sum_{i=1}^{k-1} LT_i)}{LT_k})\}] + d_1^- - d_1^+ = 40\mu m$$
- Meet low target for build time
$$\sum_{k=1}^{n}[T_{trans} + \mathbf{T}_{settle}(LT_k) + \mathbf{T}_{\exp}(LT_k)] + d_2^- - d_2^+ = 1800s$$

Minimize

Deviation function
Example scenarios:

- Both goals rated equally: $Z = \frac{1}{2}(d_1^- + d_1^+) + \frac{1}{2}(d_2^- + d_2^+)$
- Surface finish rated more than Build time: $Z = \frac{3}{4}(d_1^- + d_1^+) + \frac{1}{4}(d_2^- + d_2^+)$
- Build time rated more than Surface finish: $Z = \frac{1}{4}(d_1^- + d_1^+) + \frac{3}{4}(d_2^- + d_2^+)$
- Surface finish not important: $Z = 0 \cdot (d_1^- + d_1^+) + 1 \cdot (d_2^- + d_2^+)$
- Build time not important: $Z = 1 \cdot (d_1^- + d_1^+) + 0 \cdot (d_2^- + d_2^+)$

Figure 8.3 Modeling the slicing problem as a compromise DSP

Table 8.1 Optimum slicing schemes for various priorities to objectives

Weights given to		Optimum no. of layers (n)	Layer thicknesses (µm)	Objective function (Z)
Surf. finish	Build time			
0.5	0.5	12	131.3; 139.1; 147.8; 155.9; 164.5; 172.1; 180.6; 181.7; 181.7; 181.7; 181.7; 181.7	0.8724
0.25	0.75	10	159.3; 171.4; 182.8; 194.2; 205.3; 217.4; 217.4; 217.4; 217.4; 217.4	0.4906
0.75	0.25	16	98; 103; 107.3; 111.4; 116.4; 120.9; 126.2; 129.8; 134; 136.1; 136.1; 136.1; 136.1; 136.1; 136.1; 136.1	0.8983
1	0	40	50; 50; 50; 50; 50; 50; 50; 50; 50; 50;50; 50; 50; 50; 50; 50; 50; 50; 50; 50; 50; 50; 50; 50; 50; 50; 50; 50; 50; 50; 50; 50; 50; 50; 50; 50; 50; 50; 50; 50	0
0	1	4	500; 500; 500; 500	0

The cDSP presented in Figure 8.3 is executed by means of the adaptive slicing algorithm formulated in Chapter 7 (Figure 7.11). The Matlab code written to solve the cDSP is presented in Appendix J. The optimum slicing schemes are presented in Table 8.1.

Suppose that the process planner has the highest priority on the build time and the least priority on the surface finish. In that case, the optimum slicing scheme will be the one returned for the weights given to objectives on surface finish and build time as 0 and 1 respectively. Thus, the slicing scheme selected to implement the process planning method further is the last one in Table 8.1, with all layers being 500µm.

8.2 Generating bitmaps to be imaged

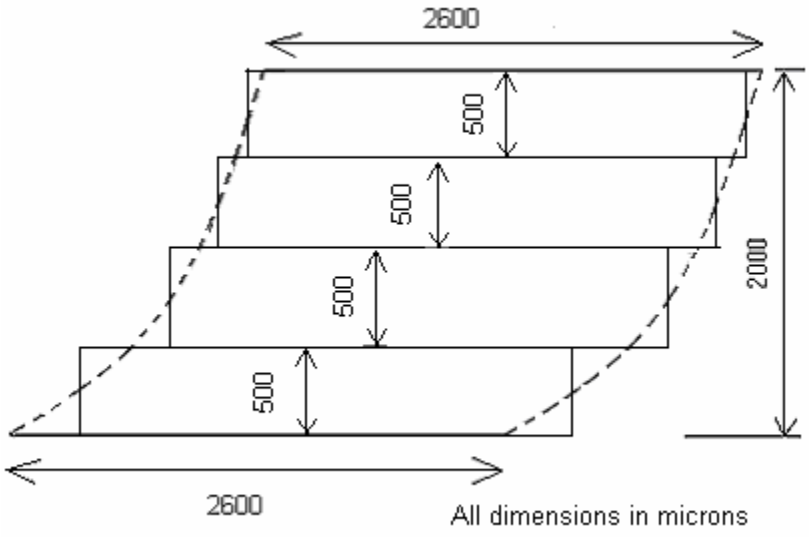

Figure 8.4 Sliced part to be built

The sliced part looks as shown in Figure 8.4. It is composed of four layers, each 500µm thick and of lateral extents 2600µmX400µm. The required down facing surface is shown by the dotted line in Figure 8.4. The four identical layers are to be cured by imaging the same bitmap onto the resin surface. In this section, the bitmap to be imaged onto the resin surface to cure a layer 2600µmX400µm, with its longer dimensions parallel to global Y axis is generated.

The layer to be cured is meshed with points. These points are mapped onto the micro-mirrors on the DMD using the "Pixel image database" (Refer to Chapter 5), in order to determine which micro-mirrors are 'ON'. Every 'ON' micro-mirror on the DMD corresponds to a black pixel on the bitmap. The bitmap generated to cure the 2600µmX400µm layer is shown in Figure 8.5. All the black pixels in Figure 8.5 correspond to 'ON' micro-mirrors.

Figure 8.5 Bitmap generated by bitmap generation model to cure the required layer

There can be seen some jaggedness at the edges of the bitmap presented in Figure 8.5. This jaggedness is because of the errors in mapping the elements to the micro-mirrors, as explained in Chapter 5. The white pixels dotting the edges are manually made black and the edges are smoothened, as explained in Chapter 5, before proceeding with the process planning method.

8.3 Applying compensation zone approach

The bitmap generated by the "bitmap generation model" is input to the multi scale irradiance model (presented in Chapter 5) and the irradiance distribution on the resin surface that would be made incident when the bitmap is imaged onto it is computed. The irradiance distribution is shown in Figure 8.6.

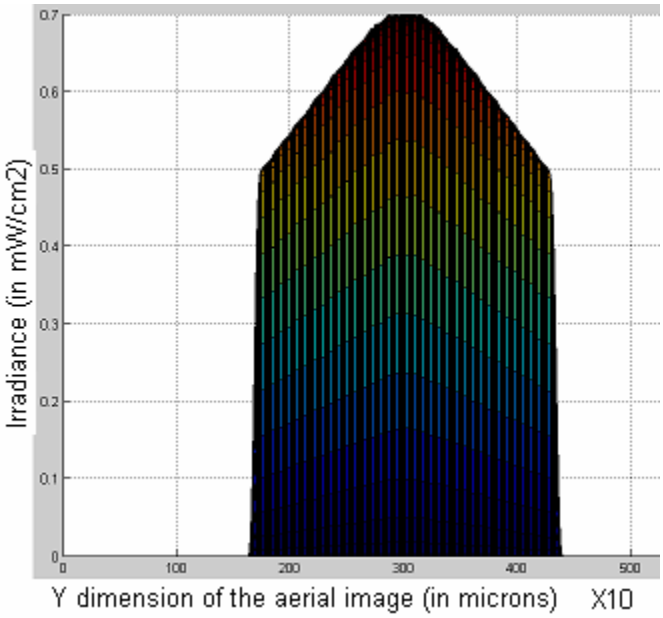

Figure 8.6 Irradiance distribution along the Y dimension of the layer to be cured

In order to build the four layered part, the same bitmap as shown in Figure 8.5 is imaged onto the resin surface. The platform is translated underneath the imaging system, along the Y direction to offset layers over each other. The times of exposures for the bitmaps need to be found out. This is determined by using the compensation zone approach.

The time of exposure for the body of every layer in Figure 8.5, is imaged for 80s, as explained in Chapter 6. We need to compute the time of exposure for the overhanging portion of every layer. Compensation zone approach is adopted at every pixel column on the part to be built. The generic formulation for the compensation zone approach is given in Figure 6.14. By solving equation 6.22 at every pixel location, the times of exposure of the overhanging region of every layer is computed. The times of exposure are shown in Figure 8.7. The Matlab code to generate these times of exposure is presented in Appendix J.

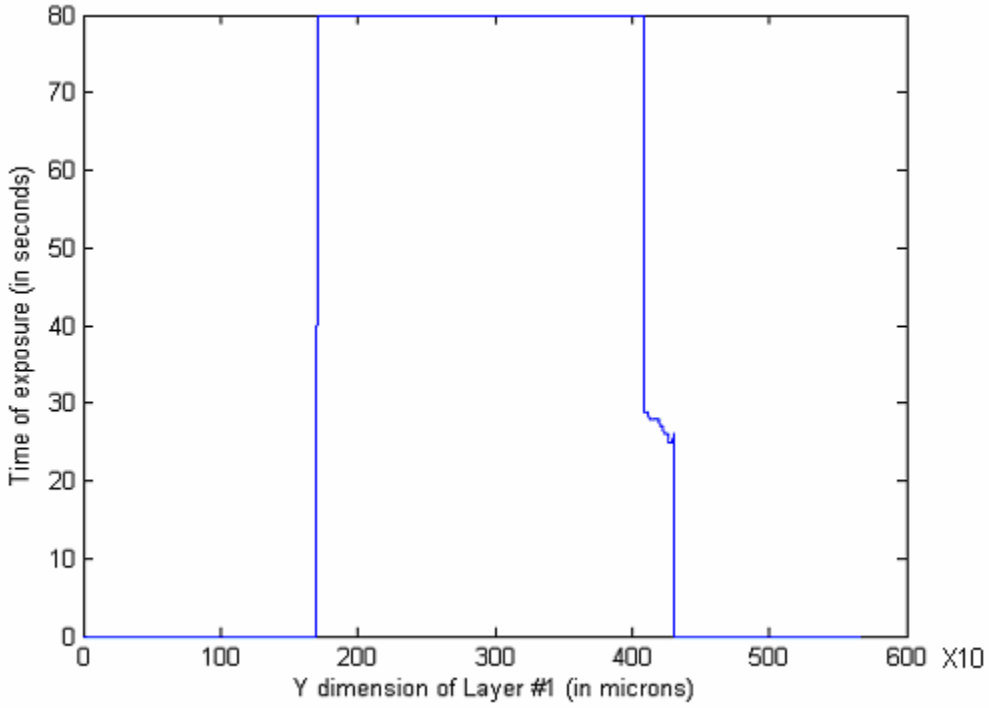

(a) Time of exposure along first layer

Figure 8.7 Times of exposure for curing the (a) first; (b) second; (c) third; and (d) fourth layer

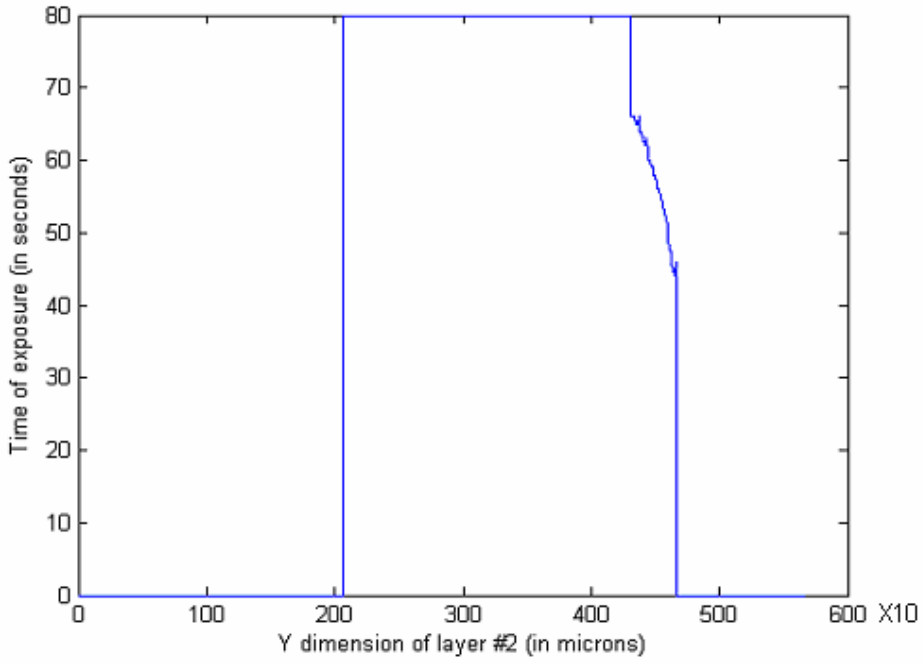

(b) Time of exposure along second layer
Figure 8.7 (continued)

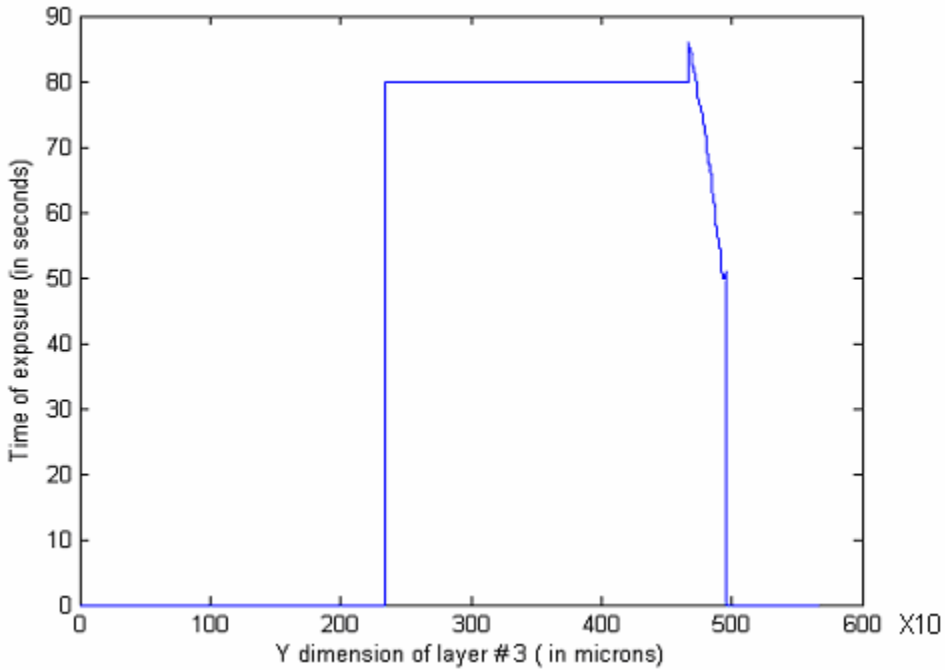

(c) Time of exposure along third layer

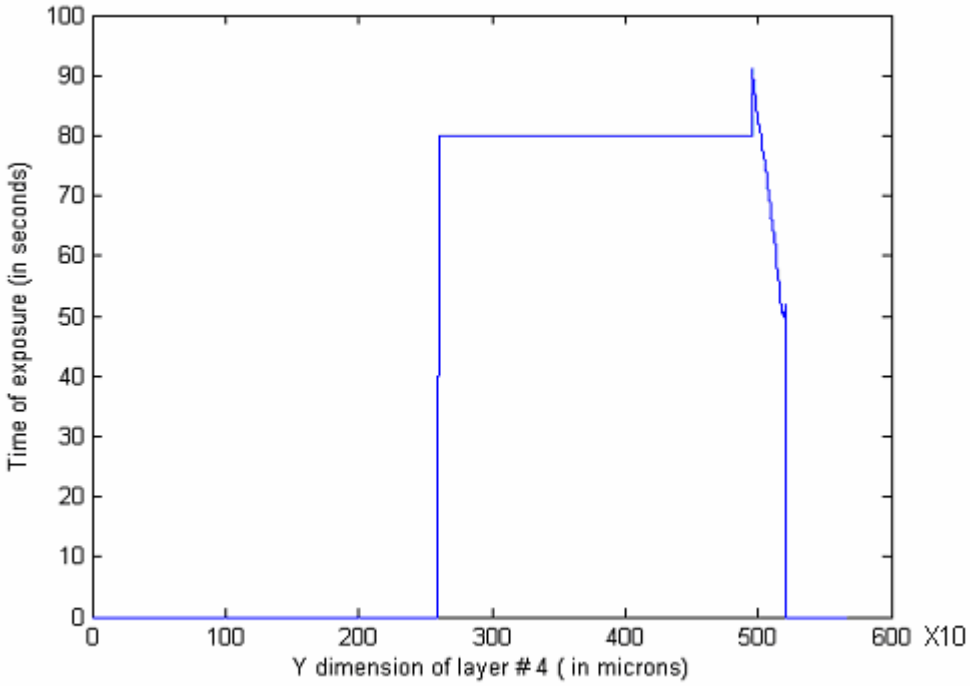

(d) Time of exposure along fourth layer

Figure 8.7 (continued)

The profile simulated upon running the times of exposure shown in Figure 8.7 through the print through model applied at every pixel location is shown in Figure 8.8.

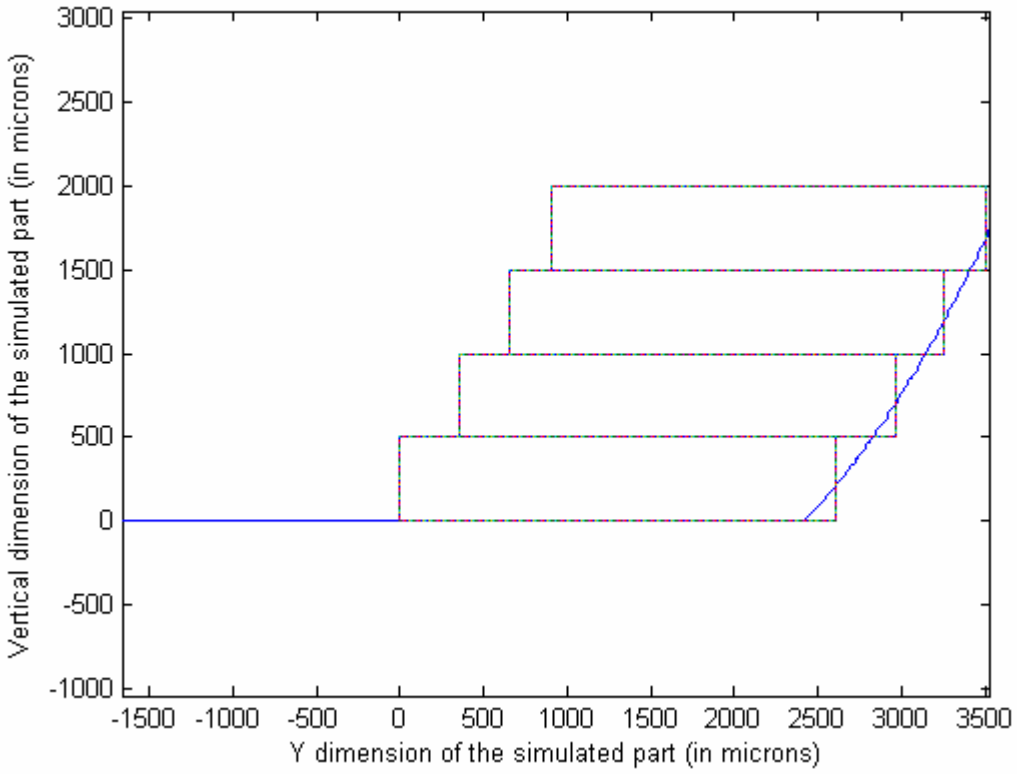

Figure 8.8 Simulated profile of the down facing surface for the times of exposure as given in Figure 8.7

In order to supply the times of exposure as shown in Figure 8.7, it would be necessary to display and image every micro mirror on the bitmap irradiation the overhanging portion of the layer separately for a given duration of time. Since this is not possible to do manually, the author computed the average time of exposure across the overhanging portion of the bitmap. Thus, every layer was cured in two steps, by imaging two bitmaps onto it. The first bitmap cured that part of the layer which bonds to the layer underneath it. The second bitmap cures the overhanging portion of the layer. This division of every bitmap into two bitmaps is explained pictorially in Figure 6.17.

The times of exposure for every layer, after those along the overhanging portion have been averaged out are shown in Figure 8.9. The times of exposure now appear as step functions, with one constant value of time of exposure across the body of the layer and another constant time of exposure across the overhanging portion of the layer.

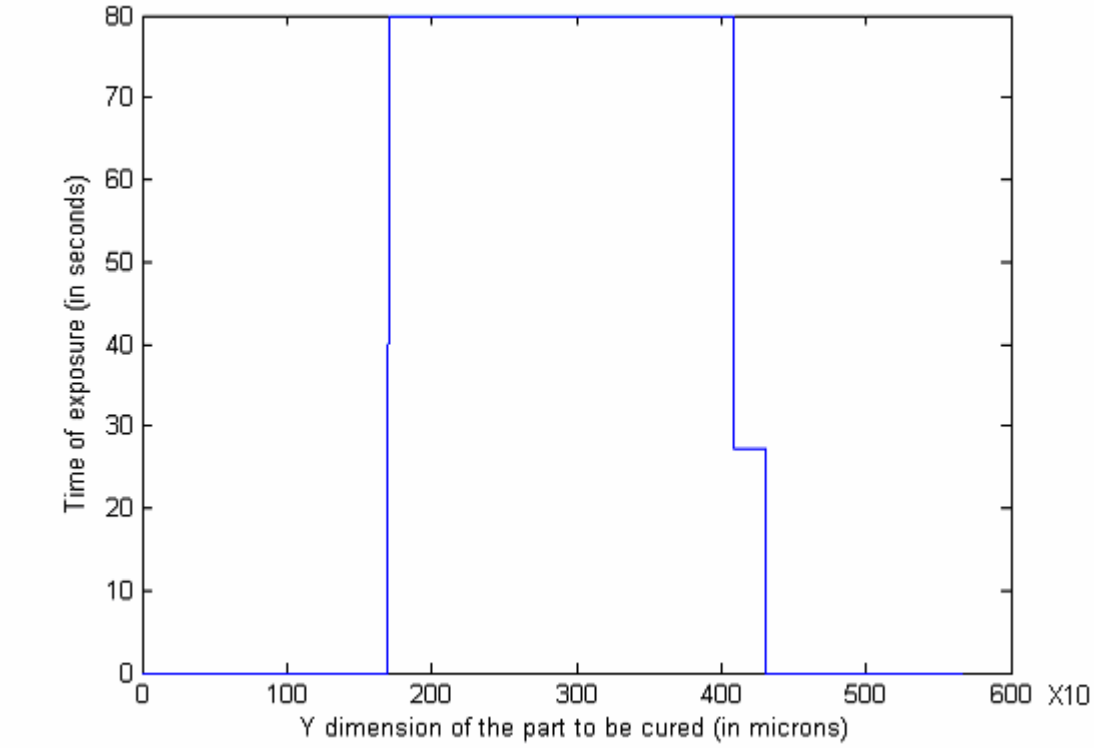

(a) Time of exposure supplied to cure the first layer

Figure 8.9 Times of exposure for the (a) first; (b) second; (c) third; and (d) fourth layer approximated by step functions

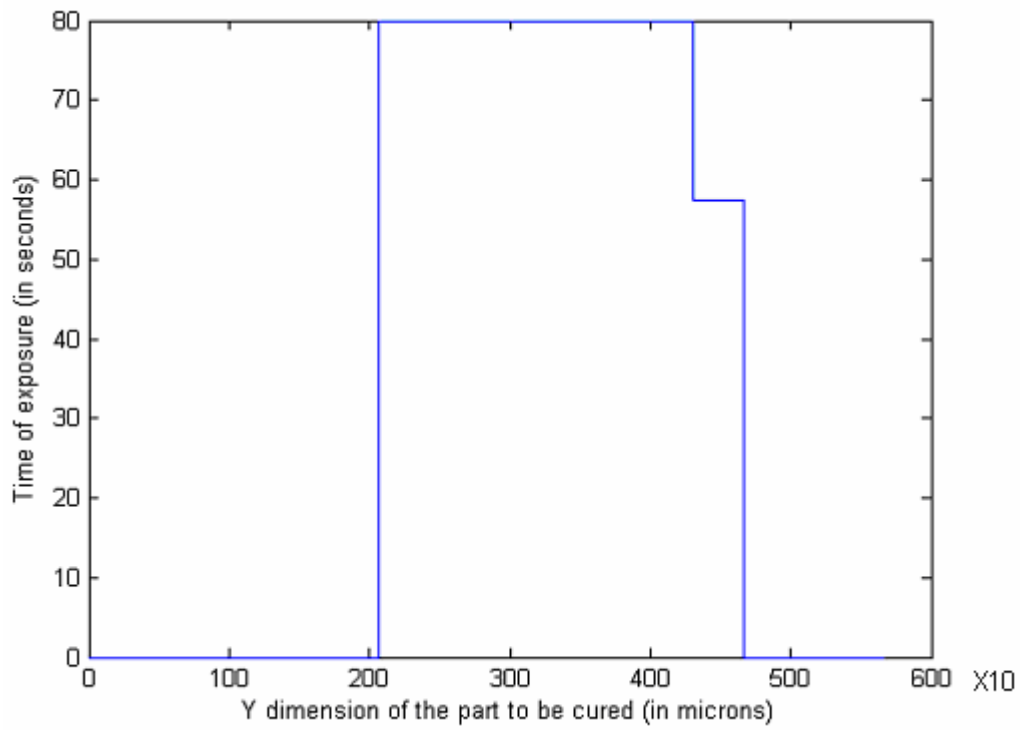

(b) Time of exposure supplied to cure the second layer

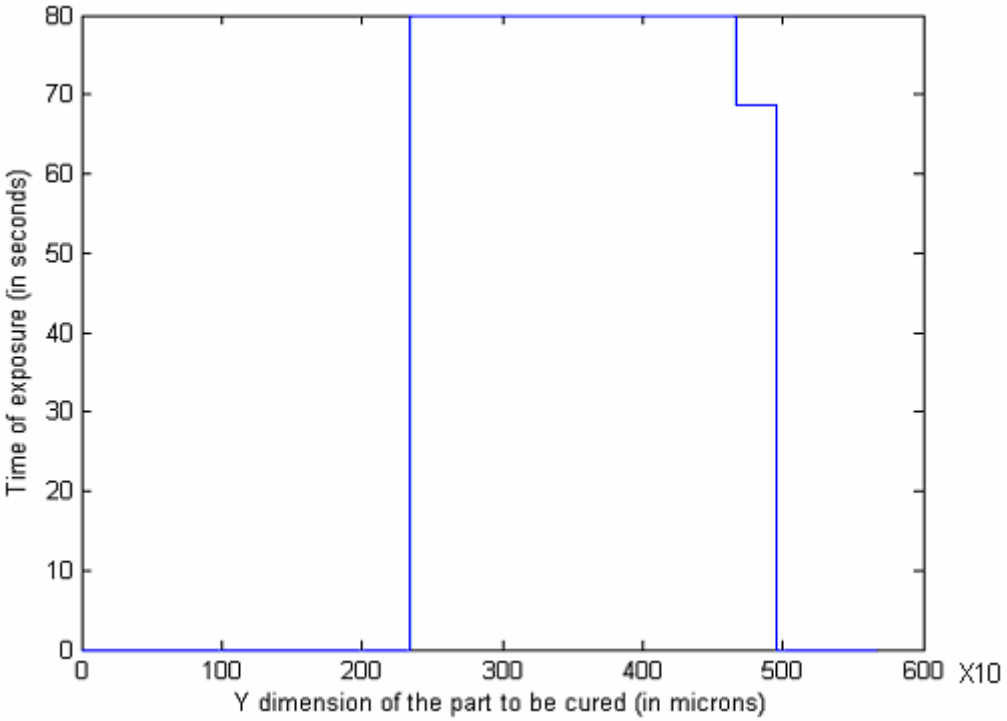

(c) Time of exposure supplied to cure the third layer

Figure 8.9 (continued)

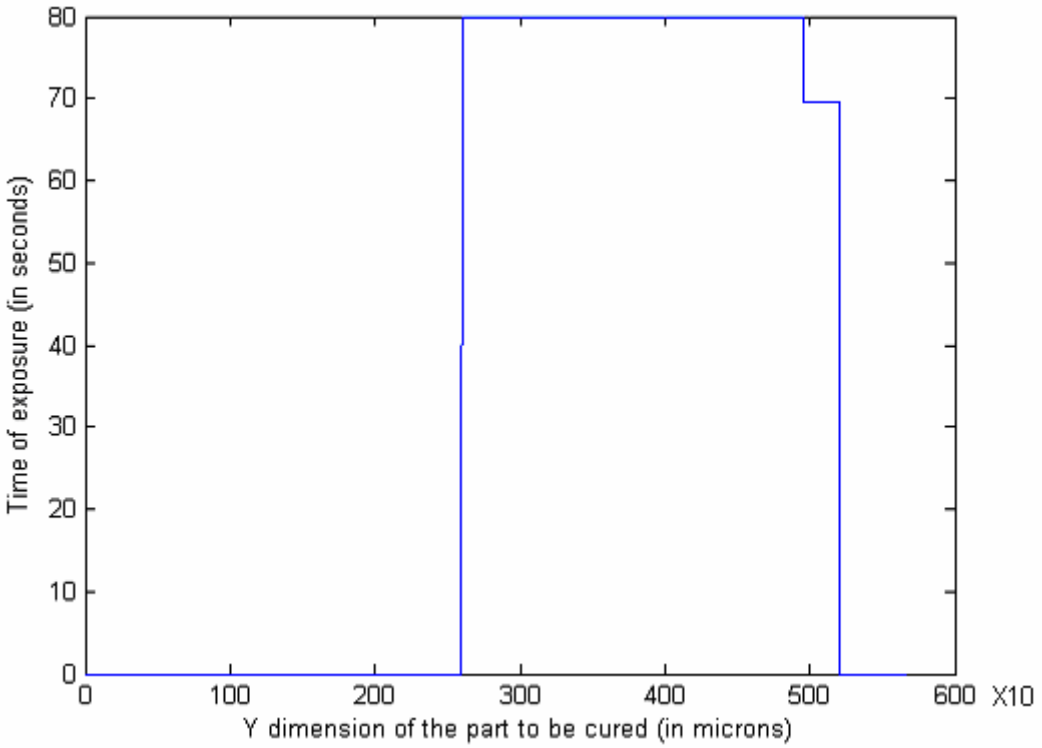

(d) Time of exposure supplied to cure the fourth layer

Figure 8.9 (continued)

The times of exposure for every layer are tabulated in Table 8.2.

Table8.2 Times of exposure for every layer

Layer # (Bottom most to top most)	**Time of exposure (s)**	
	Body of layer	Overhang of layer
Layer 1	80	27.2
Layer 2	80	57.4
Layer 3	80	68.6
Layer 4	80	69.6

The down facing profile of the part was simulated using the print through model for the times of exposure as shown in Figure 8.9. The simulated profile of the down facing surface is shown in Figure 8.10.

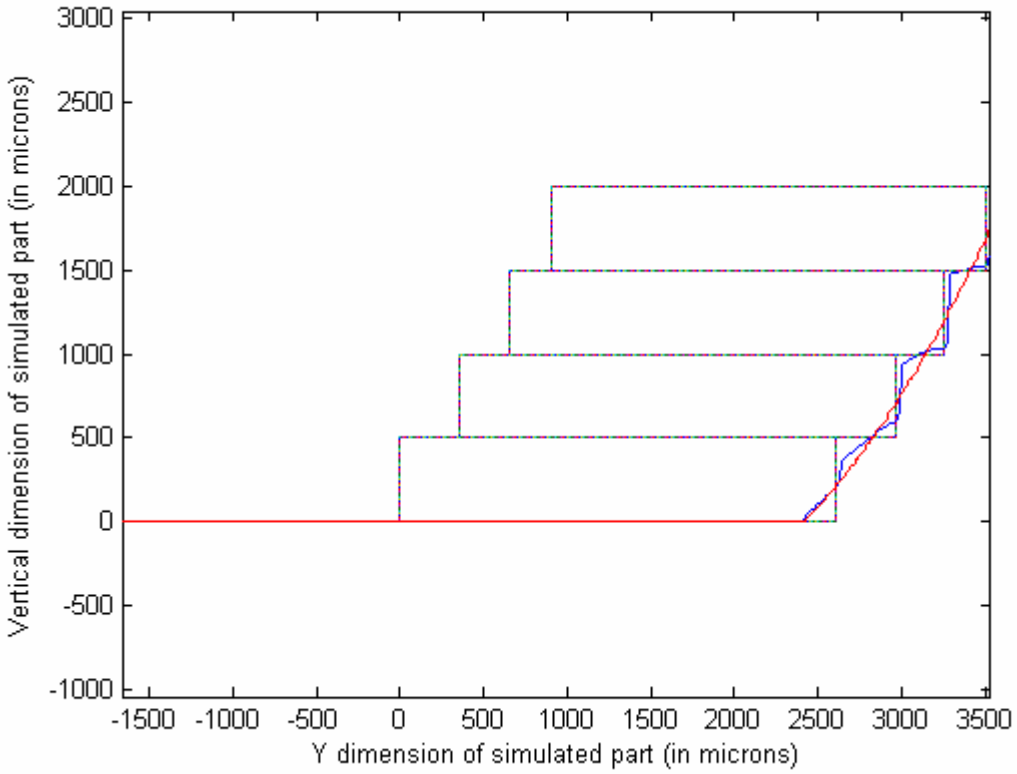

Figure 8.10 Simulated and ideal profiles of the down facing surface of the test part for the times of exposure as shown in Figure 8.9

In Figure 8.10, the blue line shows the simulated profile of the down facing surface of the part that would be built. The red line shows the ideal, quadratic profile.

8.4 Building the test part

The process plan generated in Sections 8.1 to 8.3 is used to build the part on the MPSLA system. The exposure of different portions of every layer for different times was achieved by splitting the bitmap generated in Figure 8.5 into two portions. These bitmaps were imaged onto the resin surface in succession to cure the layer, supply an exposure as given by the exposure plots presented in Figure 8.9. Thus, every layer is exposed in two steps. This process is pictorially shown in Figure 8.11.

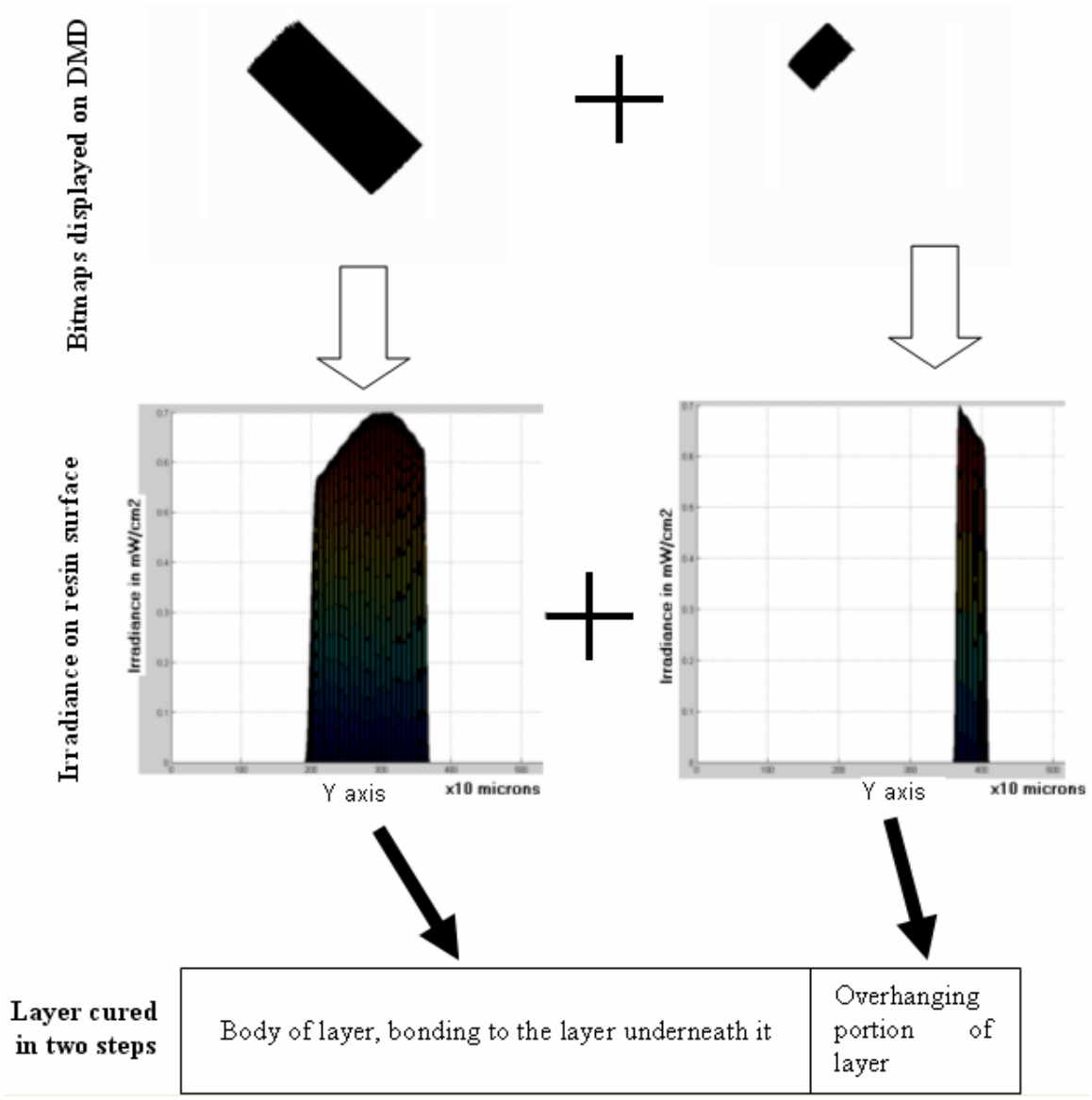

Figure 8.11 Curing every layer by imaging two bitmaps onto the resin surface in succession

The down facing profile of the part thus built is shown in Figure 8.12. In Figure 8.12, the dotted red line is the required profile given by equation 8.1. It can be seen that the down facing profile of the part cured approximate the required profile very well.

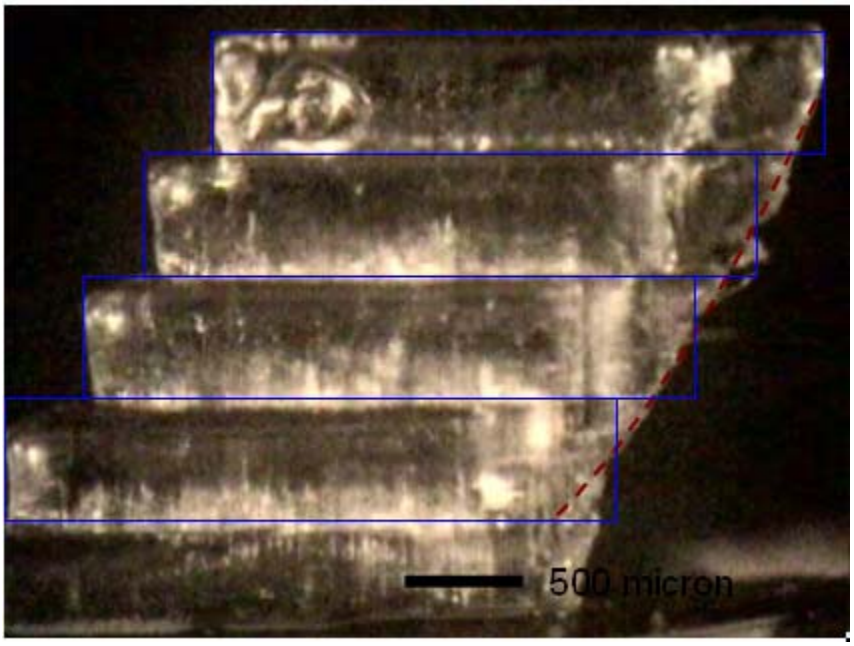

Figure 8.12 MPSLA part built by using the process plan developed in this chapter

The down facing surface profile of the simulated part presented in Figure 8.10 can be seen to be having noticeable stair steps. The cured part's down facing surface profile is exceptionally smooth. The stair steps are not visible at all. Thus, we observe again the same phenomenon of smoothing that we observed in Chapter 6, where the cured parts were significantly smoother than the simulated part. This is perhaps because of the semi cured resin lodging itself in between the stair steps of the cured part.

Another point to note is that adaptive exposure has not been applied for this case study. In spite of this, the down facing surface is exceptionally smooth. This is because, the profile of the part in Figure 8.12 has very little overhang. It is almost vertical. The Y dimensions of the steps on bottom-most layer to the top most layer are 220µm, 360µm, 290µm and 250µm respectively. For such small steps, there is not need of adaptive exposure. Also, we have seen in Chapter 7 that when the size of steps approaches 250µm, the part profile becomes exceedingly smooth.

Summary

A process planning method to build a part with constraints on dimensions, surface finish and build time is presented in Figure 8.1.The process planning method first slices the parts using the adaptive slicing algorithm presented in Chapter 7. The sliced part is built using Irradiance model and Compensation zone approach presented in Chapter 5 and 6 respectively. The process planning method is demonstrated on a test part with quadratic up facing and down facing surfaces.

Progress made towards answering the research questions

Research question 4 was concerning formulating a process planning method for MPSLA that would build a part with constraints on dimensions, surface finish and build time. The hypothesis was that the process planning should be performed in two steps. First, the CAD model is sliced so that the required trade off between surface finish of up facing surface of the part to be built and the build time is obtained. In the second step, the sliced part is to be built by using the Irradiance model and the Compensation zone approach.

In this chapter, the process planning method is formulated and demonstrated on a test part. The CAD model of the test part is sliced by using an adaptive slicing algorithm. This algorithm models the trade off between the objective of surface finish of up facing surfaces and that of build time as a compromise Decision Support Problem (cDSP). The multi objective optimization problem is solved by using a gradient projection optimization method. Bitmaps are generated for every layer of the sliced part using the "Bitmap generation method" (Chapter 5) and Compensation zone approach (Chapter 7). The part is successfully built on the MPSLA system by using the generated process plan.

CHAPTER 9 CLOSURE AND CONTRIBUTIONS

This chapter wraps up the dissertation. In Section 9.1, the entire work documented in this dissertation is summarized. In Section 9.2, the research questions posed in Chapter 4 are revisited and answered by testing the proposed hypotheses. The intellectual contributions of this work are enunciated in Section 9.3. The chapter ends with Section 9.4, which recommends the areas in which future work would be of value.

9.1 Summary of the dissertation

The objective in this research is to analyze the Mask Projection Stereolithography (MPSLA) process in order to formulate a process planning method which would enable the fabrication of dimensionally accurate 3D parts with constraints on build time and surface finish. In working towards attaining this objective, a Mask Projection Stereolithography system is designed and realized. The process of part building is modeled and the models are validated by building test parts on the MPSLA system. Optical models, that model the process of image formation on the resin surface when any bitmap displayed on the mask is imaged onto it, are formulated. The process of layer curing and the phenomenon of print through have also been modeled to understand the sources of errors in MPSLA builds. These models have been used in a process planning method to control the dimensional errors. The issue of obtaining a tradeoff between build time and surface finish of MPSLA builds has also been addressed and an algorithm that enables this tradeoff has also been presented.

Using the work presented in this dissertation, it is possible to build a MPSLA part with multiple constraints on dimensions, surface finish and build time.

9.1.1 MPSLA system designed and built

A Mask Projection Stereolithography system is designed and built as a part of this research. The design, including the bill of materials is documented in Chapter 3. A broadband UV lamp is used as the light source. A collimating system is designed, consisting of a pinhole and a converging lens, in order to collimate the light coming from UV lamp. This light is made incident onto a Digital Micromirror Device (DMD^{TM}), from Texas Instruments^{TM}, which acts as a dynamic mask. The DMD^{TM} consists of an array of individually addressable, bi-stable micro mirrors that can be selectively oriented to display any bitmap (pattern). The pattern is imaged onto a photopolymer resin contained in a vat using a 1X telecentric optical system. The optical system is designed to be telecentric because such systems are robust against variations in image and object distances. Layers are built on a platform which is mounted on an XYZ stage.

The MPSLA system is used to validate all the analytical models developed in this dissertation.

9.1.2 Modeling image formation

When any bitmap displayed on the DMD^{TM} is imaged onto the resin, an aerial image is formed on the resin surface. This aerial image is distorted due to the optical aberrations introduced by the imaging system and the diffraction effects. Due to these two phenomena, the irradiance distribution across the image is also not uniform. In order to build MPSLA parts of accurate dimensions, it is essential to model the irradiance that any point on the resin surface would receive when any given bitmap is imaged onto it. The modeling of image formation process has been presented in Chapter 5.

Two theories can be used to model image formation: the theory of physical optics, which assumes light to be traveling in the form of wave fronts; and the theory of geometric optics, which assumes light to be traveling as rays. The applicability of these theories is evaluated for the imaging module of the MPSLA system assembled as a part of this research. By performing aberration analysis, it is shown that the imaging system realized by the author is aberration limited as opposed to diffraction limited. In case of aberration limited optical systems, the diffraction effects are supposed to be ignored and geometric optics give accurate results. Thus, ray tracing is used to formulate the "Irradiance model" that models the irradiance across the resin surface, when any bitmap is imaged onto it. The Irradiance model has been validated by building test layers on the MPSLA system.

The Irradiance model, while high fidelity has a serious limitation, in that billions of rays need to be traced in order to run the model. This limitation has been tackled by adopting a multi-scale irradiance modeling strategy, in which modeling is done at two levels: micro-mirror level and bitmap level. At the micro-mirror level, the irradiance incident on the resin surface when every micro-mirror is individually imaged onto it is recorded and stored in a database. At the bitmap level, the irradiance distributions corresponding to all the 'ON' micro mirrors are mined from the database and combined to obtain the irradiance distribution on the resin surface when that bitmap is imaged onto it. This modeling strategy resulted in reduction in the computation time by a factor of 1/600.

9.1.3 Cure modeling

In Chapter 6, cure modeling is done at two levels. First, the thickness of the layer that would be cured when any bitmap is imaged onto the resin surface is modeled. Second, the print through that would result when multiple layers are cured over each other is modeled.

In Chapter 6, the transient model of layer curing is presented. This model takes into account the change in the rate of attenuation of light in the resin during exposure. It has been shown that, for large exposure times, cure depth is a linear function of exposure as opposed to being a logarithmic function. The transient layer cure model has been validated by building test layers on the MPSLA system.

The effect of diffusion of reactive species away from the bottom surface of a part being built has been quantified. When a MPSLA part is being built, reactive species are present at the bottom surface of the part, near the solid-liquid interface. These reactive species, in their excited state, carry a total energy equal to the threshold exposure of polymerization (E_c). When the part sits in the resin vat, these reactive species diffuse out carrying energy away with them. Also, oxygen from surrounding resin diffuses in and 'quenches' the excited species. Due to this, the effective exposure at the bottom surface of an MPSLA part drops down as a function of time. The rate of drop of effective exposure has been quantified in Chapter 6.

Chapter 6 also presents the "print through model", which computes the amount of print through that would occur when a multi-layered part is built. Print through is caused due to residual radiation penetrating beyond the intended layer thickness to the bottom surface of part, causing unwanted curing. The print through model is used to simulate the

profile of the down facing surface of a test four-layered part. The simulation is validated by building test parts on the MPSLA system.

The print through model is used to formulate the "compensation zone approach", which is essentially, the inverse of the print through model. The compensation zone approach enables the computation of process parameters that would result a part with the required down facing profile. The compensation zone approach is demonstrated successfully on a test part.

9.1.4 Improving surface finish of MPSLA builds

The compensation zone approach presented in Chapter 6 is validated by exposing the overhanging portion of a layer for time duration different from the duration time that its body was exposed. The method of adaptive exposure was proposed in Chapter 7. This method entailed discretizing the overhanging portion of every layer even more in order to better approximate the down-facing profile. This method was demonstrated on a test part.

The slicing of an MPSLA part influences its build time as well as its surface finish. Larger layer thicknesses result in shorter build times but poor surface finish, while smaller layer thicknesses result in smoother surfaces, but larger build times. It is essential to select a slicing scheme that would achieve a tradeoff between these two objectives.

A multi-objective slicing algorithm is formulated and demonstrated on a quadratic down facing surface in Chapter 7.

9.2 Revisiting the research questions

In this section, the research questions posed in Chapter 4 are revisited and the proposed hypotheses tested. The purpose of this research was to achieve the objective presented in Chapter 1, restated here:

"**To formulate a process planning method to build MPSLA parts with constraints on dimensions, surface finish and build time"**

This objective is broken down in Chapter 4 and research question and hypothesis are proposed for each of them. In light of the work presented in this thesis, the validity of these hypotheses is tested in this section.

Research Question 1a: Should the image formation process in the MPSLA system under consideration by modeled using physical optics or using geometric optics?

Hypothesis: The theory of geometric optics is more suitable than that of physical optics to model the image formation by the MPSLA system under consideration.

Testing the hypothesis: It has been determined from literature in optics that the Optical Path Difference (OPD) is the measure of the wave front aberrations and can be used as a guideline to choose the optical modeling method. The OPD of the imaging system of the MPSLA system was computed by modeled the system using the optical analysis software OSLO^{TM} to show that the imaging system is aberration limited.

The irradiance is modeled using ray-tracing algorithm as the "Irradiance model". This is the method of modeling an aberration limited optical system. The Irradiance model is validated by curing test layers on the MPSLA system. The close agreement in the dimensions of the cured layers and the dimensions of the aerial image formed on the

resin, computed by the Irradiance model, suggests that the Irradiance model is valid. Thus, the geometric optics has been used successfully to model the image formation process for the MPSLA system. Thus, the hypothesis has been tested and has been found to be valid.

Research Question 1b: How to model the exposure profile on the resin surface with the fidelity of the ray tracing approach, in a computationally inexpensive way?

Hypothesis: A multi scale modeling approach can be adopted. The irradiance profile can be thought of as a collection of pixels overlapping each other. Modeling should be done at two levels:

1. Curing of individual pixels (computationally expensive part)
2. Overlapping of pixels to give the exposure profile on the resin surface (computationally inexpensive part)

Testing the hypothesis: The "Pixel image model" has been formulated in Chapter 5. This models the irradiance on the resin surface when every micro-mirror is imaged individually onto it. The irradiance is stored as a matrix. This database is used to model the irradiance on the resin surface when a test bitmap was imaged onto it. The computation of the irradiance entailed simply choosing the pixels (irradiance matrices) corresponding to the 'ON' micro mirrors from the Pixel image database, and adding them up. The time to compute the irradiance computation created by a test bitmap without using the pixel image database was found to be 152 hours. Using the Pixel image database, the same irradiance distribution could be generated in less than 15 minutes.

Thus, the multi-scale modeling approach resulted in significant savings in the computation time. Thus validates the hypothesis to research question 1b.

Research Question 2: How to reduce print through errors in MPSLA builds?

Hypothesis: Print through errors can be reduced by subtracting a tailored volume (compensation zone) from underneath the CAD model which is used to build the part, in such a way that the exposure received by the down facing surface of the part is exactly equal to the threshold exposure of polymerization (E_c).

This research question was further broken down into two sub-questions in the course of this research. We test the hypotheses to these sub-research questions before testing the hypothesis to research questions 2.

Research Question 2a: How to capture the effect of the varying rate of radiation attenuation throughout the duration of exposure, as a layer gets cured?

Hypothesis: The effect of varying rate of attenuation as a layer gets cured can be captured by modeling layer curing as a transient phenomenon, by discretizing the time domain.

Testing the hypothesis: In Chapter 6, the incremental curing that would occur during an infinitesimal duration of time is modeled as a differential equation. This equation takes into account the different rate of attenuation through a cured layer and the uncured resin underneath that layer. The differential equation is solved numerically to obtain an almost linear relationship between cure depth and exposure. This linear relationship is validated by building test layers on the MPSLA system. The values of the constants of this linear

curve between cure depth and exposure are determined experimentally. Thus, layer curing has been successfully modeled as a transient process and this model has been validated. This successfully tests the hypothesis to research question 2a.

Research Question 2b: Is exposure at the bottom surface of a cured layer additive or does it get significantly affected by diffusion of radicals and oxygen into the resin vat?

Hypothesis: The exposure is not additive because there is a significant diffusion of radicals and oxygen in the resin vat.

Testing of hypothesis: The loss energy due to diffusion of radicals and oxygen underneath the bottom surface of a cured layer is assumed to be a factor k times the energy at the bottom surface of the layer when it was just cured (E_c). Layers were cured using two discrete exposure doses and allowing the layer to stay in the resin for a variable duration of time in between these two exposure doses. The value of '*k'* was found out by measuring the thickness of the layer cured after receiving both the exposure doses. The relationship between k and the time that the layer was allowed to stay in the resin in between the two exposures was found to be logarithmic. Thus, the loss of energy from underneath the bottom of a cured layer varies as the logarithm of time. This is typical of the diffusion phenomenon. This lends strong evidence that there is a loss of effective exposure from the bottom surface of a part being built due to a diffusion based phenomenon (most likely the diffusion of reactive species and oxygen molecules) thereby making the additive nature of exposure a strong function of time.

Now, we can revisit the hypothesis to research question 2. In Chapter 6, the "Print through model is formulated using the models developed in testing hypotheses 2a and 2b.

The print through model computes the print through that would occur underneath a multi-layered MPSLA build. This model is used to compute the reduced time of exposure for which the lower most layers of an MPSLA build must be exposed. When the lower most layer is exposed for a lesser duration of time, the effect is the same as subtracting a tailored volume from underneath the CAD model to be built. The compensation zone approach has been demonstrated on a test part.

Research question 3: How to implement the print through smoothing approach to obtain smoother down facing surfaces in MPSLA builds?

Hypothesis: Print through smoothing can be achieved by gray scaling the pixels near the edges of a layer to cure voxels of different heights that conform to the part's vertical profile. This method shall be called as "adaptive exposure" since it involves adapting the exposure to suit the part's vertical profile.

Testing the hypothesis: The adaptive exposure method entails modulating the exposure at the edges of the layers in such a way that profile of the edges confirm to the part's down facing vertical profile. This method has been demonstrated in Chapter 7. Exposure has been modulated at the edges by using three bitmaps to cure every layer. The improvement in surface finish is demonstrated by building a part without adaptive exposure (Chapter 6) and with adaptive exposure (Chapter 7).

Research Question 4: How to build a MPSLA part with multiple objectives of dimensional accuracy, surface finish and build time?

Hypothesis: Process planning can be done in two steps. First, a multi-objective optimization method, like the compromise DSP (Mistree et al., 1994) should be formulated and solved to select the slicing scheme, i.e. layer thicknesses that would obtain a tradeoff between the objectives of surface finish and build time. For this slicing scheme, the compensation zone approach should be adopted to obtain part with accurate vertical dimensions

Testing the hypothesis: The process planning method to build a MPSLA part with constraints on dimensions, surface finish and build time is presented in Figure 8.1. The process planning method first slices the CAD model to be built by adopting the adaptive slicing algorithm presented in Chapter 7. The compensation zone approach (Chapter 6) and Irradiance model (Chapter 5) is then used to build the sliced part. The process planning method is demonstrated on a part with quadratic up- and down facing surfaces in Chapter 8.

9.3 Contributions

The contributions made by this work can be characterized into two categories:

1. Contributions to fundamental knowledge in Stereolithography; and
2. Developmental contributions

9.3.1 Contribution to fundamental knowledge

Process planning literature available for the conventional laser scanning Stereolithography allows a manufacturer to build prototypes with the required properties. This literature can't be directly extended to Mask Projection micro Stereolithography because the nature of irradiation of the resin surface and curing characteristics of a resin

are considerably different in both the cases. The primary contributions of this work are in the realm of analyzing the MPμSLA process and explaining it in mathematical terms. The following are the contributions of the thesis to the field of MPμSLA:

The irradiation of the resin surface in the case of MPμSLA is a much more complex process than that achieved by laser scanning. While the laser beam has a Gaussian irradiance profile, which remains constant regardless of the cross section it is scanning, in case of MPμSLA, the irradiation distribution changes with the change in the pattern imaged. The method of modeling irradiance on the resin surface in a computationally feasible manner is the first contribution on this work.

The transient model is more rigorous than the conventional Stereolithography cure model, which assumes that the entire energy is delivered to the resin in one instant and that the light gets attenuated exponentially according to the Beer Lambert's law. The transient model takes into account the variation in the rate of attenuation of light during exposure. This model has been formulated and validated on the MPSLA system.

The effect of diffusion of reactive species away from, and oxygen towards, the bottom surface of a part being built has also been quantified for the first time (radical diffusion model). Standard Stereolithography texts ignore these diffusion phenomena and treat exposure to be additive. The author has shown that there is a fall in the energy at the bottom surface of a MPSLA part being built due to diffusion and has quantified the rate of loss of this energy.

The transient layer cure model and the radical diffusion model have been used to model the print through that would result when a multi layered part is built. This model is used to formulate the compensation zone approach, which enables the avoiding of print

through errors. The compensation zone approach, which deals with the tailoring of process parameters in order to avoid print through errors, is also presented for the first time in Stereolithography literature.

It is for the first time that print through smoothing has been demonstrated to approximate the vertical profile of the part, by adaptive exposure.

9.3.2 Developmental contributions

Apart from the intellectual contributions, there are a number of contributions of a developmental nature. An MPSLA system has been successfully realized. The design of the system has been documented, which will enable replication of this system.

A slicing algorithm that computes the optimum slicing scheme that achieves a tradeoff between build time and surface finish has been formulated. This algorithm can be used not just for Stereolithography, but also for any additive manufacturing process.

A process planning method that would guide a manufacturer through all steps of process planning, starting from the CAD model and ending with a finished part has been formulated.

9.4 Future work

Future work is needed from the view of bolstering confidence in the models and process planning methods presented in this thesis.

The transient layer cure model developed in Chapter 6 predicts a linear relationship between cure depth and exposure, for long durations of exposure. This model has been validated by building layers in the DSM SOMOS 10120^{TM} resin. It will be useful to validate this model on other resins.

The MPSLA system could repeatedly lay down layers only as thick as 500μm. Layers thinner than that could not be laid down with confidence. As a result, all the multi layered parts built presented in this dissertation have been built using 500μm thick layers. It would be useful to validate the compensation zone approach for layers of thicknesses smaller than 500μm. It should be noted that the compensation zone approach is based upon the transient layer cure model and the diffusion mode, both of which have been validated for cure depths starting at around 70μm. So, the compensation zone approach is definitely expected to work well at smaller layer thicknesses, even though an actual demonstration would increase confidence in it.

All the multi layered parts cured have been observed to be significantly smoother down facing surface than those predicted by the simulations. The author surmises that the smoothing is because of partially cured resin lodging itself between the stair steps. This claim however has not been validated. It would be of value of conclusively explain the cause behind the smoothing of down facing surfaces.

Future work is needed towards improving the MPSLA system. The imaging module of the current MPSLA system is severely aberration limited. This limits the size of the bitmap that can be imaged onto the resin surface within reasonable distortions. The imaging system can be made more sophisticated by introducing more number of optical components, so that aberrations can be reduced and the field of exposure can be increased.

The author has used a commercial Stereolithography resin (DSM SOMOS 10120) with his system. This resin has a very high value of depth of penetration (D_p), i.e. very low rate of attenuation of radiation. For micro applications, a resin which would result in

rapid attenuation of radiation, and hence thinner layer should be used. Another limitation of using DSM SOMOS 10120 is its high viscosity (120 cP). This high viscosity prohibits laying down of very thin films of resin. A resin with lower viscosity would enable laying down of much thinner layers.

APPENDIX A. VALIDATION OF IRRADIANCE MODEL

In this appendix, the test layers cured to validate the irradiance model formulated in Chapter 5 are presented. In all, eight cross shaped layers were cured by imaging a test bitmap onto the resin surface. The dimensions of these layers were measured and compared with the dimensions of the irradiance profile returned by the irradiance model.

The dimensions of the layers are recorded in Table 5.1.

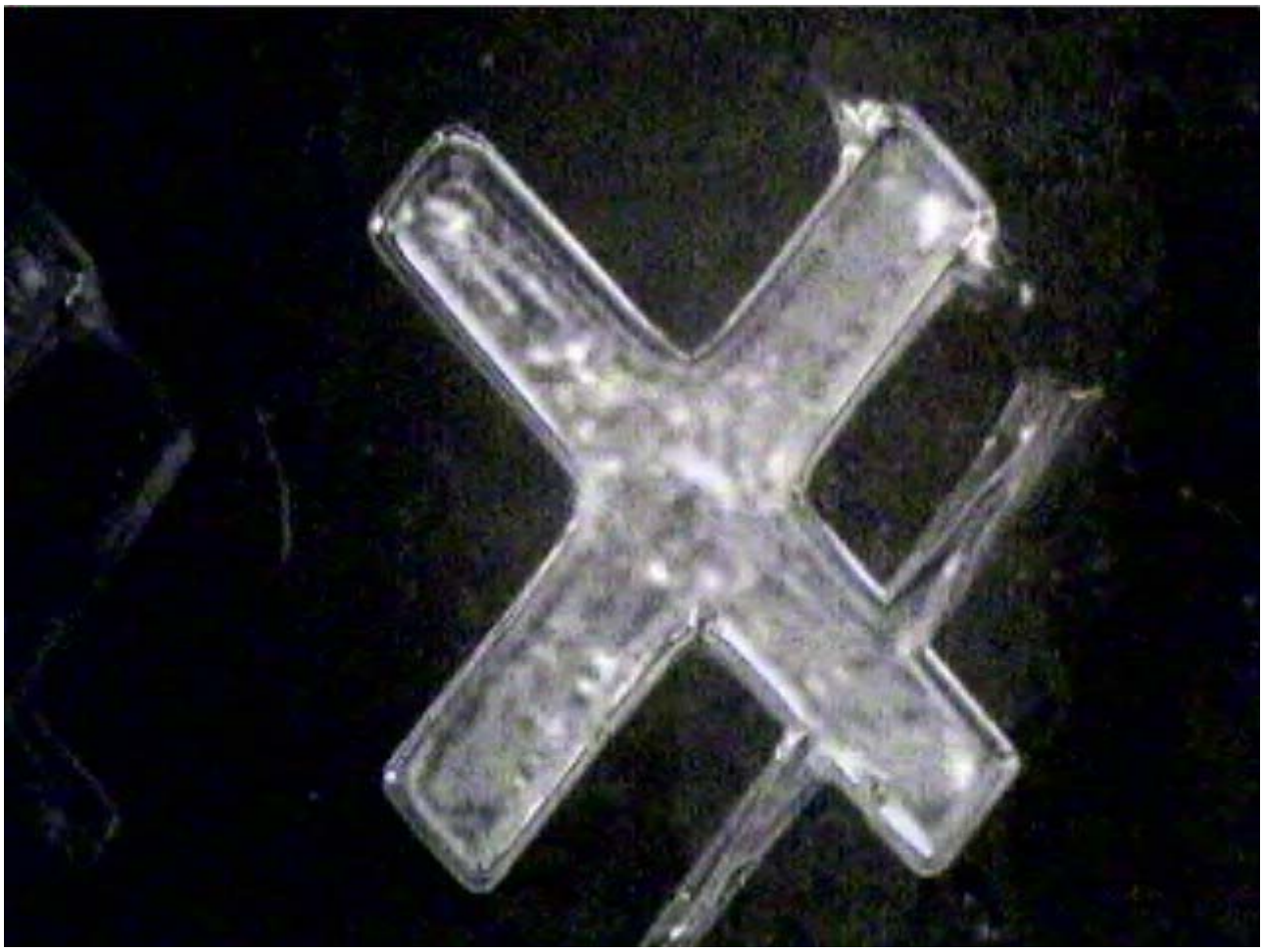

Figure A. 1 Validating irradiance model: Test layer 1

Figure A. 2 Validating irradiance model: Test layer 2

Figure A. 3 Validating irradiance model: Test layer 3

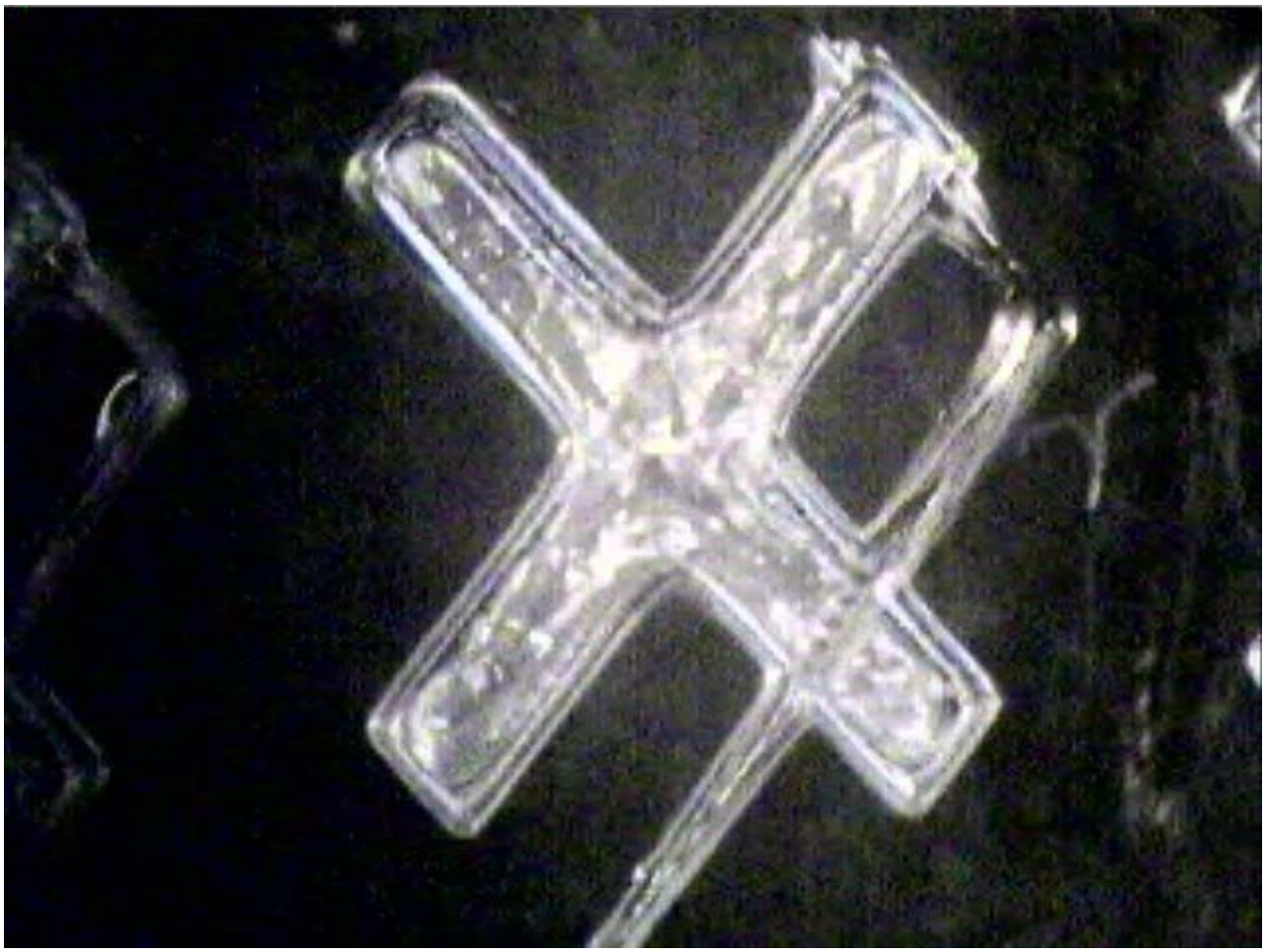

Figure A. 4 Validating irradiance model: Test layer 4

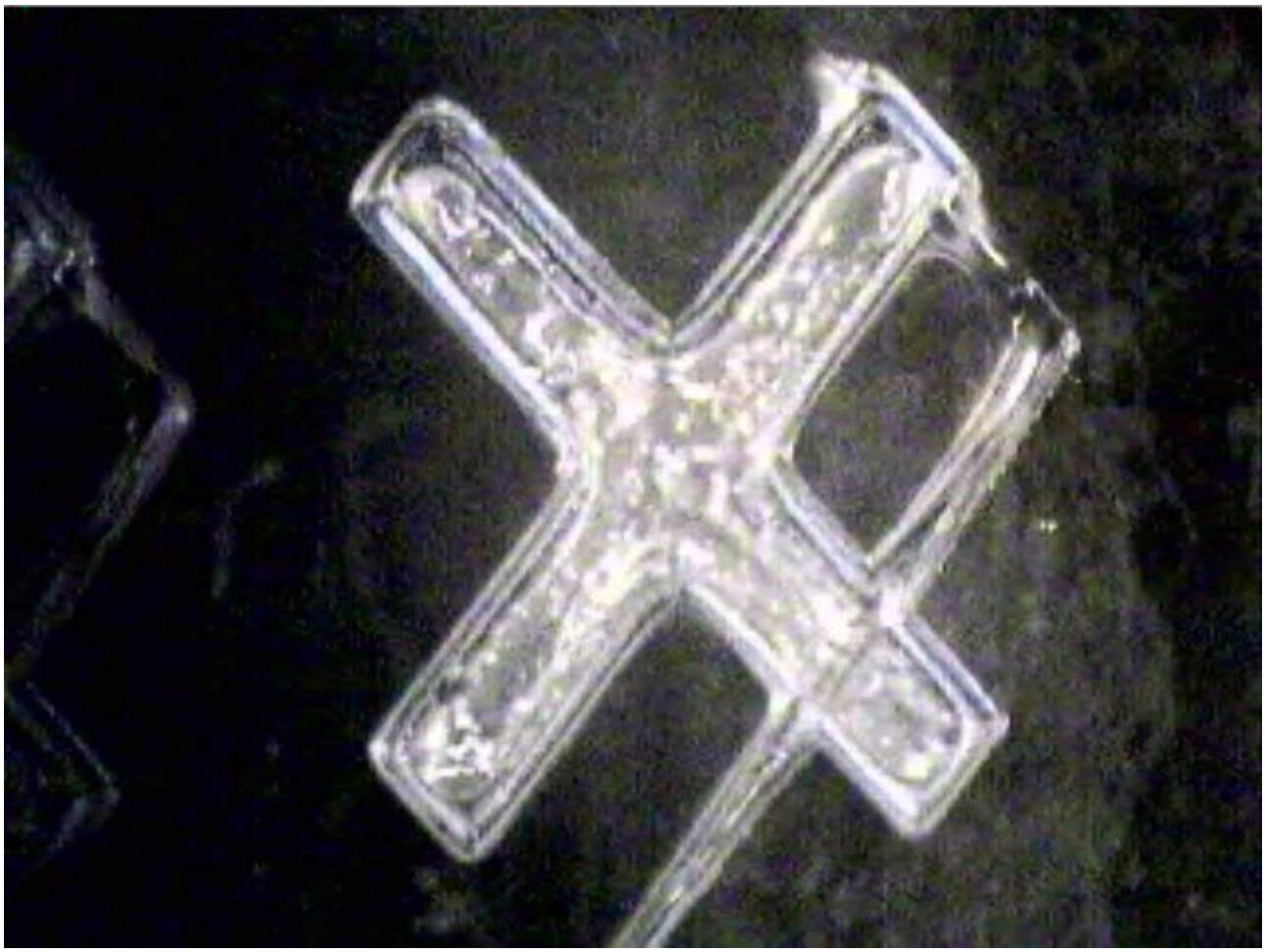

Figure A. 5 Validating irradiance model: Test layer 5

Figure A. 6 Validating irradiance model: Test layer 6

Figure A. 7 Validating irradiance model: Test layer 7

Figure A. 8 Calibration scale for measuring the dimensions of the test layers

Figure A. 9 Validating irradiance model: Test layer 8

APPENDIX B. MATLAB CODE FOR IMPLEMENTING MULTI-SCALE IRRADIANCE MODEL

In Appendix B.1, the Matlab code written to populate the pixel mapping database is presented. In Appendix B.2addition, the Matlab code that uses the pixel mapping database in order to compute the irradiance distribution on the resin surface when a bitmap is imaged onto it is documented.

Appendix B.1. Code to generate pixel mapping database

This code consists of the script: "massivedatabase.m", which computes the locations of the various 'ON' micromirrors on the DMD in 3D space. This code then employs, at every micromirror, the function "pointselector.m", which meshes every micromirror with 121 points. The function "pointselector.m", for every point on the micromirror, then calls the function "psf.m", which computes the direction cosines from every micromirror, along which a ray can be traced. The function "psf.m", in turn, calls the function "raytrace.m" which traces a ray from the given point, on a given micromirror, in a given direction through the imaging system.

These four Matlab codes are presented here.

massivedatabase.m

```
%Code to create the massive database
clear all;
for i = 1:1:300;
    for j = 1:1:300;
        tempi = i-150;
        tempj = j-150; %This is the first row
        Z1 = tempi*0.01365;
        Y1 = tempj*0.01365;
        clear tempi;
        clear tempj;
        Z2 = Z1*cos(45*pi/180) - Y1*sin(45*pi/180);
        Y2 = Z1*sin(45*pi/180) + Y1*cos(45*pi/180);%Rotating about X
axis
```

```
        clear Z1;
        clear Y1;
        %Now we rotate by 35 degrees about the Y axis
        Y(i,j) = Y2;
        Z(i,j) = Z2*cos(35*pi/180);
        clear Y2;
        clear Z2;
    end
end
clear i;
database = zeros(601,601);
for i = 1:1:300;
    for j = 1:1:50;
        database = pointselector(Z(i,j), Y(i,j));
        save (strcat('database', (int2str(i)), '.', (int2str(j)),
'.mat')),database;
        database = zeros(601,601);
    end
end
```

pointselector.m

```
%This code is used to select points on a given micromirror.
%The micromirror location is specified by its coordinates. Then, points
are
%selected on this micromirror. Rays are traced from every point using
the
%function "psf" defined seperately. psf returns the localresincount
matrix.
%We shall all that matrix to the mirrorresincount matrix, which is
%initialized to be full of zeros.

function [mirrorresincount] = pointselector(midpointz, midpointy)
meshpoints = 9;
midpointx = midpointz*tan(35*pi/180);
y0 = midpointy;
z0 = midpointz-0.0080948;

%Now, the coordinates of the midpoint of the micromirror of interest
have
%been obtained. Now, selecting the points on this micromirror.
mirrorresincount = zeros(601,601);
i = 1;
%Now, selecting the points
for l1 = 0:0.0109552/meshpoints:0.0109552;
    for l2 = 0:0.0109552/meshpoints:0.0109552;
        mirrorpointy(i) = (l1-l2)*0.8165 + y0;
        mirrorpointz(i) = (l1+l2)*0.5773 + z0;
        mirrorpointx(i) = ((mirrorpointz(i)-
midpointz)*tan(45*pi/180))+midpointx;
        mirrorresincount = mirrorresincount + psf(mirrorpointx(i),
mirrorpointy(i), mirrorpointz(i));
        i = i+1;
    end
end
```

psf.m

```
%Code written to compute the Point Spread Function (PSF)

%Code will trace rays from one point through the tleecentric imagign
%system. Rays are emitted in a cone. It is assumed that all these rays
have
%the same amount if energy. The cone angle is the variable.
%This code uses the function "raytrace" to trace rays from a given
point in a given direction. "Raytrace" which is defined seperately.
%**********************************************************************
****

%The number of rays from the point (pointx,pointy,pointz) hitting every
%small square in the resindatabase is counted and stored in the counter
%localraycount(y,z).
%For example, localraycount(1,1) will denote the square centered at (-
4.5,-4.5).
%localresincount, because it is going to measure only the rays in this
%function. Later the contents of local raycount will be transferred to
the
%matrix resincount, which shall be in the code that selects points on
the
%micromirror.
function[localresincount] = psf(pointx,pointy,pointz);

%Start point is 0,0,0

raycount = 1;
pupildistance = 100; %Entrance pupil at 100mm from start point
theta = 1.5;  %Half angle of cone. Makes pupil radius = 5mm
pupilradius = pupildistance*theta*pi/180;

for i = -pupilradius:pupilradius/15:pupilradius;
   for j = -pupilradius:pupilradius/15:pupilradius;
      if  sqrt(i^2+j^2) <= pupilradius;
            Y(raycount) = (pointy-i)/sqrt((i-pointy)^2+(j-
pointz)^2+(pupildistance-pointx)^2);
            Z(raycount) = (pointz-j)/sqrt((i-pointy)^2+(j-
pointz)^2+(pupildistance-pointx)^2);
            X(raycount) = (pupildistance-pointx)/sqrt((i-pointy)^2+(j-
pointz)^2+(pupildistance-pointx)^2);
            check(raycount) =
Y(raycount)*Y(raycount)+Z(raycount)*Z(raycount)+X(raycount)*X(raycount)
;
            [resiny(raycount), resinz(raycount)] = raytrace(pointx,
pointy, pointz, X(raycount), Y(raycount), Z(raycount));
            phi(raycount) = atan((sqrt(i^2+j^2))/pupildistance);
            weight(raycount) = 1*cos(phi(raycount))*cos(phi(raycount));
            if resiny(raycount) == 1000;
               raycount = raycount - 1;
            end
            raycount = raycount + 1;
        end
```

```
    end
 end

 sizey = max(size(resiny));
 if sizey == raycount
    resiny(raycount) = [];
    resinz(raycount) = [];
    weight(raycount) = [];
 end

clear i;
clear j;

%Now, we count the rays in the tiny squares that the resin surface is
%discretized into. The squares are 10 micron each. The extents of the
%resin are from -3 to +3 mm. The number of divisions will be (6/0.01 +
1) = 601
localresincount = zeros(601,601);
for i = 1:1:sizey-1;
    localy = int16(((resiny(i)+3)/0.01))+1;
    localz = int16(((resinz(i)+3)/0.01))+1;
    localresincount(localz,localy) = localresincount(localz,localy)+1;
end
```

raytrace.m

```
%Function to trace a single ray from a given point in a given direction
%Written by Ameya Limaye on May 19 2006

function[y6,z6]= raytrace(x1,y1,z1,X1,Y1,Z1)
x(1) = x1;
y(1) = y1;
z(1) = z1;
X(1) = X1;
Y(1) = Y1;
Z(1) = Z1;
%Inputting the system parameters
c(1) = 0; % c is the curvature of surface
c(2) = 0.028;
c(3) = -0.028;
c(4) = 0.028;
c(5) = -0.028;
c(6) = 0;
t(1) = 36.65-x1; %t is the distance
t(2) = 6.7;
t(3) = 73.3;
t(4) = 6.7;
t(5) = 36.65;
N(1) = 1; %N is the refractive index
N(2) = 1.46;
N(3) = 1;
N(4) = 1.46;
N(5) = 1;
aperture = 1; %Aperture stop = 2mm radius
```

```
%Now, tracing the ray from x1,y1,z1 in direction X1, Y1, Z1

i = 2;
%Transfer equations
e(i) = t(i-1)*X(i-1) - (x(i-1)*X(i-1) + y(i-1)*Y(i-1) + z(i-1)*Z(i-1));
Mx(i) = x(i-1) + e(i)*X(i-1) - t(i-1);
Msquare(i) = x(i-1)^2 + y(i-1)^2 + z(i-1)^2 - e(i)^2 + t(i-1)^2 -
2*t(i-1)*x(i-1);
E(i) = sqrt(X(i-1)^2 - c(i)*(c(i)*Msquare(i) - 2*Mx(i)));
L(i) = e(i) + (c(i)*Msquare(i) - 2*Mx(i))/(X(i-1)+E(i));
x(i) = x(i-1) + L(i)*X(i-1) - t(i-1);
y(i) = y(i-1) + L(i)*Y(i-1);
z(i) = z(i-1) + L(i)*Z(i-1);

%Refarction equations
 Edash(i) = sqrt(1- ((N(i-1)/N(i))^2) * (1-E(i)^2));
g(i) = Edash(i) - ((N(i-1)/N(i)))*E(i);
X(i) = (N(i-1)/N(i))*X(i-1) - g(i)*c(i)*x(i) + g(i);
Y(i) = (N(i-1)/N(i))*Y(i-1) - g(i)*c(i)*y(i);
Z(i) = (N(i-1)/N(i))*Z(i-1) - g(i)*c(i)*z(i);


clear i;
i = 3;

%Transfer equations
e(i) = t(i-1)*X(i-1) - (x(i-1)*X(i-1) + y(i-1)*Y(i-1) + z(i-1)*Z(i-1));
Mx(i) = x(i-1) + e(i)*X(i-1) - t(i-1);
Msquare(i) = x(i-1)^2 + y(i-1)^2 + z(i-1)^2 - e(i)^2 + t(i-1)^2 -
2*t(i-1)*x(i-1);
E(i) = sqrt(X(i-1)^2 - c(i)*(c(i)*Msquare(i) - 2*Mx(i)));
L(i) = e(i) + (c(i)*Msquare(i) - 2*Mx(i))/(X(i-1)+E(i));
x(i) = x(i-1) + L(i)*X(i-1) - t(i-1);
y(i) = y(i-1) + L(i)*Y(i-1);
z(i) = z(i-1) + L(i)*Z(i-1);

%Refarction equations
 Edash(i) = sqrt(1- ((N(i-1)/N(i))^2) * (1-E(i)^2));
g(i) = Edash(i) - ((N(i-1)/N(i)))*E(i);
X(i) = (N(i-1)/N(i))*X(i-1) - g(i)*c(i)*x(i) + g(i);
Y(i) = (N(i-1)/N(i))*Y(i-1) - g(i)*c(i)*y(i);
Z(i) = (N(i-1)/N(i))*Z(i-1) - g(i)*c(i)*z(i);

clear i;
i = 4;

%Transfer equations
e(i) = t(i-1)*X(i-1) - (x(i-1)*X(i-1) + y(i-1)*Y(i-1) + z(i-1)*Z(i-1));
Mx(i) = x(i-1) + e(i)*X(i-1) - t(i-1);
Msquare(i) = x(i-1)^2 + y(i-1)^2 + z(i-1)^2 - e(i)^2 + t(i-1)^2 -
2*t(i-1)*x(i-1);
E(i) = sqrt(X(i-1)^2 - c(i)*(c(i)*Msquare(i) - 2*Mx(i)));
L(i) = e(i) + (c(i)*Msquare(i) - 2*Mx(i))/(X(i-1)+E(i));
x(i) = x(i-1) + L(i)*X(i-1) - t(i-1);
```

```
y(i) = y(i-1) + L(i)*Y(i-1);
z(i) = z(i-1) + L(i)*Z(i-1);

%Refarction equations
 Edash(i) = sqrt(1- ((N(i-1)/N(i))^2) * (1-E(i)^2));
g(i) = Edash(i) - ((N(i-1)/N(i)))*E(i);
X(i) = (N(i-1)/N(i))*X(i-1) - g(i)*c(i)*x(i) + g(i);
Y(i) = (N(i-1)/N(i))*Y(i-1) - g(i)*c(i)*y(i);
Z(i) = (N(i-1)/N(i))*Z(i-1) - g(i)*c(i)*z(i);

%Check if the ray passes through the aperture stop
if (((y(3)+y(4))/2)^2 + ((z(3)+z(4))/2)^2)<= aperture^2
    clear i;
    i = 5;

    %Transfer equations
    e(i) = t(i-1)*X(i-1) - (x(i-1)*X(i-1) + y(i-1)*Y(i-1) + z(i-1)*Z(i-
1));
    Mx(i) = x(i-1) + e(i)*X(i-1) - t(i-1);
    Msquare(i) = x(i-1)^2 + y(i-1)^2 + z(i-1)^2 - e(i)^2 + t(i-1)^2 -
2*t(i-1)*x(i-1);
    E(i) = sqrt(X(i-1)^2 - c(i)*(c(i)*Msquare(i) - 2*Mx(i)));
    L(i) = e(i) + (c(i)*Msquare(i) - 2*Mx(i))/(X(i-1)+E(i));
    x(i) = x(i-1) + L(i)*X(i-1) - t(i-1);
    y(i) = y(i-1) + L(i)*Y(i-1);
    z(i) = z(i-1) + L(i)*Z(i-1);

    %Refarction equations
     Edash(i) = sqrt(1- ((N(i-1)/N(i))^2) * (1-E(i)^2));
    g(i) = Edash(i) - ((N(i-1)/N(i)))*E(i);
    X(i) = (N(i-1)/N(i))*X(i-1) - g(i)*c(i)*x(i) + g(i);
    Y(i) = (N(i-1)/N(i))*Y(i-1) - g(i)*c(i)*y(i);
    Z(i) = (N(i-1)/N(i))*Z(i-1) - g(i)*c(i)*z(i);

    clear i;
    i = 6;
    %Transfer equations
    e(i) = t(i-1)*X(i-1) - (x(i-1)*X(i-1) + y(i-1)*Y(i-1) + z(i-1)*Z(i-
1));
    Mx(i) = x(i-1) + e(i)*X(i-1) - t(i-1);
    Msquare(i) = x(i-1)^2 + y(i-1)^2 + z(i-1)^2 - e(i)^2 + t(i-1)^2 -
2*t(i-1)*x(i-1);
    E(i) = sqrt(X(i-1)^2 - c(i)*(c(i)*Msquare(i) - 2*Mx(i)));
    L(i) = e(i) + (c(i)*Msquare(i) - 2*Mx(i))/(X(i-1)+E(i));
    x(i) = x(i-1) + L(i)*X(i-1) - t(i-1);
    y(i) = y(i-1) + L(i)*Y(i-1);
    z(i) = z(i-1) + L(i)*Z(i-1);

    x6 = x(6);
    y6 = y(6);
    z6 = z(6);
else
    x6 = 1000;
    y6 = 1000;
    z6 = 1000;
end
```

```
clear i;
```

Appendix B.2. Code to use generate pixel mapping to compute irradiance distribution

The name of the Matlab code which computes the irradiance distribution using the pixel-mapping database is "bitmap_read_database.m". This code takes in the bitmap as an input and mines the irradiance distribution corresponding to every black, i.e. 'ON' pixel. These irradiance distributions are added together to obtain the irradiance distribution.

bitmap_read_database.m

```
%This is the code to get a bitmap and then use the Pixel Image Database
to
%populated the irradiance distribution.
%Code written by Ameya on April 29th
clear all;
bitmap_matrix = imread('C:\Ameya\JournalPaper3\Generating
bitmaps\layer_bitmap_GT.bmp','BMP');
irradiance_body = zeros(601,601);
for i = 1:1:300
    for j = 1:1:100
        if bitmap_matrix(i,j) == 0
           load (strcat('Database300.1to100\database', (int2str(i)),
'.', (int2str(j)), '.mat'))
           irradiance_body = irradiance_body + database;
           clear database;
           clear Z;
           clear Y;
        end
    end
end


for i = 1:1:300
    for j = 101:1:200
        if (bitmap_matrix(i,j) == 0)
           load (strcat('Database300.101to200\database', (int2str(i)),
'.', (int2str(j)), '.mat'))
           irradiance_body = irradiance_body + database;
           clear database;
           clear Z;
           clear Y;
        end
```

```
    end
end



for i = 1:1:300
    for j = 201:1:300
        if bitmap_matrix(i,j) == 0
           load (strcat('Database300.201to300\database', (int2str(i)),
'.', (int2str(j)), '.mat'))
           irradiance_body = irradiance_body + database;
           clear database;
           clear Z;
           clear Y;
        end
    end
end

for i = 1:1:601;
    for j = 1:1:601;
        for k = 1:1:2;
            B(i,j,k) = irradiance_body(i,j);
        end
    end
end

A = smooth3(smooth3(B));
irradiance = A(:,:,1);
for i = 1:1:601;
    X(i) = 10*i-10;
end
factor = 0.7/max(max(irradiance));
irradiance = irradiance*factor;
plot(X,max(irradiance));
AMEYA = 100

clear bitmap_matrix

irradiance_strip = zeros(601,601);
bitmap_matrix = imread('C:\Ameya\JournalPaper3\4 layer linear part 500
layer thick_ AT EDGE\strip1.bmp','BMP');
for i = 1:1:300
    for j = 1:1:100
        if bitmap_matrix(i,j) == 0
           load (strcat('Database300.1to100\database', (int2str(i)),
'.', (int2str(j)), '.mat'))
           irradiance_strip = irradiance_strip + database;
           clear database;
           clear Z;
           clear Y;
        end
    end
end
```

```
for i = 1:1:300
    for j = 101:1:200
        if bitmap_matrix(i,j) == 0
           load (strcat('Database300.101to200\database', (int2str(i)),
'.', (int2str(j)), '.mat'))
           irradiance_strip = irradiance_strip + database;
           clear database;
           clear Z;
           clear Y;
        end
    end
end

for i = 1:1:300
    for j = 201:1:300
        if bitmap_matrix(i,j) == 0
           load (strcat('Database300.201to300\database', (int2str(i)),
'.', (int2str(j)), '.mat'))
           irradiance_strip = irradiance_strip + database;
           clear database;
           clear Z;
           clear Y;
        end
    end
end
```

APPENDIX C. MATLAB CODE TO IMPLEMENT INVERSE IRRADIANCE MODEL

In this Appendix, the Matlab code "element_micromirror_mapping" is presented. This code meshes the layer to be cured with 10μmX10μm squares. Then, for every element that is at the center of any pixel in the pixel-mapping-database, it designates the corresponding micro-mirror on the DMD 'ON'. Once the micro-mirrors to be turned 'ON' are known, the bitmap is generated by making every corresponding pixel black.

element_micromirror_mapping.m

```
%Code to map the a layer ont oa bitmap using the lement database
%Code writen by Ameya on 3rh May
%***************************%
%This code takes in an element. Then, it sees if it is at the center of
any
%micromirror. It goes to every micromirror and sees inf the element of
%interest is at its center. Very long, inefficient algorithm:(

clear all
load 'elements.mat'
bitmap_matrix = imread('strip.bmp')
bitmap = ones(300,300);
for p = 1:1:300
    for q = 1:1:300
        if bitmap_matrix(p,q) == 0
            layerelementz = (150+p);
            layerelementy = (150+q);
            for i = 1:1:300;
                for j = 1:1:300;
                    if abs(elementz(i,j)-layerelementz) < 1 &
abs(elementy(i,j) - layerelementy) < 1
                        bitmap(i,j) = 0;
                    end
                end
            end
        end
    end
end
imwrite(bitmap,'strip_bitmap.bmp','bmp')
```

APPENDIX D. VALIDATION OF TRANSIENT LAYER CURE MODEL

In this appendix, the test layers cured to validate the transient layer cure model, formulated in Chapter 4 are presented. The layers are cured by supplying different exposures. The thicknesses of the layers cured are tabulated against the time of exposure and exposure in Table 6.1.

Three layers were cured for each value of exposure. The layer thickness was measured for seven values of times of exposure. Thus, in all, 21 layers were cured. For 15s exposure, no layer was cured, i.e. the thickness of the cured layer for 15s exposure is 0μm.

These layers are cured against a glass slide. So, in the pictures, their reflection is also visible. The top part of the figure is the true layer, while, the bottom part is the reflection.

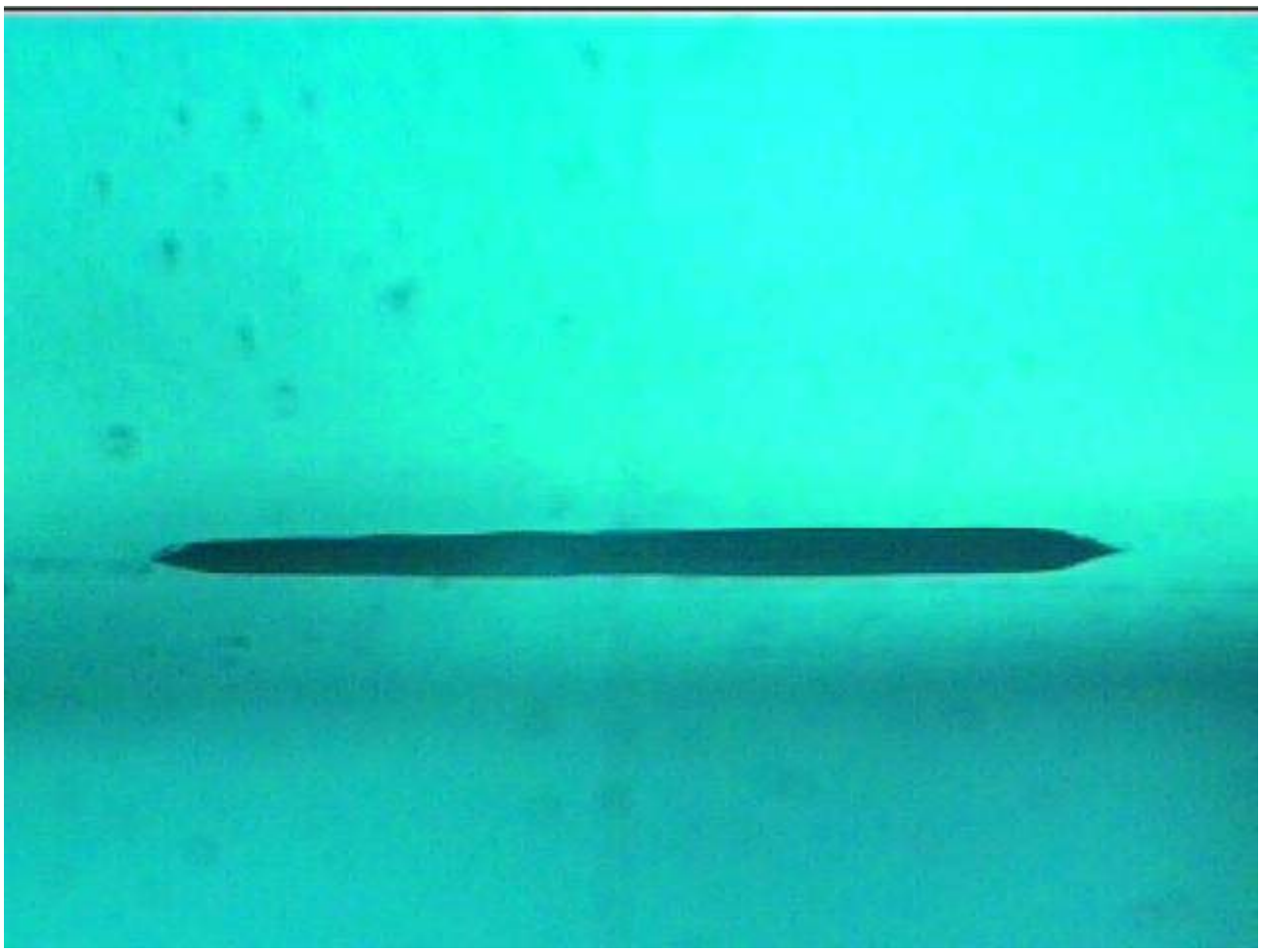

Figure D. 1 Layer cured for 20s exposure: Validation layer 1

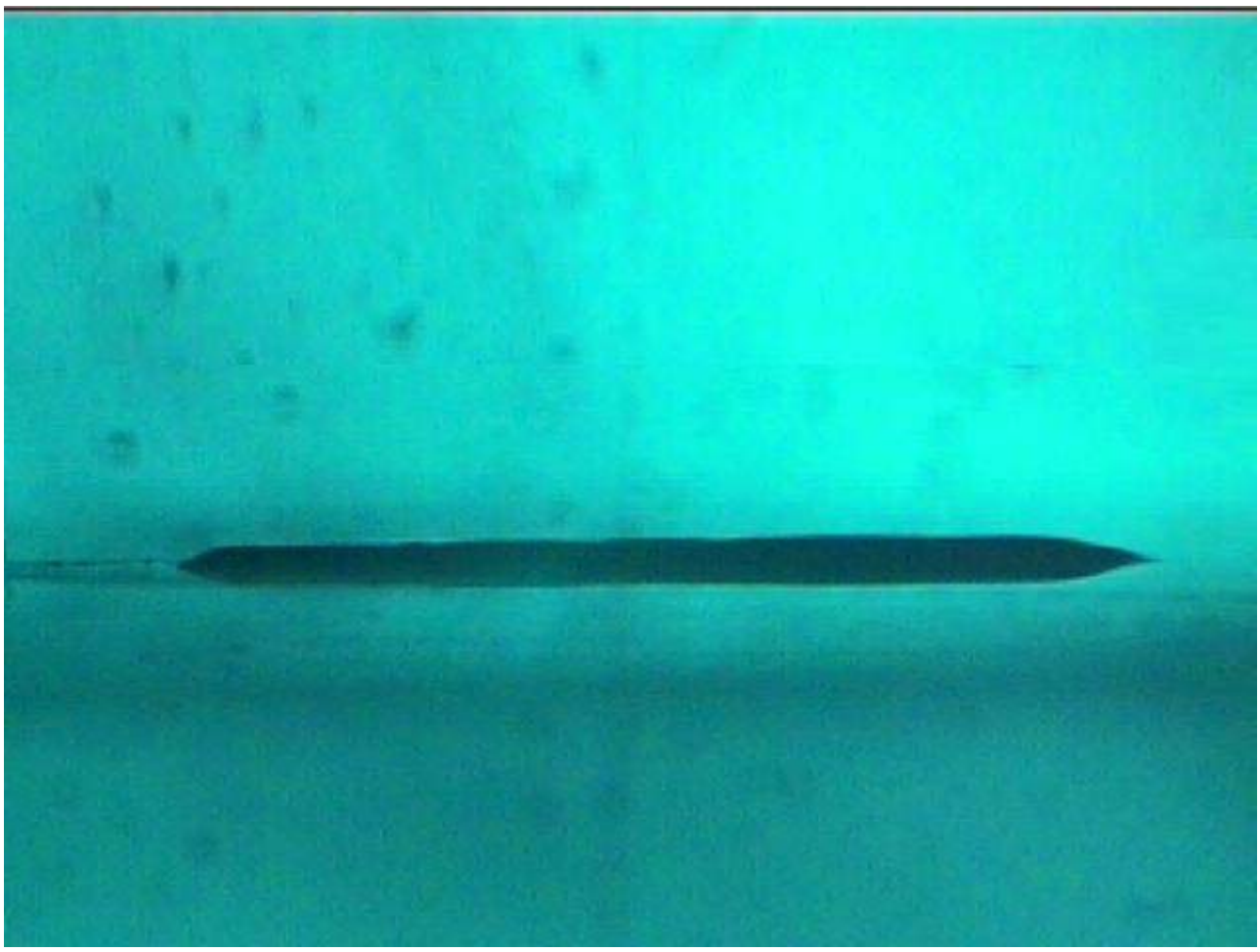

Figure D. 2 Layer cured for 20s exposure: Validation layer 2

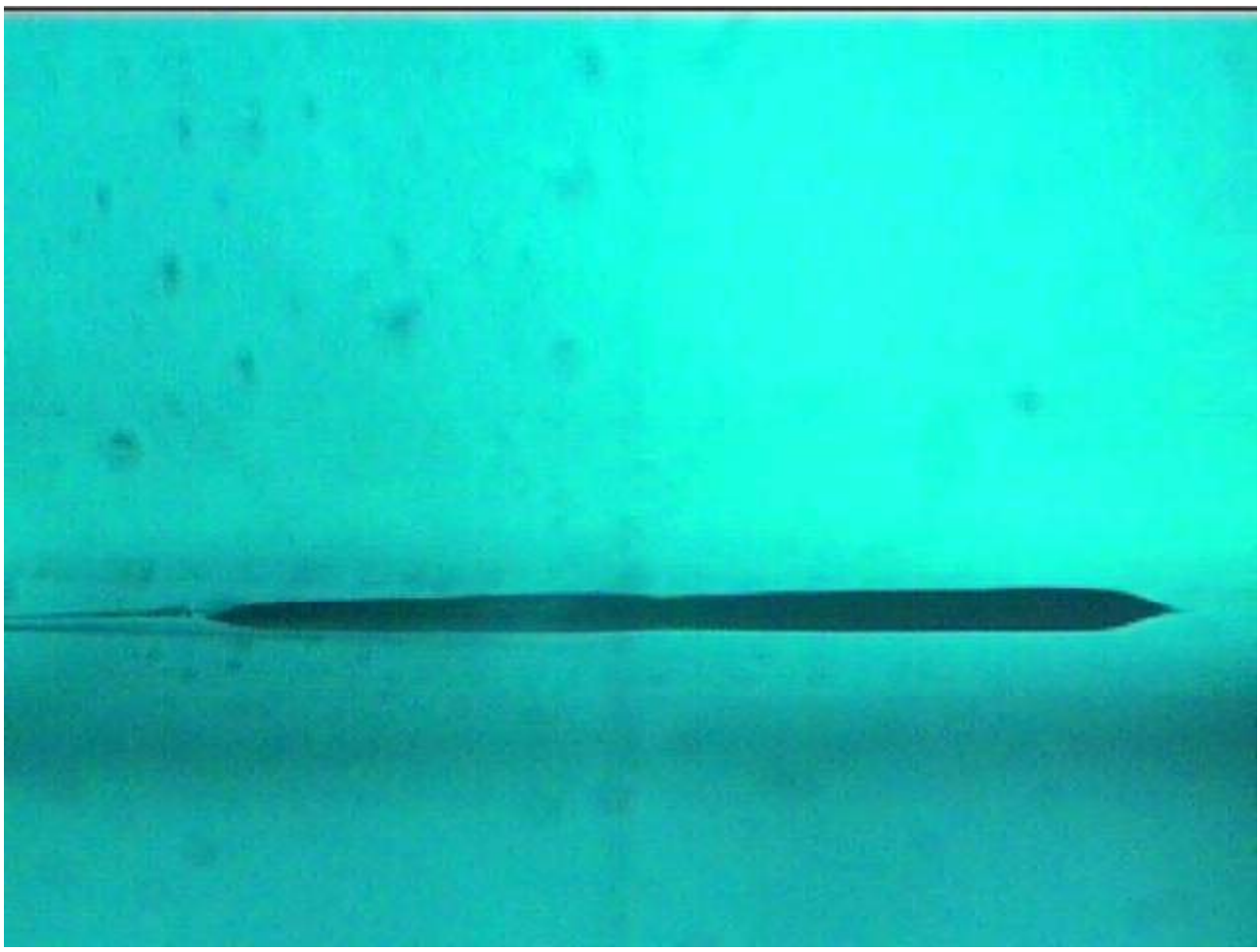

Figure D. 3 Layer cured for 20s exposure: Validation layer 3

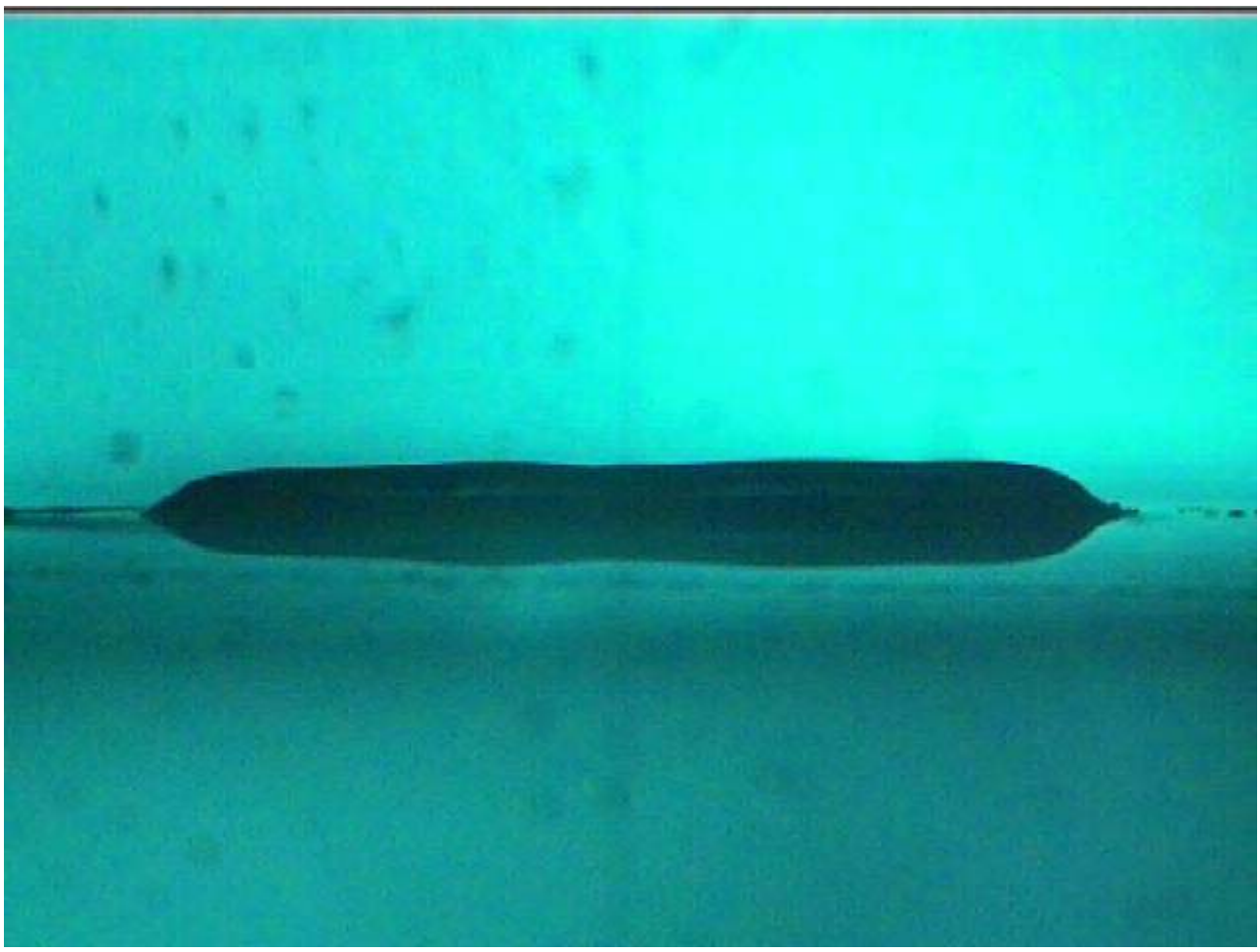

Figure D. 4 Layer cured for 25s exposure: Validation layer 1

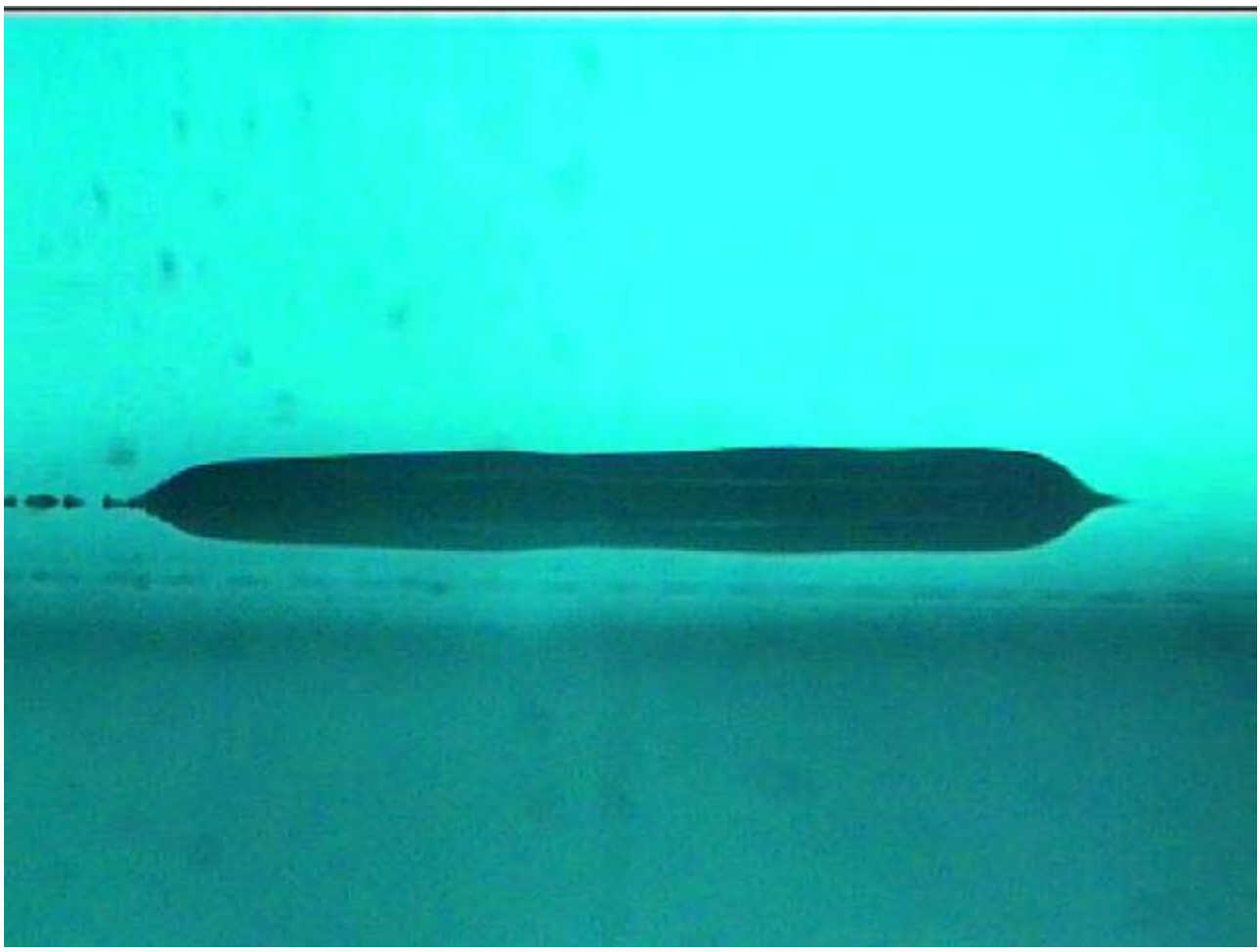

Figure D. 5 Layer cured for 25s exposure: Validation layer 2

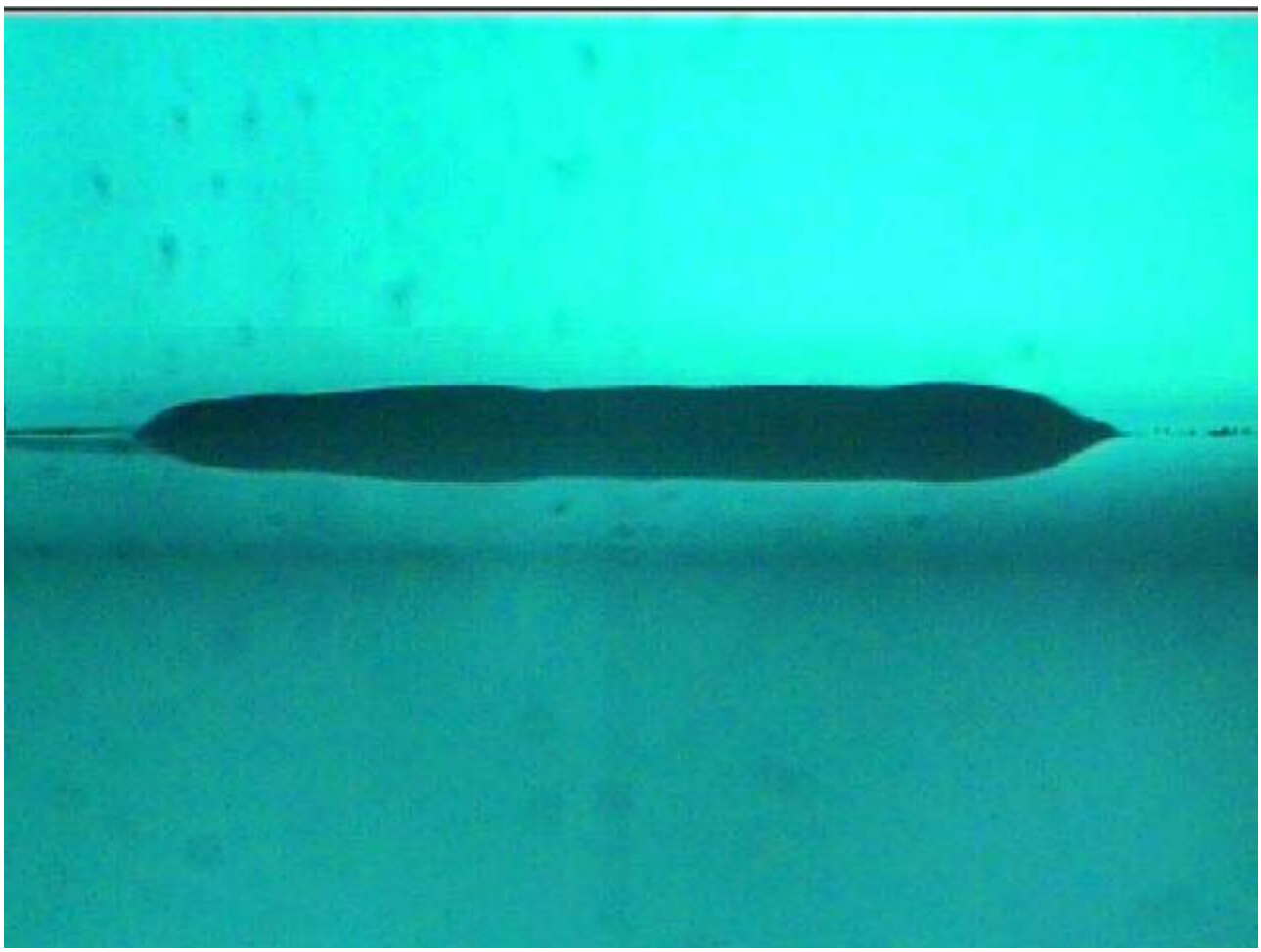

Figure D. 6 Layer cured for 25s exposure: Validation layer 3

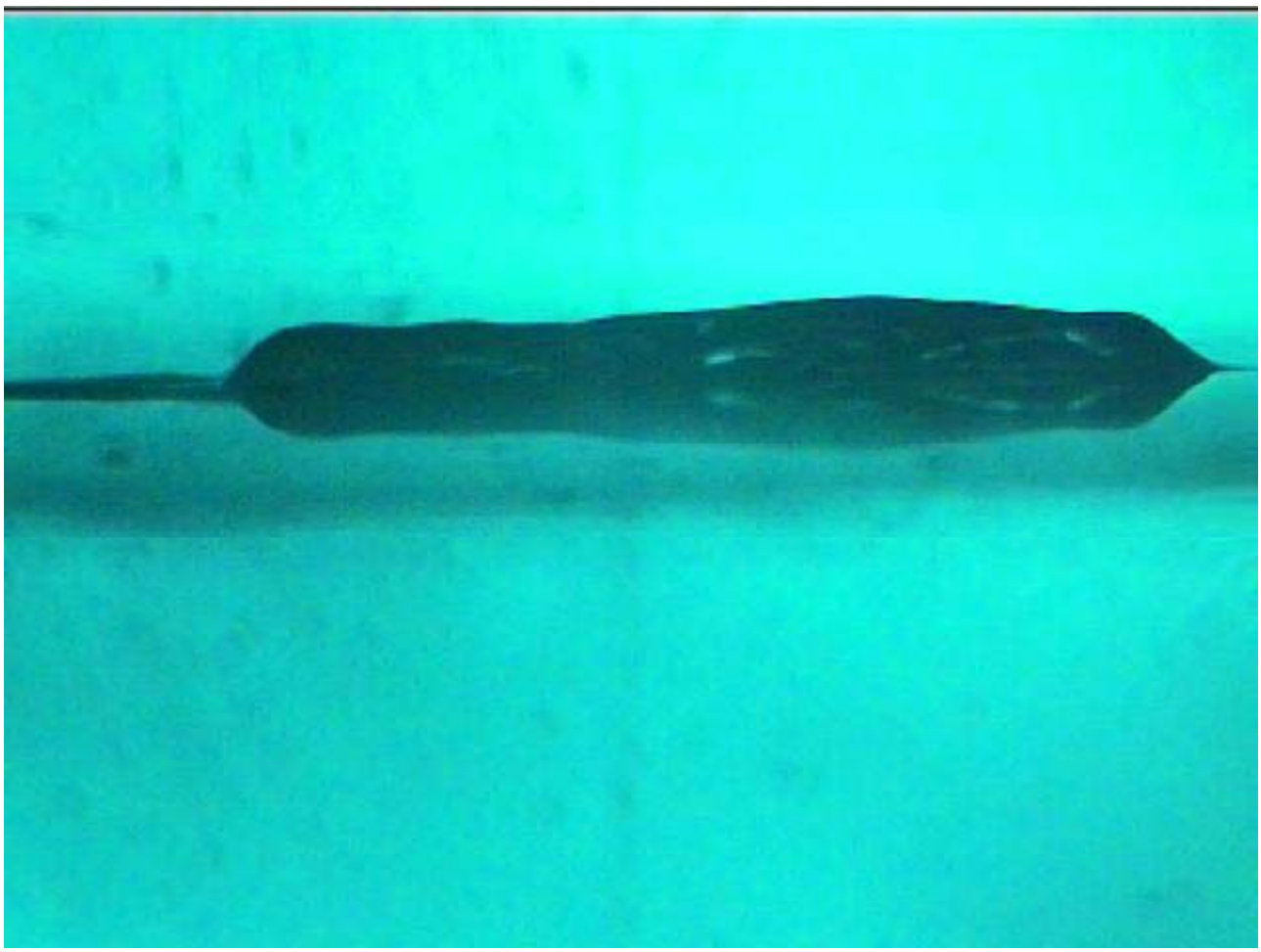

Figure D. 7 Layer cured for 30s exposure: Validation layer 1

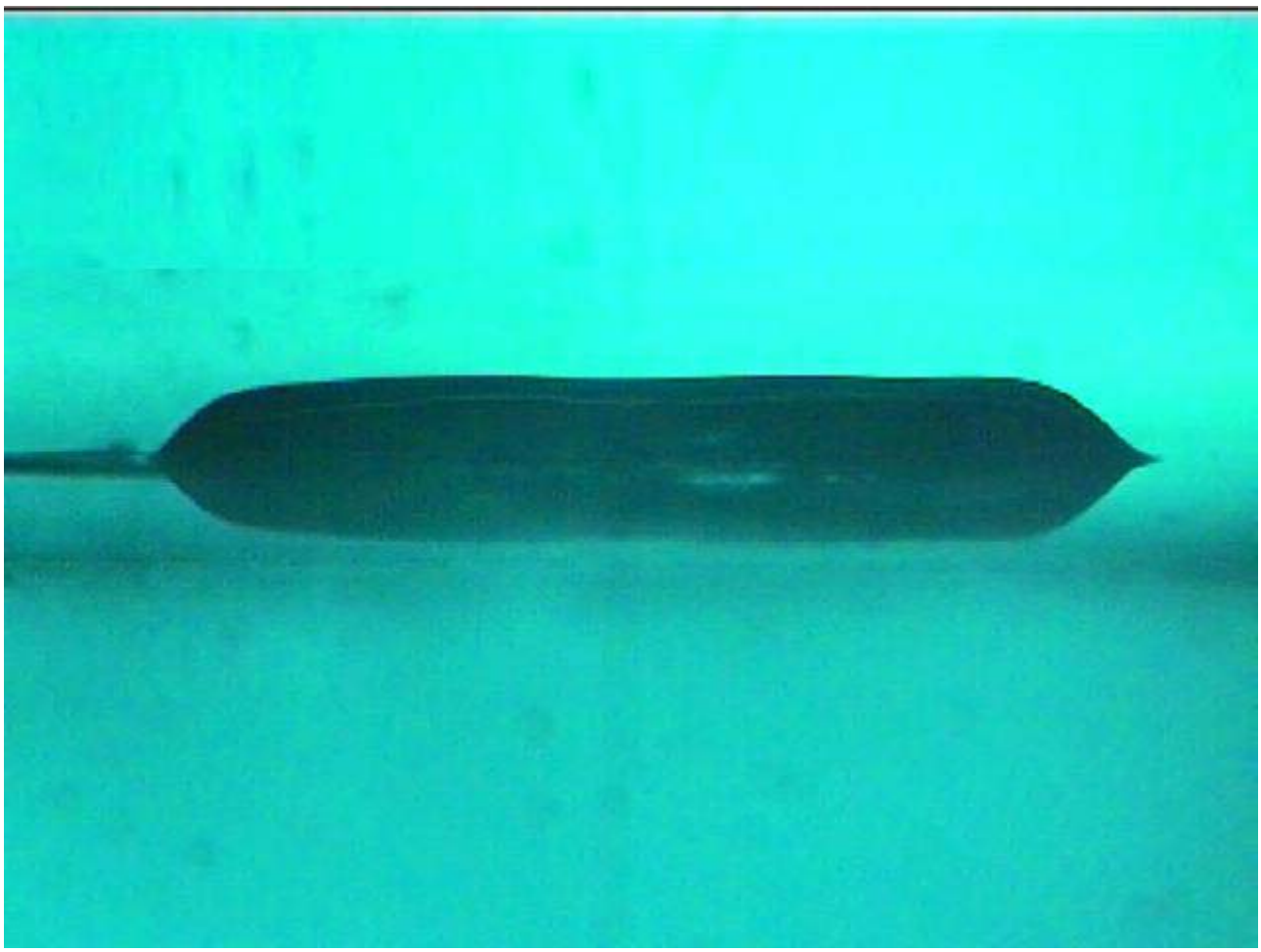

Figure D. 8 Layer cured for 30s exposure: Validation layer 2

Figure D. 9 Layer cured for 30s exposure: Validation layer 3

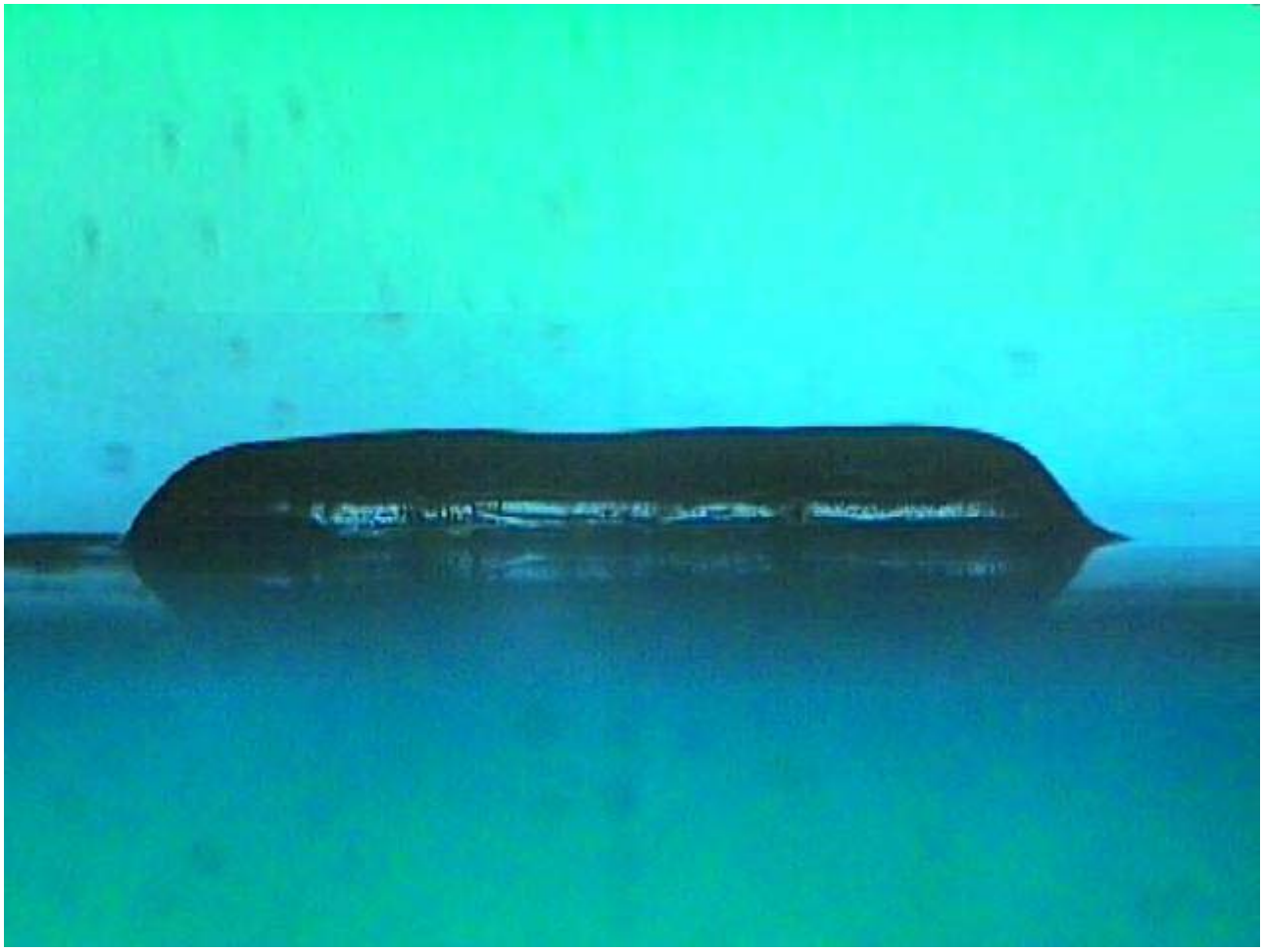

Figure D. 10 Layer cured for 35s exposure: Validation layer 1

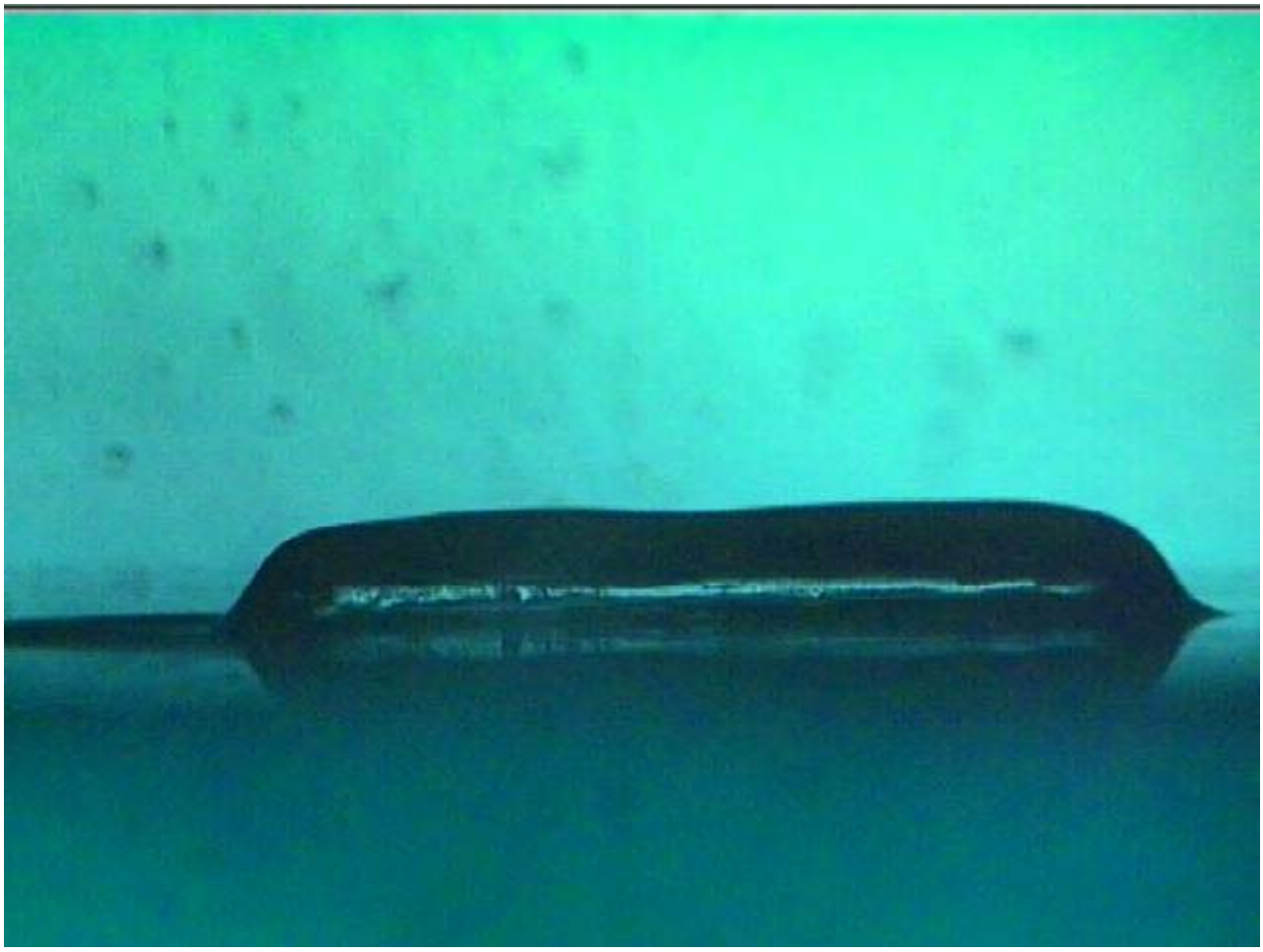

Figure D. 11 Layer cured for 35s exposure: Validation layer 2

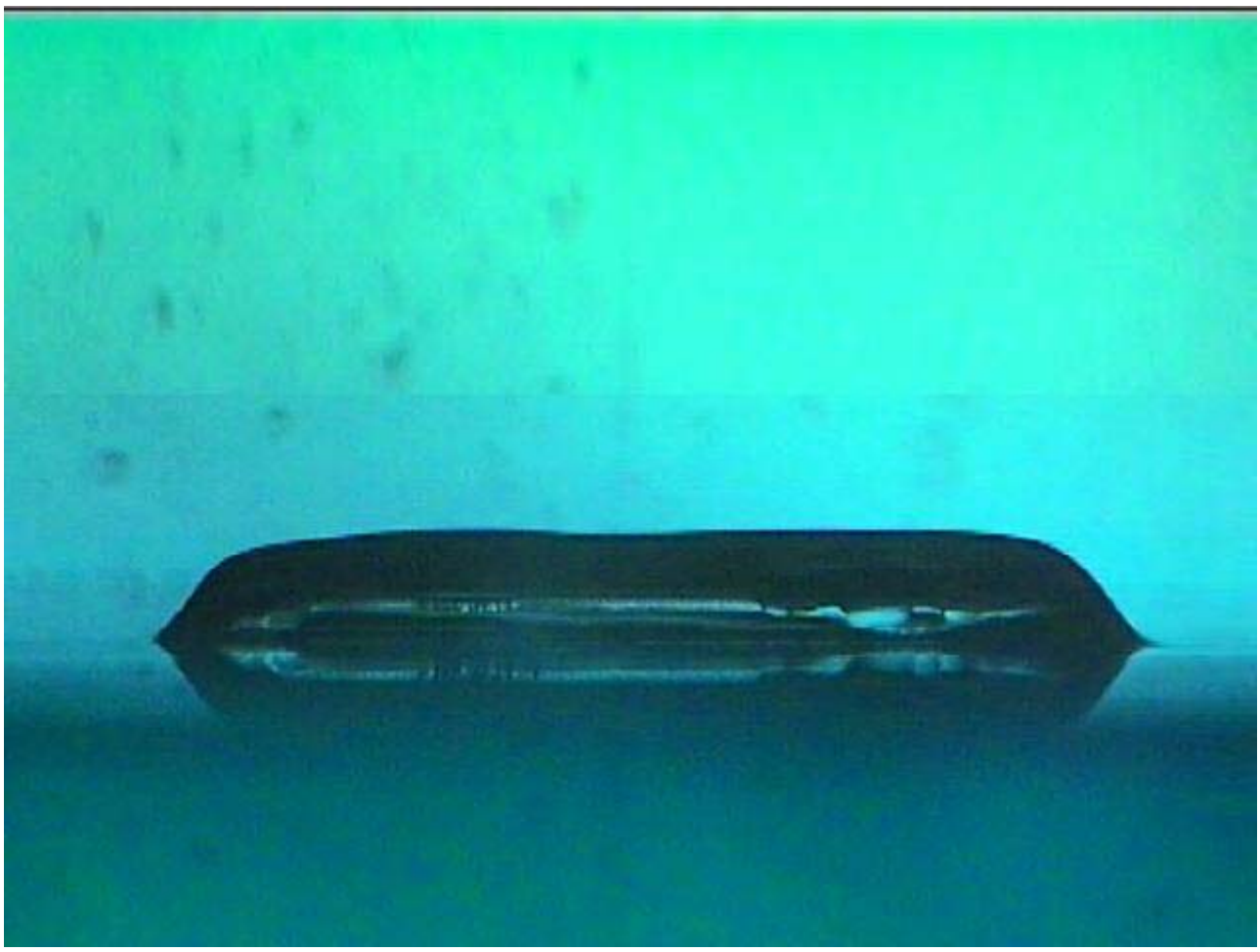

Figure D. 12 Layer cured for 35s exposure: Validation layer 3

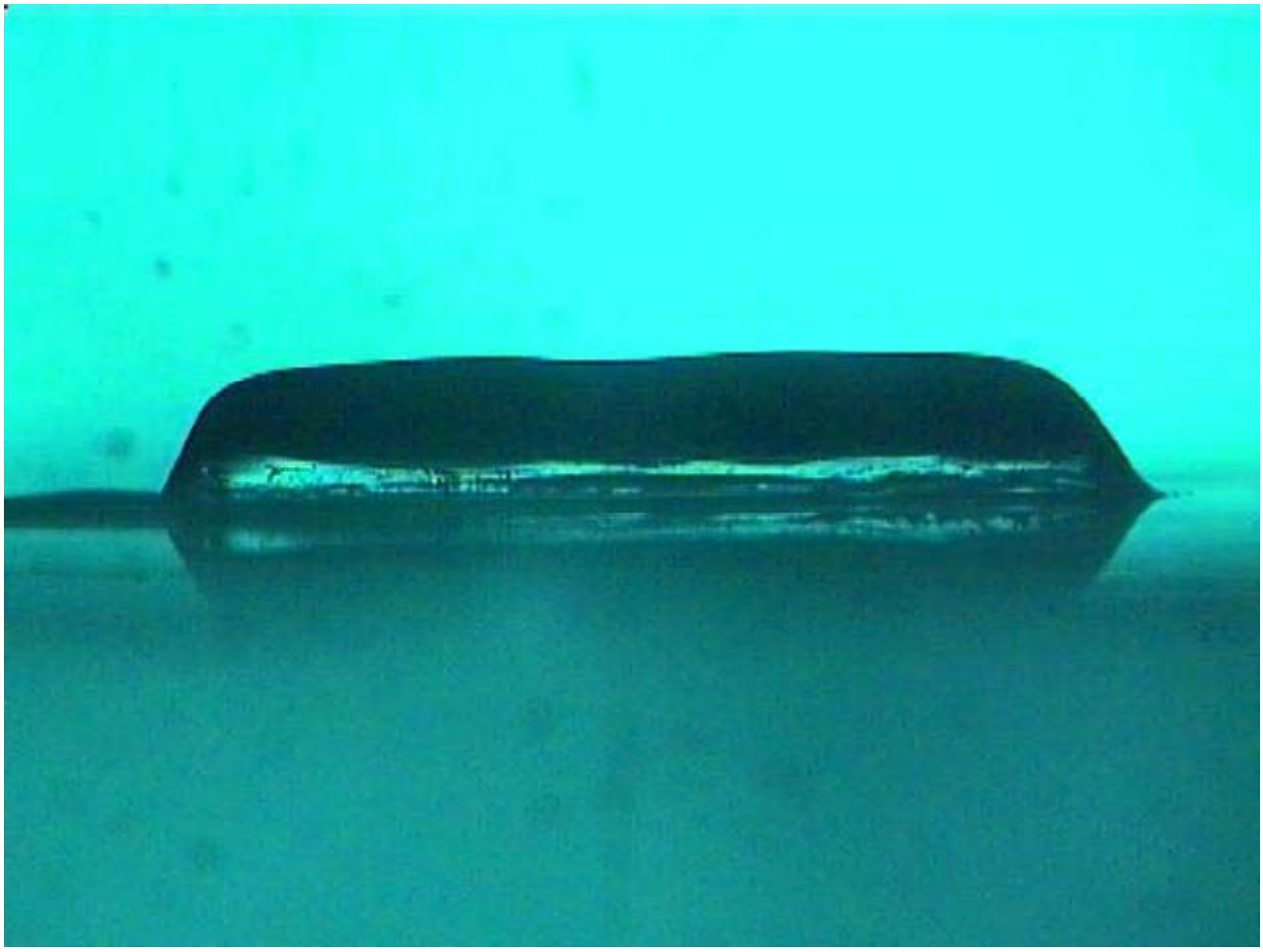

Figure D. 13 Layer cured for 40s exposure: Validation layer 1

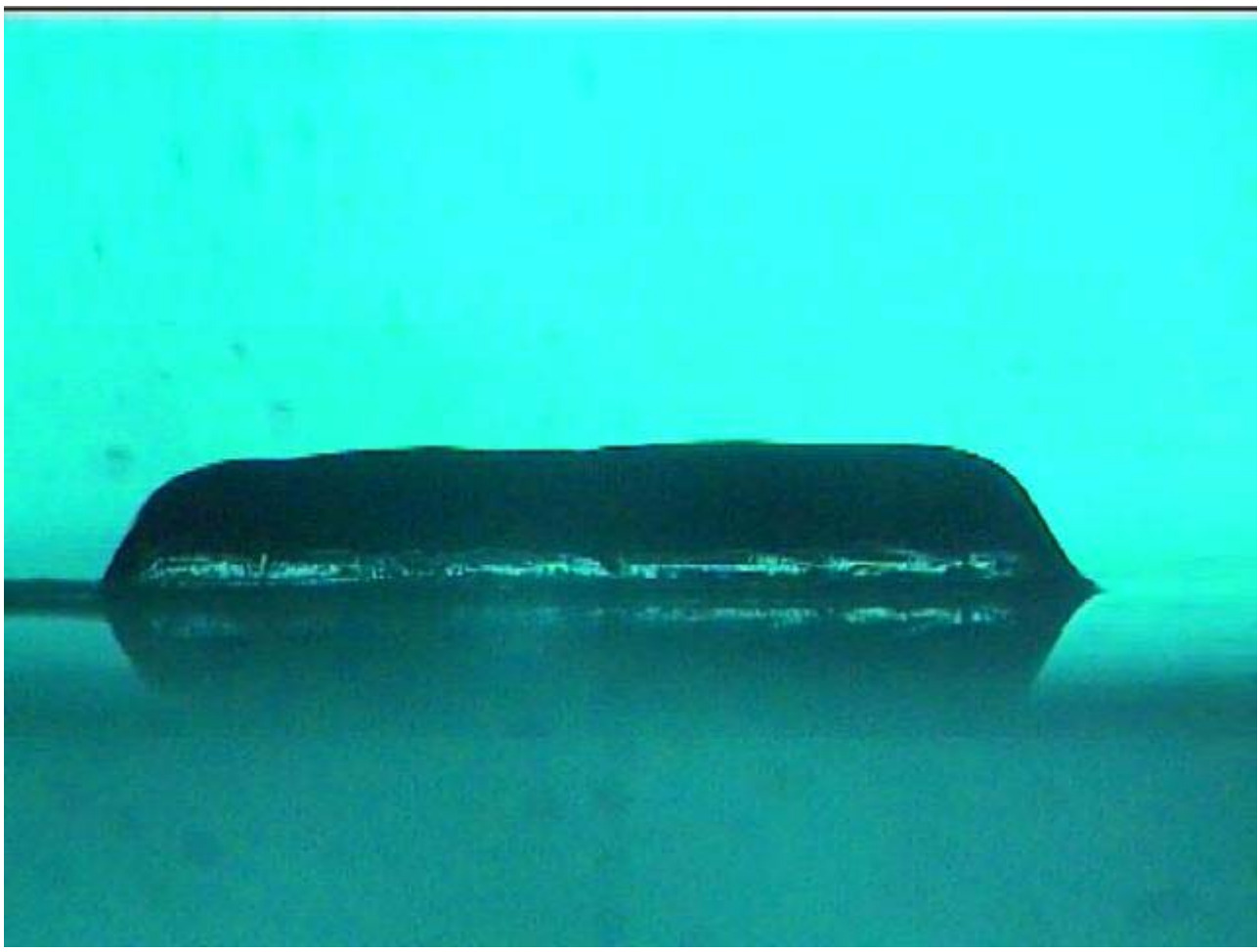

Figure D. 14 Layer cured for 40s exposure: Validation layer 2

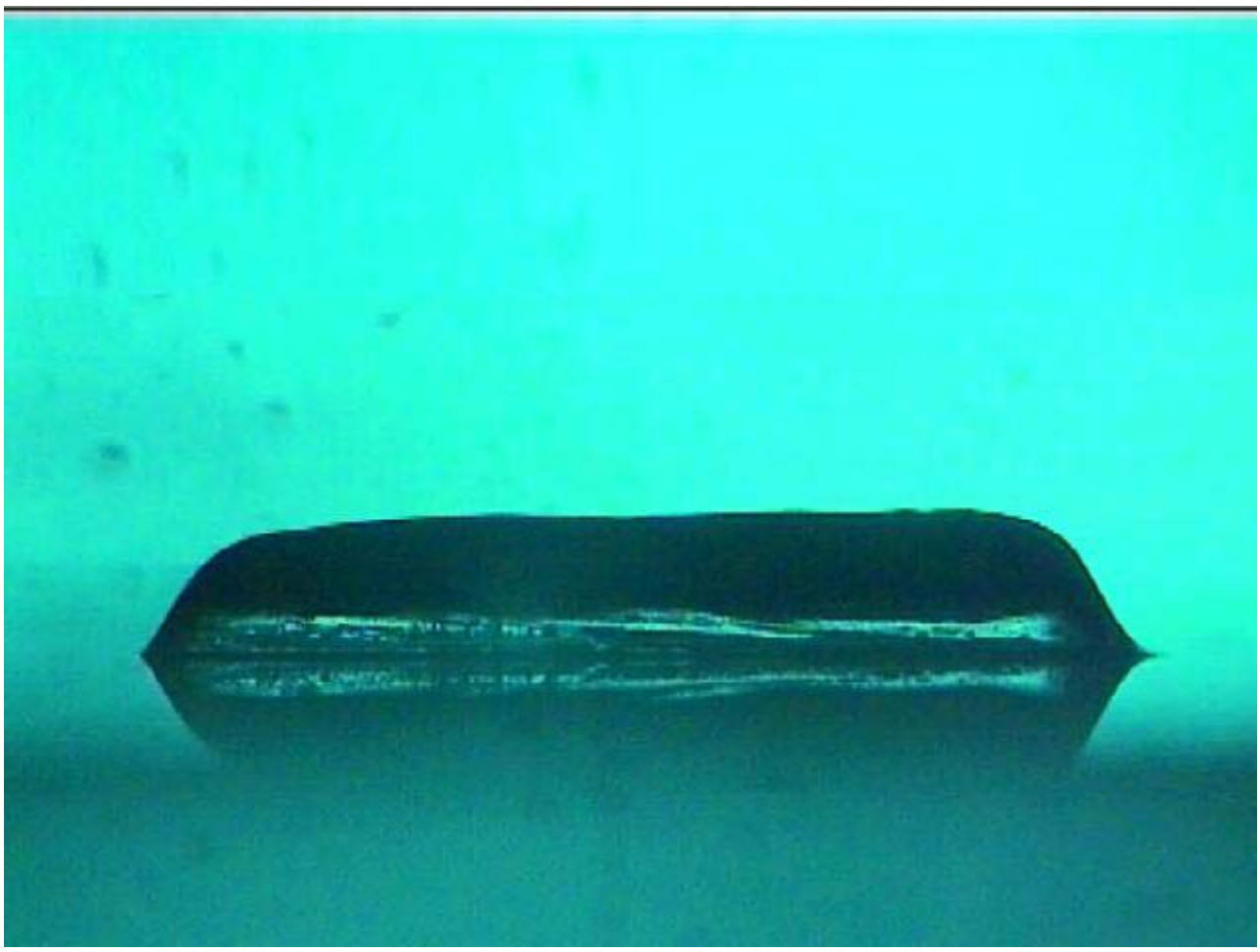

Figure D. 15 Layer cured for 40s exposure: Validation layer 3

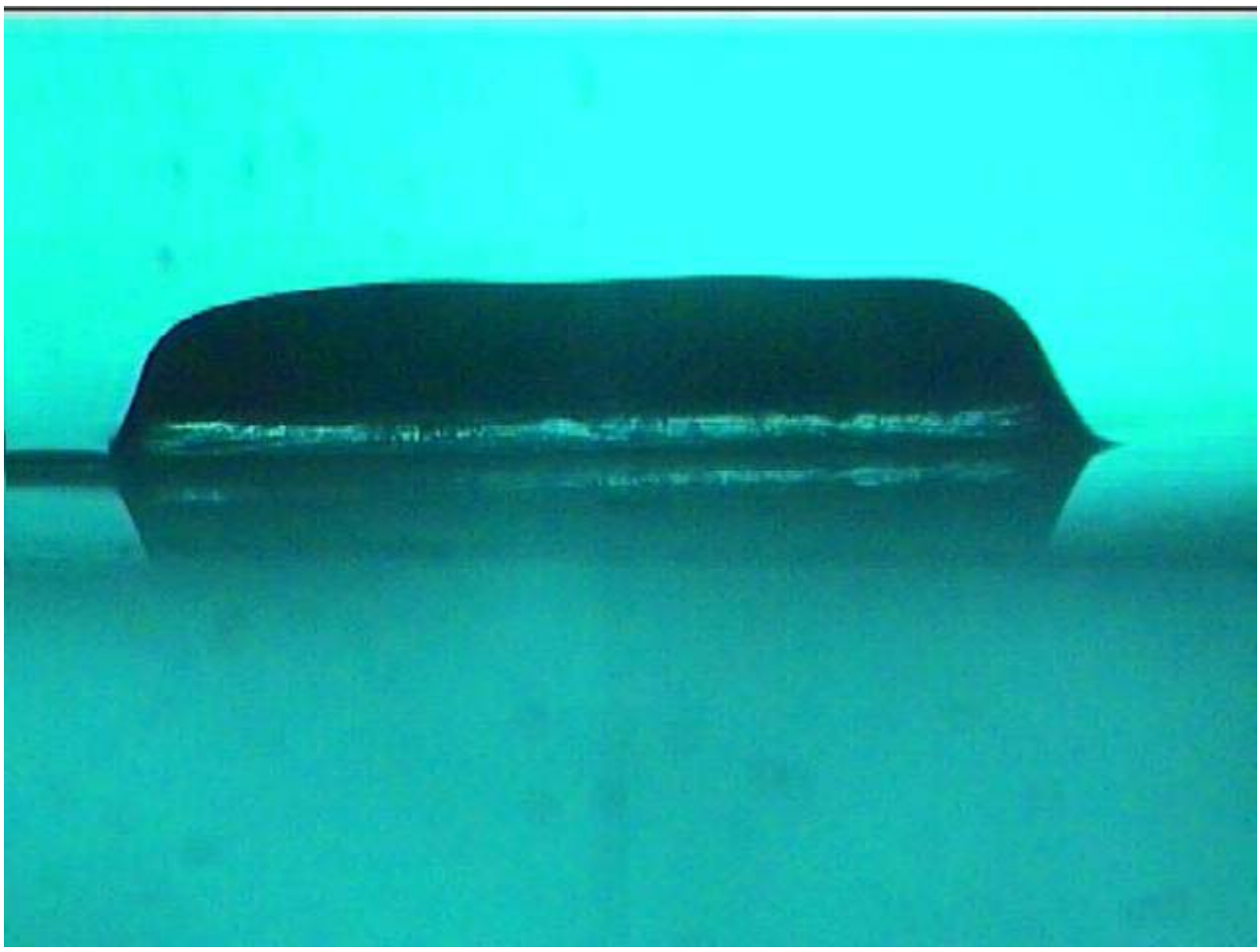

Figure D. 16 Layer cured for 45s exposure: Validation layer 1

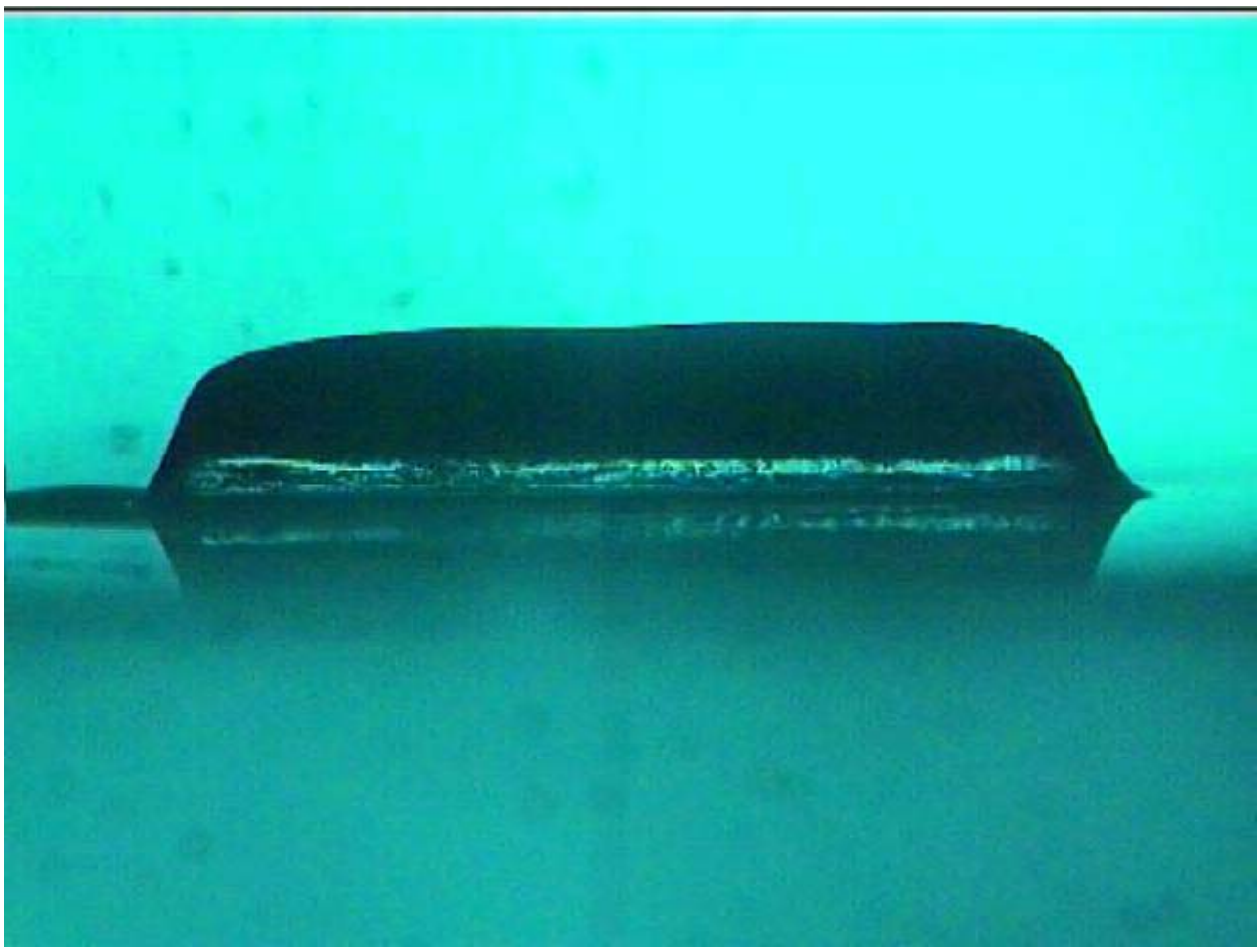

Figure D. 17 Layer cured for 45s exposure: Validation layer 2

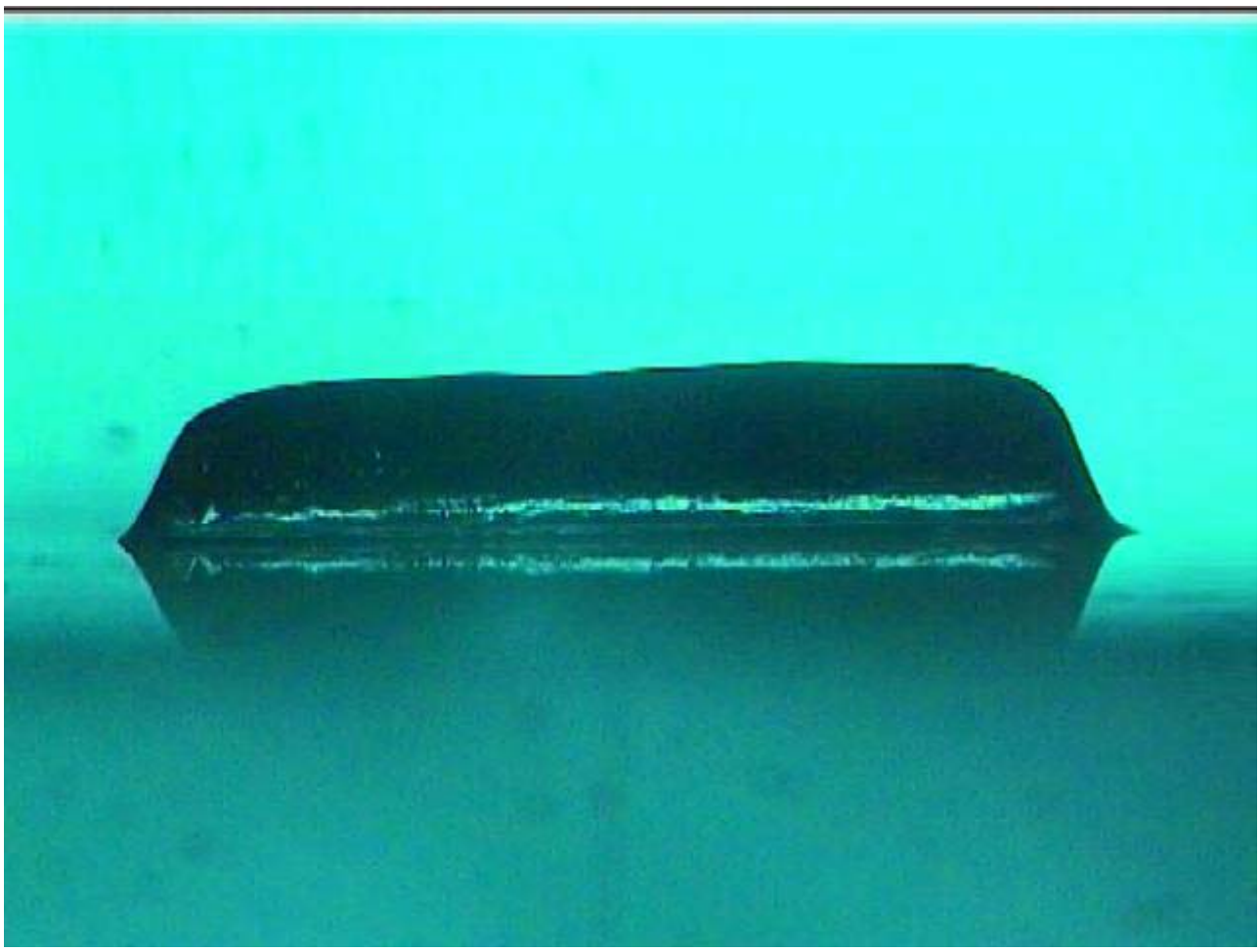

Figure D. 18 Layer cured for 45s exposure: Validation layer 3

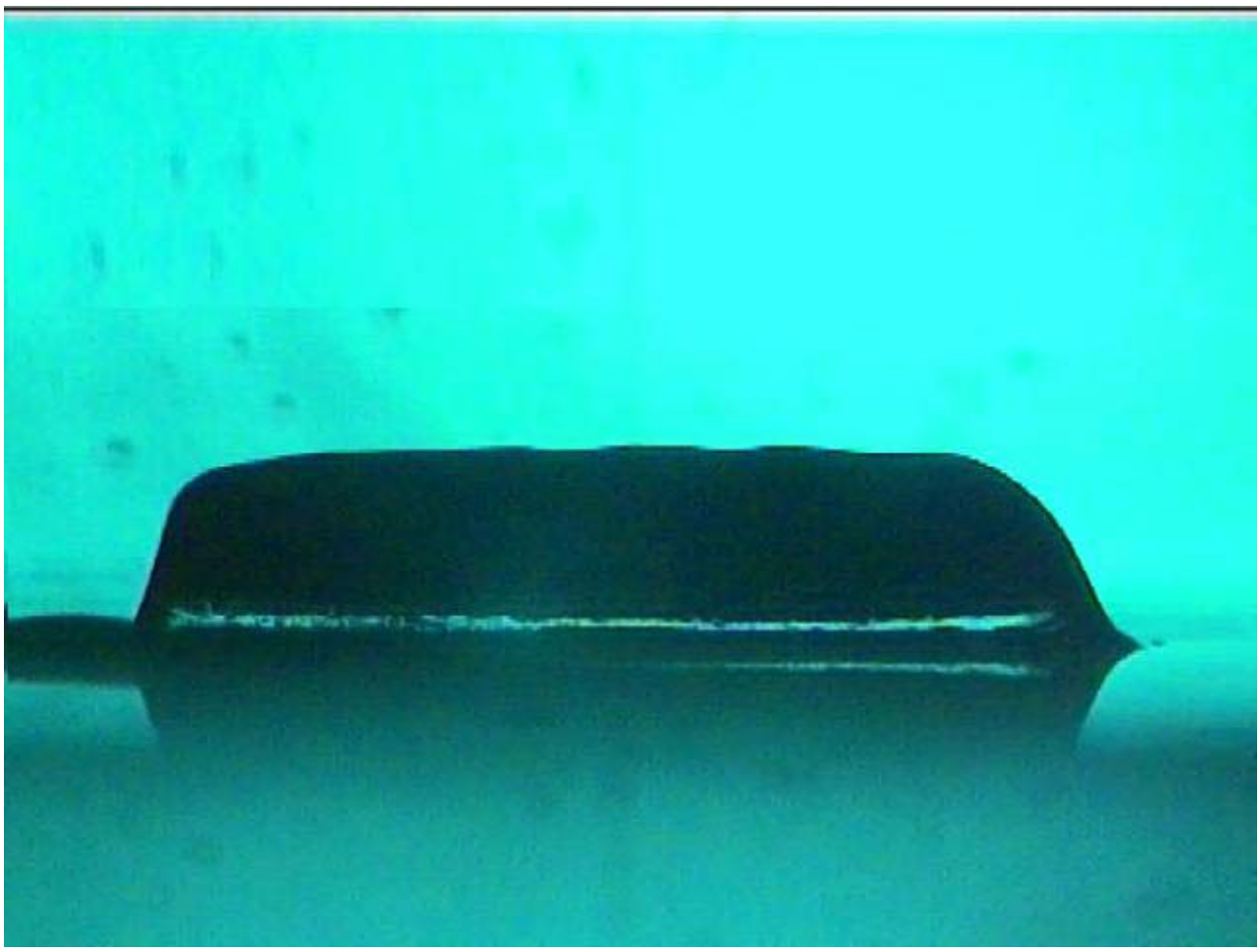

Figure D. 19 Layer cured for 50s exposure: Validation layer 1

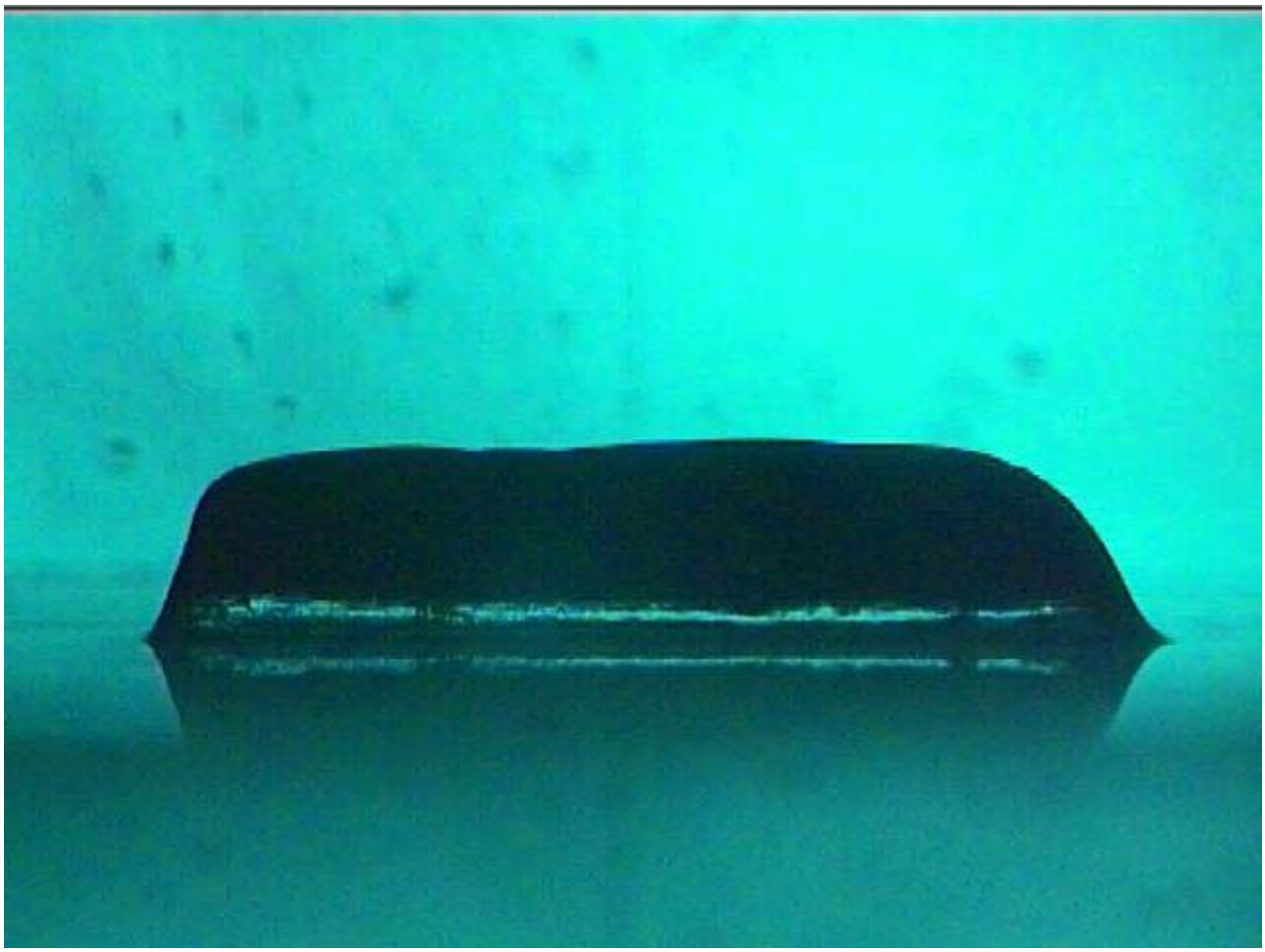

Figure D. 20 Layer cured for 50s exposure: Validation layer 2

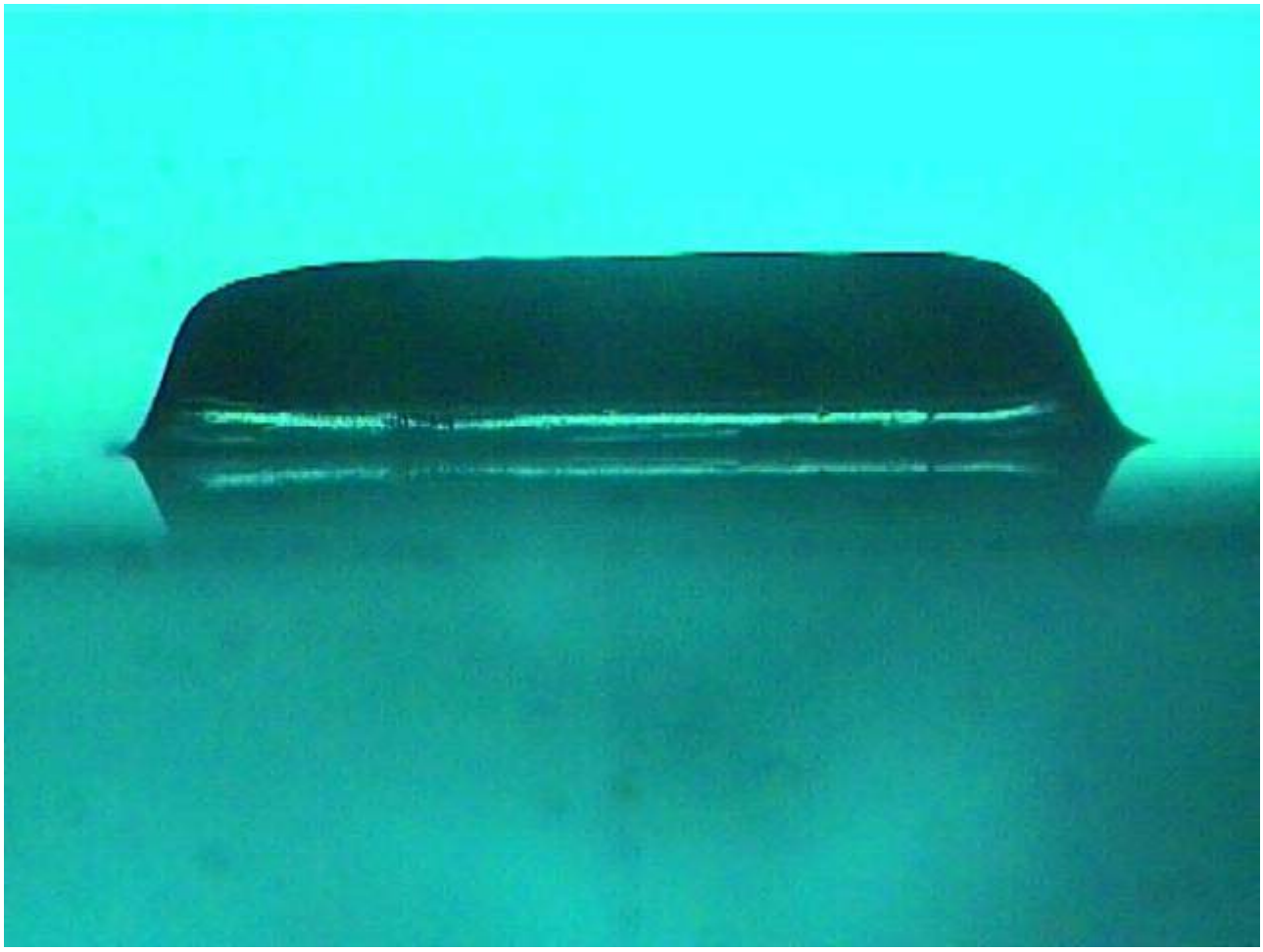

Figure D. 21 Layer cured for 50s exposure: Validation layer 3

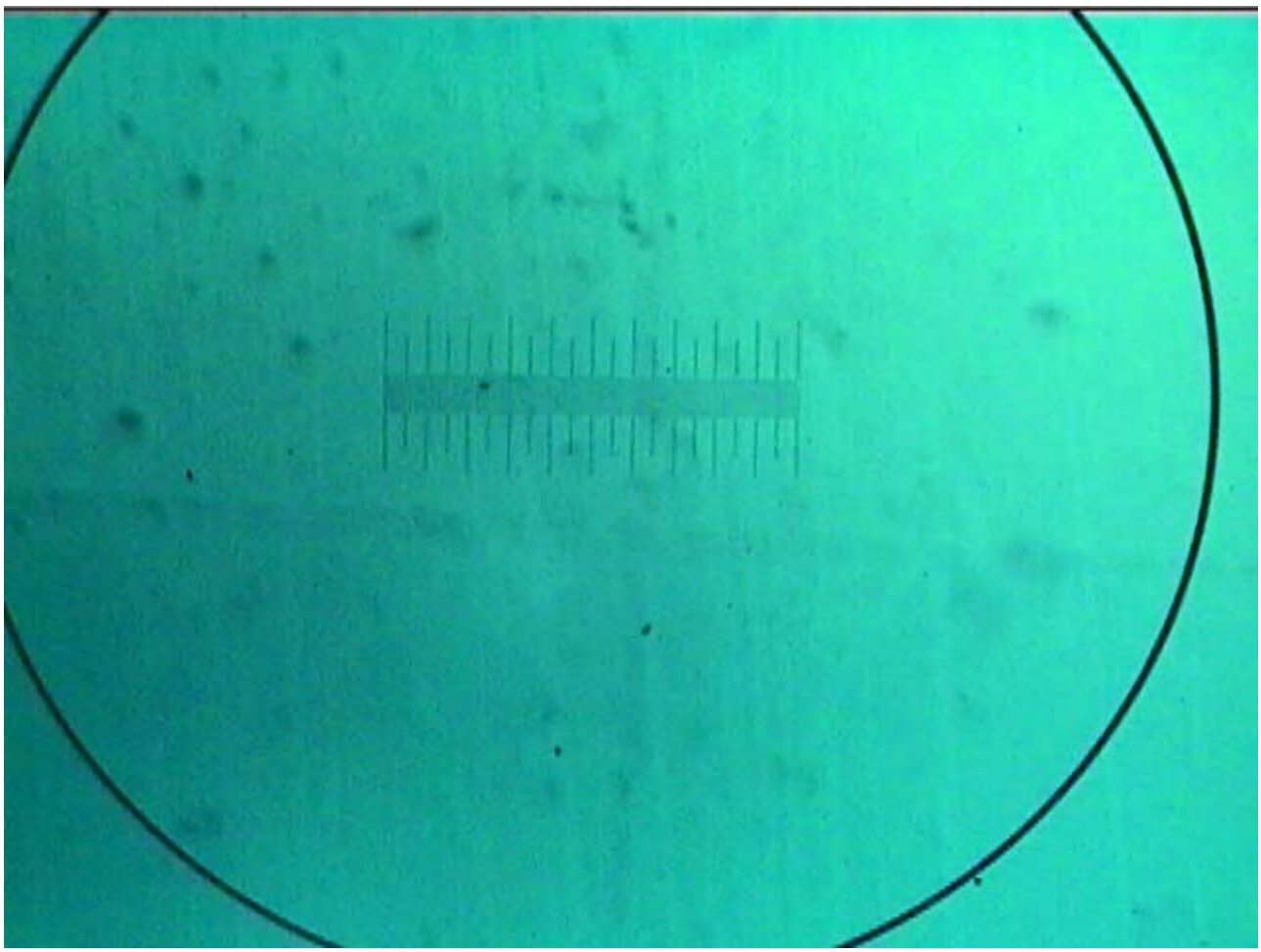

Figure D. 22 Calibration scale for validation layers (Distance shown in 1mm)

APPENDIX E. QUANTIFYING EFFECT OF RADICAL DIFFUSION

In this appendix, the pictures of the layers cured by supplying two discrete exposure doses of 25s each are presented. The variable is the time interval (called waiting time) allowed in between these two exposure doses. Greater the "waiting time", greater is the loss of energy from the bottom surface and smaller is the thickness of the layer cured after the second exposure dose.

Experiments are conducted for 5 waiting times, of 4s, 30s, 60s, 120s, and 180s. Three repeat experiments are conducted for each of these waiting times.

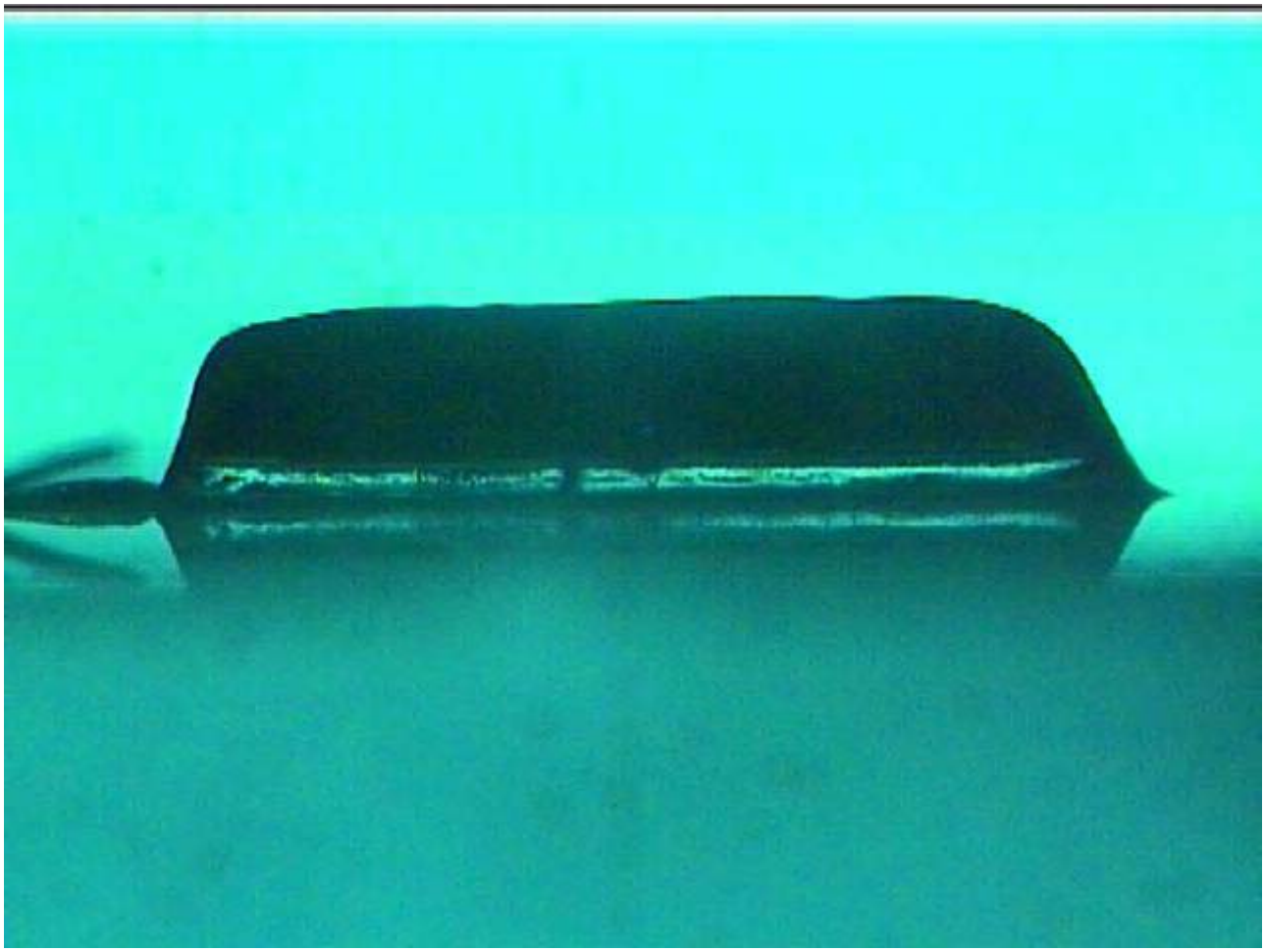

Figure E.1 Waiting time between exposures = 4s. Test layer 1

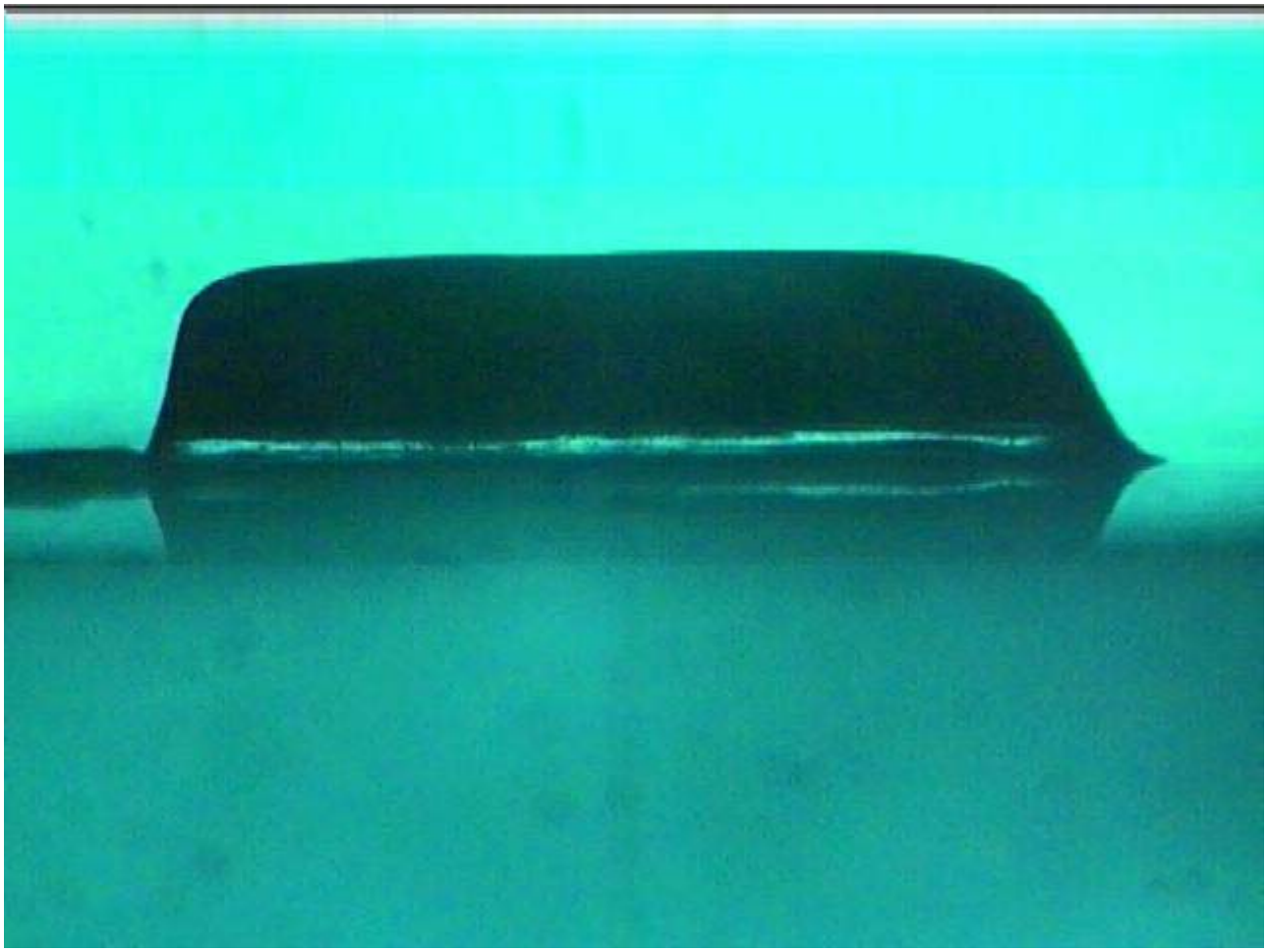

Figure E.2 Waiting time between exposures = 4s. Test layer 2

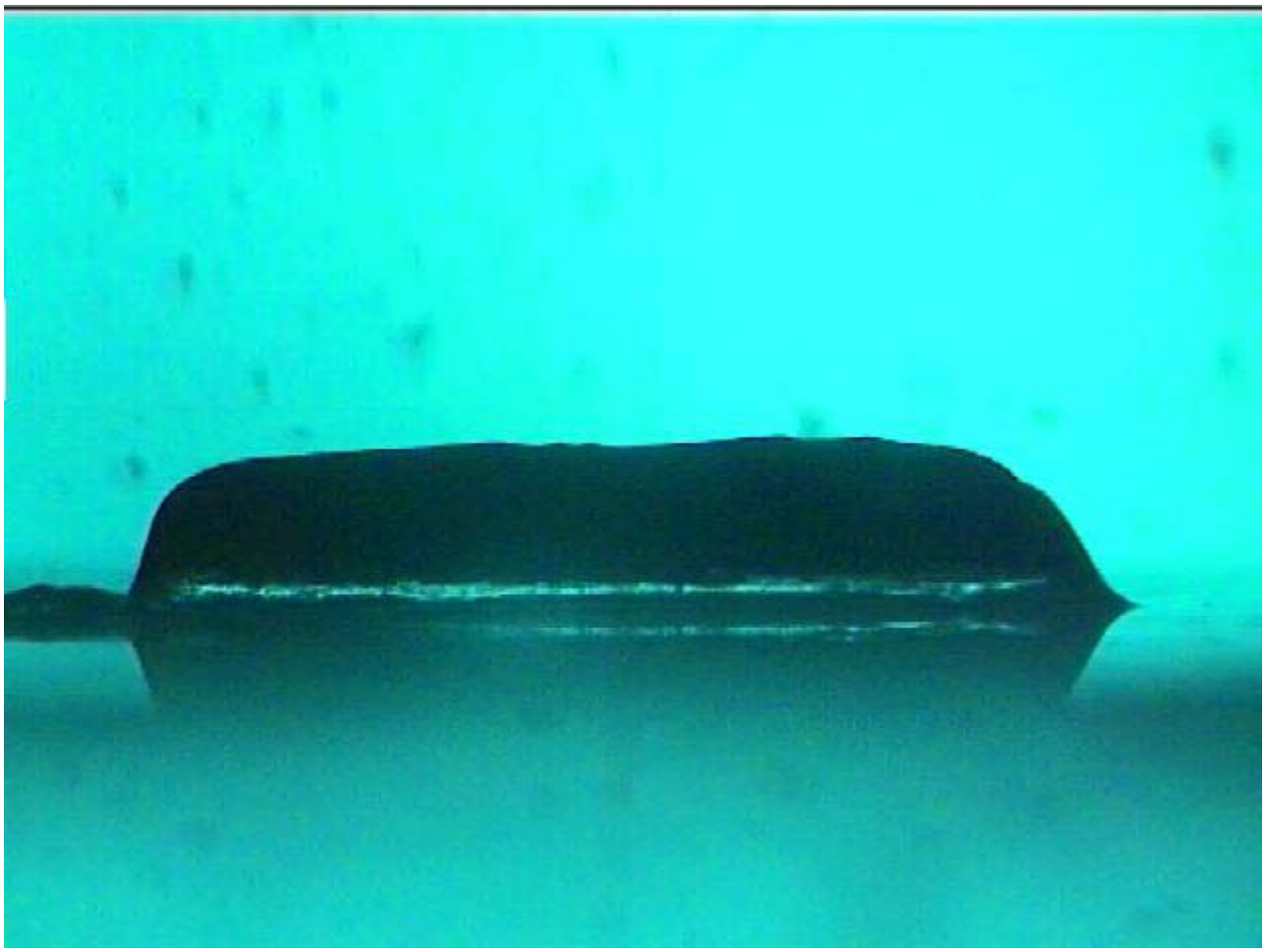

Figure E.3 Waiting time between exposures = 30s. Test layer 1

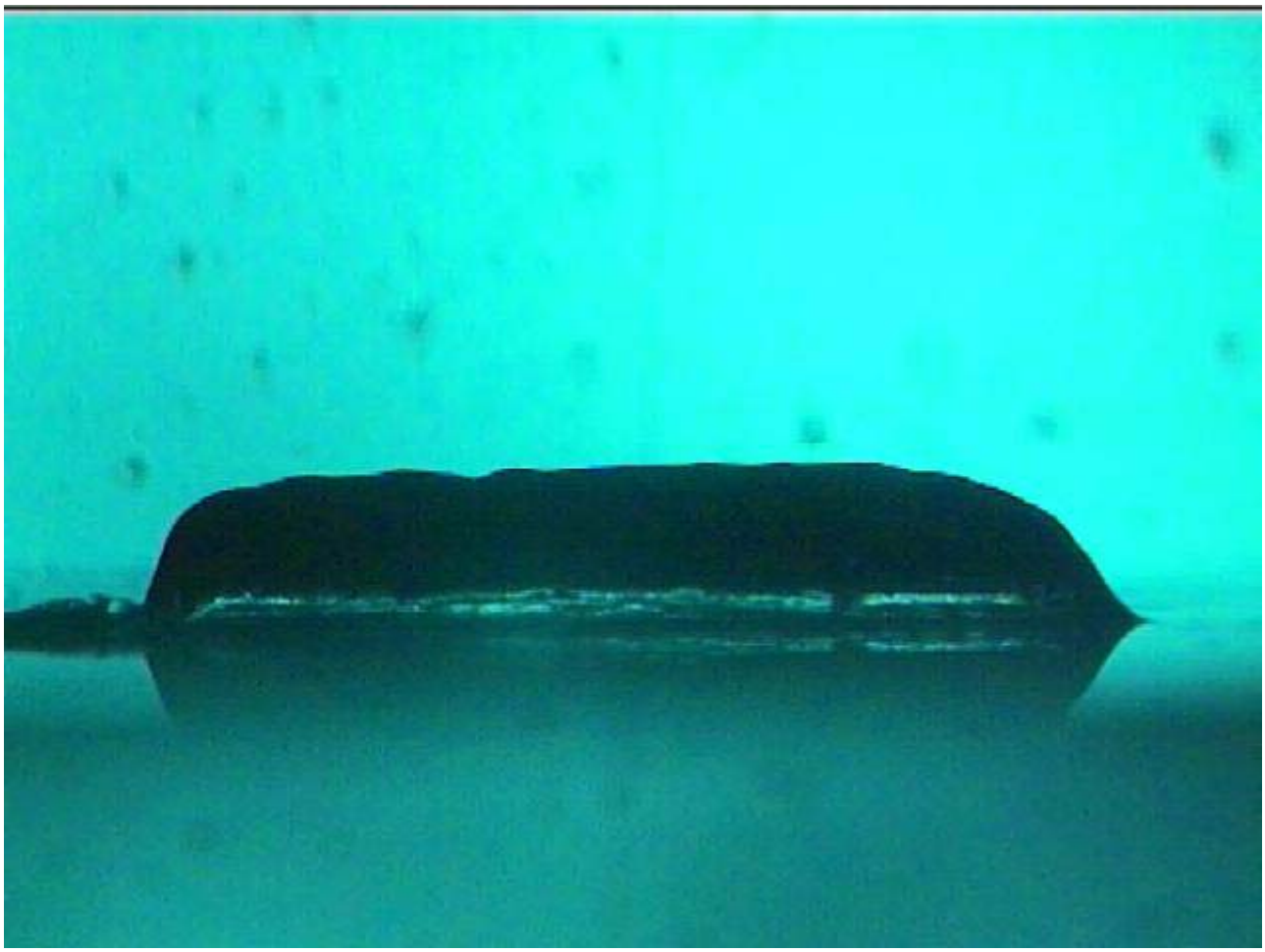

Figure E.4 Waiting time between exposures = 30s. Test layer 2

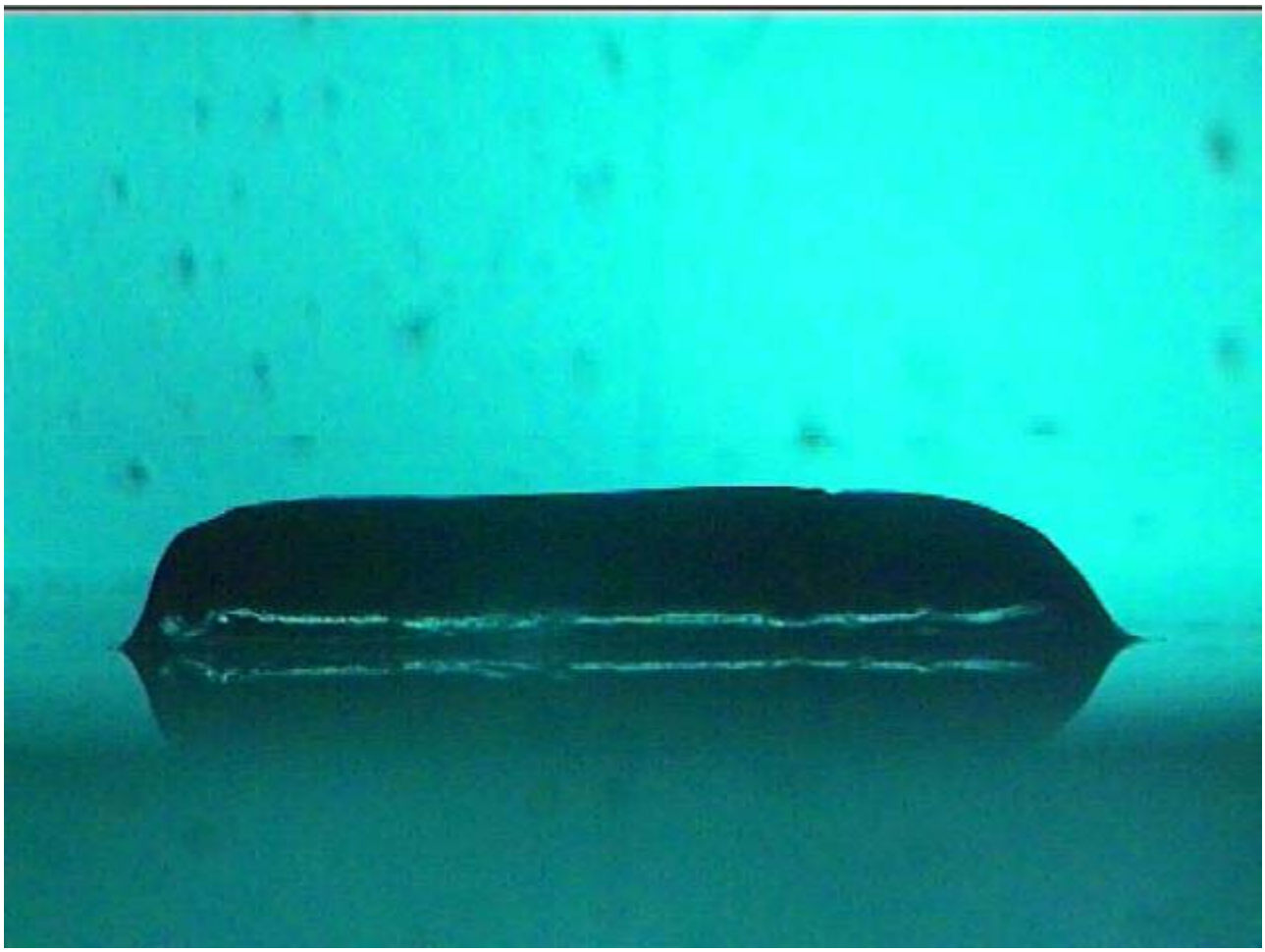

Figure E.5 Waiting time between exposures = 30s. Test layer 3

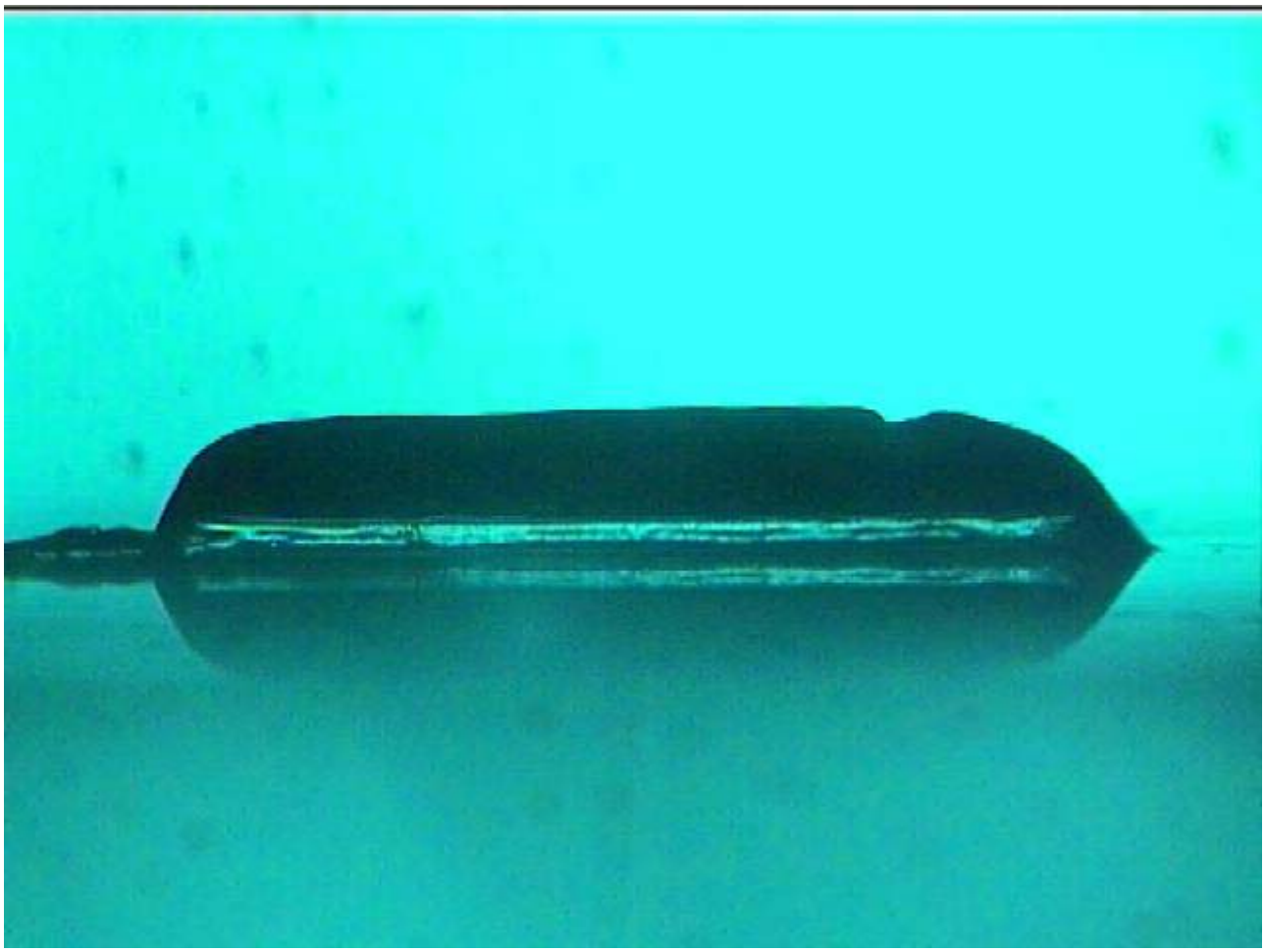

Figure E.6 Waiting time between exposures = 60s. Test layer 1

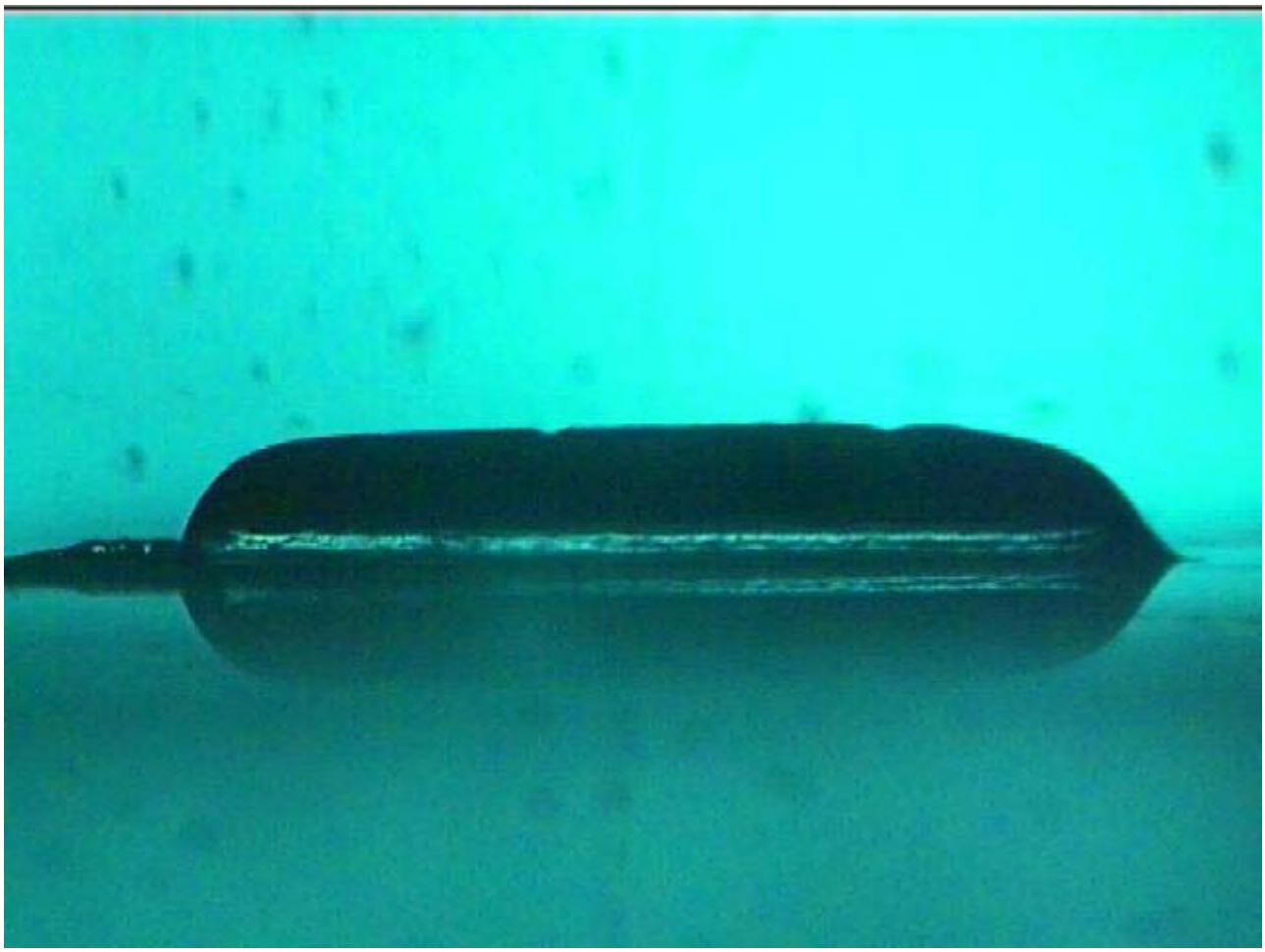

Figure E.7 Waiting time between exposures = 60s. Test layer 2

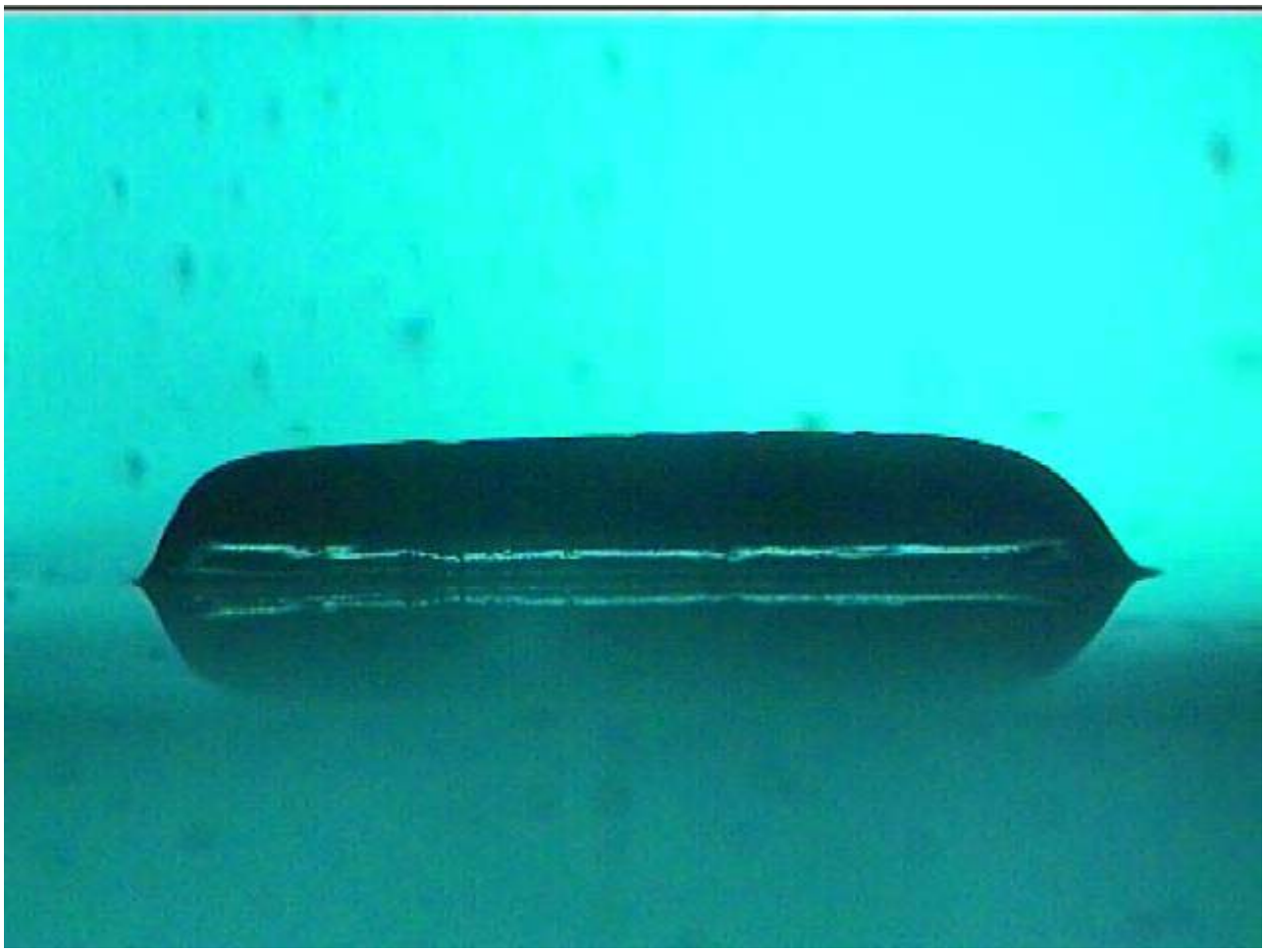

Figure E.8 Waiting time between exposures = 60s. Test layer 3

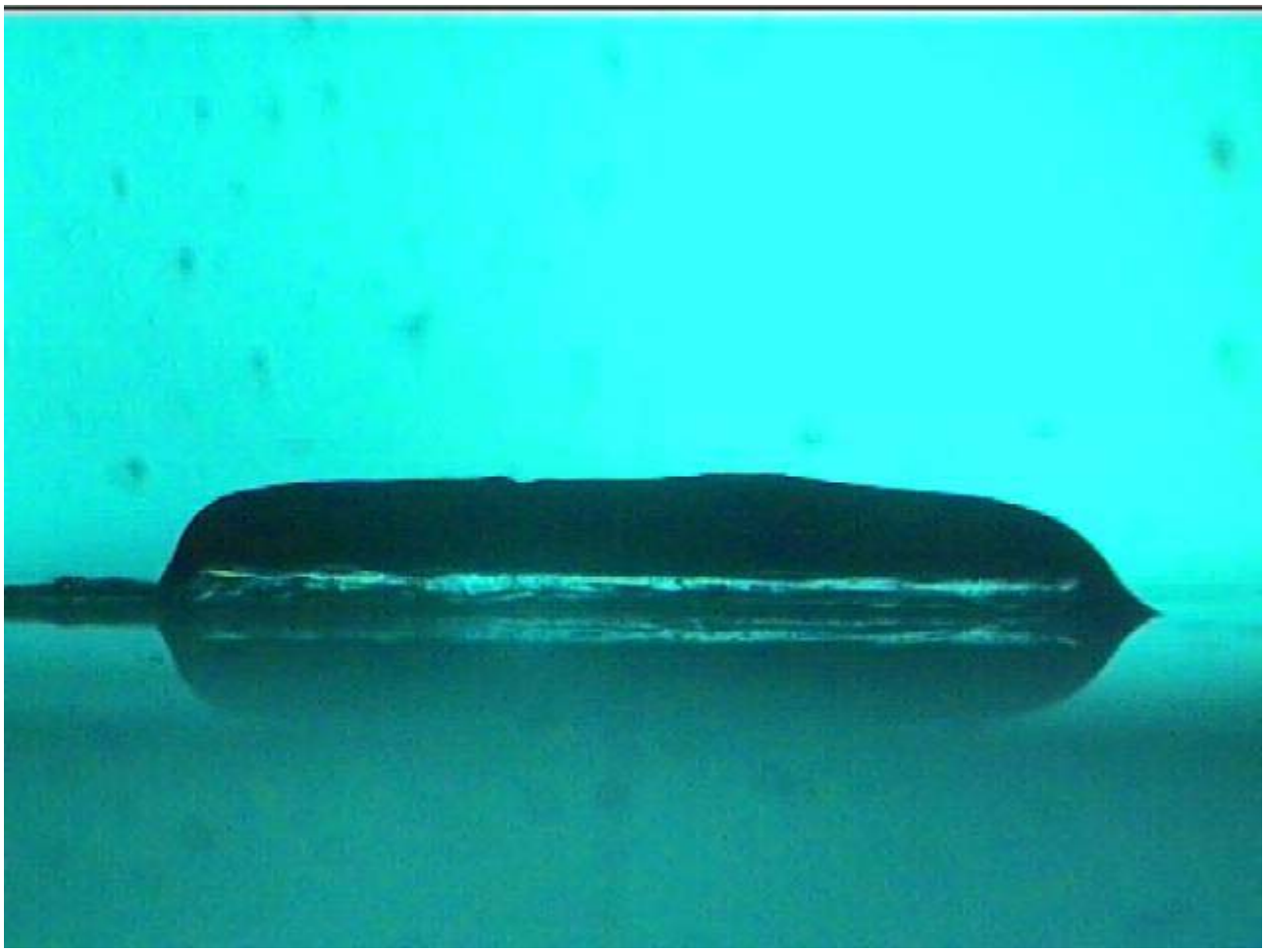

Figure E.9 Waiting time between exposures = 120s. Test layer 1

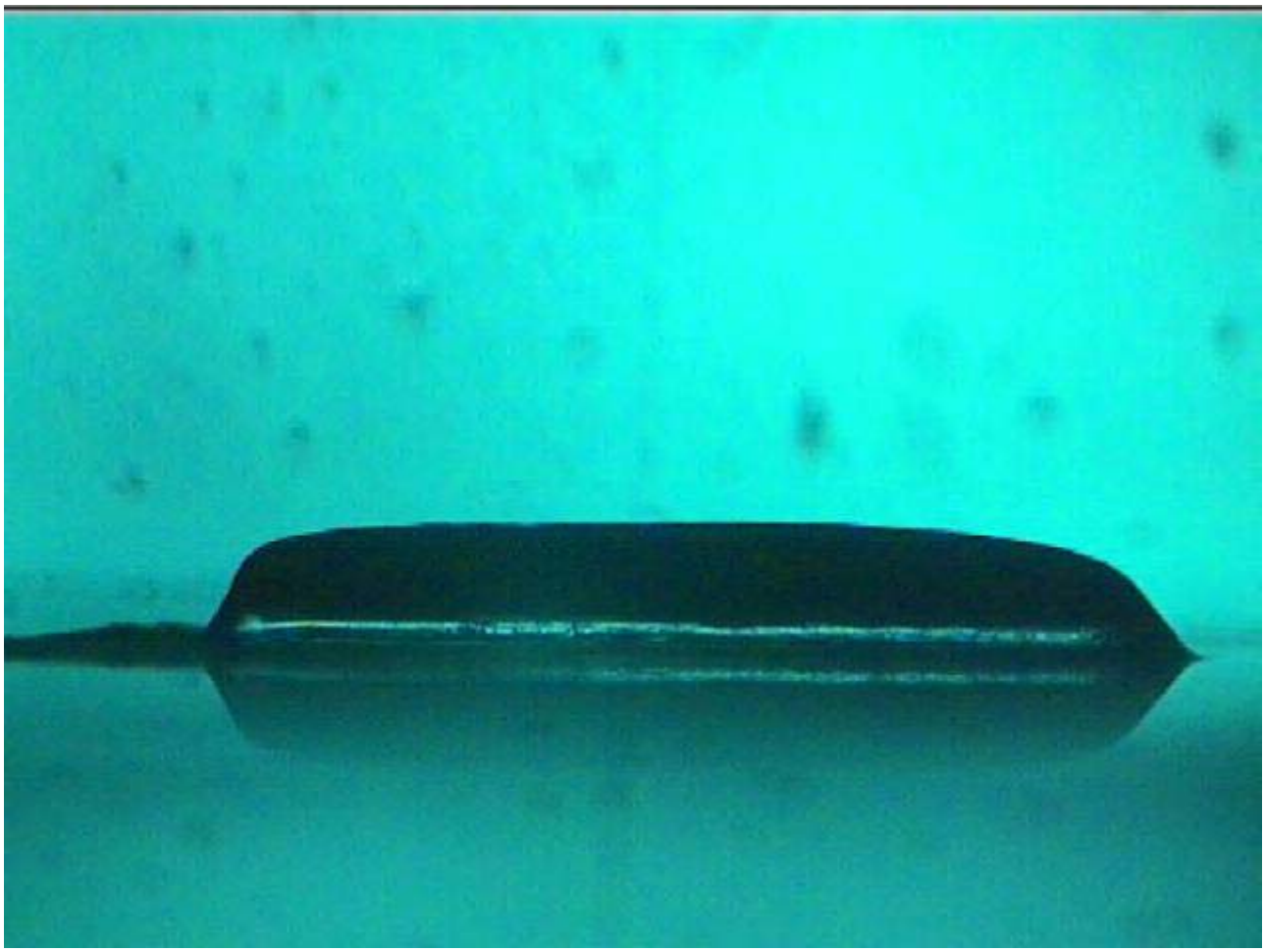

Figure E.10 Waiting time between exposures = 120s. Test layer 2

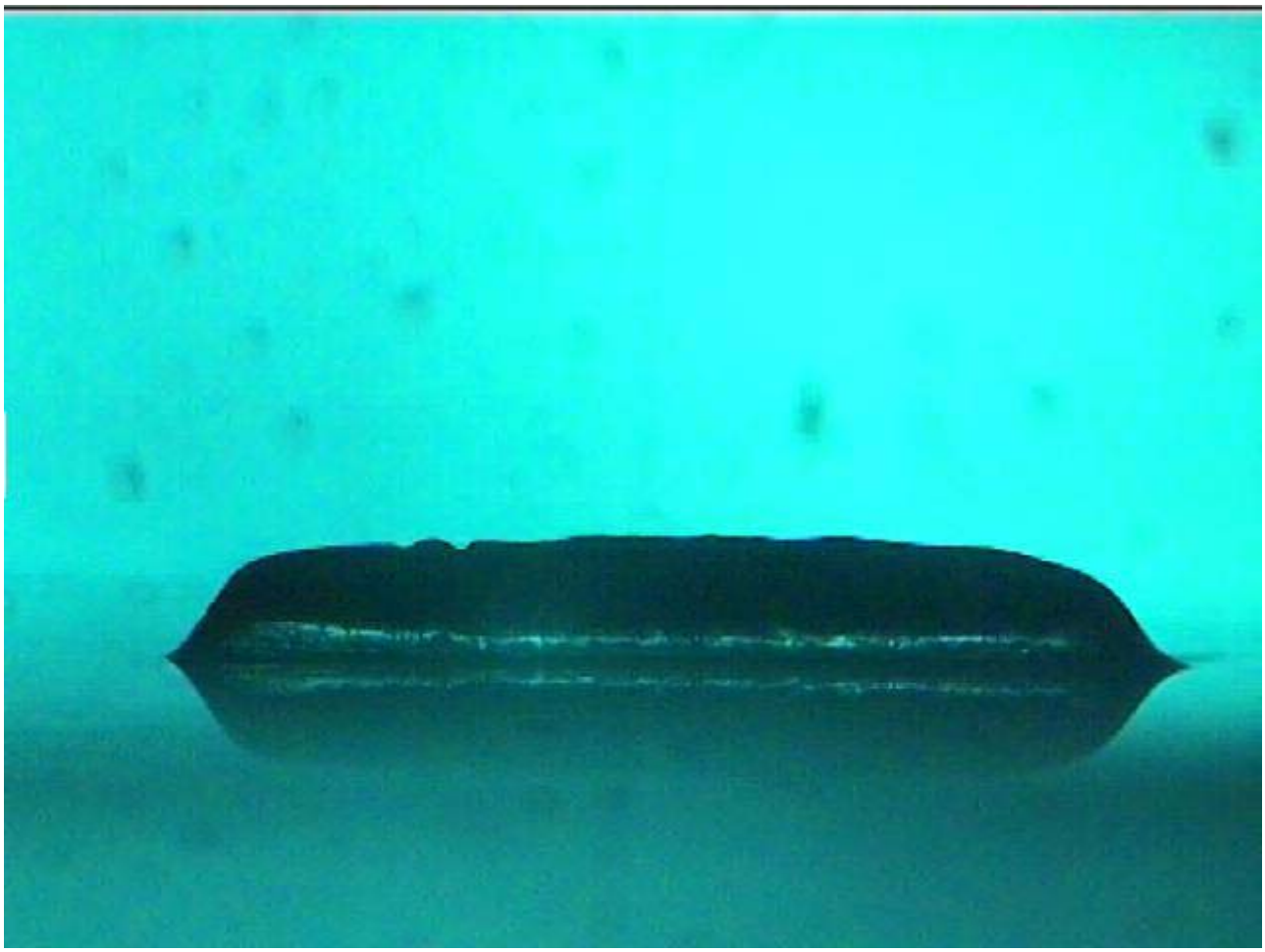

Figure E.11 Waiting time between exposures = 120s. Test layer 3

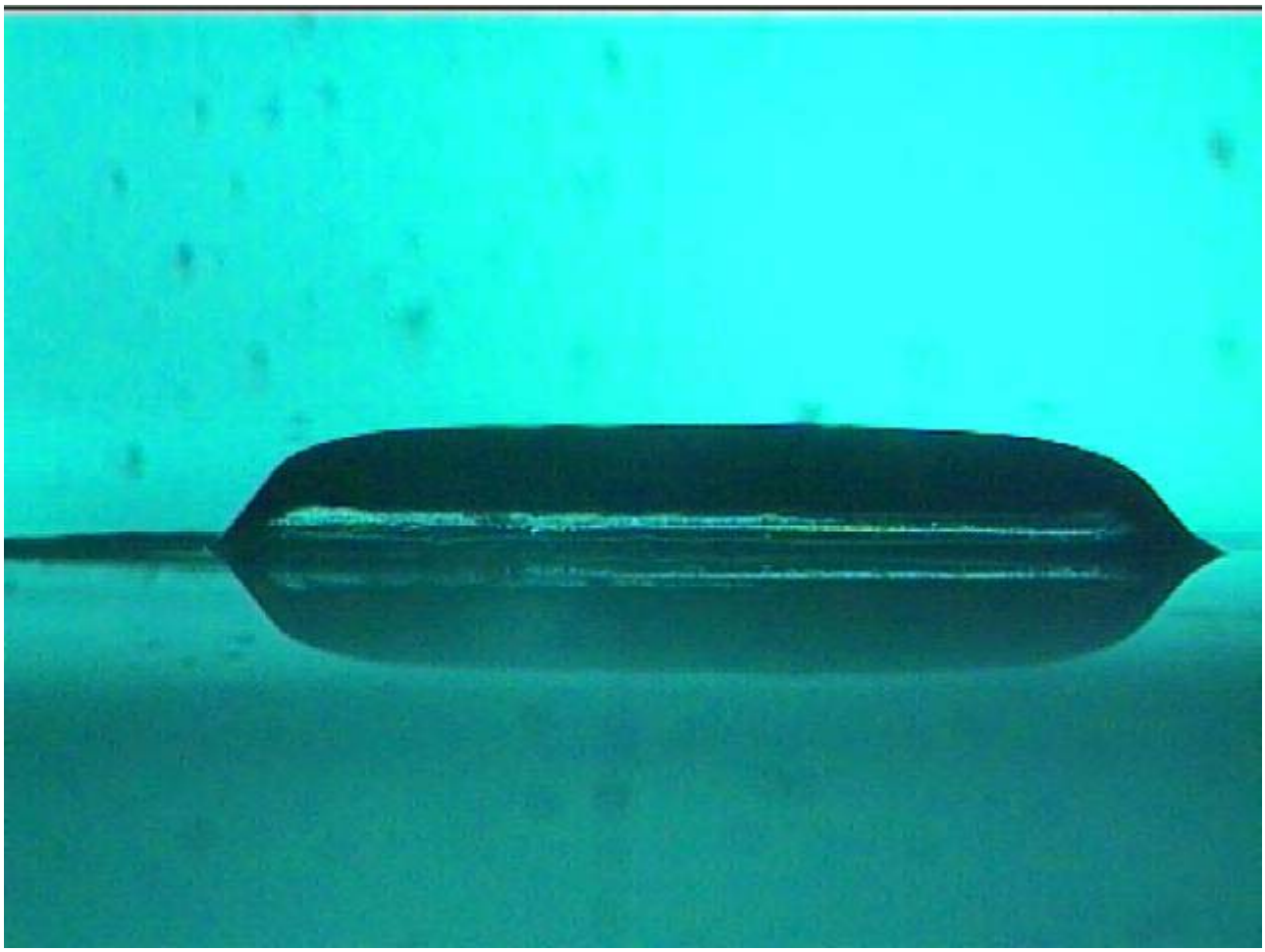

Figure E.12 Waiting time between exposures = 180s. Test layer 1

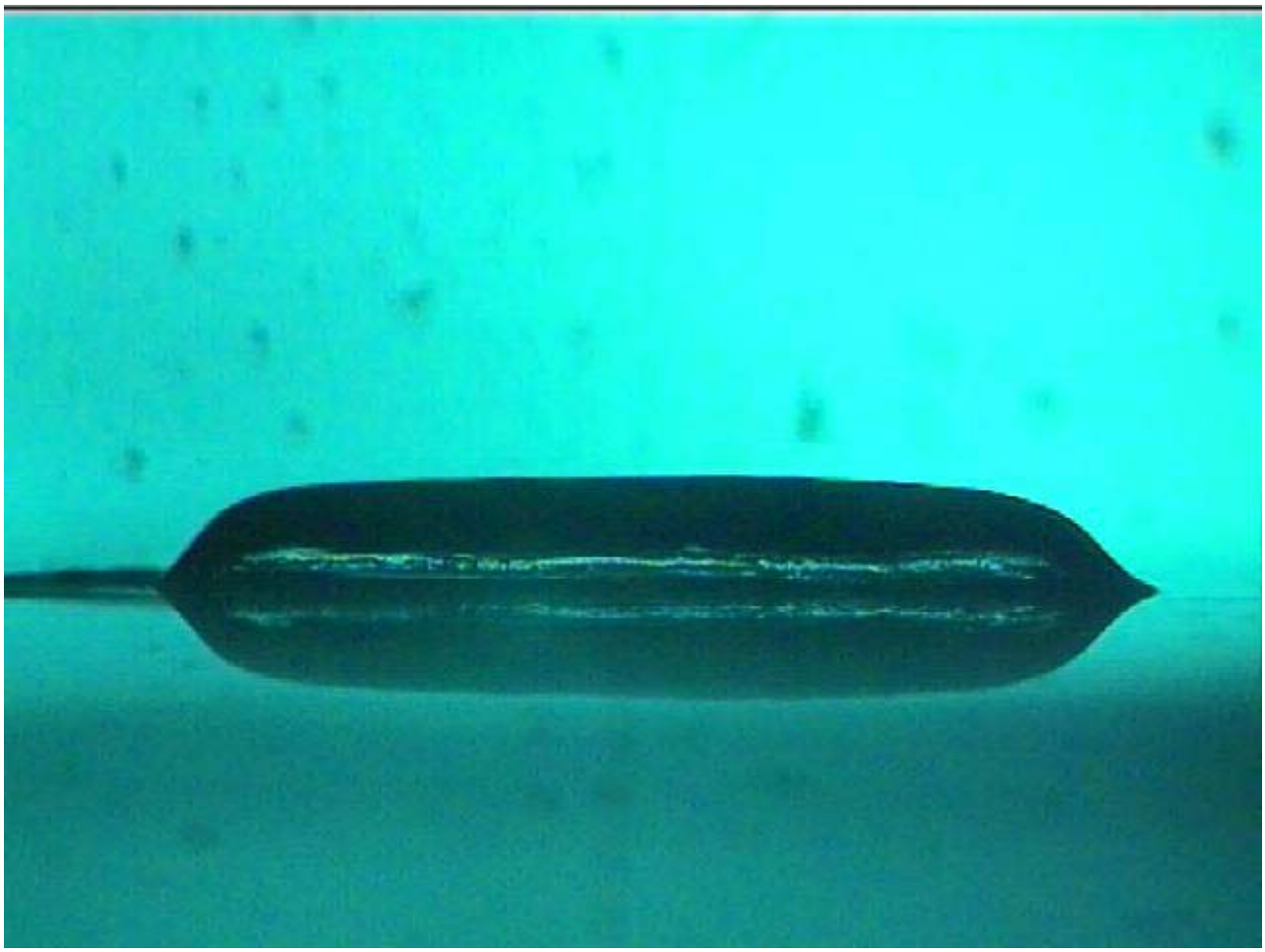

Figure E.13 Waiting time between exposures = 180s. Test layer 2

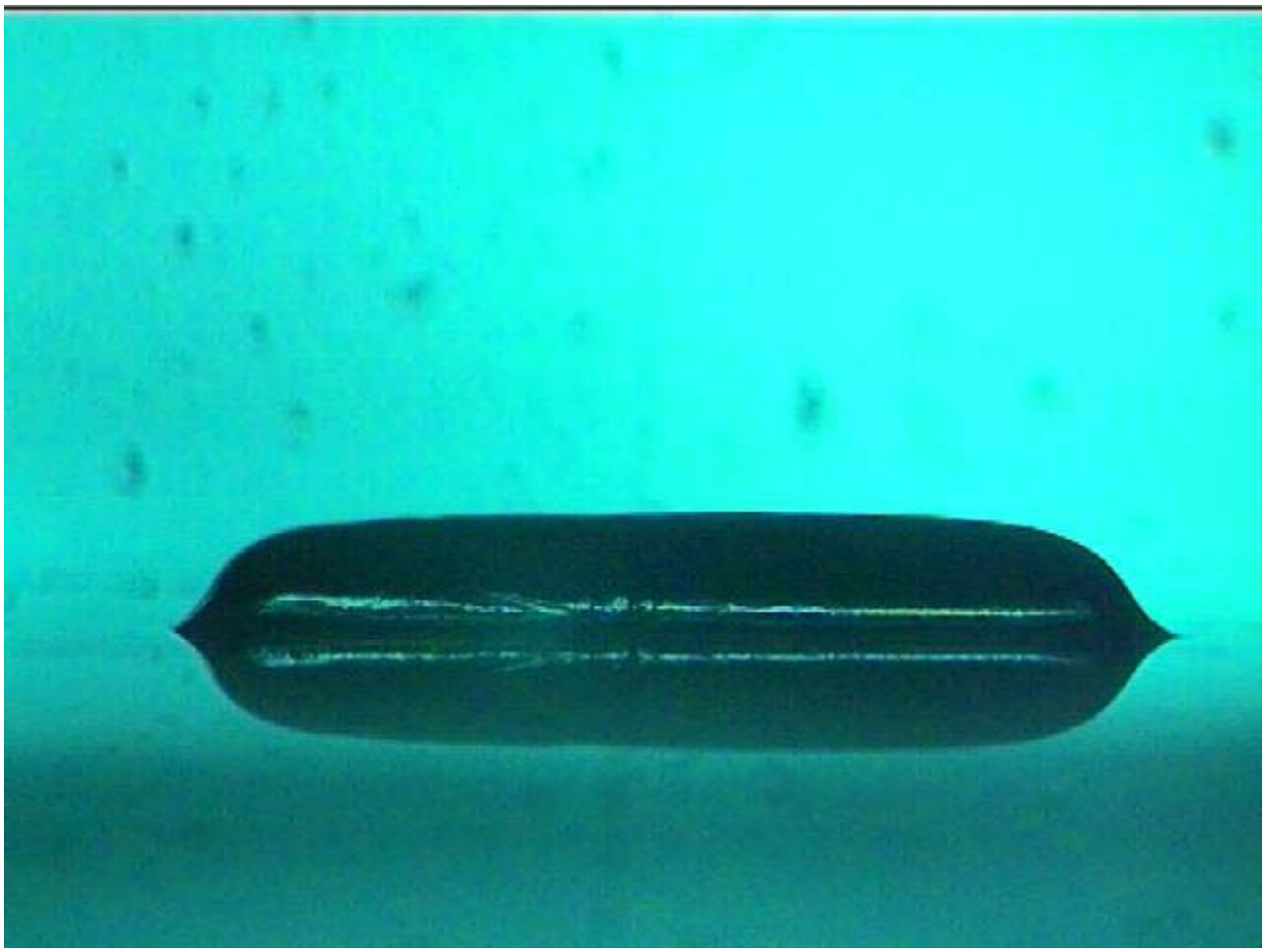

Figure E.14 Waiting time between exposures = 180s. Test layer 3

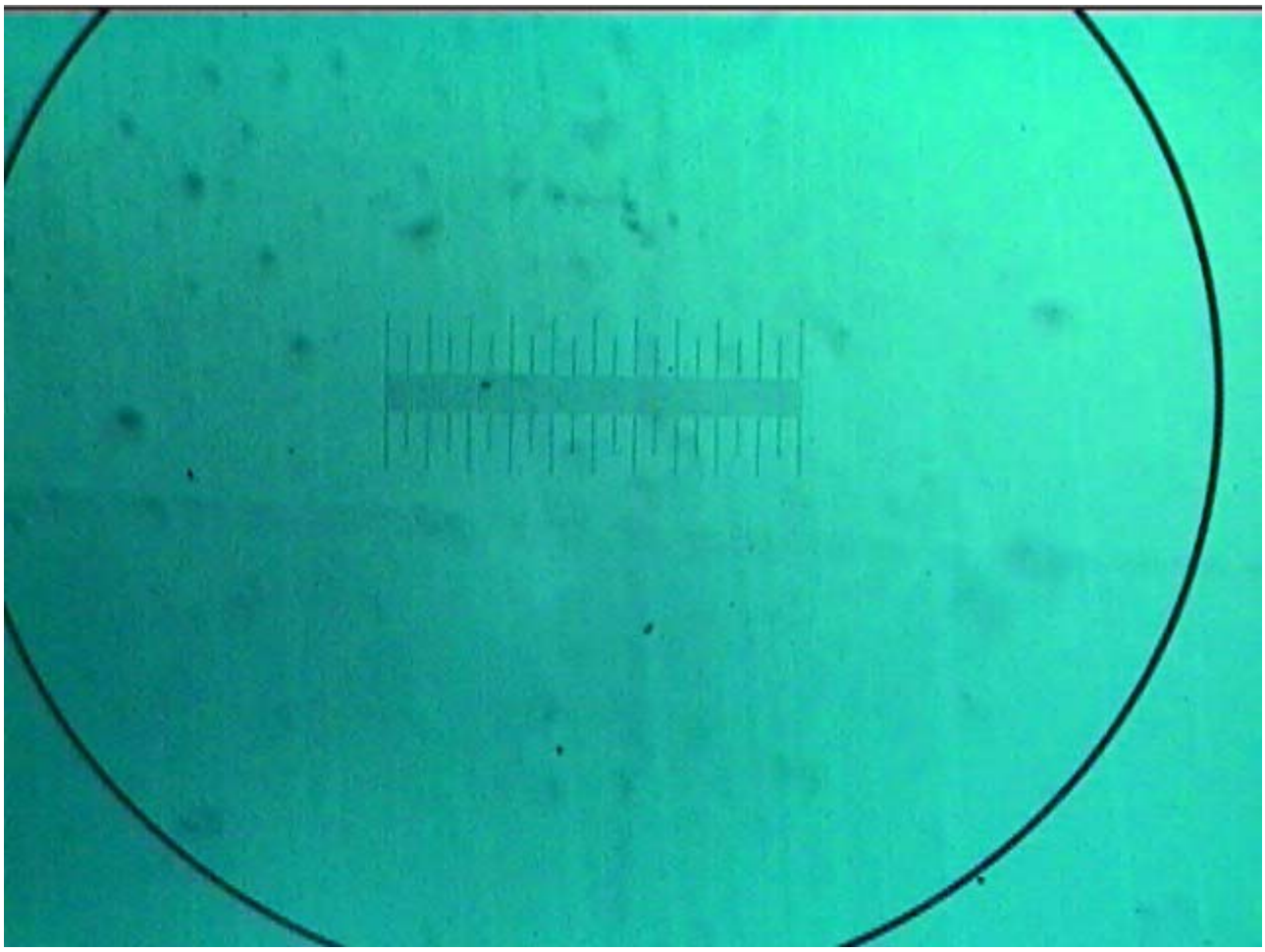

Figure E.15 Calibration scale for above layers (1 mm)

APPENDIX F. MATLAB CODE TO GENERATE DOWNFACING PROFILE OF A MULTI-LAYERED PART

The code "simulating_downfacing.m" is written to simulate the downfacing surface profile at the center of the four layered test part as shown in Figure 6.9. The code generates the irradiance distribution for the four layers using the code "bitmap_read_database", as presented in Appendix B and then computes the print through at the center of every pixel by using the Print-through model presented in Section 6.3.

simulating_downfacing.m

```
%Code reads bitmap and computes irradiance profile. Bitmap stored in
%another folder as shown in the code

clear all;
bitmap_matrix = imread('C:\Ameya\JournalPaper3\4 layer linear part 500
layer thick_ AT EDGE\layer_alongZ.bmp','BMP');
irradiance_body = zeros(601,601);
for i = 1:1:300
    for j = 1:1:100
        if bitmap_matrix(i,j) == 0
           load
(strcat('C:\Ameya\JournalPaper3\Database300.1to100\database',
(int2str(i)), '.', (int2str(j)), '.mat'))
           irradiance_body = irradiance_body + database;
           clear database;
           clear Z;
           clear Y;
        end
    end
end


for i = 1:1:300
    for j = 101:1:200
        if (bitmap_matrix(i,j) == 0)
           load
(strcat('C:\Ameya\JournalPaper3\Database300.101to200\database',
(int2str(i)), '.', (int2str(j)), '.mat'))
           irradiance_body = irradiance_body + database;
           clear database;
           clear Z;
           clear Y;
        end
    end
```

```
end



for i = 1:1:300
    for j = 201:1:300
        if bitmap_matrix(i,j) == 0
           load
(strcat('C:\Ameya\JournalPaper3\Database300.201to300\database',
(int2str(i)), '.', (int2str(j)), '.mat'))
           irradiance_body = irradiance_body + database;
           clear database;
           clear Z;
           clear Y;
        end
    end
end

for i = 1:1:601;
    for j = 1:1:601;
        for k = 1:1:2;
            B(i,j,k) = irradiance_body(i,j);
        end
    end
end

A = smooth3(smooth3(B));
irradiance = A(:,:,1);
for i = 1:1:567;
    X(i) = 10*i;
end
factor = 0.7/max(max(irradiance));
irradiance = irradiance*factor;
plot(X,max(irradiance));


%*******************************************

%Code written to compute the cure depth taking into account that there
is
%different attenuation through a cured layer and through uncured resin

%This code takes in the irradiance distribution on a resin surface.
Then,
%given a time of exposure, it computes the cure depth at all the points
on
%the resin surface. The time domain is discretized into deltat seconds.

%DpL is the depth of penetration throug liquid and DpS through solid.

%Code written by Ameya on June 27, 2007
clear irradiance1;
clear irradiance2;
clear irradiance3;
clear irradiance4;
```

```
irradiance1 = irradiance;
for z = 600:-1:180;
    irradiance2(z,:) = irradiance1((z-50),:);
end
for z = 600:-1:180;
    irradiance3(z,:) = irradiance1((z-100),:);
end
for z = 600:-1:180;
    irradiance4(z,:) = irradiance1((z-150),:);
end

%Creating the four exposure matrices

clear cd;
clear Cd;

clear T1;
clear T2;
clear T3;
clear T4;



% Now, we have a seperate code for the four steps.

%************************************************%
%Step on layer 1 from z = 368 to 417
T1 = 32;
T2 = 80;
T3 = 80;
T4 = 80;

for z = 1:1:367;
    cd(z) = 2000;
end

LT1 = 500;
LT2 = 500;
LT3 = 500;
LT4 = 500;
DpL = 190;
Ec = 9.81;
for z = 368:1:417;
    y = 300
    H1 = irradiance1(z,y);
    H2 = irradiance2(z,y);
    H3 = irradiance3(z,y);
    H4 = irradiance4(z,y);
    E1 = H1*T1;
    E2 = H2*T2;
    E3 = H3*T3;
    E4 = H4*T4;
```

```
    PT1 = 19.649*E1-207.72-LT1;


    EPT2 = E2 - (LT2+207.72)/19.649; %Energy seeping from 2nd layer
    waitingtime2 = 60 + (LT2+207.72)/19.649/H2; % Total waiting time
    k2 = 0.2629*log(waitingtime2)-0.3637; %Radical diffusion factor
    Eb = (1-k2)*Ec; %Energy already at bottom surfacel
    Eb2 = Eb + EPT2; %Total energy causing print through;
    PT2 = 19.649*Eb2-207.72;
    if PT2 < 0
       PT2 = 0;
    end

    EPT3 = E3 - (LT3+207.72)/19.649; %Energy seeping from 3rd layer
    waitingtime3 = 60 + (LT3+207.72)/19.649/H3; % Total waiting time
    k3 = 0.2629*log(waitingtime3)-0.3637; %Radical diffusion factor
    Eb = (1-k3)*Ec; %Energy already at bottom surfacel
    Eb3 = Eb + EPT3; %Total energy causing print through;
    PT3 = 19.649*Eb3-207.72;
    if PT3 < 0
        PT3 = 0;
    end

    EPT4 = E4 - (LT4+207.72)/19.649; %Energy seeping from 4th layer
    waitingtime4 = 60 + (LT4+207.72)/19.649/H4; % Total waiting time
    k4 = 0.2629*log(waitingtime4)-0.3637; %Radical diffusion factor
    Eb = (1-k4)*Ec; %Energy already at bottom surfacel
    Eb4 = Eb + EPT4; %Total energy causing print through;
    PT4 = 19.649*Eb4-207.72;
    if PT4 < 0
        PT4 = 0;
    end

    cd(z) = LT1 + LT2 + LT3 + LT4 + PT1 + PT2 + PT3 + PT4;
end

%Step on layer 1
finished************************************************************%


%***********************************************%
%Step on layer 2 from z = 418 to 467
clear T1;
clear T2;
clear T3;
clear T4;

T2 = 60;
T3 = 80;
T4 = 80;


LT2 = 500;
```

```
LT3 = 500;
LT4 = 500;
DpL = 190;
Ec = 9.81;
for z = 418:1:467;
    y = 300;
    H2 = irradiance2(z,y);
    H3 = irradiance3(z,y);
    H4 = irradiance4(z,y);
    E2 = H2*T2;
    E3 = H3*T3;
    E4 = H4*T4;

    PT2 = 19.649*E2-207.72-LT2;

    EPT3 = E3 - (LT3+207.72)/19.649; %Energy seeping from 3rd layer
    waitingtime3 = 60 + (LT3+207.72)/19.649/H3; % Total waiting time
    k3 = 0.2629*log(waitingtime3)-0.3637; %Radical diffusion factor
    Eb = (1-k3)*Ec; %Energy already at bottom surfacel
    Eb3 = Eb + EPT3; %Total energy causing print through;
    PT3 = 19.649*Eb3-207.72;
    if PT3 < 0
        PT3 = 0;
    end

    EPT4 = E4 - (LT4+207.72)/19.649; %Energy seeping from 4th layer
    waitingtime4 = 60 + (LT4+207.72)/19.649/H4; % Total waiting time
    k4 = 0.2629*log(waitingtime4)-0.3637; %Radical diffusion factor
    Eb = (1-k4)*Ec; %Energy already at bottom surfacel
    Eb4 = Eb + EPT4; %Total energy causing print through;
    PT4 = 19.649*Eb4-207.72;
    if PT4 < 0
       PT4 = 0;
    end

    cd(z) = LT2 + LT3 + LT4 + PT2 + PT3 + PT4;
end

%Step on layer 2
finished**********************************************************%

%************************************************%
%Step on layer 3 from z = 468 to 517
clear T1;
clear T2;
clear T3;
clear T4;

T3 = 65;
T4 = 80;


LT3 = 500;
LT4 = 500;
DpL = 190;
```

```
Ec = 9.81;
for z = 468:1:517;
    y = 300;
    H3 = irradiance3(z,y);
    H4 = irradiance4(z,y);
    E3 = H3*T3;
    E4 = H4*T4;

    PT3 = 19.649*E3-207.72-LT3;

    EPT4 = E4 - (LT4+207.72)/19.649; %Energy seeping from 4th layer
    waitingtime4 = 60 + (LT4+207.72)/19.649/H4; % Total waiting time
    k4 = 0.2629*log(waitingtime4)-0.3637; %Radical diffusion factor
    Eb = (1-k4)*Ec; %Energy already at bottom surfacel
    Eb4 = Eb + EPT4; %Total energy causing print through;
    PT4 = 19.649*Eb4-207.72;
    if PT4 < 0
       PT4 = 0;
    end

    cd(z) = LT3 + LT4 + PT3 + PT4;
end

%Step on layer 3
finished************************************************************%

%*********************************************%
%Step on layer 4 from z = 518 to 567

clear T1;
clear T2;
clear T3;
clear T4;


T4 = 84;

LT4 = 500;
DpL = 190;
Ec = 9.81;
for z = 518:1:567;
    y = 300;
    H4 = irradiance4(z,y);
    E4 = H4*T4;

    PT4 = 19.649*E4-207.72-LT4;

    cd(z) = LT4 + PT4;
end
%Step on layer 4
finished************************************************************%

for i = 1:1:567;
    Y(i) = X(i)-4170+2500;
```

```
end
Cd = 2000-cd
plot(Y,Cd);

axis equal
line(1500:4000,2000)
line(1500:4000,1500)
line(4000,1500:2000)
line(1500,1500:2000)
line(1000:3500,1500)
line(1000:3500,1000)
line(3500,1000:1500)
line(1000,1000:1500)
line(500:3000,1000)
line(500:3000,500)
line(3000,500:1000)
line(500,500:1000)
line(0:2500,500)
line(0:2500,0)
line(2500,0:500)
line(0,0:500)
```

APPENDIX G. MATLAB CODE USED TO IMPLEMENT COMPENSATION ZONE APPROACH

The code "simulating_downfacing_inverse_design.m" is used to implement the Compensation zone approach. This code computes the time of exposure of every micromirror on the overhanging portion of every layer in order to obtain the exact linear down facing surface on the test part in Figure 6.9.

simulating_downfacing_inverse_design.m

```
%Code reads bitmap and computes irradiance profile. Bitmap stored in
%another folder as shown in the code

clear all;
bitmap_matrix = imread('C:\Ameya\JournalPaper3\4 layer linear part 500
layer thick_ AT EDGE\layer_alongZ.bmp','BMP');
irradiance_body = zeros(601,601);
for i = 1:1:300
    for j = 1:1:100
        if bitmap_matrix(i,j) == 0
            load
(strcat('C:\Ameya\JournalPaper3\Database300.1to100\database',
(int2str(i)), '.', (int2str(j)), '.mat'))
            irradiance_body = irradiance_body + database;
            clear database;
            clear Z;
            clear Y;
        end
    end
end


for i = 1:1:300
    for j = 101:1:200
        if (bitmap_matrix(i,j) == 0)
            load
(strcat('C:\Ameya\JournalPaper3\Database300.101to200\database',
(int2str(i)), '.', (int2str(j)), '.mat'))
            irradiance_body = irradiance_body + database;
            clear database;
            clear Z;
            clear Y;
        end
    end
end
```

```
for i = 1:1:300
    for j = 201:1:300
        if bitmap_matrix(i,j) == 0
           load
(strcat('C:\Ameya\JournalPaper3\Database300.201to300\database',
(int2str(i)), '.', (int2str(j)), '.mat'))
           irradiance_body = irradiance_body + database;
           clear database;
           clear Z;
           clear Y;
        end
    end
end

for i = 1:1:601;
    for j = 1:1:601;
        for k = 1:1:2;
            B(i,j,k) = irradiance_body(i,j);
        end
    end
end

A = smooth3(smooth3(B));
irradiance = A(:,:,1);
for i = 1:1:567;
    X(i) = 10*i;
end
factor = 0.7/max(max(irradiance));
irradiance = irradiance*factor;
%plot(X,max(irradiance));


%*******************************************

%Code written to compute the cure depth taking into account that there
is
%different attenuation through a cured layer and through uncured resin

%This code takes in the irradiance distribution on a resin surface.
Then,
%given a time of exposure, it computes the cure depth at all the points
on
%the resin surface. The time domain is discretized into deltat seconds.

%DpL is the depth of penetration throug liquid and DpS through solid.

%Code written by Ameya on June 27, 2007
clear irradiance1;
clear irradiance2;
clear irradiance3;
clear irradiance4;


irradiance1 = irradiance;
for z = 600:-1:180;
```

```
    irradiance2(z,:) = irradiance1((z-50),:);
end
for z = 600:-1:180;
    irradiance3(z,:) = irradiance1((z-100),:);
end
for z = 600:-1:180;
    irradiance4(z,:) = irradiance1((z-150),:);
end

%Creating the four exposure matrices

clear cd;
clear Cd;

clear T1;
clear T2;
clear T3;
clear T4;



% Now, we have a seperate code for the four steps.

%************************************************%
%Step on layer 1 from z = 368 to 417
T1 = 80;
T2 = 80;
T3 = 80;
T4 = 80;

for z = 1:1:392;
    cd(z) = 2000;

end

LT1 = 500;
LT2 = 500;
LT3 = 500;
LT4 = 500;
DpL = 190;
Ec = 9.81;

for z = 168:1:392;
    Time1(z) = 80;
end

for z = 418:1:567;
    Time1(z) = 0;
end

for z = 393:1:417;
    y = 300
    T1 = 80
    fun = 3000;
```

```
    target = 2000-10*(z-392);
    H1 = irradiance1(z,y);
    H2 = irradiance2(z,y);
    H3 = irradiance3(z,y);
    H4 = irradiance4(z,y);
    while abs(fun - target)> 10;
        E1 = H1*T1;
        E2 = H2*T2;
        E3 = H3*T3;
        E4 = H4*T4;

        PT1 = 19.649*E1-207.72-LT1;

        EPT2 = E2 - (LT2+207.72)/19.649; %Energy seeping from 2nd layer
        waitingtime2 = 60 + (LT2+207.72)/19.649/H2; % Total waiting
time
        k2 = 0.2629*log(waitingtime2)-0.3637; %Radical diffusion factor
        Eb = (1-k2)*Ec; %Energy already at bottom surfacel
        Eb2 = Eb + EPT2; %Total energy causing print through;
        PT2 = 19.649*Eb2-207.72;
        if PT2 < 0
           PT2 = 0;
        end

        EPT3 = E3 - (LT3+207.72)/19.649; %Energy seeping from 3rd layer
        waitingtime3 = 60 + (LT3+207.72)/19.649/H3; % Total waiting
time
        k3 = 0.2629*log(waitingtime3)-0.3637; %Radical diffusion factor
        Eb = (1-k3)*Ec; %Energy already at bottom surfacel
        Eb3 = Eb + EPT3; %Total energy causing print through;
        PT3 = 19.649*Eb3-207.72;
        if PT3 < 0
            PT3 = 0;
        end

        EPT4 = E4 - (LT4+207.72)/19.649; %Energy seeping from 4th layer
        waitingtime4 = 60 + (LT4+207.72)/19.649/H4; % Total waiting
time
        k4 = 0.2629*log(waitingtime4)-0.3637; %Radical diffusion factor
        Eb = (1-k4)*Ec; %Energy already at bottom surfacel
        Eb4 = Eb + EPT4; %Total energy causing print through;
        PT4 = 19.649*Eb4-207.72;
        if PT4 < 0
            PT4 = 0;
        end

        fun = LT1 + LT2 + LT3 + LT4 + PT1 + PT2 + PT3 + PT4;
        if fun>target;
            T1 = T1-1;
        end
        if fun<target;
            T1 = T1+1;
        end
    end
Time1(z) = T1;
cd(z) = fun;
```

```
end

%Step on layer 1
finished************************************************************%


%************************************************%
%Step on layer 2 from z = 418 to 467
clear T1;
clear T2;
clear T3;
clear T4;

T2 = 80;
T3 = 80;
T4 = 80;


LT2 = 500;
LT3 = 500;
LT4 = 500;
DpL = 190;
Ec = 9.81;

for z = 218:1:417;
    Time2(z) = 80;
end

for z = 468:1:567;
    Time2(z) = 0;
end

for z = 418:1:467;
    y = 300;
    T2 = 80;
    fun = 3000;
    target = 2000-10*(z-392);
    H2 = irradiance2(z,y);
    H3 = irradiance3(z,y);
    H4 = irradiance4(z,y);
    while abs(fun-target)>10;

        E2 = H2*T2;
        E3 = H3*T3;
        E4 = H4*T4;

        PT2 = 19.649*E2-207.72-LT2;

        EPT3 = E3 - (LT3+207.72)/19.649; %Energy seeping from 3rd layer
        waitingtime3 = 60 + (LT3+207.72)/19.649/H3; % Total waiting
time
        k3 = 0.2629*log(waitingtime3)-0.3637; %Radical diffusion factor
        Eb = (1-k3)*Ec; %Energy already at bottom surfacel
```

```
        Eb3 = Eb + EPT3; %Total energy causing print through;
        PT3 = 19.649*Eb3-207.72;
        if PT3 < 0
            PT3 = 0;
        end

        EPT4 = E4 - (LT4+207.72)/19.649; %Energy seeping from 4th layer
        waitingtime4 = 60 + (LT4+207.72)/19.649/H4; % Total waiting
time
        k4 = 0.2629*log(waitingtime4)-0.3637; %Radical diffusion factor
        Eb = (1-k4)*Ec; %Energy already at bottom surfacel
        Eb4 = Eb + EPT4; %Total energy causing print through;
        PT4 = 19.649*Eb4-207.72;
        if PT4 < 0
           PT4 = 0;
        end

        fun = LT2 + LT3 + LT4 + PT2 + PT3 + PT4;
        if fun > target;
            T2 = T2-1;
        end
        if fun < target;
            T2 = T2 + 1;
        end
    end
    Time2(z) = T2;
    cd(z) = fun;
end

%Step on layer 2
finished*****************************************************%

%************************************************%
%Step on layer 3 from z = 468 to 517
clear T1;
clear T2;
clear T3;
clear T4;

T3 = 80;
T4 = 80;


LT3 = 500;
LT4 = 500;
DpL = 190;
Ec = 9.81;

for z = 268:1:467;
    Time3(z) = 80;
end

for z = 518:1:567;
    Time3(z) = 0;
end
```

```
for z = 468:1:517;
    y = 300;
    T3 = 80;
    fun = 3000;
    target = 2000-10*(z-392);
    H3 = irradiance3(z,y);
    H4 = irradiance4(z,y);
    while abs(fun-target)>10;
        E3 = H3*T3;
        E4 = H4*T4;

        PT3 = 19.649*E3-207.72-LT3;

        EPT4 = E4 - (LT4+207.72)/19.649; %Energy seeping from 4th layer
        waitingtime4 = 60 + (LT4+207.72)/19.649/H4; % Total waiting
time
        k4 = 0.2629*log(waitingtime4)-0.3637; %Radical diffusion factor
        Eb = (1-k4)*Ec; %Energy already at bottom surfacel
        Eb4 = Eb + EPT4; %Total energy causing print through;
        PT4 = 19.649*Eb4-207.72;
        if PT4 < 0
           PT4 = 0;
        end

        fun = LT3 + LT4 + PT3 + PT4;

        if fun > target;
            T3 = T3 -1;
        end
        if fun < target;
            T3 = T3 + 1;
        end
    end
    Time3(z) = T3;
    cd(z) = fun;

end

%Step on layer 3
finished************************************************************%

%*********************************************%
%Step on layer 4 from z = 518 to 567

clear T1;
clear T2;
clear T3;
clear T4;


T4 = 80;

LT4 = 500;
```

```
DpL = 190;
Ec = 9.81;

for z = 317:1:517;
    Time4(z) = 80;
end

for z = 518:1:567;
    y = 300;
    fun = 3000;
    target = 2000-10*(z-392);
    while abs(fun-target) > 10;
        H4 = irradiance4(z,y);
        E4 = H4*T4;

        PT4 = 19.649*E4-207.72-LT4;

        fun = LT4 + PT4;
        if fun > target;
            T4 = T4 - 1;
        end
        if fun < target;
            T4 = T4 + 1;
        end
    end
    Time4(z) = T4;
    cd(z) = fun;
end
%Step on layer 4
finished*********************************************************%

for i = 1:1:567;
    Y(i) = X(i)-4170+2500;
end
Cd = 2000-cd
plot(Y,Cd);

axis equal
line(1500:4000,2000)
line(1500:4000,1500)
line(4000,1500:2000)
line(1500,1500:2000)
line(1000:3500,1500)
line(1000:3500,1000)
line(3500,1000:1500)
line(1000,1000:1500)
line(500:3000,1000)
line(500:3000,500)
line(3000,500:1000)
line(500,500:1000)
line(0:2500,500)
line(0:2500,0)
line(2500,0:500)
line(0,0:500)
```

APPENDIX H. MATLAB CODE TO SIMULATE THE DOWN FACING SURFACE PROFILE OF A PART WITH THE OVERHANGING PORTION DISCRETIZED INTO TWO REGIONS

In the Matlab code "simulating_downfacing_discretized.m", profile of the part that would be cured for the times of exposure for every layer as mentioned in Section 6.5.2 is presented.

Simulating_downfacing_discretized.m

```
%Code reads bitmap and computes irradiance profile. Bitmap stored in
%another folder as shown in the code

clear all;
bitmap_matrix = imread('C:\Ameya\JournalPaper3\4 layer linear part 500
layer thick_ AT EDGE\layer_alongZ.bmp','BMP');
irradiance_body = zeros(601,601);
for i = 1:1:300
    for j = 1:1:100
        if bitmap_matrix(i,j) == 0
           load
(strcat('C:\Ameya\JournalPaper3\Database300.1to100\database',
(int2str(i)), '.', (int2str(j)), '.mat'))
           irradiance_body = irradiance_body + database;
           clear database;
           clear Z;
           clear Y;
        end
    end
end


for i = 1:1:300
    for j = 101:1:200
        if (bitmap_matrix(i,j) == 0)
           load
(strcat('C:\Ameya\JournalPaper3\Database300.101to200\database',
(int2str(i)), '.', (int2str(j)), '.mat'))
           irradiance_body = irradiance_body + database;
           clear database;
           clear Z;
           clear Y;
        end
    end
end



for i = 1:1:300
```

```
    for j = 201:1:300
        if bitmap_matrix(i,j) == 0
           load
(strcat('C:\Ameya\JournalPaper3\Database300.201to300\database',
(int2str(i)), '.', (int2str(j)), '.mat'))
           irradiance_body = irradiance_body + database;
           clear database;
           clear Z;
           clear Y;
        end
    end
end

for i = 1:1:601;
    for j = 1:1:601;
        for k = 1:1:2;
            B(i,j,k) = irradiance_body(i,j);
        end
    end
end

A = smooth3(smooth3(B));
irradiance = A(:,:,1);
for i = 1:1:567;
    X(i) = 10*i;
end
factor = 0.7/max(max(irradiance));
irradiance = irradiance*factor;
plot(X,max(irradiance));


%*******************************************

%Code written to compute the cure depth taking into account that there
is
%different attenuation through a cured layer and through uncured resin

%This code takes in the irradiance distribution on a resin surface.
Then,
%given a time of exposure, it computes the cure depth at all the points
on
%the resin surface. The time domain is discretized into deltat seconds.

%DpL is the depth of penetration throug liquid and DpS through solid.

%Code written by Ameya on June 27, 2007
clear irradiance1;
clear irradiance2;
clear irradiance3;
clear irradiance4;


irradiance1 = irradiance;
for z = 600:-1:180;
    irradiance2(z,:) = irradiance1((z-50),:);
```

```
end
for z = 600:-1:180;
    irradiance3(z,:) = irradiance1((z-100),:);
end
for z = 600:-1:180;
    irradiance4(z,:) = irradiance1((z-150),:);
end

%Creating the four exposure matrices

clear cd;
clear Cd;

clear T1;
clear T2;
clear T3;
clear T4;



% Now, we have a seperate code for the four steps.

%************************************************%
%Step on layer 1 from z = 368 to 417

T2 = 80;
T3 = 80;
T4 = 80;

for z = 1:1:392;
    cd(z) = 2000;
end

LT1 = 500;
LT2 = 500;
LT3 = 500;
LT4 = 500;
DpL = 190;
Ec = 9.81;
for z = 393:1:417;
    T1 = 13.3
    Time1(z) = T1;
    y = 300
    H1 = irradiance1(z,y);
    H2 = irradiance2(z,y);
    H3 = irradiance3(z,y);
    H4 = irradiance4(z,y);
    E1 = H1*T1;
    E2 = H2*T2;
    E3 = H3*T3;
    E4 = H4*T4;

    PT1 = 19.649*E1-207.72-LT1;
```

```
    EPT2 = E2 - (LT2+207.72)/19.649; %Energy seeping from 2nd layer
    waitingtime2 = 60 + (LT2+207.72)/19.649/H2; % Total waiting time
    k2 = 0.2629*log(waitingtime2)-0.3637; %Radical diffusion factor
    Eb = (1-k2)*Ec; %Energy already at bottom surfacel
    Eb2 = Eb + EPT2; %Total energy causing print through;
    PT2 = 19.649*Eb2-207.72;
    if PT2 < 0
       PT2 = 0;
    end

    EPT3 = E3 - (LT3+207.72)/19.649; %Energy seeping from 3rd layer
    waitingtime3 = 60 + (LT3+207.72)/19.649/H3; % Total waiting time
    k3 = 0.2629*log(waitingtime3)-0.3637; %Radical diffusion factor
    Eb = (1-k3)*Ec; %Energy already at bottom surfacel
    Eb3 = Eb + EPT3; %Total energy causing print through;
    PT3 = 19.649*Eb3-207.72;
    if PT3 < 0
        PT3 = 0;
    end

    EPT4 = E4 - (LT4+207.72)/19.649; %Energy seeping from 4th layer
    waitingtime4 = 60 + (LT4+207.72)/19.649/H4; % Total waiting time
    k4 = 0.2629*log(waitingtime4)-0.3637; %Radical diffusion factor
    Eb = (1-k4)*Ec; %Energy already at bottom surfacel
    Eb4 = Eb + EPT4; %Total energy causing print through;
    PT4 = 19.649*Eb4-207.72;
    if PT4 < 0
        PT4 = 0;
    end

    cd(z) = LT1 + LT2 + LT3 + LT4 + PT1 + PT2 + PT3 + PT4;
end


%Step on layer 1
finished*****************************************************%


%************************************************%
%Step on layer 2 from z = 418 to 467
clear T1;
clear T2;
clear T3;
clear T4;


T3 = 80;
T4 = 80;


LT2 = 500;
LT3 = 500;
LT4 = 500;
```

```
DpL = 190;
Ec = 9.81;
for z = 418:1:442;
    T2 = 40.1;
    Time2(z) = T2;
    y = 300;
    H2 = irradiance2(z,y);
    H3 = irradiance3(z,y);
    H4 = irradiance4(z,y);
    E2 = H2*T2;
    E3 = H3*T3;
    E4 = H4*T4;

    PT2 = 19.649*E2-207.72-LT2;

    EPT3 = E3 - (LT3+207.72)/19.649; %Energy seeping from 3rd layer
    waitingtime3 = 60 + (LT3+207.72)/19.649/H3; % Total waiting time
    k3 = 0.2629*log(waitingtime3)-0.3637; %Radical diffusion factor
    Eb = (1-k3)*Ec; %Energy already at bottom surfacel
    Eb3 = Eb + EPT3; %Total energy causing print through;
    PT3 = 19.649*Eb3-207.72;
    if PT3 < 0
        PT3 = 0;
    end

    EPT4 = E4 - (LT4+207.72)/19.649; %Energy seeping from 4th layer
    waitingtime4 = 60 + (LT4+207.72)/19.649/H4; % Total waiting time
    k4 = 0.2629*log(waitingtime4)-0.3637; %Radical diffusion factor
    Eb = (1-k4)*Ec; %Energy already at bottom surfacel
    Eb4 = Eb + EPT4; %Total energy causing print through;
    PT4 = 19.649*Eb4-207.72;
    if PT4 < 0
       PT4 = 0;
    end

    cd(z) = LT2 + LT3 + LT4 + PT2 + PT3 + PT4;
end

for z = 443:1:467;
    T2 = 26.3;
    Time2(z) = T2;
    y = 300;
    H2 = irradiance2(z,y);
    H3 = irradiance3(z,y);
    H4 = irradiance4(z,y);
    E2 = H2*T2;
    E3 = H3*T3;
    E4 = H4*T4;

    PT2 = 19.649*E2-207.72-LT2;

    EPT3 = E3 - (LT3+207.72)/19.649; %Energy seeping from 3rd layer
    waitingtime3 = 60 + (LT3+207.72)/19.649/H3; % Total waiting time
    k3 = 0.2629*log(waitingtime3)-0.3637; %Radical diffusion factor
    Eb = (1-k3)*Ec; %Energy already at bottom surfacel
```

```
    Eb3 = Eb + EPT3; %Total energy causing print through;
    PT3 = 19.649*Eb3-207.72;
    if PT3 < 0
        PT3 = 0;
    end

    EPT4 = E4 - (LT4+207.72)/19.649; %Energy seeping from 4th layer
    waitingtime4 = 60 + (LT4+207.72)/19.649/H4; % Total waiting time
    k4 = 0.2629*log(waitingtime4)-0.3637; %Radical diffusion factor
    Eb = (1-k4)*Ec; %Energy already at bottom surfacel
    Eb4 = Eb + EPT4; %Total energy causing print through;
    PT4 = 19.649*Eb4-207.72;
    if PT4 < 0
       PT4 = 0;
    end

    cd(z) = LT2 + LT3 + LT4 + PT2 + PT3 + PT4;
end
%Step on layer 2
finished************************************************************%

%************************************************%
%Step on layer 3 from z = 468 to 517
clear T1;
clear T2;
clear T3;
clear T4;


T4 = 80;


LT3 = 500;
LT4 = 500;
DpL = 190;
Ec = 9.81;
for z = 468:1:492;
    T3 = 56.4;
    Time3(z) = T3;
    y = 300;
    H3 = irradiance3(z,y);
    H4 = irradiance4(z,y);
    E3 = H3*T3;
    E4 = H4*T4;

    PT3 = 19.649*E3-207.72-LT3;

    EPT4 = E4 - (LT4+207.72)/19.649; %Energy seeping from 4th layer
    waitingtime4 = 60 + (LT4+207.72)/19.649/H4; % Total waiting time
    k4 = 0.2629*log(waitingtime4)-0.3637; %Radical diffusion factor
    Eb = (1-k4)*Ec; %Energy already at bottom surfacel
    Eb4 = Eb + EPT4; %Total energy causing print through;
    PT4 = 19.649*Eb4-207.72;
    if PT4 < 0
       PT4 = 0;
```

```
    end

    cd(z) = LT3 + LT4 + PT3 + PT4;
end

for z = 493:1:517;
    T3 = 46.8;
    Time3(z) = T3;
    y = 300;
    H3 = irradiance3(z,y);
    H4 = irradiance4(z,y);
    E3 = H3*T3;
    E4 = H4*T4;

    PT3 = 19.649*E3-207.72-LT3;

    EPT4 = E4 - (LT4+207.72)/19.649; %Energy seeping from 4th layer
    waitingtime4 = 60 + (LT4+207.72)/19.649/H4; % Total waiting time
    k4 = 0.2629*log(waitingtime4)-0.3637; %Radical diffusion factor
    Eb = (1-k4)*Ec; %Energy already at bottom surfacel
    Eb4 = Eb + EPT4; %Total energy causing print through;
    PT4 = 19.649*Eb4-207.72;
    if PT4 < 0
       PT4 = 0;
    end

    cd(z) = LT3 + LT4 + PT3 + PT4;
end
%Step on layer 3
finished************************************************************%

%************************************************%
%Step on layer 4 from z = 518 to 567

clear T1;
clear T2;
clear T3;
clear T4;




LT4 = 500;
DpL = 190;
Ec = 9.81;
for z = 518:1:542;
    T4 = 71.8;
    Time4(z) = T4;
    y = 300;
    H4 = irradiance4(z,y);
    E4 = H4*T4;

    PT4 = 19.649*E4-207.72-LT4;
```

```
    cd(z) = LT4 + PT4;
end

for z = 543:1:567;
    T4 = 57.4;
    Time4(z) = T4;
    y = 300;
    H4 = irradiance4(z,y);
    E4 = H4*T4;

    PT4 = 19.649*E4-207.72-LT4;

    cd(z) = LT4 + PT4;
end
%Step on layer 4
finished*****************************************************%

for i = 1:1:567;
    Y(i) = X(i)-4170+2500;
end
Cd = 2000-cd
plot(Y,Cd);

axis equal
line(1500:4000,2000)
line(1500:4000,1500)
line(4000,1500:2000)
line(1500,1500:2000)
line(1000:3500,1500)
line(1000:3500,1000)
line(3500,1000:1500)
line(1000,1000:1500)
line(500:3000,1000)
line(500:3000,500)
line(3000,500:1000)
line(500,500:1000)
line(0:2500,500)
line(0:2500,0)
line(2500,0:500)
line(0,0:500)
```

APPENDIX I. MATLAB CODE TO IMPLEMENT ROSEN'S GRADIENT PROJECTION ALGORITHM TO OPTIMIZE THE DEVIATION FUNCTION OF THE SLICING COMPROMISE DSP

In the Matlab code "gradient_projection.m", an exhaustive search across the entire range of the possible number of layers, from 3 to 30 is performed. For every number of layers, the gradient projection method is executed as explained in Chapter 7. The Matlab code "f.m" computes the value of the deviation function. "f.m" is called as a function from the code "gradient_pojection.m".

gradient_projection.m

```
%Rosens gradient projectin method to solve the slicing optimization
problem
%Written on 15th September 2007

clear all;

%Calculating the projection matrix
for n = 3:1:30;


    for i = 1:1:n;

       B(i) = 1;
    end
    clear i;
    P = eye(n)- transpose(B)*(inv(B*transpose(B)))*B;

    %Calculating delf

    for i = 1:1:n;
       xstart(i) = 1800/n;
    end



    clear i;
    direction = [100,100];
    clear count;
    count = 1;
    while (sum(abs(direction))>1e-5 & count < 100);
       direction1 = direction;
       clear direction;
       Z = f(xstart);
       for i = 1:1:n;
```

```
            xstart1 = xstart;
            xstart1(i) = xstart(i) + 0.1;
            Z1 = f(xstart1);
            delf(i) = Z1-Z;
            clear xstart1;
        end
        clear i;
        delf = transpose(delf);
        d0 = P*delf;
        direction = d0;
        d0 = -d0;
        maxd0 = max(abs(d0));
        if maxd0>0;
            d0 = d0/maxd0;
            alpha = 2;
            while alpha >=(1/4096)
                 xstart1 = xstart + alpha*transpose(d0);
                 if f(xstart1) < f(xstart)
                    xstart = xstart1;
                 else
                     alpha = alpha/2;
                 end
            end
        end
         clear delf;
         count = count + 1;
    end
         n
         xstart
         f(xstart)
end
```

f.m

```
%Here, the function f is defined
function Z = f(x)

%Evaluating delta and d1plus
for count1 = 2:1:max(size(x));
    sum1 = 0;
    sum2 = 0;
    for i = 1:1:count1;
        sum1 = sum1 + x(i);
    end
    clear i;
    for i = 1:1:count1-1;
        sum2 = sum2 + x(i);
    end

    if  sum1 <= 1200;
        r1 = ((1200-sum1)^2)/7200 + 400;
    end
    if sum1 >1200;
        r1 = -((sum1-1200)^2)/1200 + 400;
    end
```

```
    if  sum2 <= 1199;
        r2 = ((1200-sum2)^2)/7200 + 400;
    end
    if sum2 >1200;
        r2 = -((sum2-1200)^2)/1200 + 400;
    end
    deltar(count1) = abs(r1-r2);
    theta(count1) = atan(deltar(count1)/x(count1));
    delta(count1) = x(count1)*sin(theta(count1));
end
theta1 = atan(abs(((1200-x(1))^2/7200-200)/x(1)));
delta1 = abs((x(1)*sin(theta1)));
Max1Delta = max(delta);
MaxDelta = max(Max1Delta, delta1);
d1plus = (MaxDelta - 40)/40;
if d1plus < 0;
    d1plus = 0;
end
clear count1;

%Now, evaluating the build time
BT = 0;
for i = 1:1:max(size(x))
       Ttrans = 10;
       Tsettle = 30000/x(i);
       Texp = ((x(i)+40)/19.172+10.5)/0.7;
       BT = BT + Ttrans + Tsettle + Texp;
       clear Ttrans;
       clear Tsettle;
       clear Texp;
end
d2plus = (BT-4200)/4200;

if d2plus < 0;
    d2plus = 0;
end
%Evauating the penalty function
penalty = 0;
for i = 1:1:max(size(x));
    if x(i) - 600 < 0;
        temp1 = 0;
    else
        temp1 = x(i) - 600;
    end
    if 60-x(i) < 0;
        temp2 = 0;
    else
        temp2 = 60-x(i);
    end
    penalty = penalty + temp1 + temp2;
    clear temp1;
    clear temp2;
end

Z = 0*d1plus + 1*d2plus + 1000000*penalty;
```

REFERENCES

Accumax Toolkit User Guide, 1996, 3D Systems Inc., Valencia CA.

Bayt R. and Breuer K., 2000, "Fabrication and testing of micron sized cold-gas thrusters", Progress in Astronautics and Aeronautics series, 147, pp.381.

Belegundu A. D., Chadrupatla T. R., 1999, "Optimization Concepts and Applications in Engineering", Prentice Hall Inc.

Beluze L., Bertsch A., Renaud P., 1999, "Microstereolithography: a new process to build complex 3D objects", SPIE Symposium on design, test and microfabrication of MEMS/MOEMS, Vol. 3680, pp. 808-17.

Bertsch A., Zissi S., Jezequel J., Corbel S., Andre J., 1997, "Microstereolithography using liquid crystal display as dynamic mask-generator", Microsystems Technologies, pp.42-47.

Bertsch A., Jezequel J. Y., Andre J.C., 1997, "Study of spatial resolution of a new 3D microfabrication process: the microstereolithography using a dynamic mask-generator technique", Journal of Photochemistrey ad Photobiology A: Chemistry 107, pp. 275-281.

Bertsch A., Bernhard P., Vogt C., Renaud P., 2000, "Rapid prototyping of small size objects", Rapid Prototyping Journal, Vol. 6, Number 4, pp. 259-266.

Bertsch A., Bernhard P., Renaud P., 2001, "Microstereolithography: Concepts and applications", IEEE pp. 289-298.

Bertsch A., Jiguet S., Renaud P., 2004, "Microfabrication of ceramic components by microstereolithography", Journal of Micromechanics and Microengineering, pp.197-203

Chatwin C., Farsari M., Huang S., Heywood M., Birch P., Young R., Richardson J., 1998, "UV microstereolithography system that uses spatial light modulator technology", Applied Optics, Vol. 37, pp.7514-22.

Chatwin C., Farsari M., Huang S., Heywood M., Young R., Bitch P., Claret-Tournier F., Richardson J., 1999, "Characterisation of epoxy resins for microstereolithographic rapid prototyping", International Journal of Advanced Manufacturing technologies, Vol. 15, pp.281-6.

Chen C. and Sullivan P., 1996, "Predicting total build time and the resultant cure depth of the 3D stereolithography process", Rapid Prototyping Journal, Vol. 2, Number 4, pp.27-40

Drobny J., 2002, “Radiation technology for polymers”, CRC press.
Dudley D., Duncan W., Slaughter J., 2003, “Emerging Digital Micromirror Device (DMD) applications”, SPIE proceedings, Vol. 4985.

Edmund Industrial Optics 2003, “Optical and optical instruments Catalog”.

Farsari M., Huang S., Birch P., Claret-Tournier F., Young R., Budgett D., Bradfield C., Chatwin C., 1999, “Microfabrication by use of spatial light modulator in the ultraviolet: experimental results”, Optics Letters, Vol. 24, No. 8, pp. 549-50.

Farsari M., Claret-Tournier F., Huang S., Chatwin C., Budgett D., Birch P., Young R., Richardson J., 2000, “A novel high-accuracy microstereolithography method employing an adaptive electro-optic mask”, Journal of Material Processing Technology 107, pp. 167-172.

Fujimasa I., 1996, “Micromachines: A new era in Mechanical Engineering”, Oxford University Press.

Gardner J., Varadan V., Awadelkarim O., 2001, “Microsensors MEMS and Smart Devices”, John Wiley and Sons.

Hadipoespito G., Yang Y., Choi H., Ning G., Li X., 2003, “Digital Micromirror device based microstereolithography for micro structures of transparent photopolymer and nanocomposites”, Proceedings of the Solid Freeform Fabrication Symposium, Austin Texas, pp. 13-24.

Hope R., Roth R., Jacobs P., 1997, “Adaptive slicing with sloping layer surfaces”, Rapid Prototyping Journal, Vol. 3, Number 3, pp. 89-98

Ikuta K., Hirowatari K., 1993, “Real three dimensional micro fabrication using Stereolithography and metal molding”, Proceedings IEEE MEMS, pp.42-47.

Ikuta K., Maruo S., Yuichiro F., Fujisawa T., 1998, “Biomedical IC chip towards cell free DNA protein synthesis”, Proceedings of the IEEE International Workshop on Micro Electro Mechanical Systems (MEMS98), pp. 131-136

Ikuta K., Maruo S., Fujisawa T., Yamada A., 1999, “Micro concentrator with Opto-sense Micro Reactor for Biochemical IC Chip Family-3D Composite Structure and Experimental Verification-, Twelfth IEEE conference on Micro Electro Mechanical Systems, pp. 376-381

Jacobs P., 1992, "Rapid Prototyping and Manufacturing Fundamentals of StereoLithography", Society of Manufacturing Engineers.

Laoui T., Shaik S., Hall, R., Schneider A., 2005, "Microfabrication of dental root implants with porous surface layer by Microstereolithography", Proceedings of the 2nd international conference on advanced research in Rapid Prototyping, Leiria, Portugal, 28 September-1 October, pp. 47-51.

Limaye A., Rosen D., 2004, "Quantifying dimensional accuracy of a Mask Projection Micro Stereolithography System", Proceedings of the 15th Solid Freeform Fabrication Symposium, Austin TX, pp. 481-492.

Limaye A., 2004, "Design and Analysis of a Mask Projection Micro-Stereolithography System", Masters Thesis, Georgia Institute of Technology, Atlanta GA.

Limaye A., Rosen D., 2005, "Process planning method for curing accurate microparts using Mask Projection Micro Stereolithography", Proceedings of the 2nd international conference on advanced research in Rapid Prototyping, Leiria, Portugal, 28 September-1 October, pp. 441-448.

Limaye, A., and Rosen, D., 2006, "Compensation zone approach to avoid print-through errors in Mask projection Stereolithography builds", Rapid Prototyping Journal, Vol. 12, Number 5, pp. 283-291.

Limaye, A., Rosen, D, 2007, "Process planning method for mask projection micro-Stereolithography", Rapid Prototyping Journal, Vol.13, Number 2, pp.76-84.

Lynn-Charney C. and Rosen D., 2000, "Usage of accuracy models in stereolithography process planning", Rapid Prototyping Journal, Vol. 6, Number 2, pp. 77-86.

Mani K., Kulkarni P., Dutta D., 1999, "Region based adaptive slicing", Computer-Aided Design, Vol. 31, pp. 317-333.

Maruo S., Nakamura O., Kawata S., 1997, "Three-dimensional microfabrication with two-photon-absorbed photopolymerization", Optical Letters, Vol. 22, Number 2, pp.132-134.

Maruo S. and Kawata S., 1998, "Two-photon-absorbed near –infrared photopolymerization for three-dimensional microfabrication", Journal of Microelectromechanical Systems, Vol. 7, Number 4, pp. 411-415.

Meacham J., Ejimofor C., Kumar S., Degertekin F., Fedorov A., 2004, "Micromachines ultrasonic droplet generator based on a liquid horn structure", Review of Scientific Instruments, Vol. 75, Issue 5, pp. 1347-1352.

Mistree F., Patel B., Vadde S., 1994, "On modeling multiple objectives and multi-level decisions in concurrent design", Proceedings ASME Design Automation conference, Vol. 69, Issue 2, pp. 151-161.

Monneret S., Loubere V., Corbel S., 1999, "Microstereolithography using dynamic mask generator and a non-coherent visible light source", Proc. SPIE, Vol.3680, pp.553-561.

Monneret S., Provin C., Le Gall H., 2001, "Micro-scale rapid prototyping by stereolithography", 8th IEEE international conference on emerging technologies and factory automation (ETFA 2001), Vol. 2, pp. 299-304.

Myers R.and Montgomerry D., 1995, "Response susrface methodology: process and product optimization using designed experiments", New York: Wiley.

Nakamoto T, Yamaguchi K., 1996, "Consideration on the producing of high aspect ratio microparts using UV sensitive photopolymer", Proceedings 7th International Symposium on Micromachine Human Sciences, pp.53-58

Nakamoto T., Yamaguchi K., Abraha P., Mishima K., 1996, "Manufacturing of htree-dimensional micro-parts by UV laser induced polymerization", Journal of Micromachining and Microengineering, pp.204-253

www.newport.com (11th August 2005)

Oriel instruments, 2003, "The Book of Photon Tools".

O'Shea D., 1985, "Elements of Modern Optical Design", Wiley.

Pahl G., Beitz W., 1996, "Engineering Design: A Systematic Approach", Springer Verlag.

Paul B. and Voorakarnam V., 2001, "Effect of layer thickness and orientation angle on surface roughness in laminated object manufacturing", Journal of Manufacturing Processes, Vol. 3, Number 2, pp. 94-101.

Reeves P. and Cobb R., 1997, "Reducing the surface deviation of stereolithography using in-process techniques", Rapid Prototyping Journal, Vol. 3, Number 1, pp. 20-31.

Sabourin E., Houser S., Helge Bohn J., 1996, "Adaptive slicing using stepwise uniform refinement", Rapid Prototyping Journal, Vol. 2, Number 4, pp. 20-26.

Sager B. and Rosen D., 2005, "Development and use of analytical cure models to improve stereolithography surface finish", Proceedings of the 2nd international conference

on advanced research in Rapid Prototyping, Leiria, Portugal, 28 September-1 October, pp. 493-500.

Smith W., 1990, “Modern optical engineering: the design of optical systems”, McGraw Hill.

Suh Y. and Wozny M., 1994, “Adaptive slicing of solid freeform fabrication processes”, Proceedings of the Solid Freeform Fabrication Symposium, Austin TX, pp. 404-411.

Sun C., Fang N., Wu D., Zhang X., 2005, “Projection micro-stereolithography using digital micro-mirror dynamic mask”, Sensors and Actuators A., Vol. 121, pp. 113-120.

Tyberg J., Bohn J., 1998, “Local adaptive slicing”, Rapid Prototyping Journal, Vol. 4, Number 3, pp.118-127.

West A., Sambu S., Rosen D., 2001, “A process planning method for improving build performance in stereolithography”, Computer-Aided Design, Vol. 33, pp. 65-79.

Zhao Z., Laperriere L., 2000, “Adaptive direct slicing of the solid model for rapid prototyping”, International Journal of Production Research, Vol. 38, Number 1, pp. 69-83.